Fracture in Reinforced Concrete

Computational and Analytical Studies

By

Olivier J. Gastebled

Submitted for the degree of Doctor of Philosophy at Heriot-Watt University

On completion of research in the Department of Civil and Offshore Engineering

December 1999

I hereby declare that the work presented in this thesis was carried out by myself at Heriot-Watt University, Edinburgh, except where due acknowledgement is made, and has not been submitted for any other degree.

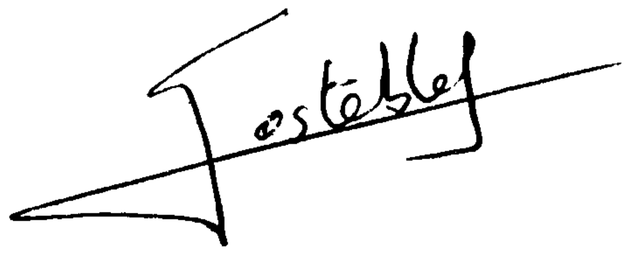

OLIVIER J. GASTEBLED

Candidate

Prof. IAN M. MAY

Supervisor

Date 03/04/2000

Abstract

Fracture plays a decisive role in the failure mechanism of certain reinforced concrete structures. While the customary approach to the design of reinforced members is to ignore the tensile contribution of concrete, it is not possible to do so when the bond between the steel reinforcement and the surrounding concrete is an essential structural component of a member. Much research effort has been devoted recently to the study of the fracture mechanics of plain concrete. However, no definitive results have been reached that could be applied to reinforced concrete. This is mainly due to the fact that reinforced concrete does not simply act as the sum of the reinforcement and the concrete, but as a composite material where concrete and steel behaviours are coupled.

The objective of this study was to gain a physical insight into the fracture mechanics of bond in reinforced concrete so that analytical models could be developed and applied to modes of failures where bond plays a decisive role.

A review of the strain softening fracture in plain concrete is given. This chapter comprises essentially the theories developed by others to understand and model strain softening fracture. A phenomenological approach is first presented, followed by the theory of fracture mechanics applied to concrete and by the numerical methods available to simulate fracture in concrete, including non-linear finite element analysis.

Using these various approaches, the fracture mechanics of bond in reinforced concrete is then investigated. A complex finite element model is developed to simulate the cracking mechanisms taking place in reinforced concrete tension specimens. The mechanism of ultimate bond failure is identified as the propagation of a splitting crack. An analytical fracture mechanics model considering the energy balance of the concrete and the reinforcing bar is proposed to predict the splitting load.

This fracture mechanics model is introduced into a more complex numerical model and full simulation of the cracking behaviour of tension specimens is achieved and showed to compare well with experimental data. Following the validation of the bond model, the shear failure of beams without stirrups is identified as a bond failure by splitting. Consequently, a mechanical model is developed including the fracture mechanics model for splitting. The analytical formula obtained is shown to be in agreement with an empirical formula given by the CEB-FIP code.

Finally, the premature peeling failure of beams strengthened by plate gluing is tackled with the same approach. A phenomenological approach reveals that peeling is a phenomenon similar to bond failure by splitting. Two separate fracture mechanics models are developed to predict the peeling failure, one for peeling in pure bending and one for the flexural-shear mode of peeling. The models are successfully benchmarked against over a hundred experimental results.

Conclusions and recommendations for further work are presented in the last part of this thesis.

Keywords

bond, finite element analysis, flexural-shear failure, fracture mechanics, plated beams, peeling failure, reinforced concrete, splitting crack, strain softening.

Résumé

L'objectif de cette étude est de parvenir à une meilleure compréhension du lien béton/acier dans les structures de béton armé, sous l'angle de la mécanique de la rupture, ceci dans le but de développer des modèles analytiques pouvant être appliqués à des modes de ruine où le lien béton/acier joue un rôle décisif. Une revue critique des publications sur la rupture adoucissante est réalisée. Ce chapitre présente, en majeure partie, des théories développées par d'autres chercheurs. Partant de ces théories, le lien béton/acier est étudié en détail. Un modèle aux éléments finis est développé pour simuler les mécanismes de fissuration présents dans les tests en traction d'éléments de béton armé. Le mécanisme de rupture du lien béton/acier est identifié comme étant la propagation d'une fissure de séparation. Un modèle analytique de mécanique de la rupture est proposé pour prévoir la charge de séparation. Après avoir validé ce modèle en comparant les résultats d'une simulation numérique avec des résultats expérimentaux, le mode de ruine des poutres en béton armé sans armatures transversales est identifié comme étant dû à la propagation d'une fissure de séparation. La formule analytique est validée par comparaison avec une formule empirique du code CEB-FIP. Finalement, la ruine prématurée par délaminage des poutres renforcées par collage extérieur de plaques est étudiée. L'approche phénoménologique révèle que le délaminage est un phénomène similaire à la rupture du lien béton/acier par séparation. Deux modèles distincts de mécanique de la rupture sont développés pour prévoir la charge de délaminage, le premier modèle étant applicable au cas de la flexion pure et le deuxième aux cas mixtes en flexion-cisaillement. Ces modèles sont vérifiés par comparaison avec plus d'une centaine de résultats expérimentaux.

Mots clés

analyse aux éléments finis, béton armé, collage extérieur de plaques, délaminage, fissure de séparation, lien béton/acier, mécanique de la rupture, poutre renforcée par collage extérieur de plaques, rupture adoucissante.

Samenvatting

Het doel van het hier gepresenteerde onderzoek is het verkrijgen van fysisch inzicht in breukvorming van verbindingen in gewapend beton, zodat analytische modellen ontwikkeld kunnen worden. De modellen moeten worden toegepast in situaties waar verbindingen een beslissende rol spelen in het optreden van breukvorming. Eerst wordt een overzicht gegeven van strain-softening breukgedrag in ongewapend beton. De behandelde theorieën over breukvorming zijn door anderen ontwikkeld. Deze theorieën worden uitgebreid zodat ze ook toepasbaar worden op gewapend beton. Een complex eindige elementen model is ontwikkeld voor de simulatie van scheurmechanismen die optreden in gewapend beton onder spanning. Het uiteindelijke bezwijken van verbindingen wordt verklaard door de voortplanting van barsten. Vervolgens wordt een analytisch model geïntroduceerd om de splijtbelasting te voorspellen. De geldigheid van dit model is getest door de uitkomst van een numerieke simulatie van monsters onder druk te vergelijken met experimentele data, het afschuiffaalgedrag van balken zonder beugel kan verklaard worden als bindingsbezwijking door splijten. Een mechanisch model voor afschuifbuigbreuk is ontwikkeld, inclusief het breukvormingsmodel voor splijten. De verkregen analytische formule komt overeen met de empirische formule zoals gegeven in de CEB-FIP code. Tenslotte is het vroegtijdig afschuiven van platen van betonconstructies met uitwendig opgelijmde platen aangepakt. Een fenomenologische aanpak laat zien dat het afschuiven van de platen vergelijkbaar is met de bindingsbezwijking door splijten. Twee aparte breuk mechanische modellen zijn ontwikkeld om het loslaatgedrag te voorspellen, één voor het afschuiven in het geval van alleen buiging en één voor het geval van afschuifbuigbreuk. De geldigheid van de modellen is met succes getoetst aan meer dan honderd experimentele resultaten.

Trefwoorden:

afschuifbuigbreuk, breukmechanisme, eindige elementen analyse, gewapend beton, loslaat-gedrag, opgelijmde platen, spanningsreductie, splijtgedrag, verbinding.

Acknowledgements

I would like to express my gratitude and my sincere thanks to my supervisor, Prof. Ian M. May, for the many stimulating talks we had, for his advice and his encouragement. Prof. Ian M. May has been a source of great help and guidance throughout the period of my study.

I am grateful to my family, my parents for their loving support and my brother for his patience and care. I want to thank sincerely my parents without whose help it would not have been possible to undertake this PhD.

I would also like to thank my friends in Edinburgh, Judith, Paul and Javad, whose care and friendship I could always count on.

Finally, I would also like to thank the other members of staff of the department of Civil and Offshore Engineering who provided me with their help when I needed it.

Contents

List of Tables

List of Figures

Notation and Abbreviations

A_{frac}	projected area of fractured surface	[m^2]
A_c	area of concrete influence by the reinforcement	[m^2]
A_s	area of the reinforcing bar	[m^2]
C	structural compliance matrix	[m/N]
$C_{N,T}$	normal and tangential crack opening compliance	[m/N]
$D^{I,II}$	normal and tangential crack opening stiffness	[N/m]
D^e	material elastic stiffness matrix	[N/m]
D^{cr}	material softening stiffness matrix	[N/m]
$E_{(c,s)}$	modulus of elasticity (indices: c = concrete, s = steel)	[N/m^2]
E_{kin}	kinetic energy	[J] or [N.m]
F	applied load (generalised force)	[N]
F_c	compressive force in concrete	[kN]
F_{cr}	ultimate applied load	[kN]
F_s	force in reinforcing steel	[kN]
F_{sp}	applied force at onset of visible splitting	[N]
F_u	ultimate load	[N]
F_I	fracture mechanics function, LEFM analysis of a ring	-
G	fracture energy consumed by cracking	[J] or [N.m]
G_f	specific fracture energy	[J/m^2] or [$N.m/m^2$]
G_{fo}	base value of G_f (defined by CEB-FIP Model Code)	[J/m^2] or [$N.m/m^2$]
G_s	shear modulus of steel	[N/m^2]
$G(x)$	bordered stiffness matrix	-
H	height of the beam	[m]
Id	identity matrix	-
K	structural stiffness matrix	[N/m]
K_{ini}	initial stiffness of the specimen per unit length	[N/m^2]
K_s	secant structural stiffness matrix	[N/m]
K_{sp}	stiffness of the split specimen per unit length	[N/m^2]
K_t	tangential structural stiffness matrix	[N/m]
$K_{I,II,III}$	stress intensity factors in mode I, II, III fracture	[$N.m^{1/2}/m^2$] or [$N.m^{-3/2}$]
K_{IC}	mode I fracture toughness (critical stress intensity factor)	[$N.m^{1/2}/m^2$] or [$N.m^{-3/2}$]
L	bar length	[m]
L_{av}	average crack spacing	[m]
L_{max}	length over which slip between steel and concrete occurs	[m]
M	bending moment	[kN.m]
M_{cr}	critical bending moment	[kN.m]

M_{exp}	experimental ultimate bending moment	[kN.m]
M_{num}	analytical ultimate bending moment	[kN.m]
M_s	serviceability bending moment	[kN.m]
M_u	ultimate bending moment	[kN.m]
N	transformation matrix	-
R	energy release rate of a fracturing structure	[J/m^2] or [N.m/m^2]
$T_{0\text{-}7}$	forces carried by a component of the model	[N]
U_{el}	elastic strain energy stored in the structure	[J] or [N.m]
U_{el}^{ini}	elastic strain energy in the initial cross-section	[J]
U_{el}^{sp}	elastic strain energy in the split cross-section	[J]
V	shear force	[kN]
V_b	maximum bond stress shear capacity	[kN]
V_{exp}	experimental ultimate shear force	[kN]
V_c	shear carried by the concrete in the compression zone	[kN]
V_{cr}	ultimate shear force	[kN]
V_d	dowel force in the longitudinal reinforcement	[kN]
V_{fl}^{0}	minimal flexural peeling shear force	[kN]
V_{fl}^{cr}	shear force at the onset of flexural cracking	[kN]
V_{fl}^{α}	flexural peeling shear force	[kN]
V_{num}	theoretical ultimate shear force	[kN]
V_{sh}^{0}	minimal flexural-shear peeling load	[kN]
V_{sh}	flexural-shear peeling load	[kN]
V_{th}	theoretical ultimate shear force	[kN]
W_{ext}	work of external loads on the structure	[J] or [N.m]
W_f	energy available for fracture	[J] or [N.m]
W_0	work of external force in a three-point bend test	[J] or [N.m]
a	crack extent	[m] or [m^2]
a_c	distance of critical flexural-shear section from support	[m]
a_s	shear span	[m]
a_0	initial crack extent	[m]
b	breadth of the specimen	[m]
b_p	breadth of the plate	[m]
c	concrete cover	[m]
c_f	fully developed effective crack extension	[m]
c_l	longitudinal distance from the concrete surface	[mm]

c_n	depth of the neutral axis	[m]
d	effective depth of the beam	[m]
d_{agg}	maximum aggregate size	[m]
d_b	bar diameter	[m]
d_{ch}	characteristic dimension of the structure	[m]
e	radius of cracked ring	[m]
e_c	critical extent of the cracked ring	[m]
e_0	eigen-vector of zero eigen-value	[m]
e_{ch}	characteristic element size	[m]
e^{cr}	cracking strain in the coordinate system of the crack	-
f_c	concrete compressive strength	[MPa]
f_{c0}	base value of f_c (defined by CEB-FIP Model Code)	[MPa]
f_t	concrete tensile strength	[MPa]
f_y	yield strength	[N/m^2]
g	acceleration of gravity	[m/s^2]
$g(x)$	out-of-balance forces (in finite element formulation)	[N]
h	crack band width	[m]
l_{ch}	material characteristic length	[m]
m	self-weight	[kg]
n	number of ribs in front of the considered cross-section	-
$\vec{n}$	unit vector normal to the cracking plane	-
$\vec{n}_0$	initial $\vec{n}$	-
p_i	internal pressure in ring	[N/m^2]
p_k	internal variables	-
q	nominal load vector (in finite element formulation)	[N]
r	radial distance from crack tip	[m]
r_i	ring internal radius (bar radius)	[m]
r_s	rib spacing	[m]
r_0	ring outer radius	[m]
r_{ef}	distance of the effective elastic stress from crack tip	[m]
r_{nl}	radius of the non-linear process zone around crack tip	[m]
s^{cr}	cracking stress in the coordinate system of the crack	[N/m^2]
s	steel-to-concrete slip	[m]
t	thickness	[m]
t_f	transfer length	[m]
$\vec{t}, \vec{s}$	unit vectors in the cracking plane	-
u	displacement(s) at the application point(s) of F	[m]

w	crack width	[mm]
w^{cr}	crack opening displacement	[m]
w_{ult}^{cr}	ultimate crack opening displacement	[m]
w_{Tc}	critical crack-tip opening displacement (Jenq and Shah)	[m]
$x = \begin{pmatrix} u \\ \lambda \end{pmatrix}$	augmented variable vector (in finite element formulation)	-
x^*	singular point	-
y	lever arm between the reinforcing bar and the centroid of the compressive stresses	[m]
y_{cr}	depth of the neutral axis in the cracked cross-section	[m]
$\bar{y}$	distance from the centroid of the compressive stresses to the top fiber	[m]
Δa_e	effective crack extension	[m]
ΔS_{int}	internal entropy produced by cracking	[J/°K]
Γ	fracture energy required per unit length extension of the splitting crack	[J/m]
Π	potential energy of the structure	[J] or [N.m]
Σ_s	reduced cross-section of the steel bar	[m^2]
Ω	non-local damage variable	-
α	correction factor for the fracture energy of conical cracks	-
α_{cc}	conical crack angle	-
α_c	crack extent ratio	-
$\alpha_{c,u}$	ultimate crack extent ratio	-
α_F	material constant defining the ultimate crack opening	-
β	y to H ratio	-
β_s	shear retention factor	-
γ	d to H ratio	-
γ_{nt}	shear strain in the plane $(\vec{n}, \vec{t})$	-
δe	incremental splitting extent	[m]
δ_s	unbonded length of the longitudinal reinforcement	[m]
δ_v	unbonded length of the stirrups	[m]
ε	total strain	-
ε^e	elastic strain	-

ε_s^e	elastic strain in the reinforcing bar	-
ε^p	plastic strain	-
ε_{ct}	cracking strain of concrete	-
ε_{nn}	direct strain in the direction $\vec{n}$	-
ε_s^y	plastic strain in the reinforcing bar	-
ε_s	strain in the steel bar	-
$\tilde{\varepsilon}^f$	maximum cracking strain in the loading history	-
ϕ	angle of the diagonal crack	-
ϕ_s	diameter of the longitudinal reinforcement	[m]
ϕ_v	diameter of the stirrups	[m]
φ^*	initial direction vector of the bifurcated branch	-
γ_m	safety factor as defined in BS 8110	-
λ	scalar load factor	-
μ	softening variable of plasticity theory	-
$\mu_{exp/num}$	mean value of experimental results around the prediction	-
ν	Poisson's ratio	-
ν_s	Poisson's ratio of steel	-
θ	rotation angle in the flexural-shear failures	-
θ_{cr}	threshold angle for the multi-directional crack model	-
ρ	density	-
ρ_s	reinforcement ratio (A_s/A_c)	-
σ	total stress	[N/m^2]
$\sigma_{exp/num}$	standard deviation of experimental results around the prediction	-
σ_n	longitudinal stress due to n ribs	[N/m^2]
σ_{nn}	direct stress in the direction $\vec{n}$	[N/m^2]
σ_N	nominal stress	[N/m^2]
$\sigma_{N,u}$	ultimate nominal stress	[N/m^2]
σ_h	ring hoop stress	[N/m^2]
σ_r	ring radial stress	[N/m^2]
σ_s^e	elastic stress in the reinforcing bar	[N/m^2]
σ_t^{cr} or σ_t	normal tensile stress across crack	[N/m^2]
σ_y	vertical stress	[N/m^2]
τ	bond stress	[N/m^2]
τ_e	shear stress at the tip of the conical crack	[N/m^2]

τ_{max}	maximum bond stress	[N/m^2]
$\tau_{\max}^{sp}$	maximum bond stress due to splitting	[N/m^2]
$\tau_{\max}^{sc}$	maximum bond stress due to secondary cracking	[N/m^2]
ω	scalar damage variable	-
ω_T	tangential damage variable	-

1. INTRODUCTION

1.1. Fracture in Reinforced Concrete

It is normal practice when designing reinforced concrete members in bending to consider the cracked concrete under the neutral axis as a continuous medium resisting shear and transverse compression but unable to carry any tension. The adoption of this simplified assumption, together with empirical design rules aimed at satisfying serviceability requirements, is assumed to provide safe and durable design in bending.

While this approach is conservative and results in ductile behaviour for flexural modes of failure, this is not necessarily the case for other types of failure[1,2]. Ignoring the tensile strength of concrete is only acceptable when the concrete in tension plays a minor role in the load carrying mechanism considered, as in the bending case. This is no longer true if structural shear and local steel-to-concrete bond are considered. These mechanisms, essential to the integrity of all reinforced concrete structures, are covered in present codes of practice by semi-empirical design rules[3-5], where no clear indication is made of the role played by the tensile capacity of concrete.

The lack of physical insight in the customary design methods is particularly problematical when confronted by unexpected brittle modes of failure in unconventional structures. When designing structures outside the range of normal practice, either by their size[6,7], by the use of new materials (high performance concrete[8] or composite materials[9]), or by the need of structural upgrading involving various strengthening techniques[10], it is necessary to understand the mechanisms of load transfer in the cracked structure to ensure that the tensile strength of concrete and the ability of the structure to redistribute the load after cracking are not critical. This is the reason why the study of concrete fracture has become a major area of reinforced concrete research in the last decade.

It is believed that it is desirable to develop a better understanding of the tensile behaviour of reinforced concrete to achieve effective and safe designs. Much research effort has been devoted recently to the study of the fracture behaviour of plain concrete. However, no definitive results were reached that could directly be applied to reinforced concrete design. This is mainly due to the fact that reinforced concrete does not simply act as the sum of the reinforcement and the concrete, but as a composite material where steel and concrete behaviours are coupled. Consequently, the behaviour of the two materials acting together needs to be considered. While steel and concrete material behaviours are reasonably well understood, this is not the case of steel-to-concrete bond, the knowledge of which remains essentially empirical. It is foreseen that if adequate modelling of bond could be achieved, a unified approach to fracture problems in reinforced concrete could be developed.

1.2. Research Objectives and Scope

Considering the present state of the knowledge on the fracture of reinforced concrete, it is clear that more physical insight into the tensile behaviour of cracked reinforced concrete needs to be gained. The objective of this study is therefore to understand and make use of the numerous experimental data available in the literature in order to:

- develop a predictive analytical model for reinforced concrete in tension based on physically sound grounds,
- and thus come closer to a unified approach to tensile failures of reinforced concrete members as proposed by the ASCE-ACI committee on shear and torsion [4].

As stated in the previous section, steel-to-concrete bond plays a decisive role in tensile failure of reinforced concrete members. Consequently, this study will focus on the simulation and the modelling of bond in reinforced concrete. In this thesis, two types of problems will be described:

- bond related failure in reinforced concrete members,
- and premature failure of beams strengthened by plate gluing.

Although the various problems tackled in this thesis may seem at first sight heterogeneous, it is shown that the failure modes considered are qualitatively similar, thus providing consistency to the thesis.

1.3. Methodology

A scientific investigation requires a robust and objective methodology adapted to the subject and the aims of the study. From the experience gained during the first part of his research time, the author has developed and adopted a methodology appropriate for the subject of this study. This methodology can be divided into the following steps:

- Start with a phenomenological approach, compiling and interpreting the qualitative experimental data available, gaining insight into the phenomenon considered.
- Identify and classify the different modes of failure.
- Further the understanding of the mechanics of the considered mode of failure (load path, cracking pattern, redistribution, stability) using non-linear finite element analysis.
- Identify the critical failure mechanism.
- Determine the important parameters and develop an analytical model, which may include a certain number of simplifying assumptions.
- Eventually, benchmark and validate the model against experimental data and empirical formulae.

This methodology is adopted for each individual problem tackled in this study.

1.4. Outline of the Thesis

Chapter 2 is an extensive review of the different approaches to strain-softening fracture in plain concrete. The phenomenological aspect of the problem is first introduced, compiling the qualitative experimental knowledge available in the literature. Then the fracture mechanics approach to concrete cracking is presented. The fundamental formulae of fracture mechanics are introduced and explained. Ways of determining the different fracture mechanics parameters are provided. The numerical tools for the simulation of strain-softening are then presented. Special emphasis is placed on the finite element method. Various constitutive models for concrete developed by other researchers are described. Problems arising in the application of non-linear solution techniques are discussed. An example of structural bifurcation is simulated by finite element analysis as an illustration of possible singular non-linear phenomena.

In the following chapter, the fracture mechanics of bond in reinforced concrete is investigated. Adopting the methodology described in the previous section and using the methods and theories presented in Chapter 2, a physical insight is gained into the mechanics of bond. A phenomenological approach is first conducted to identify and classify the different cracking mechanisms considered. A review of the existing models for bond is then presented. Further understanding is gained by developing a complex finite element model to simulate the cracking mechanisms taking place in reinforced concrete tension specimens. The mechanism of complete bond loss is identified as the propagation of a splitting crack. Finally, an analytical fracture mechanics model considering the energy balance of the concrete and the reinforcing bar acting together is proposed to predict the splitting load.

Chapter 4 deals with the application of the fracture mechanics model for splitting to reinforced concrete structures. A non-linear numerical model is built on the basis of the model for splitting to simulate the cracking history of tension specimens. Comparison with experimental results obtained by others shows that the model predicts the correct mode of failure and that the level of

accuracy of the predictions is satisfactory. Using a phenomenological approach, the flexural-shear failure of reinforced concrete beams without stirrups is shown to be triggered by splitting bond failure. Consequently, a new mechanical model for the flexural-shear failure is developed on the basis of the fracture mechanics model for splitting. The analytical formula thus obtained is successfully benchmarked against an empirical formula for flexural-shear failure given by the CEB-FIP Model Code (1990)[5].

Chapter 5 is concerned with the premature peeling failure of beams strengthened by plate gluing. The phenomenological approach reveals that peeling is a phenomenon similar to bond failure by splitting. Therefore, the fracture mechanics model for splitting can be introduced in a model for peeling. Two separate models are developed. The first model is limited to the case of peeling in pure bending, while the second model deals with peeling with the plate ending in the shear span. The models are checked against over a hundred experimental results. The resulting equations prove to predict accurately the peeling loads.

Conclusions and recommendations for further works are presented in the last chapter of this thesis.

2. STRAIN SOFTENING FRACTURE IN PLAIN CONCRETE

2.1. Phenomenological Approach

Concrete is a strong, coherent, robust, composite material consisting of stiff particles (aggregates) imbedded in a very brittle, less stiff, matrix (cement paste). While its compressive strength, f_c, typically reaches 30 to 50 MPa for normal strength concrete, its tensile strength is approximately one tenth (3 to 5 MPa).

The term concrete fracture is used to describe the tensile failure of concrete, which is characterised by the localisation and propagation of cracking along a failure surface normal to the principal tensile stress. Although compressive failure also results from the nucleation and propagation of microcracks, it differs from fracture inasmuch as cracks tends to form parallel to the principal compressive stress and remain smeared in the bulk of the material up to ultimate loss of integrity[11].

The study of concrete tensile behaviour has attracted much research effort over the past two decades. Many experimental investigations have been carried out, allowing the development of a better understanding of the fracture process. Wittman (1983)[12] was the first to introduce the concept of the "three level approach" for concrete. This approach consisted of studying experimentally the same phenomenon at three different scales and using the understanding gained at a finer level to build up the material model for the next level. The three levels are termed "micro", "meso" and "macro". They respectively describe the study of the structure of the hardened cement paste, Fig. 2-4; the study of concrete as a composite material made of the aggregates, the cement matrix and their interfaces, Fig. 2-5; and the study of concrete as an

equivalent homogenous isotropic continuum at the structural scale, Fig. 2-6.

At the micro-level, mechanical and chemical properties of the cement paste are studied. Microscopic observation shows that, even before any external load is applied to concrete, many flaws and microcracks exist in the body of the material (Fig. 2-1). The nature of the initial flaws range from discontinuities in the cement paste, to voids caused by shrinkage or incomplete compaction. These flaws can act as many potential microcrack initiators.

Micro level

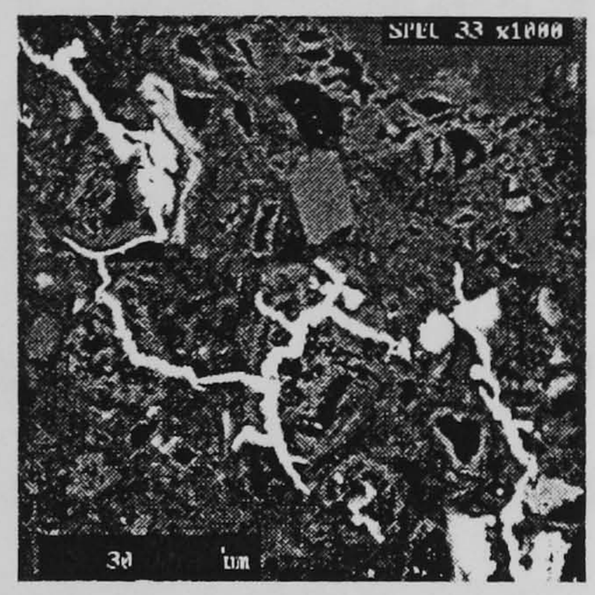

Fig. 2-1

Microcracks in cement paste

Meso level

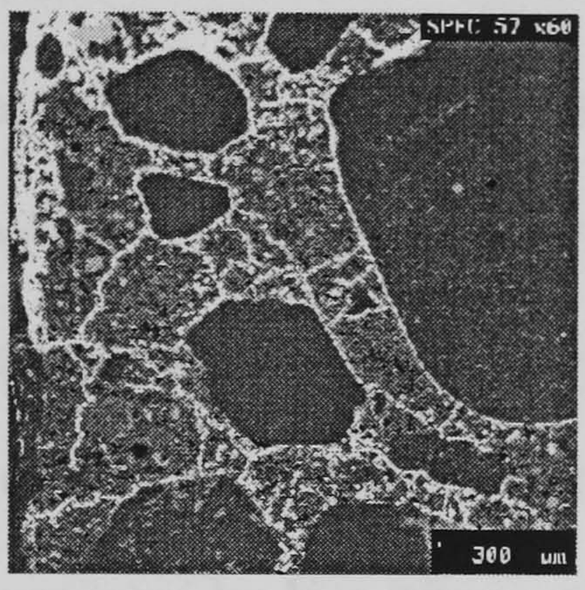

Fig. 2-2

Aggregates in cracked matrix

Macro level

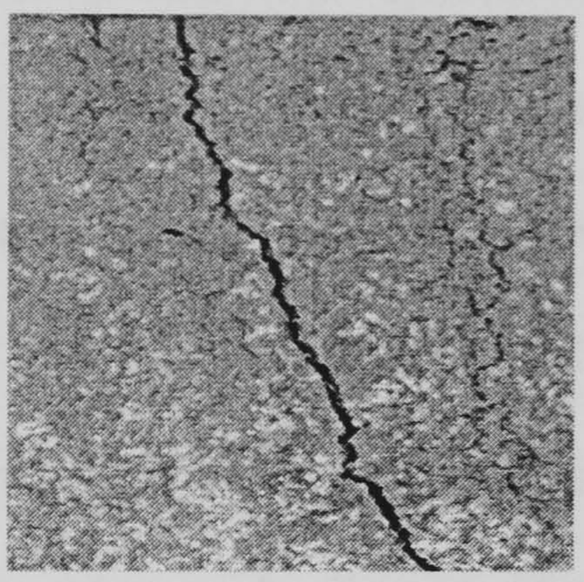

Fig. 2-3

Localisation of a macrocrack

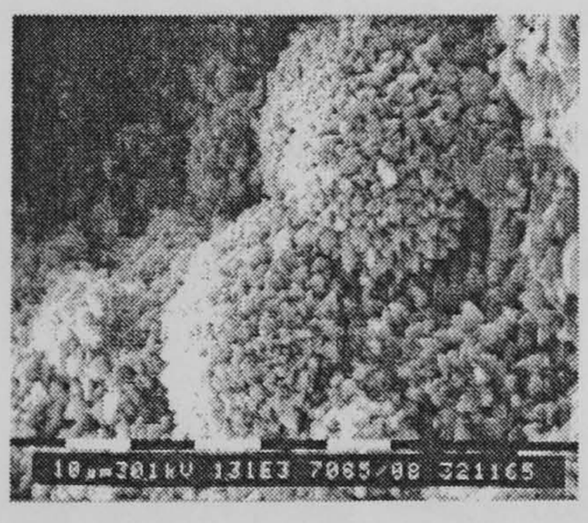

Fig. 2-4

Calcite crystals (CaCO3) in the form of a bunch

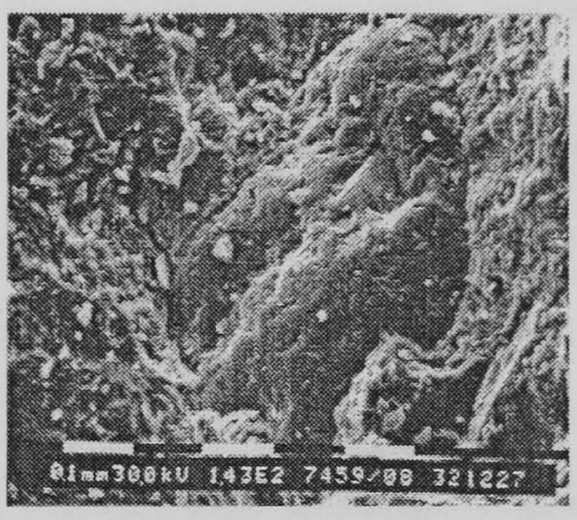

Fig. 2-5

Silicious aggregate coated by cement paste

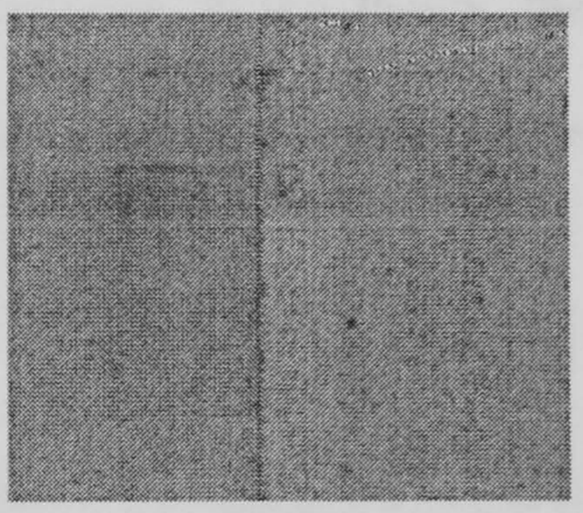

Fig. 2-6

Plain concrete

At the meso-level, the prominent role played by the aggregate-mortar interface, acting as a weaker link in the composite material, is considered[13], Fig. 2-2. Experimental observation of crack propagation[14] and finite element simulation of the composite material using lattice models[15] show that macrocracking is preceded by material damage developing from aggregate-mortar interfaces. This damaged area is termed the fracture process zone (FPZ) and consists of a

web of unconnected expanding cracks. For cross-sectional cracking in the presence of a uniform stress field, the fracture process zone precedes in time the appearance of the localised macrocrack[16] (Fig. 2-3), while, for a progressive crack front with a stress concentration at its tip, the fracture process zone precedes the macrocrack in space, in the form of a more or less smeared plume-shaped area of damaged material[17]. With new experimental techniques, it is now possible to observe directly the shape of the fracture process zone. Otsuka (1992)[18] used x-rays with contrast medium to observe the system of precursory cracks. Microscopy, interferometric techniques and acoustic emissions are other possible observation techniques.

The fracture process zone is characterised by a strain softening material behaviour. That is to say that, although the cement paste is a very brittle material, concrete actually retains some stress carrying capacity beyond cracking cut-off[19]. This phenomenon has given rise to different interpretations. Duda (1991)[20] suggested a grain model, based on the friction that occurs if aggregates are pulled from the cement paste. However, experimental observation favours the hypothesis of crack-bridging first suggested by Van Mier[21], and later taken up by Bažant. The idea is based on the fact that small precursory cracks developing in front of the main crack tip are never aligned with the former, due to the composite nature of concrete. In this theory, the untorn ligaments of mortar existing between the main crack tip and the offset precursory cracks account for the softening behaviour of concrete.

At the macro-level, strain-softening is observed in uniaxial tensile tests if the loading process is controlled by prescribed deformations[22]. The load-displacement curve is then made of an approximately linear ascending branch, followed by an exponentially-shaped descending curve accounting for strain-softening. Investigations carried out at the Stevin Laboratory (Delft University of Technology, The Netherlands) by Reinhardt (1984)[23], Van Mier (1986)[24] and Hordijk (1991)[25] has shown that a direct and unbiased determination of the softening parameters is a difficult and tedious task. The difficulty lies in separating material behaviour from structural effects (non-uniform cracking and boundary condition effects).

To date, it is still not clear if strain-softening can be considered as a constitutive material law for concrete. While the curves obtained from direct tensile tests are satisfactorily consistent and seem solely material dependent, there is no proof that strain-softening arising ahead of a cracking front in a concrete structure consistently displays the same softening curve. Since the fracture process zone is a distributed phenomenon, there are concerns that the softening process may be influenced by the nature of the stress field surrounding the crack tip. Bažant[14] showed that the crack propagation was shifting from stable to unstable when four-point bend specimens were tested instead of three-point bend tests. He explained this phenomenon by the differences in the shape and size of the fracture process zones displayed by the two types of test. This would contradict the concept of "autonomy of the fracture process zone" formalised by Broberg (1982)[26] and considered as a fundamental principle of concrete's non-linear fracture mechanics (NLFM). Although the question remains open, most of the recent studies on concrete fracture assume that the strain-softening behaviour of concrete is solely material dependant.

2.2. Fracture Mechanics Approach

Traditionally, prediction of cracking is based on a strength criterion. Cracking is expected to occur when the tensile principal stress reaches the cracking strength of the material, f_t. This approach is appropriate for cross-sectional cracking in the presence of a uniform stress field. However, after Inglis (1913)[27] obtained the solution for the stress distribution around a crack tip in a perfectly elastic material and showed that there is a stress concentration in which the stress is tending towards infinity no matter how small the applied load, it became obvious that the strength criterion is irrelevant for the prediction of unstable crack propagation. This led Griffith (1921[28], 1924[29]) to propose an energy criterion of failure, which is the basis of modern fracture mechanics.

The incompatibility of the two criteria of failure is easily verified by considering for instance

the well known "size effect" defined as follows. The strength criterion predicts that similar structures of different sizes always fail at the same nominal stress, while the energy criterion of the fracture mechanics predicts a decrease of the nominal stress at failure with increasing size of the structure[7]. This apparent duality in the failure criterion was elucidated recently as the understanding of the non-linear phenomena involved in fracture improved. Broberg (1982)[26] stated that, while the onset of stable crack growth is a phenomenon locally governed by the tensile strength of the material, unstable crack propagation is a question of global energetic stability. Consequently, for concrete structures with a characteristic size smaller than the length of a fully developed fracture process zone, failure will be controlled by the onset of cracking, that is the strength criterion. But for large structures, where non-linear phenomena can develop completely, failure due to crack propagation is driven by energetic instability. The aim of fracture mechanics is to predict the threshold of energetic instability and to study the transition between strength controlled failure and energy driven fracture.

2.2.1. Linear Elastic Fracture Mechanics

Linear Elastic Fracture Mechanics (LEFM), which deals with the propagation of sharp cracks in elastic bodies, forms the basis of Fracture Mechanics. The fundamental principles of LEFM were first stated by Griffith (1921)[28] who formulated the crack growth criterion as an energy conservation principle.

Fundamental Principle

The fundamental principle can be expressed as follows. For a crack front to progress, enough energy must be released by the load-structure system during this propagation to feed the fracture

energy consumption. This results in the following equalities for an incremental progress of the crack front:

$$\delta G = \delta W_f \qquad \textit{(Eq. 2-1)}$$

with δG, the energy consumed by the incremental progress of the crack front

and δW_f, the energy available for fracture

δW_f, is determined by energy balance:

$$\delta W_f = \delta W_{ext} - \delta U_{el} - \delta E_{kin} \qquad \textit{(Eq. 2-2)}$$

with δW_{ext}, the incremental work of the loads

δU_{el}, the incremental variation of the elastic strain energy stored in the structure

and δE_{kin}, the incremental variation of the kinetic energy

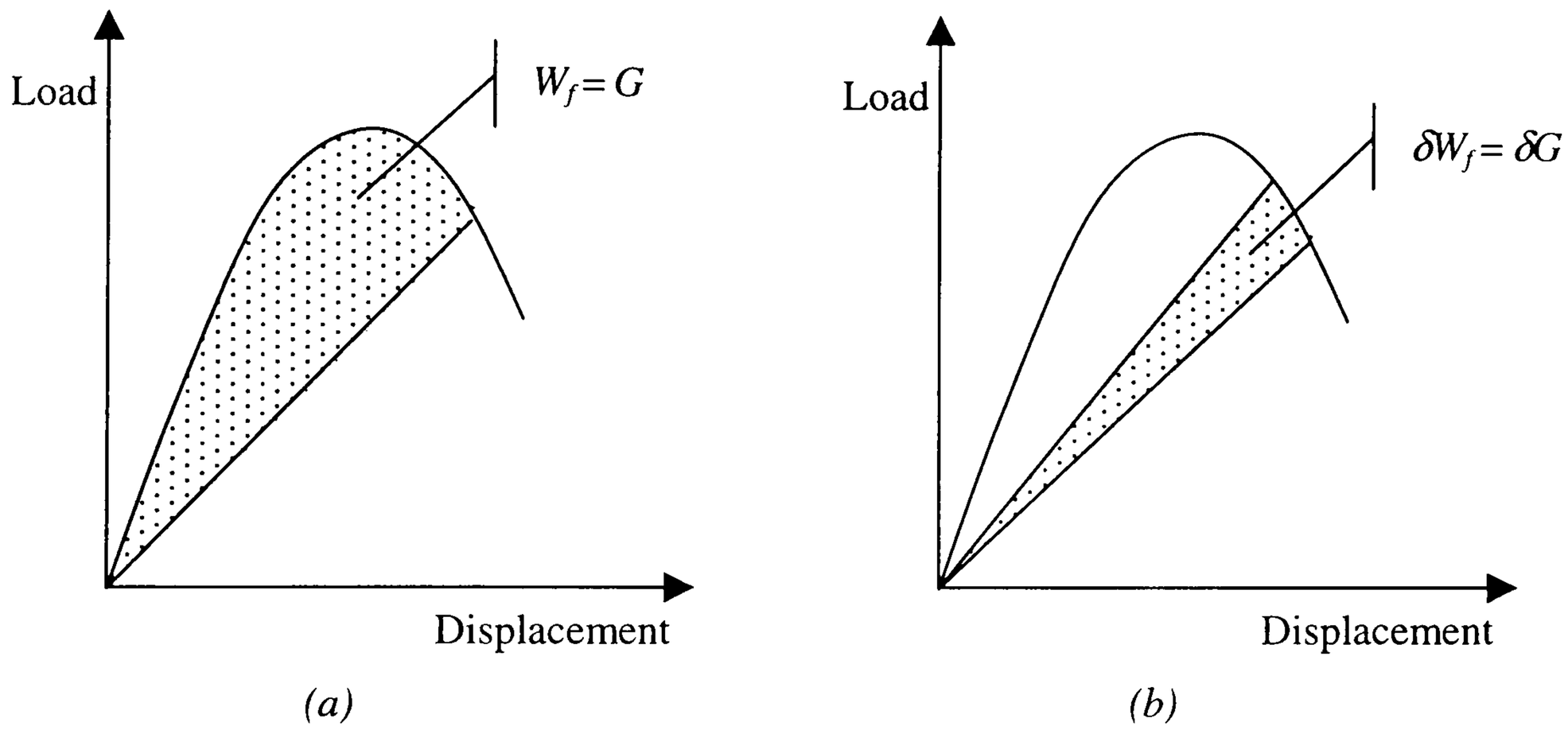

Fig. 2-7: Fracture energy (a) and incremental fracture energy (b) for a single load system

A graphical representation of fracture energy is given in Fig. 2-7 for the case of a single load acting on a structure in static equilibrium.

The conservation principle is further formalised by the definition of two quantities: the energy release rate of the load-structure system, denoted R, and the specific fracture energy, denoted G_f. R is a measure of the energy release capability and ductility of the structure when crack growth occurs. G_f is the energy required per unit area of fracture. G_f is assumed to be a material

characteristic. Using these two quantities, the principle writes directly[7]:

if $R < G_f$: no crack propagation (stable state) *(Eq. 2-3)*

if $R = G_f$: possible static crack propagation (stable or critical) *(Eq. 2-4)*

if $R > G_f$: dynamic crack propagation (unstable state) *(Eq. 2-5)*

Thus, the study of crack propagation in a particular structure reduces to the experimental determination of G_f and the analytical or numerical determination of R.

Energy Release Rate

To define the energy release rate further, consider an elastic body with a crack of area a, subjected to an external load F (in the case of multiple proportional stresses and forces acting on the body, F may be understood as a generalised force). The potential energy of the structure-load system is denoted Π, with $\Pi = U_{el} - W_{ext}$, where U_{el} is the elastic strain energy stored in the body and W_{ext} is the work due to F. The energy release rate is defined[30] as the opposite of the rate of variation of Π under increase of the cracked area, a, at constant displacements, u:

$$R = -\left[\frac{\partial \Pi}{\partial a}\right]_u = \left[\frac{\partial (W_{ext} - U_{el})}{\partial a}\right]_u \qquad \textit{(Eq. 2-6)}$$

Since u, the displacements at the application points of F, remain constant, no incremental work is done by F. Therefore, R reduces to[7]:

$$R = -\left[\frac{\partial U_{el}}{\partial a}\right]_u \qquad \textit{(Eq. 2-7)}$$

Considering a small increase of cracked area, δa, under static equilibrium, $\delta E_{kin} = 0$. Then (Eq. 2-1) and (Eq. 2-2) can be rewritten:

$$\delta G = \delta W_{ext} - \delta U_{el} = F\,\delta u - \left(\left[\frac{\partial U_{el}}{\partial u}\right]_a \delta u + \left[\frac{\partial U_{el}}{\partial a}\right]_u \delta a\right) \qquad \textit{(Eq. 2-8)}$$

Using Castigliano's second theorem valid for any elastic body:

$$F = \left[\frac{\partial U_{el}}{\partial u}\right]_a \qquad \textit{(Eq. 2-9)}$$

and introducing the specific fracture energy, $G_f = \delta G/\delta a$, (Eq. 2-8) becomes:

$$G_f \delta a = -\left[\frac{\partial U_{el}}{\partial a}\right]_u \delta a = R \delta a \qquad \textit{(Eq. 2-10)}$$

This confirms the criterion for static crack propagation, $R = G_f$, given in *(Eq. 2-4)*.

Stability of the Fracture Process

For LEFM where G_f is considered to be a material constant, the stability of the fracture process can be determined from the variation in the energy release rate as the crack progresses, $\frac{\partial R}{\partial a}$.

Three cases are identified[31]:

$$\frac{\partial R}{\partial a} < 0 \ : \qquad \text{stable equilibrium} \qquad \textit{(Eq. 2-11)}$$

$$\frac{\partial R}{\partial a} = 0 \ : \qquad \text{critical equilibrium} \qquad \textit{(Eq. 2-12)}$$

$$\frac{\partial R}{\partial a} > 0 \ : \qquad \text{unstable equilibrium} \qquad \textit{(Eq. 2-13)}$$

(Eq. 2-11) corresponds to the case for which crack propagation transforms the configuration of the elastic body so that the capacity of the structure to release energy is decreased at constant load level. For a structure with a single load F, R is proportional to F^2. Consequently, a load increment is necessary to meet again the fracture criterion $R = G_f$, which means that the crack extension is stable under load control.

(Eq. 2-12) corresponds to the case where the configuration of the fracturing structure is unaltered by crack propagation. Therefore, the criterion $R = G_f$ is maintained at constant load level.

(Eq. 2-13) corresponds to the case where crack propagation results in an increase in R at constant load. In the case of load control, the load will not be decreased to satisfy equilibrium. Consequently, the criterion for unstable (dynamic) crack propagation, $R > G_f$, is met.

Formulation adapted to Structural Failure by Unstable Crack Propagation

In the case of a single point load acting on a perfectly elastic body, further simplification can be deduced from Clapeyron's theorem :

$$U_{el} = \tfrac{1}{2} F u \qquad \textit{(Eq. 2-14)}$$

(Eq. 2-8) can be rewritten:

$$\delta G = \delta W_{ext} - \delta U_{el} = F\delta u - \tfrac{1}{2}\left(F\delta u + u\delta F\right) \qquad \textit{(Eq. 2-15)}$$

For crack extension at constant load, δU_{el} reduces to $\frac{1}{2} F\delta u$, that is:

$$\delta G = \tfrac{1}{2} F\delta u = \delta U_{el} = \tfrac{1}{2}\delta W_{ext} \qquad \textit{(Eq. 2-16)}$$

This equality is of particular interest for determining the ultimate load of structures if the following conditions are met:

- a single load acts on the structure,
- the structure is submitted to load control,
- structural failure occurs by unstable crack propagation,
- the onset of stable crack propagation arises before the ultimate load,
- the extent of stable crack propagation remains limited enough not to alter significantly the original configuration of the structure.

In this particular case, the equilibrium path, drawn in the load-displacement plane, presents a horizontal slope just before failure.

This can be explained in the following way:

- the maximum load, i.e. failure under load control, corresponds to the loss of stability both at the structural level and at the level of crack propagation,
- and, critical crack propagation, i.e. the limit between stable and unstable crack propagation, is reached in a continuous way due to the steady transition between stable and unstable cracking.

Consequently, in the vicinity of the failure point, the assumption of constant load of (Eq. 2-16) is satisfied. Therefore, (Eq. 2-16) can be used to predict the ultimate failure load.

The first order approximations of the fracture energy defined by (Eq. 2-10) and (Eq. 2-16) are compared in Fig. 2-8.

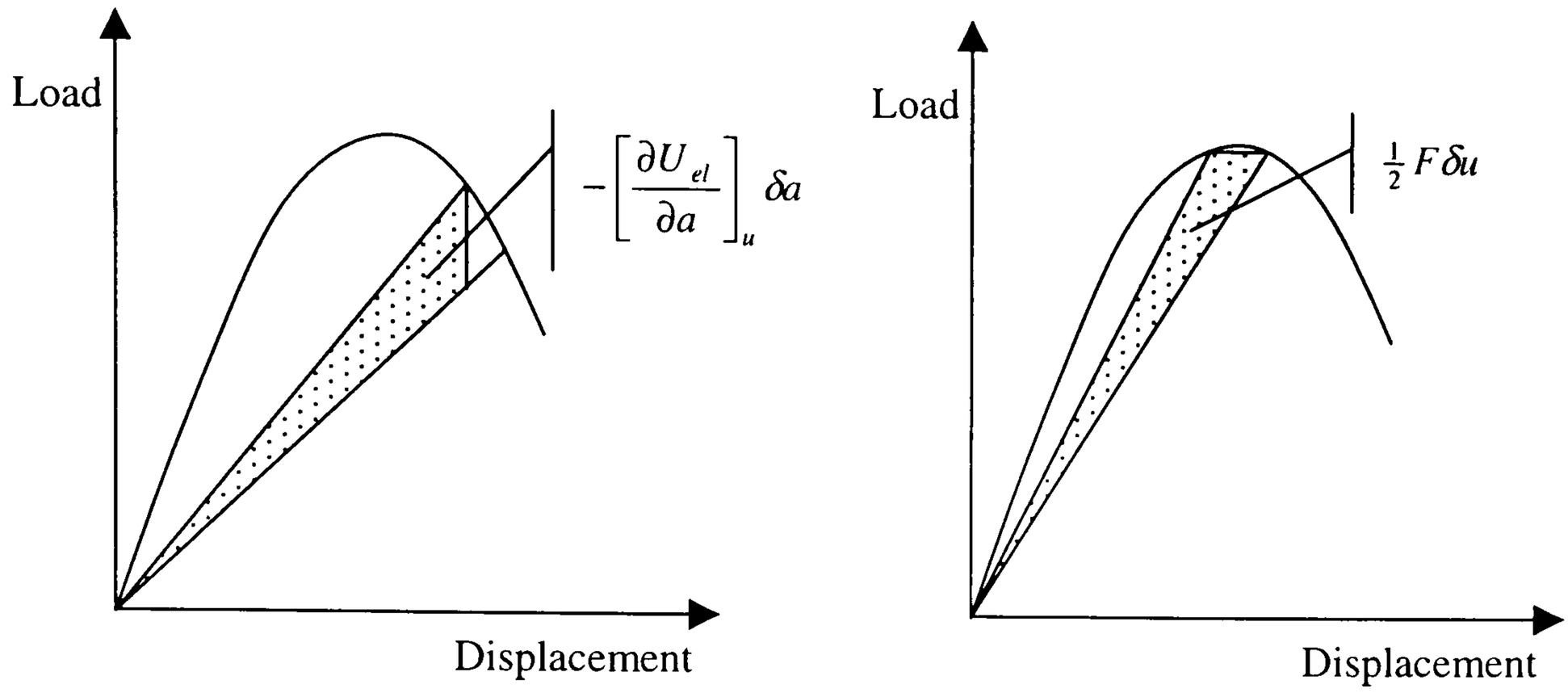

(a) area defined by (Eq. 2-10) *(b) area defined by* (Eq. 2-16)

Fig. 2-8: First order approximations of the incremental fracture energy

LEFM and Stress Intensity Factor

Three different modes of fractures can be identified: the direct opening mode (mode I), the shearing mode (mode II), and the tearing mode (mode III). The need for combining these different modes in fracture analysis prompted Irwin (1957)[32] to introduced the concept of a stress intensity factor K for each mode (K_I, K_{II} and K_{III}), which has the advantage of being additive, while Griffith's energy release rate is not. In the following, the discussion will be limited to mode I, as there is no major conceptual difference between the various modes.

The stress intensity factor, K_I, defines a good approximation of the effective elastic stress over a radius r_{ef} from the crack tip. This stress is assumed to control the fracture process. The assumption is that non-linear phenomena are well enough confined at the crack tip not to disturb the asymptotic elastic field at the distance r_{ef}. In this case, Inglis' formula for the distribution of elastic stresses can be written using the stress intensity factor:

$$\sigma_{(r)} = \frac{K_I g(\theta)}{\sqrt{2\pi r}} \qquad \textit{(Eq. 2-17)}$$

with r, the radial distance from crack tip

$g(\theta)$, a directional function depending on the polar angle, θ, only

and K_I, the stress intensity factor in mode I, with the dimension [N.$\sqrt{\text{m}}$ /m^2]

The fracture propagation is assumed to be linear in the sense of Irwin[32], if the size of the non-linear fracture process zone (radius r_{nl}), and the size of the controlling zone (radius r_{ef}) are small enough compared to the characteristic dimension of the cracked body, d_{ch}, and to the extent of the crack, a. Indicative orders of magnitudes are:

$$a, d_{ch} > 10\, r_{ef} \qquad \textit{(Eq. 2-18)}$$

and $r_{ef} > 5\, r_{nl}$ that is $a, d_{ch} > 50\, r_{nl}$ *(Eq. 2-19)*

With these hypotheses, the calculation of the energy release may be expressed on the basis of the stress intensity factor[30]:

$$R = \left[\frac{\partial(W_{ext} - U_{el})}{\partial a}\right]_u = \frac{K_I^2}{E} \qquad \textit{(Eq. 2-20)}$$

with E, the modulus of elasticity of the material

Therefore checking the energy conservation principle for crack initiation, (Eq. 2-4), amounts to checking the stress intensity factor:

$$K_I = K_{IC} \qquad \textit{(Eq. 2-21)}$$

K_{IC} is the critical intensity factor or fracture toughness of the material. It is supposed to be a material characteristic, on the same basis as G_f.

A general formulation of K_I can be written[30]:

$$K_I = \sigma_N \cdot \sqrt{\pi a} \cdot f(\alpha_c) \qquad \textit{(Eq. 2-22)}$$

with a, the crack length,

$\alpha_c = a/d_{ch}$, the crack extent ratio,

σ_N, the nominal stress: $\sigma_N = F/td_{ch}$ in 2 dimensions and $\sigma_N = F/d_{ch}^2$ in 3 dimensions,

F, the external load,

d_{ch}, the characteristic dimension,

t, the thickness for 2 dimensional problems,

$f(\alpha_c)$, a geometry correction function.

The values of $f(\alpha_c)$ have been calculated analytically and tabulated for some simple cases[33]. However, its general determination is a stress analysis problem and requires computational aid. Finite element analysis is the most commonly used method.

Size Effect Law

As mentioned previously, the strength criterion predicts that failure always arises at the same stress level, whatever the size of the considered structure. On the contrary, LEFM predicts a size effect on the nominal stress at failure, $\sigma_{N,u}$. The size effect law for LEFM is deduced combining (Eq. 2-21) and (Eq. 2-22):

$$\sigma_{N,u} = \frac{K_{IC}}{\sqrt{d_{ch}} \cdot \sqrt{\pi \alpha_{c,u}}\, f(\alpha_{c,u})} = \frac{K_{IC}}{\sqrt{d_{ch}} \cdot \Phi(\alpha_{c,u})} \qquad \textit{(Eq. 2-23)}$$

For geometrically identical structures of various sizes, $\Phi(\alpha_c)$ is the same function. Consequently, $K_{IC} / \Phi(\alpha_{c,u})$ is a constant and the ultimate nominal stress varies with $1/\sqrt{d_{ch}}$. Using a logarithmic formulation, the size effect law writes[30]:

$$log(\sigma_{N,u}) = log\left(\frac{K_{IC}}{\Phi(\alpha_{c,u})}\right) - \frac{1}{2} log(d) \qquad \textit{(Eq. 2-24)}$$

This is the equation of a straight line of slope –1/2 in the plane $\sigma_{N,u}$- d_{ch} with logarithmic scale, Fig. 2-9.

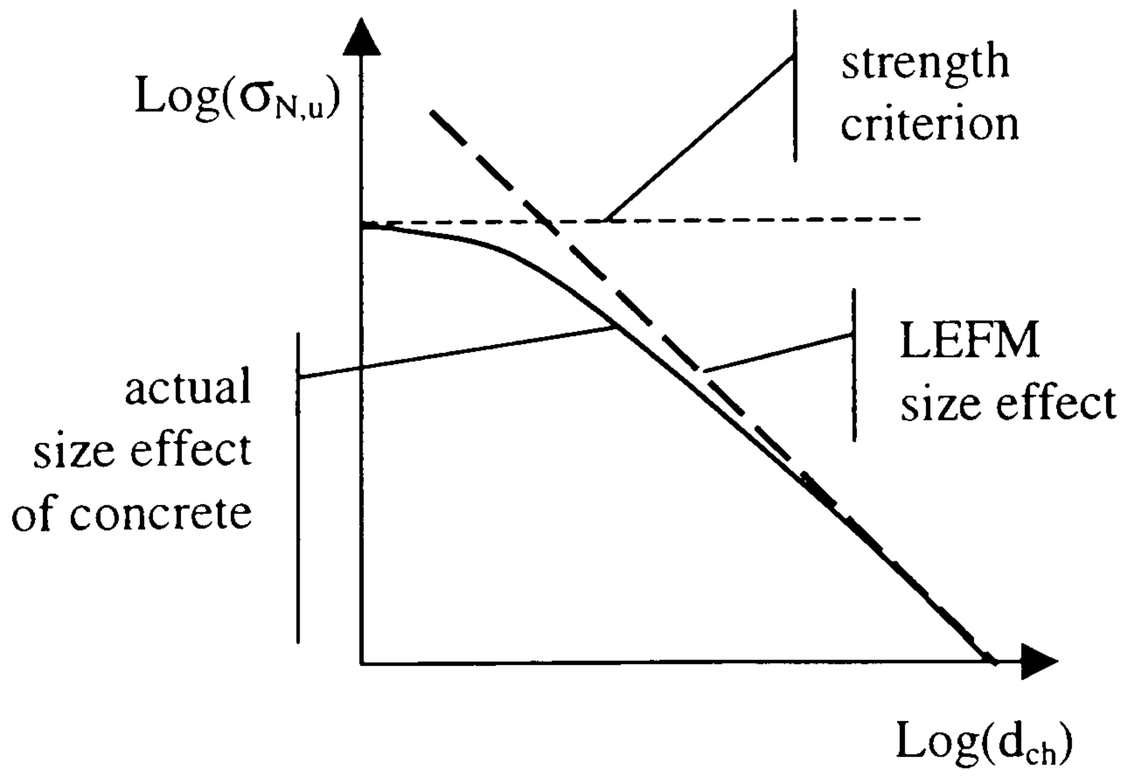

Fig. 2-9: Plot of the size effect law in the plane $log(\sigma_{N,u})$-$log(d_{ch})$

Limitations of LEFM

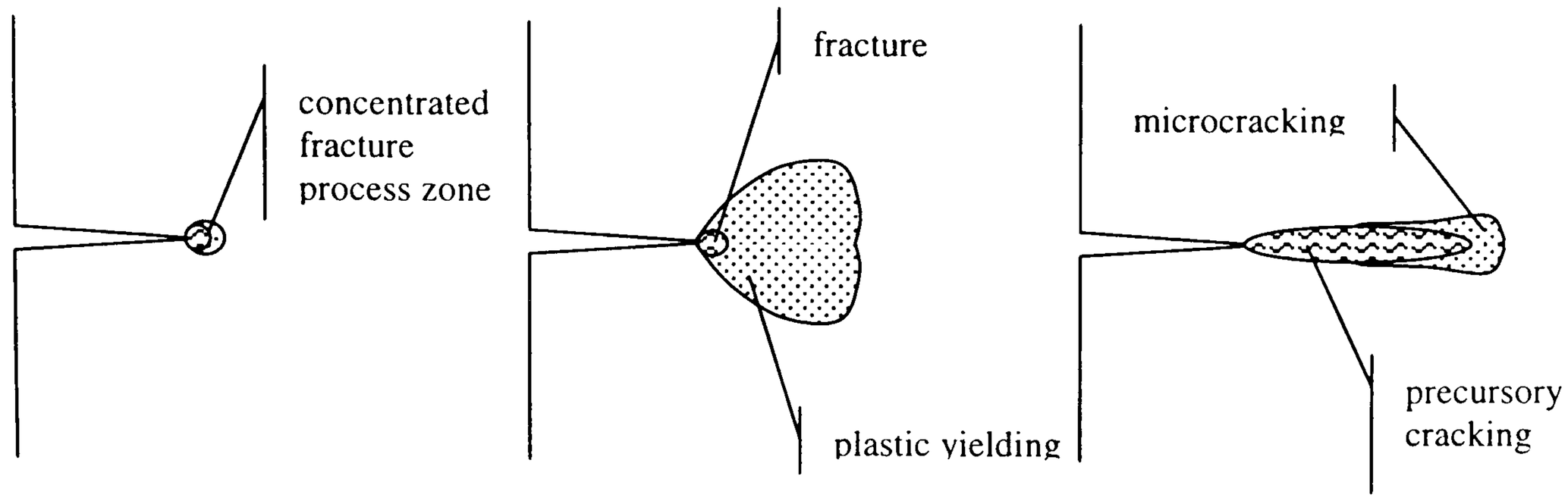

(a) Brittle material *(b) Ductile material* *(c) Quasi-brittle material*

Fig. 2-10: Structure of different fracture process zones

The most demanding restriction on LEFM is the limitation of the size of the fracture process zone, (Eq. 2-18) and (Eq. 2-19). LEFM applies perfectly to brittle materials like glass, plexiglass, brittle ceramics and brittle metals, as they present very concentrated fracture process zones (FPZ), Fig. 2-10. However, two other types of fracturing materials present relatively large FPZ[30]:

- ductile metals, like tough steel,
- and quasi-brittle materials, like concrete, rock, ice, stiff clay and fibre composites.

In the case of ductile materials, yielding is the dominating non-linear phenomenon. The FPZ is partitioned into a small softening fracture zone at the tip of the crack, surrounded by a large yielding zone. Using the concept of effective crack extension, Irwin (1958)[34] obtained an approximate assessment of the length of the FPZ for ductile materials:

$$r_{nl} \approx \frac{1}{\pi}\left(\frac{K_{IC}}{f_y}\right)^2 \qquad \textit{(Eq. 2-25)}$$

with f_y, the yield strength

More accurate assessments of r_{nl} resulted subsequently in the condition formulated in the ASTM E399 (1983)[35]:

$$a, d_{ch} > 2.5\left(\frac{K_{IC}}{f_y}\right)^2 \qquad \textit{(Eq. 2-26)}$$

In the case of quasi-brittle materials, the dominating non-linear phenomenon is strain softening.

The size of the FPZ is about ten times as large as the yielding zone of ductile metals. The FPZ is constituted of precursory cracks responsible for strain softening, surrounded by a relatively thin area of hardening damaged material (microcracking for concrete).

Based on experimental evidences (Bažant and Pfeiffer 1987[36]), the ACI Committee 446 on Fracture Mechanics (1992)[30] suggested the following restrictions for the limit of applicability of LEFM to concrete:

for eccentric compression specimens: $d_{ch} > 46\, d_{agg}$ *(Eq. 2-27)*

for three-point bend specimens: $d_{ch} > 135\, d_{agg}$ *(Eq. 2-28)*

for concentric tension specimens: $d_{ch} > 420\, d_{agg}$ *(Eq. 2-29)*

where d_{agg} is the maximum aggregate size

2.2.2. Non-linear Fracture Mechanics

Kaplan (1961)[37] was the first to apply LEFM to concrete, but concluded that it was not appropriate as the size of the FPZ was generally to large for the considered structures. From then on, efforts have been made to develop a fracture theory applicable to quasi-brittle materials.

Equivalent Elastic Crack Models

One of the early ideas to compensate for the softening FPZ in front of the crack tip has been to add a fictitious crack extent, Δa_e, to the actual crack length, a_0. LEFM is then applied to the fictitious crack length so that the actual softening distribution of crack-closing-stresses is replaced by a shifted distribution of asymptotic crack-closing-stresses. This is called the far field equivalence and the models based on this concept are called equivalent elastic crack models, Fig. 2-11.

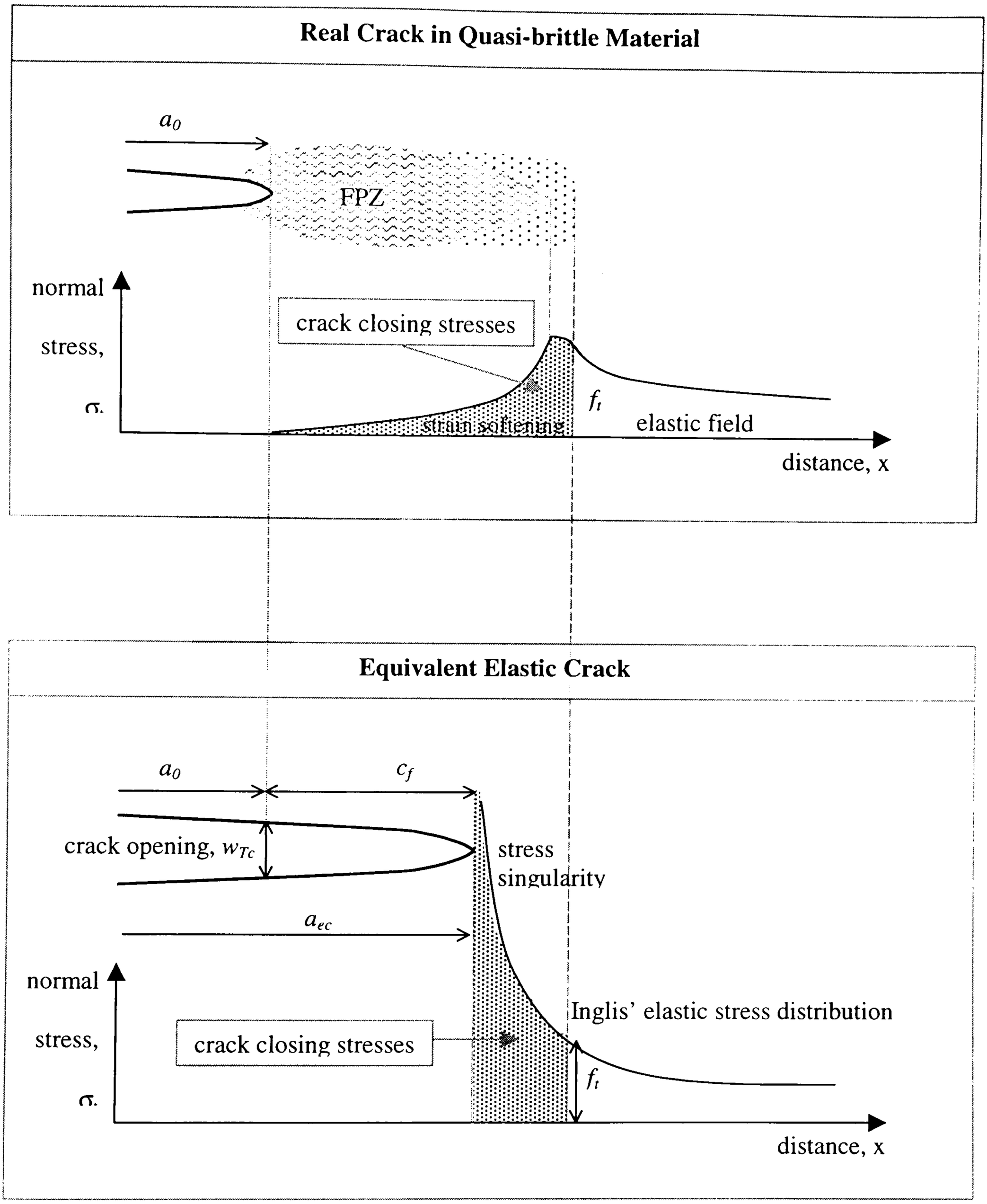

Fig. 2-11: Equivalent crack concept.

If the length of the FPZ is written using (Eq. 2-26), $r_{nl} = \eta(K_I/f_t)^2$, the effective crack extension can be written[7]:

$$\Delta a_e = \left(\eta - \frac{1}{2\pi}\right)\left(\frac{K_I}{f_t}\right)^2 \qquad \textit{(Eq. 2-30)}$$

Therefore Δa_e depends on the extension of the FPZ which depends on the geometry and the load level. Thus the model becomes non-linear. At the limit, when the FPZ is supposed to be fully developed in an infinitely large body, Δa_e equals c_f, a length assumed to be a material constant. The equivalent elastic crack concept is usually applied to the critical situation.

Most of the models developed from the equivalent crack concept are not predictive but rely on the experimental measurement of the effective crack extension. They have mainly been used to experimentally deduce the real fracture toughness of materials from their apparent fracture toughness[38].

A similar model is the two-parameter model of Jenq and Shah[39]. The material constant is not the extent of the equivalent crack but the crack-tip opening displacement, w_{Tc}. Fracture is assumed to occur when $K = K_{IC}$ at the tip of the equivalent crack and the opening of the equivalent crack at the tip of the real crack is equal to the material constant, w_{Tc}, Fig. 2-11.

It should be noted that in these models a strength criterion is indirectly enforced besides the LEFM energy criterion.

R-Curves:

At this point, a precision on the notation must be given. So far, G has been used to refer to the fracture energy of the material, i.e. the crack growth resistance, since the notation commonly adopted for the critical fracture energy of concrete is G_f. Consistently, R has been adopted for the energy release rate. However, other authors (dealing with fracture mechanics of steel), use R for the crack growth resistance and G for the energy release rate. Exceptionally, this notation will be used in this sub-section.

An extension of the equivalent elastic crack model aimed at determining the full load displacement curves is the R-curve approach. In this approach, the crack growth resistance, R, is varied from a base value at onset of cracking (often zero) to the LEFM critical fracture energy G_f when the crack propagates with a fully developed FPZ. For a given structure size and geometry, the crack growth resistance becomes a function of the effective crack extension, termed the R-curve:

$$R = F(\Delta a_e) = G_f\, f\left(\frac{\Delta a_e}{c_f}\right) \qquad \textit{(Eq. 2-31)}$$

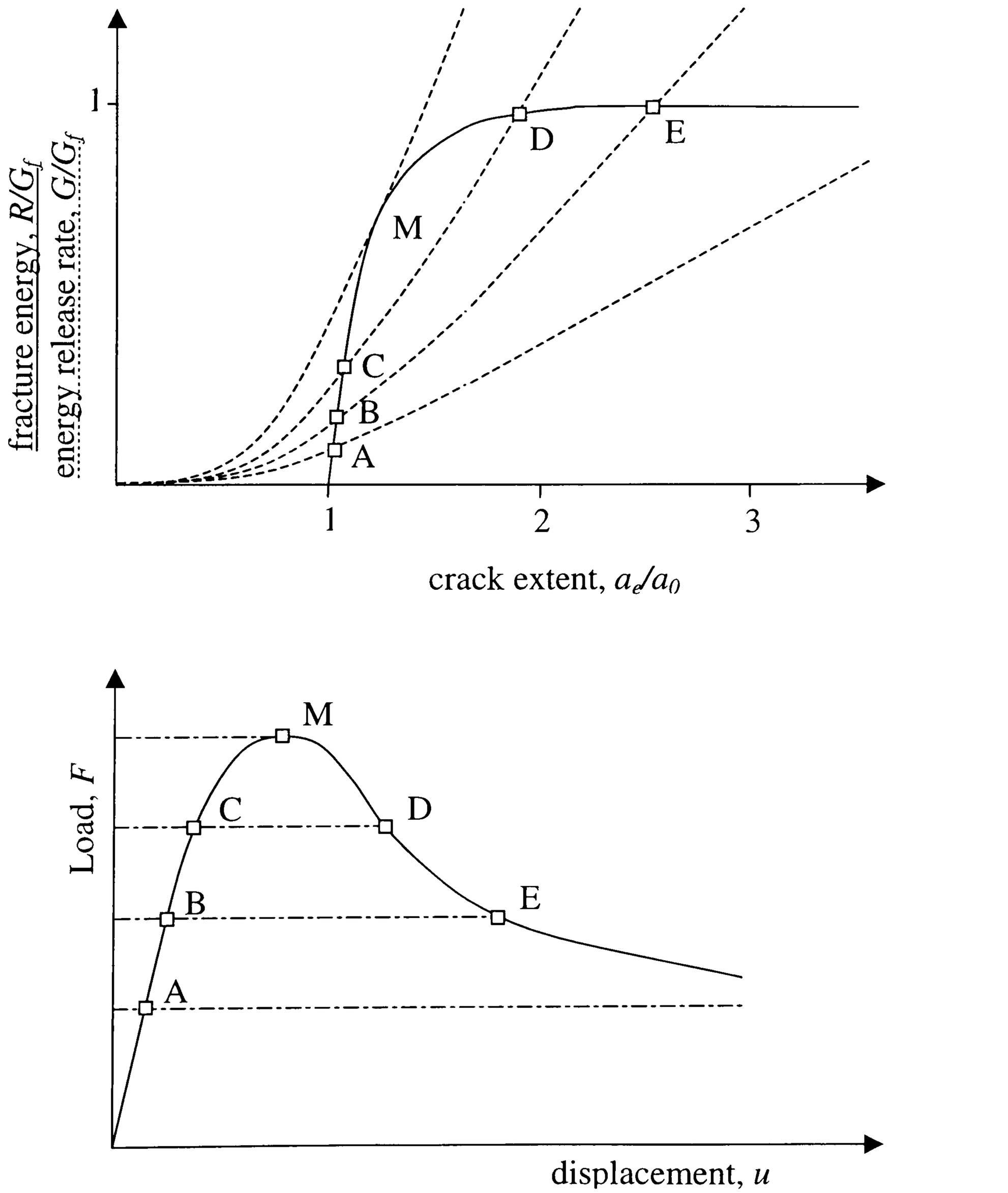

Fig. 2-12: Graphical solution of a crack propagation problem using R-curves

On the other hand, the energy release rate is a function of the intensity of the load and of the effective crack extension:

$$G = \phi(P, a_e) \qquad \textit{(Eq. 2-32)}$$

Enforcing the condition for quasi-static fracture process, $R = G$, along with the static equilibrium of the structure, $F = K \cdot u$, provides a sufficient system of equations to determine the complete load-displacement curve. This system can be solved graphically, Fig. 2-12.

It was first thought that the R-curve was dependent on the material only. But it has been shown that both the geometry and the size of the structure have a significant influence on the R-curves.

Cohesive Crack Models:

With so many variables, the equivalent crack models and the R-curve approach appeared not to be practical. Consequently, a more physical approach was sought. To this aim, the actual distribution of softening stresses had to be simulated. Hillerborg (1976)[40] introduced the fictitious crack model where the zone of softening material ahead of the crack tip is lumped into a linear interface in front of the simulated crack. The distribution of the crack-closing-stresses is then modelled by a one-dimensional approximation.

In this model, the elastic response of the bulk material and the non-linear softening response of the crack opening are treated separately. As shown in Fig. 2-13, the softening behaviour observed experimentally in the load-displacement behaviour for a tension specimen is decomposed into the elastic stress-strain relationship of uncracked concrete and the crack-opening-displacement curve of the fracturing cross-section.

The fundamental hypothesis for this model is that a constitutive relationship between average crack opening and softening stress exists in the FPZ. This hypothesis is difficult to check, as has already been mentioned. The strain-softening curves obtained from displacement-controlled

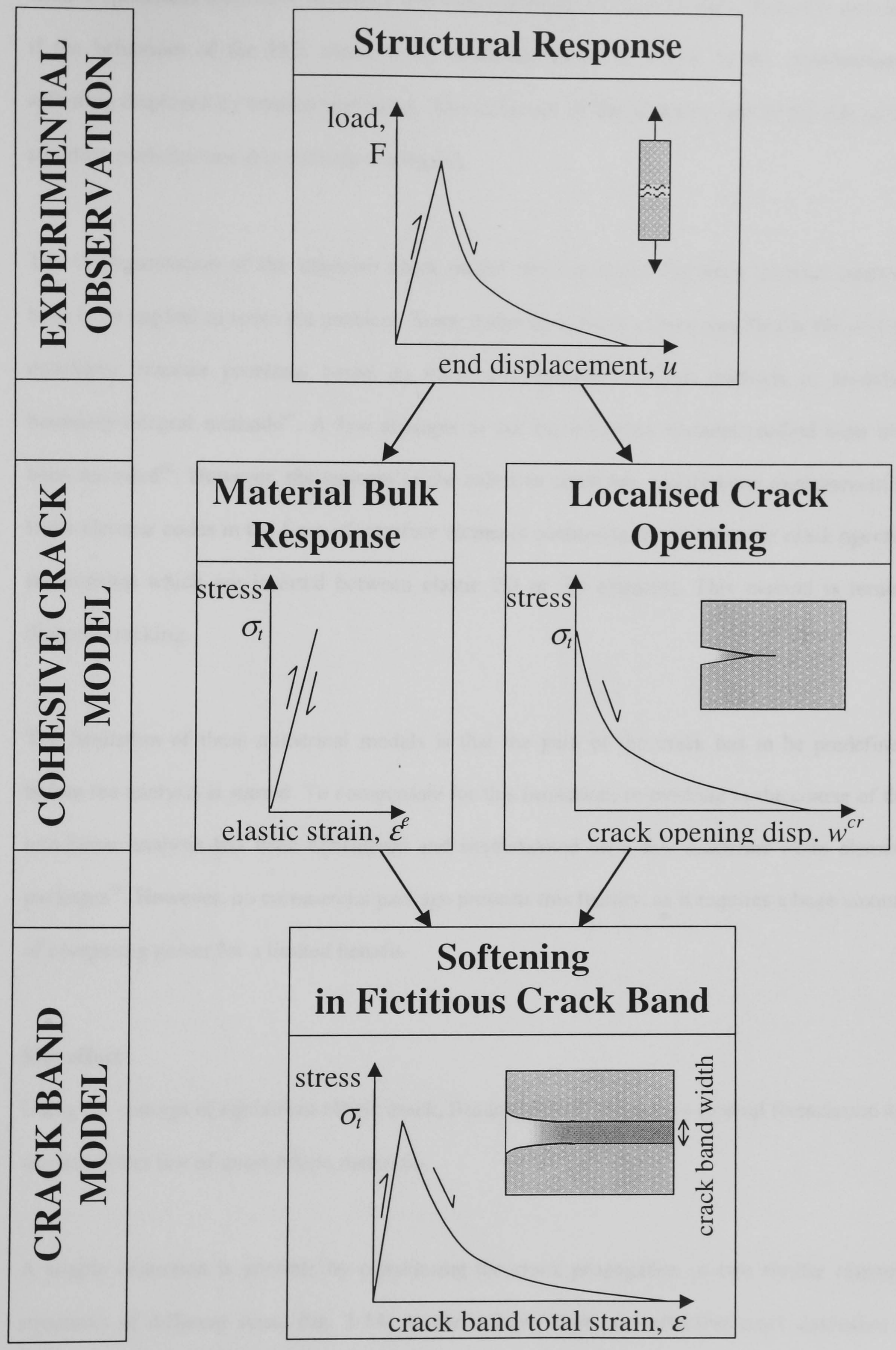

Fig. 2-13: Decomposition of the strain-softening behaviour in various models

tension specimens must have boundary and structural effects removed. Even then, it is not clear if the behaviour of the FPZ ahead of an advancing crack is similar to the cross-sectional softening displayed by tension specimens. The influence of the geometry and of the size of the structure modelled are also difficult to estimate.

The implementation of the cohesive crack model requires numerical tools. Several methods have been applied to solve the problem. Some codes have been written specifically for solving non-linear fracture problems based on traditional boundary-integral methods or modified boundary-integral methods[41]. A few attempts to use the boundary element method have also been recorded[42]. However, the concept of the cohesive crack has mainly been implemented in finite element codes in the form of interface elements containing the constitutive crack opening relationship which are inserted between elastic 2D or 3D elements. This method is termed discrete cracking.

The limitation of these numerical models is that the path of the crack has to be predefined before the analysis is started. To compensate for this limitation, re-meshing in the course of the non-linear analysis has been considered and implemented on a few academic finite element packages[43]. However, no commercial package presents this facility, as it requires a huge amount of computing power for a limited benefit.

Size effect

Using the concept of equivalent elastic crack, Bazant (1984)[44] deduced a general formulation for the size effect law of quasi-brittle materials.

A simple deduction is possible by considering the crack propagation in two similar concrete structures of different sizes, Fig. 2-14. At the stability limit, the effective crack extension is suppose to be constant and equal to c_f. The area relieved by crack extension is supposed to

radiate at 45 deg. from the crack tip. The condition for static crack propagation of (Eq. 2-1) is:

$$\delta W_f = 2t(a_o + c_f)\frac{\sigma_N^2}{2E} \cdot \delta a = bG_f \cdot \delta a \qquad \textit{(Eq. 2-33)}$$

where t is the plate thickness

a_0 is the initial crack length

c_f the critical effective crack extension

$\sigma_{N,u}$ the ultimate nominal stress

E the modulus of elasticity

and δa the incremental crack extension.

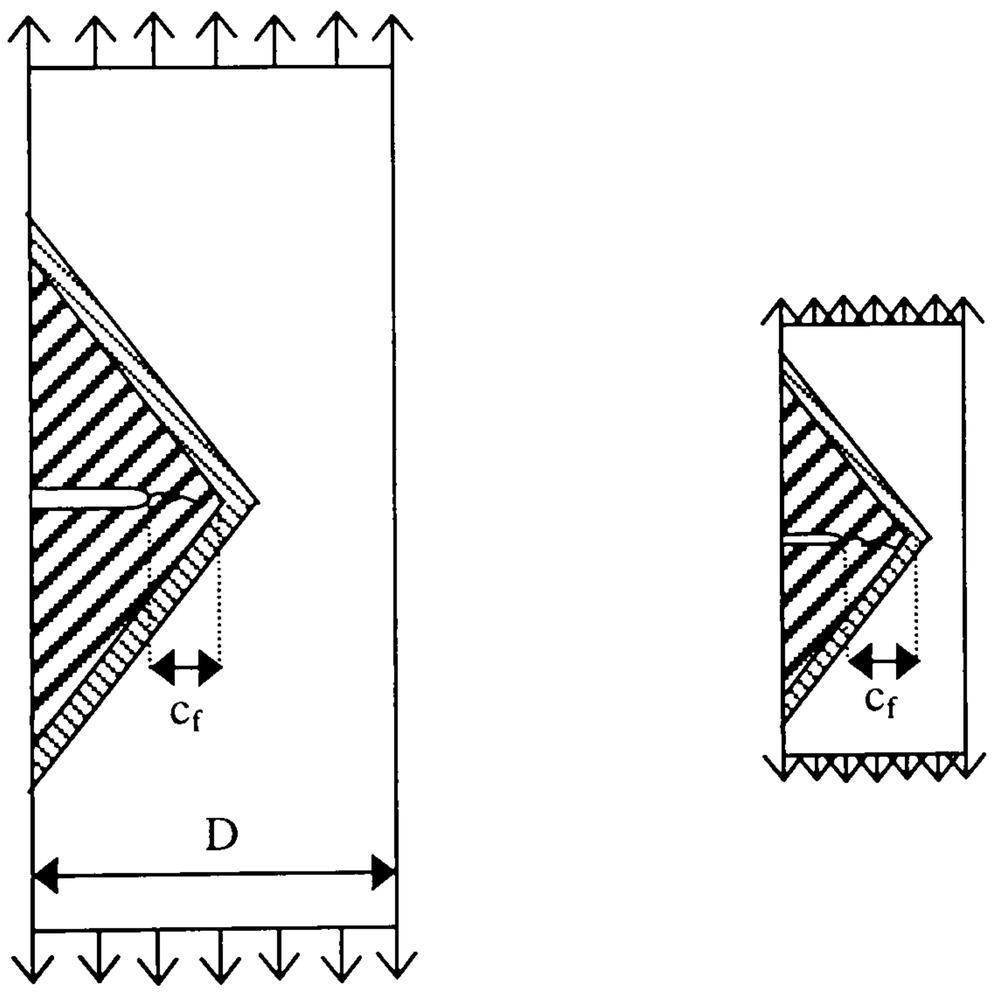

Fig. 2-14: Deduction of Bazant (1984) non-linear size effect law.

This leads to the following formulation of the size effect law:

$$\sigma_{N,u} = \sqrt{\frac{EG_f / c_f}{1 + a_0 / c_f}} \qquad \textit{(Eq. 2-34)}$$

from (Eq. 2-20) and (Eq. 2-30), c_f can be expressed as follows:

$$c_f = \beta\left(\frac{K_{IC}}{f_t}\right)^2 = \beta\frac{EG_f}{f_t^2} \qquad \textit{(Eq. 2-35)}$$

with β a material constant.

and a_0 can be expressed as a fraction of the structural dimension, D: $a_0 = \alpha \cdot D$

Consequently, (Eq. 2-34) can be rewritten:

$$\sigma_{N,u} = \frac{Bf_t}{\sqrt{1 + D/D_0}} \qquad \textit{(Eq. 2-36)}$$

where B is a dimensionless constant and $D_0 = c_f/\alpha$ is an internal length. Both B and D_0 depend on the material and the structure geometry but not on the structure size. (Eq. 2-36) is the general formulation of Bazant's non-linear size effect law, Fig. 2-9, p17.

2.2.3. Determination of the fracture parameters

In non-linear fracture mechanics, the definition of material properties requires three parameters. These parameters can be determined experimentally or deduced from empirical formulae as a function of the concrete compressive strength and the maximum aggregate size.

The first parameter is the tensile strength, which is easily accessible experimentally by cube, cylinder or splitting test. For concrete, the CEB-FIP Model Code 90[5] (eq. 2.1-4, sec. 2.1.3.3.1) provides an empirical relationship between the tensile strength, f_t, and the compressive strength, f_c:

$$f_t = 1.4 \cdot \left(\frac{f_c}{10} \right)^{2/3} MPa \qquad \textit{(Eq. 2-37)}$$

where f_c is expressed in MPa.

The second parameter is either the specific fracture energy, G_f, or the critical fracture toughness, K_{IC}. The relation between the two quantities is described in (Eq. 2-20). The fracture toughness can be determined experimentally using a three point bending test on notched beams. A method using LEFM inspired from ASTM standard E399 (1983)[35] is presented in Murakami (1987)[33]. Methods based on the equivalent elastic crack concept called compliance calibration and modified compliance calibration have been developed by Swartz et al.[45]. All these methods are thoroughly described in the state-of-the-art report by ACI Committee 446 on Fracture Mechanics (1992)[30].

The most widely adopted method for the determination of G_f is the work-of-fracture method proposed by Hillerborg (1985) [46], which was later adopted as a standard method by RILEM TC50 FMC (1985)[47]. The method is based on the fictitious crack concept and thus is not an LEFM method. G_f is deduced from the load-displacement curve of a notched beam in three-point bending, taking into account the effect of the self-weight:

$$G_f = \frac{W_o + mg\,\delta_0}{A_{frac}} \qquad \textit{(Eq. 2-38)}$$

where W_0 is the area under the recorded load displacement curve, i.e. the work of the external force up to failure,

$mg\,\delta_0$ is the additional work done by self-weight up to failure

and A_{frac} is the projected area of the fractured surface.

Guinea, Planas and Elices (1992)[48] tried to improve the formula by developing correction methods for the effect of the bulk energy dissipation, the experimental procedure and the size effect. It should be noted that three-point bending tests can adequately be replaced by the more stable wedge-splitting test refined by Brűhwiler (1988)[49].

Based on the results of many tests on concrete, the CEB-FIP Model Code 90[5] proposed an empirical formula (eq. 2.1-7, sec. 2.1.3.3.2) for the assessment of G_f based on the concrete compressive strength and the maximum aggregate size:

$$G_f = G_{f0}\left(\frac{f_c}{f_{c0}}\right)^{0.7} \qquad \textit{(Eq. 2-39)}$$

where $f_{c0} = 10$ MPa

and G_{fo} is the base value of the fracture energy depending on the maximum aggregate size, d_{agg} :

d_{agg} (mm)	G_{fo} (N.m/m2)
8	25
16	30
32	58

It is possible to deduced an interpolation curve for the expression of G_{f0}. Consequently, the formula can be rewritten:

$$G_f = \left(0.0469 \cdot d_{agg}^2 - 0.5 \cdot d_{agg} + 26\right) \cdot \left(\frac{f_c}{10}\right)^{0.7} \quad [\text{N.m/m}^2] \qquad \textit{(Eq. 2-40)}$$

The last parameter necessary for the implementation of the fictitious crack concept is the shape of the strain-softening curve, considered to be a material property.

The most direct way to obtain experimentally the strain-softening curve of fracturing concrete is to use a uniaxial tensile test. To be able to follow the descending branch of the load-displacement diagram, displacement control has to be enforced. This can be achieved either with an extremely stiff test rig and a constant displacement speed, or with a servo-controlled loading process where the crack mouth opening is monitored.

If constant speed of displacement is implemented, the specimen length must be short enough so that elastic contraction in the softening phase does not produce a snap back, which could not be followed. If crack-mouth-opening-displacement control is used, the measuring apparatus needs to be placed at the cross-section where cracking localises. The position of cracking can be forced by using notched or bone shaped tension specimens. Documented testing procedures are available in Hordijk (1989)[50] and Daerga (1992)[51].

Extensive testing experience acquired at the Stevin Laboratory[16] suggested that boundary conditions and the specimen shape had to be carefully chosen to avoid asymmetric cracking to take place, inducing structural effects on the strain-softening curve. The end-platens have to be rotationally fixed and the specimen length short enough to avoid rotation in the cracking plane. At the same time the cracking has to occur in a cross-section far enough from the extremities to avoid boundary effects.

Experimental observation of the strain-softening behaviour of concrete has resulted in the formulation of several dimensionless equations. The two conditions that the curves have to satisfy are that the initial value of the stress σ_t should be equal to f_t and that the area under the stress-crack-opening curve should be equal to G_f. This results in the ultimate crack opening, w_{ult}^{cr}, being proportional to G_f/f_t.

The simplest softening curve is the linear approximation directly deduced from the two conditions. This model will not be discussed here as it is too far from the physical behaviour that occurs to provide realistic results. The next model, with increasing complexity, is the bi-linear curve. The CEB-FIP Model Code 90[5] suggests a bi-linear model with the position of the discontinuity point depending on the maximum aggregate size:

$$\frac{\sigma_t}{f_t} = 1 - 0.85\frac{w^{cr}}{w_1} \qquad \text{for} \quad 0.15f_t < \sigma_t < f_t \qquad \textit{(Eq. 2-41)}$$

$$\frac{\sigma_t}{f_t} = 0.15\frac{w_{ult}^{cr} - w^{cr}}{w_{ult}^{cr} - w_1} \qquad \text{for} \quad 0 < \sigma_t < 0.15f_t \qquad \textit{(Eq. 2-42)}$$

where σ_t is the stress across the crack and w_{cr} is the crack opening

$$w_1 = 2\frac{G_f}{f_t} - 0.15w_c$$

and

$$w_{ult}^{cr} = \alpha_F \frac{G_f}{f_t}$$

The coefficient α_F depends on the maximum aggregate size d_{agg} and is comprised between 5 and 8 for d_{agg} varying between 8 and 32 mm.

Other bi-linear curves have been developed, notably by Petersson (81)[52] and Wittmann (88)[53].

Reinhardt et al (1986) [22] developed a non-linear curve referred to as Moelands and Reinhardt's power law[23]:

$$\frac{\sigma_t^{cr}}{f_t} = 1 - \left(\frac{w^{cr}}{w_{ult}^{cr}}\right)^{0.31} \qquad \textit{(Eq. 2-43)}$$

with the ultimate crack opening $w_{ult}^{cr} = 4.226 \cdot \frac{G_f}{f_t}$

Van der Veen (1990)[54] proposed a similar power law. By fitting experimental data, different, although very similar, constants resulted:

$$\frac{\sigma_t^{cr}}{f_t} = 1 - \left(\frac{w^{cr}}{w_{ult}^{cr}} \right)^{0.248} \qquad \textit{(Eq. 2-44)}$$

with the ultimate crack opening $w_{ult}^{cr} = 5.14 \cdot \frac{G_f}{f_t}$

Rosati et al (1991)[55] suggested a different formulation with a parameter, κ, allowing the initial slope of the softening curve to be set:

$$\frac{\sigma_t^{cr}}{f_t} = \frac{1 - w^{cr} / w_{ult}^{cr}}{1 + \kappa \, w / d_{agg}} \qquad \textit{(Eq. 2-45)}$$

Hillerborg formulated a quasi-exponential curve with its shape depending on a single parameter assumed to be a material constant: $\alpha_F = \frac{w_{ult}^{cr} \cdot f_t}{G_f}$. As mentioned before, α_F is assumed to be dependent on the maximum aggregate size according to the CEB-FIP Code 90. Most authors set α_F between 4 and 5. Hillerborg formula varies from linear softening for $\alpha_F = 2$ to full-exponential for $\alpha_F = \infty$. The equation is given by:

$$\frac{\sigma_t^{cr}}{f_t} = (1 + c_1) \cdot exp\left(c_2 \frac{w^{cr}}{w_{ult}^{cr}} \right) - c_1 \qquad \textit{(Eq. 2-46)}$$

where $w_{ult}^{cr} = \alpha_F \frac{G_f}{f_t}$

and $\begin{cases} c_2 = 1 - c_1 \, ln \dfrac{1 + c_1}{c_1} \\ \dfrac{1 - c_2}{c_1 c_2} = \alpha_F \end{cases}$

The most reliable curve, however, is the curve developed by Reinhardt et al (1986)[22], referred as Hordijk's exponential softening curve[16,25]. It was compared with normal strength and light-weight concrete and was shown to give satisfactory results. Hordijk has set the constants for normal strength concrete as follows:

$$\frac{\sigma_t^{cr}}{f_t} = \left\{ 1 + \left(3 \cdot \frac{w^{cr}}{w_{ult}^{cr}} \right)^3 \right\} exp\left(-6.93 \cdot \frac{w^{cr}}{w_{ult}^{cr}} \right) - 28 \cdot exp(-6.93) \cdot \frac{w^{cr}}{w_{ult}^{cr}} \qquad \textit{(Eq. 2-47)}$$

with the ultimate crack opening $w_{ult}^{cr} = 5.136 \cdot \frac{G_f}{f_t}$

The different curves, (Eq. 2-41) to (Eq. 2-47), are plotted and compared in Fig. 2-15 to Fig. 2-17.

2.2.4. Reasons for applying Fracture mechanics to concrete

For structures failing in unstable fracture propagation, a strength criterion is not applicable as the theory of the deformation of elastic material predicts an infinite stress concentration at the crack tip. Plasticity on the other hand, allows for non-linear stress redistribution, but does not simulate appropriately the quasi-brittle behaviour of concrete. However, the structural analysis must agree with the lack of yield plateau from the load-deflection diagram.

The two important pieces of information expected from a suitable simulation for design purposes is the ultimate load, corresponding to unstable crack propagation, and the post-peak behaviour, characteristic of the energy absorption capability and the ductility of the structure. A strength criterion can only predict the onset of stable cracking, which can occur at a much lower load than crack instability. A plasticity approach on the other hand, even if it can satisfy the energy consumption requirement, always predicts a ductile behaviour in contrast with the experimentally observed behaviour in certain modes of failure.

In conclusion, for plain concrete structures, fracture mechanics should always be used to predict the ultimate cracking load and the post-peak behaviour. For reinforced concrete, when structural failure is controlled by steel yielding across the cracks, plasticity analysis is suitable. However, when failure is completely controlled by fracture, like shear failure of beams without stirrups or bond failure by splitting of concrete, the plastic behaviour of steel is not the prominent phenomenon and failure should be predicted by fracture mechanics.

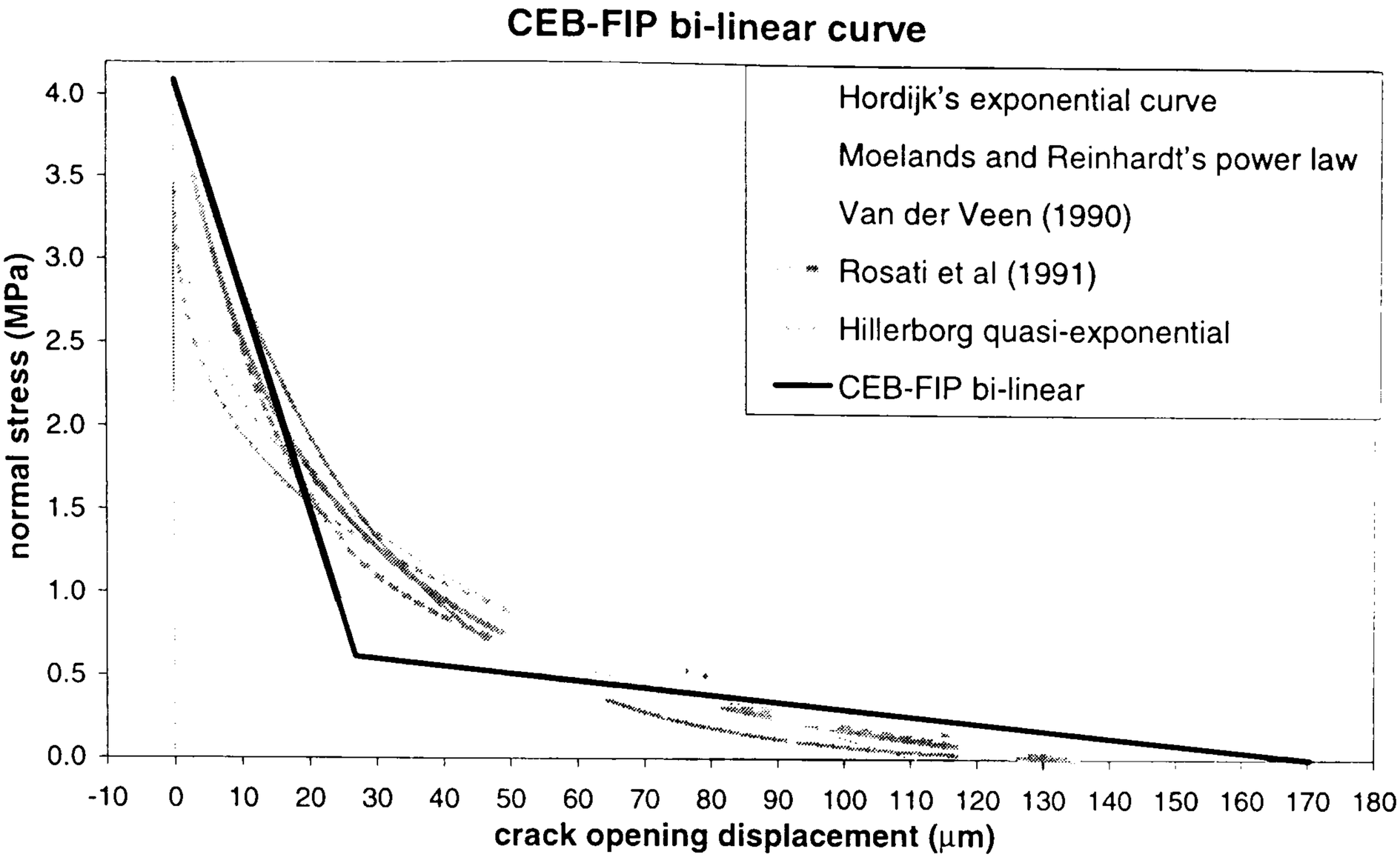

Fig. 2-15: CEB-FIP bi-linear softening curve

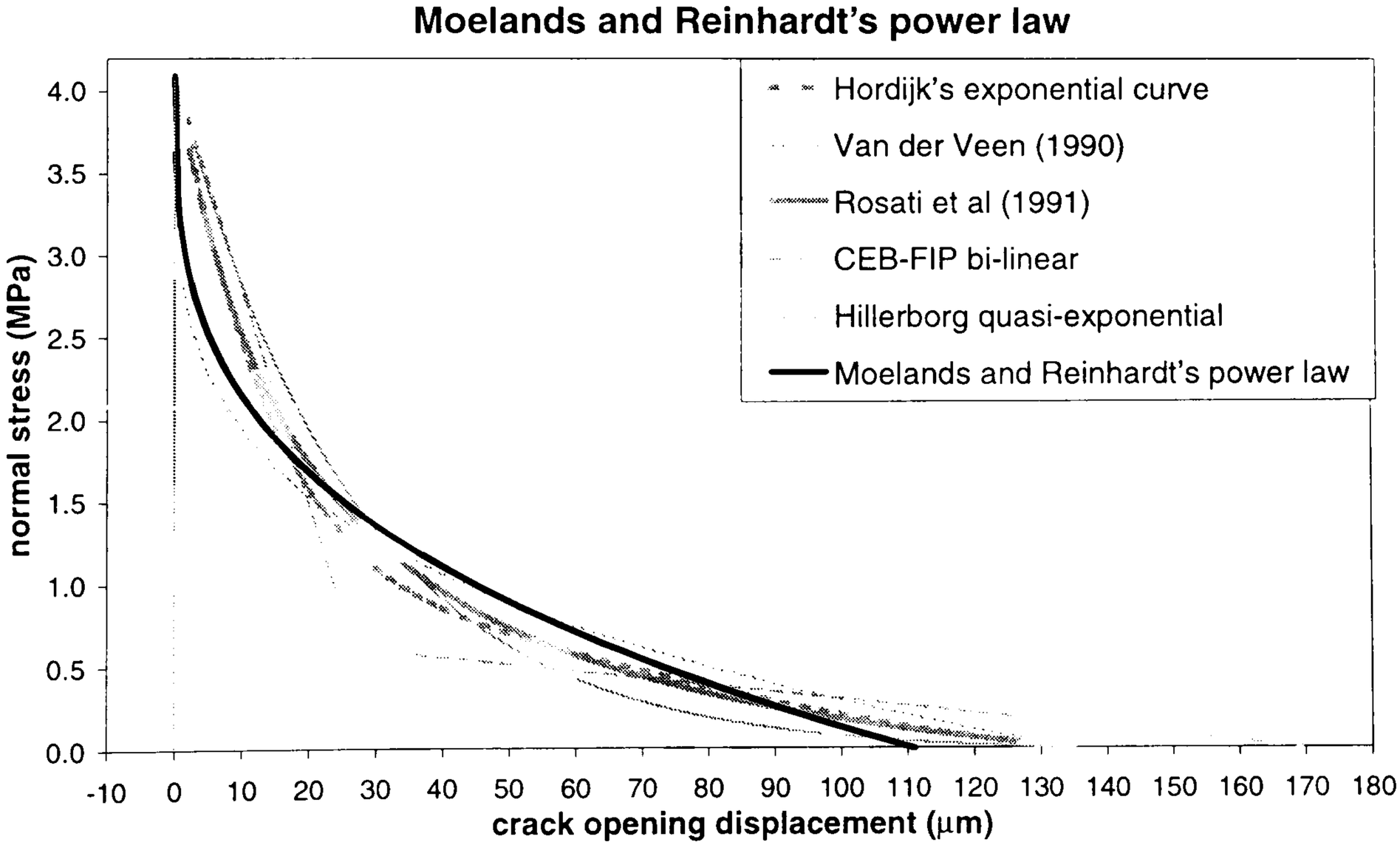

Fig. 2-16: Moelands and Reinhardt's power law

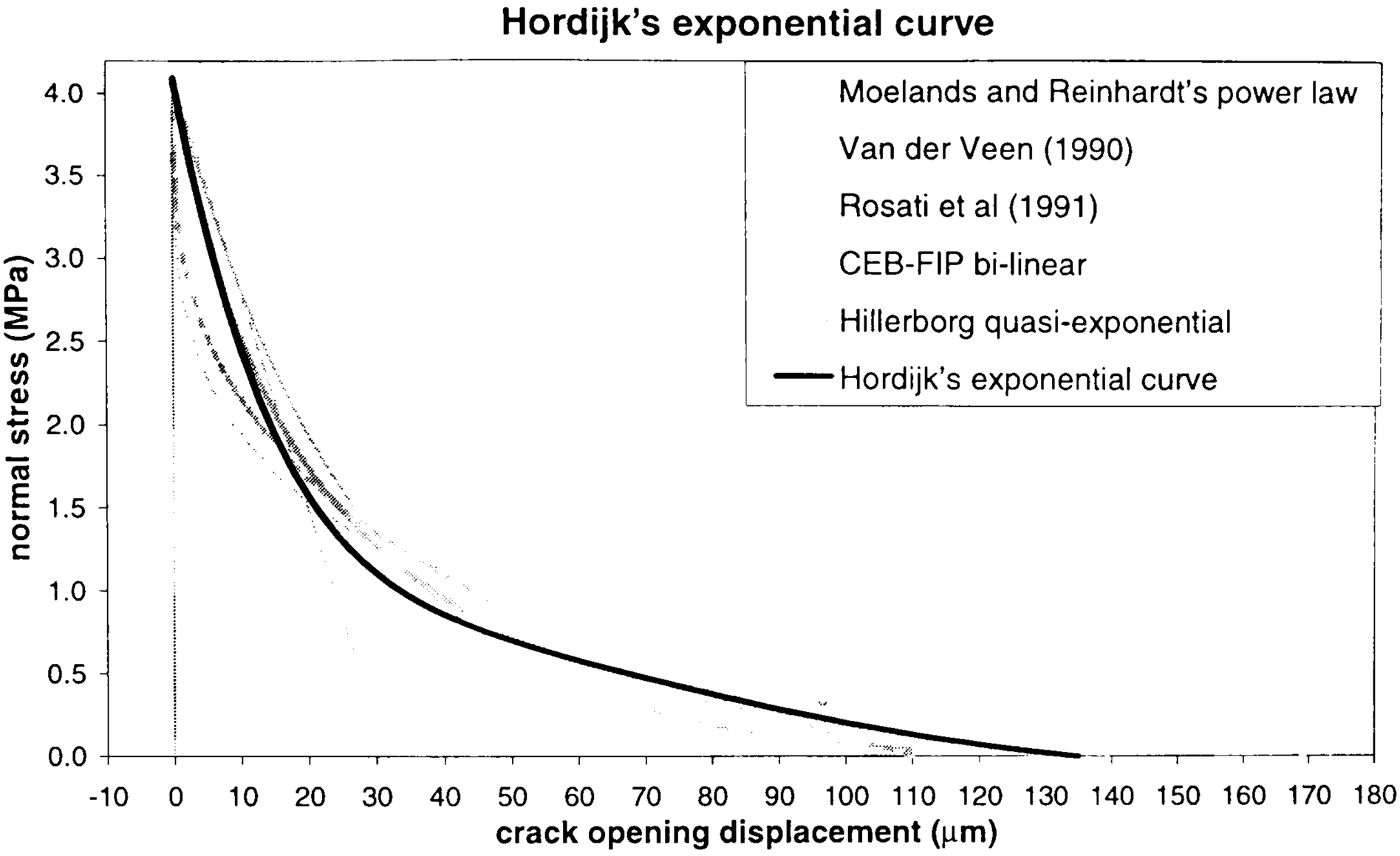

Fig. 2-17: Hordijk's exponential curve

2.3. Finite Element Methods and Continuum Formulations

By definition, fracture is a discontinuous phenomenon. The implementation of the fictitious crack concept in finite element analysis by inserting discrete interface elements describes fracture in a discontinuous manner, but lacks generality and is a cumbersome procedure. The finite element method was first developed to simulate continuous elastic bodies and its formulation is thus more appropriate to describe continuum mechanics phenomena. Consequently, efforts have been put into developing a continuum formulation equivalent, at the macroscopic scale, to the cohesive crack concept.

To this aim, the strain distribution described by a dirac function in the discrete crack approach has to be replaced by a finite strain distribution in the continuum approach, i.e. the continuity of the displacement field has to be restored. This is achieved in the smeared crack approach, where the crack opening is smeared over a certain crack band, in a direction perpendicular to the crack extension. Over this crack band, the strains are decomposed into elastic and fracturing strains. The former models the reversible isotropic elastic deformation of the material in the crack band, while the latter accounts for the dissipative orthotropic behaviour caused by crack opening.

Continuum mechanics is based on four fundamental principles[56]. The two first principles are mechanical principles, which enforce the conservation of the mass and the theorem of virtual works. These two principles are implicitly satisfied in the formulation of the finite element method.

This is not the case, however, of the two other principles stemming from thermodynamics. The first one is the conservation of the energy, stating that the internal energy, Π, is a state function depending only on the state of the structure. This corresponds to the fundamental principle of

fracture mechanics, (Eq. 2-1). The second principle defines the entropy of the system as a purely additive state function, remaining constant for reversible processes, while increasing for dissipative processes. In the case of concrete cracking, the entropy can be understood as a measure of the fracture energy dissipated, or as a measure of damage or material disorder caused by fracture. For the two thermodynamics principles to be satisfied, special care must be taken in the formulation of the constitutive models used in the smeared cracking approach.

2.3.1. Constitutive models

General Description

The derivation of the general description of the constitutive equations for strain-softening is based on thermodynamics considerations. The reader may refer to the book by Lemaitre and Chaboche (1985)[57] for full details. Only the fundamental conclusions will be reproduced in this section.

The state of the structure at a given point is supposed to be entirely defined by the strain tensor and a set of internal variables, p_k. Theoretically, these variables do not need to have a physical meaning, but most of the models developed adopt physical variables as it eases the determination of constitutive evolution laws. The internal variables commonly adopted are the maximum cracking strain in the loading history, $\tilde{\varepsilon}^f$, and the cracking plane defined by its normal vector, $\vec{n}$.

A system of equation relating the stress, to the strain and to the internal variables is necessary. With the hypothesis of linearity in the infinitesimal strain tensor, the general relation can be written:

$$\varepsilon = C(p_k)\sigma + \varepsilon^p(p_k) \qquad \textit{(Eq. 2-48)}$$

where $C(p_k)$ is the secant compliance tensor and ε^p is the irrecoverable or plastic strain, both

depending on the internal variables, p_k. This corresponds to a constitutive models where strain-softening can occur either by stiffness degradation or by strength degradation.

Eventually, a set of evolution rules, also called flow rules in reference to plasticity, have to be formulated. These rules state the criteria defining the evolution of the internal variables with the loading conditions. The compliance of these rules with the second principle of thermodynamics must be ensured.

The evolution rules can be stated either in an integral form or in an incremental form. A common choice is to adopt loading functions obtained by generalisation of classical plasticity. The softening criterion is defined by a yield surface:

$$F(\sigma, p_k, \mu) \leq 0 \qquad \textit{(Eq. 2-49)}$$

And the evolution of softening is defined by an associated incremental flow rule:

$$\dot{p}_k = H_k(p_k, \sigma, \mu)\dot{\mu} \qquad \textit{(Eq. 2-50)}$$

where μ is the softening variable, with $\dot{\mu} \geq 0$ and H_k are the softening functions.

A few typical formulations are presented in the following.

Damage Model with Stiffness Degradation

In the damage model, softening is entirely due to stiffness degradation, i.e. the relation between stresses and strains has a secant formulation:

$$\varepsilon = C(\tilde{\varepsilon}^f, \vec{n}) \cdot \sigma \qquad \textit{(Eq. 2-51)}$$

where the compliance tensor C depends on the maximum cracking strain in the loading history, $\tilde{\varepsilon}^f$, and on the direction of cracking, $\vec{n}$. This does make physical sense as the internal variables describe the history-dependent state of damage at a given point.

The property of isotropy of the material induces that fracture in the normal mode and fracture in the tangential mode are uncoupled. Using this property and decomposing the strain into elastic

and cracking strain leads to the following formulation:

$$\varepsilon = \frac{1+\nu}{E}\sigma - \frac{\nu}{E}tr(\sigma)\cdot Id + C_N\left(\tilde{\varepsilon}^f\right)\cdot \vec{n}\otimes\vec{n} + C_T\left(\tilde{\varepsilon}^f\right)\cdot \tfrac{1}{2}\left(\vec{\sigma}_T\otimes\vec{n} + \vec{n}\otimes\vec{\sigma}_T\right) \qquad \textit{(Eq. 2-52)}$$

where the two first terms corresponds to the elastic strain, the third term to the direct crack opening and the last term to the tangential crack sliding.

Expressing (Eq. 2-52) in the local coordinate system of the crack, $(\vec{n},\vec{t},\vec{s})$, and arranging the stresses in the six-dimensional column format yields:

$$\begin{Bmatrix}\varepsilon_{nn}\\ \varepsilon_{ss}\\ \varepsilon_{tt}\end{Bmatrix} = \frac{1}{E}\begin{bmatrix}1+EC_N & -\nu & -\nu\\ -\nu & 1 & -\nu\\ -\nu & -\nu & 1\end{bmatrix}\begin{Bmatrix}\sigma_{nn}\\ \sigma_{ss}\\ \sigma_{tt}\end{Bmatrix} \qquad \textit{(Eq. 2-53)}$$

and

$$\begin{Bmatrix}\gamma_{ns}\\ \gamma_{st}\\ \gamma_{tn}\end{Bmatrix} = \frac{1}{G}\begin{bmatrix}1 & 0 & 0\\ 0 & 1+GC_T & 0\\ 0 & 0 & 1+GC_T\end{bmatrix}\begin{Bmatrix}\tau_{ns}\\ \tau_{st}\\ \tau_{tn}\end{Bmatrix} \qquad \textit{(Eq. 2-54)}$$

Considering a uni-axial state of tensile stress, the equation reduces to:

$$\varepsilon = \frac{\sigma}{E} + C_N\sigma \qquad \textit{(Eq. 2-55)}$$

Using one of the monotonic softening curves, (Eq. 2-41) to (Eq. 2-47), of the form $\sigma = \phi(w^{cr})$ and assuming that the crack band width, over which the crack is smeared, is known and equal to h, the expression for C_N can be deduced:

$$C_N = \frac{\tilde{\varepsilon}^f_{nn}}{\phi(h\cdot\tilde{\varepsilon}^f_{nn})} \qquad \textit{(Eq. 2-56)}$$

where $\tilde{\varepsilon}^f_{nn}$ is the maximum cracking strain normal to the cracking plane.

For the sake of simplicity, C_N is generally assumed to be independent of the tangential strains, γ_{ns} and γ_{nt}.

As very few experimental data are available on the tangential behaviour, the definition of C_T is mostly speculative. Brittle tangential behaviour, i.e. $C_T = \infty$ at onset of cracking, was shown to

produce unstable analyses. Therefore, a so-called shear retention factor is artificially introduced. Since very little is known about the evolution of the shear stiffness of a crack as it opens, the shear retention factor, β_s, is generally set as a constant. C_T and β_s are linked in the following way:

$$C_T = \frac{1-\beta_s}{\beta_s G} \qquad \textit{(Eq. 2-57)}$$

Another solution is to assume C_T proportional to C_N. This amounts to considering that the softening behaviour is totally controlled by a single internal variable, the maximum normal cracking strain, $\tilde{\varepsilon}_{nn}^{f}$:

$$C_T = c_T \cdot C_N\left(\tilde{\varepsilon}_{nn}^{f}\right) \qquad \textit{(Eq. 2-58)}$$

It is now possible to formulate the model as a classical scalar damage model, with a single scalar variable, ω, which defines the percentage of damage at a particular point:

$$\omega = \frac{EC_N}{1+EC_N} \quad \text{and} \quad \omega_T = \frac{G \cdot c_T}{E} \cdot \omega \qquad \textit{(Eq. 2-59)}$$

and the definition of ω from the softening curve is given by:

$$\omega = \frac{E\tilde{\varepsilon}_{nn}^{f}}{E\tilde{\varepsilon}_{nn}^{f} + \phi(h \cdot \tilde{\varepsilon}_{nn}^{f})} \qquad \textit{(Eq. 2-60)}$$

The stress-strain relation then reduces to the classical expression:

$$\begin{Bmatrix} \varepsilon_{nn} \\ \varepsilon_{ss} \\ \varepsilon_{tt} \end{Bmatrix} = \frac{1}{E}\begin{bmatrix} 1/(1-\omega) & -\nu & -\nu \\ -\nu & 1 & -\nu \\ -\nu & -\nu & 1 \end{bmatrix}\begin{Bmatrix} \sigma_{nn} \\ \sigma_{ss} \\ \sigma_{tt} \end{Bmatrix} \qquad \textit{(Eq. 2-61)}$$

and

$$\begin{Bmatrix} \gamma_{ns} \\ \gamma_{st} \\ \gamma_{tn} \end{Bmatrix} = \frac{1}{G}\begin{bmatrix} 1 & 0 & 0 \\ 0 & 1/(1-\omega_T) & 0 \\ 0 & 0 & 1/(1-\omega_T) \end{bmatrix}\begin{Bmatrix} \tau_{ns} \\ \tau_{st} \\ \tau_{tn} \end{Bmatrix} \qquad \textit{(Eq. 2-62)}$$

To define an irreversible fracturing constitutive model with unloading to its origin, Fig. 2-18-a),

the following evolution rules needs to be adopted:

$$\varepsilon_{nn}^{f} - \tilde{\varepsilon}_{nn}^{f} \leq 0 \qquad \textit{(Eq. 2-63)}$$

and the associated flow rule:

$$\dot{\tilde{\varepsilon}}_{nn}^{f} = \dot{\varepsilon}_{nn}^{f} \qquad \text{with} \qquad \dot{\varepsilon}_{nn}^{f} \geq 0 \qquad \textit{(Eq. 2-64)}$$

Elasto-plastic Model with Strength Degradation

The elasto-plastic model adopts a simple stress-strain relation based on the decomposition of the strains into elastic and irrecoverable plastic strains:

$$\varepsilon = \varepsilon^{e} + \varepsilon^{p} = \frac{1+\upsilon}{E} \cdot \sigma - \frac{\upsilon}{E} tr(\sigma) \cdot Id + \varepsilon^{p}\left(\tilde{\varepsilon}^{p}\right) \qquad \textit{(Eq. 2-65)}$$

where $\tilde{\varepsilon}^{p}$ corresponds to the set of internal variables.

Various flow rules can then be adopted. When complex states of mixed tension-compression stresses needs to be modelled, a Mohr-Coulomb or a Drucker-Prager type of yield condition needs to be adopted.

However, when compressive stresses are assumed to be low enough not to influence the cracking behaviour, a simple Rankine yield criterion is sufficient. The Rankine criterion corresponds to a square yield criterion in the plane of the principal stresses:

$$\sigma_1 - \phi(h \cdot \tilde{\varepsilon}_{nn}^{p}) \leq 0 \qquad \textit{(Eq. 2-66)}$$

where σ_1 is the largest principal stress, ϕ is the unidirectional strain-softening law, h is the assumed crack band width and $\tilde{\varepsilon}_{nn}^{p}$ is the equivalent uni-axial plastic strain.

The associated flow rules simply states that the plastic strain takes place in the direction of the maximum principal stress, i.e. the normality rule:

$$\dot{\varepsilon}^{p} = \dot{\tilde{\varepsilon}}_{nn}^{p} \cdot \vec{n} \otimes \vec{n} \qquad \textit{(Eq. 2-67)}$$

where $\vec{n}$ is the direction of the maximum principal stress, σ_1.

Consequently, in the Rankine type of elasto-plastic model, the crack plane is assumed to co-rotate with the principal stresses, so that no tangential cracking strain ever occurs.

With this evolution rule, softening is entirely achieved by strength degradation. Upon unloading, only the elastic strains are recovered, Fig. 2-18-b). During the loading history, the principal softening strain increases monotonically.

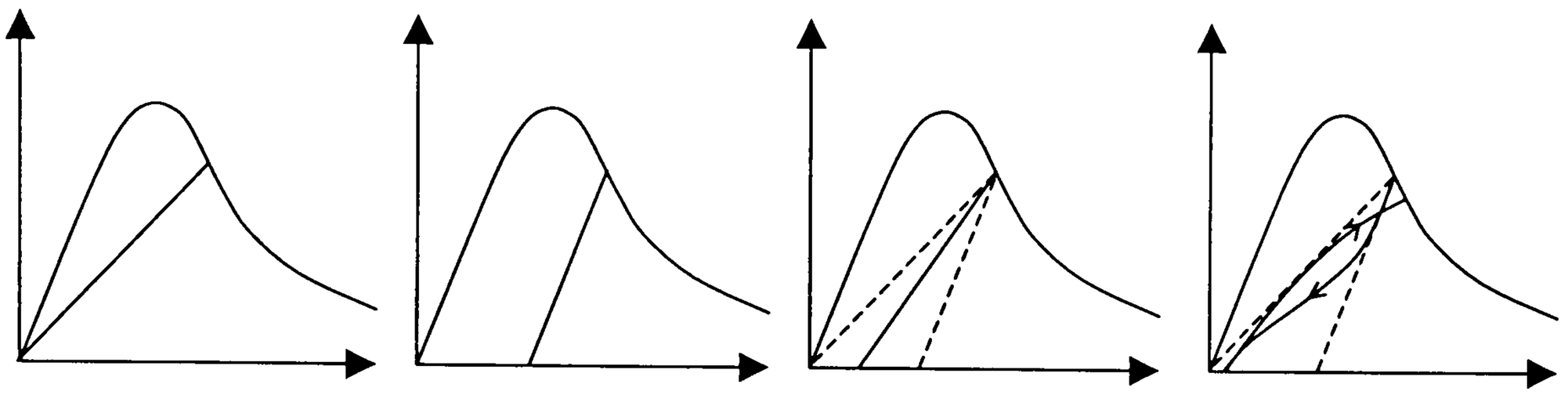

a) damage model *b) elasto-plastic model* *c) mixed model* *d) experimental response*

Fig. 2-18: Loading-unloading response of various constitutive models

Mixed Model

The main difference between the two aforementioned constitutive models is their response upon unloading, Fig. 2-18. Experimental uni-axial unloading-reloading curves display a complex behaviour comprising hysteresis loops, Fig. 2-18-d), which neither the damage nor the plastic model can simulate. It is felt that the damage model makes more physical sense to describe fracture, while the plasticity is more appropriate to model complex triaxial states with critical tensile and compressive stresses.

A response upon unloading closer to experimental curves can however be achieved by adopting mixed models, where softening occurs both by stiffness and strength degradation, Fig. 2-19:

$$\varepsilon = \varepsilon^e + C^f \sigma + \varepsilon^p \qquad \textit{(Eq. 2-68)}$$

For the sake of simplicity, the fracture plane can be assumed to co-rotate with the maximum

principal stress, σ_I and the Rankine yield criterion can be adopted for the plastic strain:

$$\varepsilon = \varepsilon^e + \eta(\tilde{\varepsilon}^f) \cdot \sigma_1 \cdot \vec{n} \otimes \vec{n} + H(\tilde{\varepsilon}^f) \vec{n} \otimes \vec{n} \qquad \textit{(Eq. 2-69)}$$

where η and H are material functions related to the softening curve ϕ. The maximum normal cracking strain in the loading history, $\tilde{\varepsilon}^f$, is the only internal variable.

The softening criterion writes:

$$\sigma_1 - \phi(\tilde{\varepsilon}^f) \leq 0 \qquad \textit{(Eq. 2-70)}$$

and the associated evolution rules:

$$\dot{\tilde{\varepsilon}}^f = \dot{\varepsilon}^f_{nn} \qquad \text{with} \qquad \dot{\varepsilon}^f_{nn} \geq 0 \qquad \textit{(Eq. 2-71)}$$

and

$$\dot{\varepsilon}^p = \frac{dH(\tilde{\varepsilon}^f)}{d\tilde{\varepsilon}^f} \cdot \dot{\tilde{\varepsilon}}^f \cdot \vec{n} \otimes \vec{n} \qquad \textit{(Eq. 2-72)}$$

Considering the case of uni-axial tension, the relation between η, H and ϕ is obtained:

$$\begin{aligned} \tilde{\varepsilon}^f &= \eta(\tilde{\varepsilon}^f) \cdot \phi(\tilde{\varepsilon}^f) + H(\tilde{\varepsilon}^f) \\ \therefore \eta(\tilde{\varepsilon}^f) &= \frac{\tilde{\varepsilon}^f - H(\tilde{\varepsilon}^f)}{\phi(\tilde{\varepsilon}^f)} \end{aligned} \qquad \textit{(Eq. 2-73)}$$

where $H(\tilde{\varepsilon}^f)$ represents the permanent strain remaining after unloading, Fig. 2-18-c).

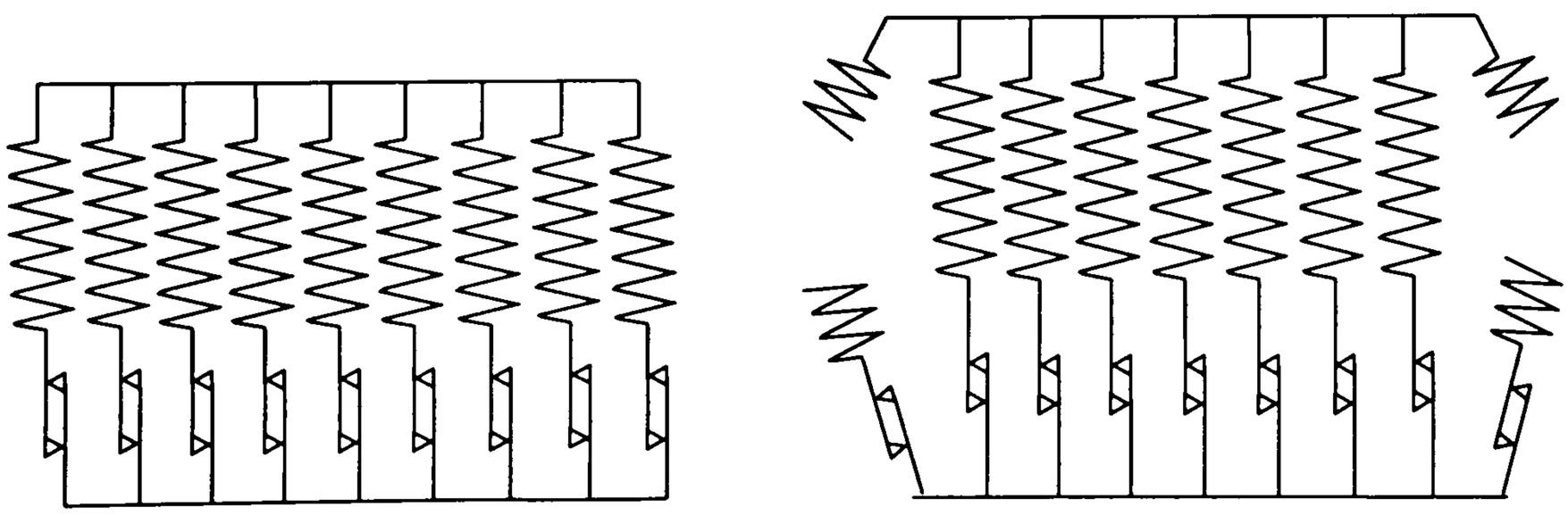

a) elastic stage *b) softening stage*

Fig. 2-19: Schematic representation of the mixed constitutive model

2.3.2. Localisation and boundary value problem

Models based on the cohesive crack concept have been shown to require three material parameters, namely, the tensile strength, f_t, the specific fracture energy, G_f, and the shape of the softening curve. This information is entirely contained in the equation of the softening curve, $\sigma_t = \phi(w^{cr})$. In the continuum formulation of strain-softening, the crack opening w^{cr} is not explicitly known, and the definition of the evolution rules from $\phi(w^{cr})$ implies that the band width, h, over which the crack opening is smeared, is known in advance, Fig. 2-13, p24..

Some authors have assumed that the crack band width is a physical parameter, and ought to be determined from material characteristics, e.g. the maximum aggregate size. This assumption, based on the fact that the FPZ observed experimentally displays an inherent width, is in fact erroneous in the framework of the classical finite element formulation. As noted by Rots (1988)[61], although it is possible to argue that the smeared crack concept appropriately simulates the dispersion of the FPZ ahead of the crack tip, the portion of the crack behind the crack tip is indisputably a discontinuous phenomenon for which the smeared crack concept is an artifice introduced for computational convenience.

The width over which cracking strain will be smeared is indeterminate in finite element analysis, unless some kind of localisation limiter is introduced. This can be demonstrated simply by considering the example of a plain concrete bar loaded in uni-axial tension.

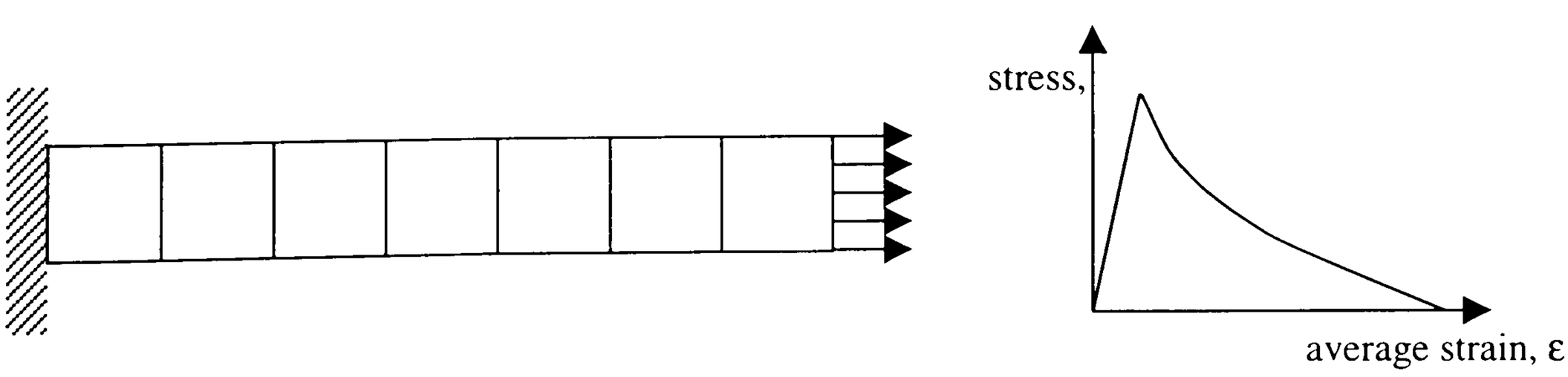

a) finite element discretisation *b)adopted constitutive law*

Fig. 2-20: Plain concrete bar loaded in uni-axial tension

The bar is discretised along its length into n identical elements, Fig. 2-20-a). The load is then increased up to the cracking point. At this point, a uniform state of stress exists throughout the bar. The cracking strength f_t is reached in all the elements at the same time. From that point onwards, it can be shown[58] that static equilibrium on the descending branch can be achieved by any combination of elements either softening or elastically unloading, Fig. 2-21-b). The two extreme behaviours are uniform softening occurring in all the elements and localisation of softening in only one element while all the others are unloading. In the first case, the crack band width is equal to the total length of the bar, $h = L$, while in the second case, the crack band width is equal to the length of a single element, $h = L / n$. Any combination is statically acceptable and can theoretically be predicted by finite element simulation. The cracking point is termed a bifurcation point as several equilibrium branches emerge from it.

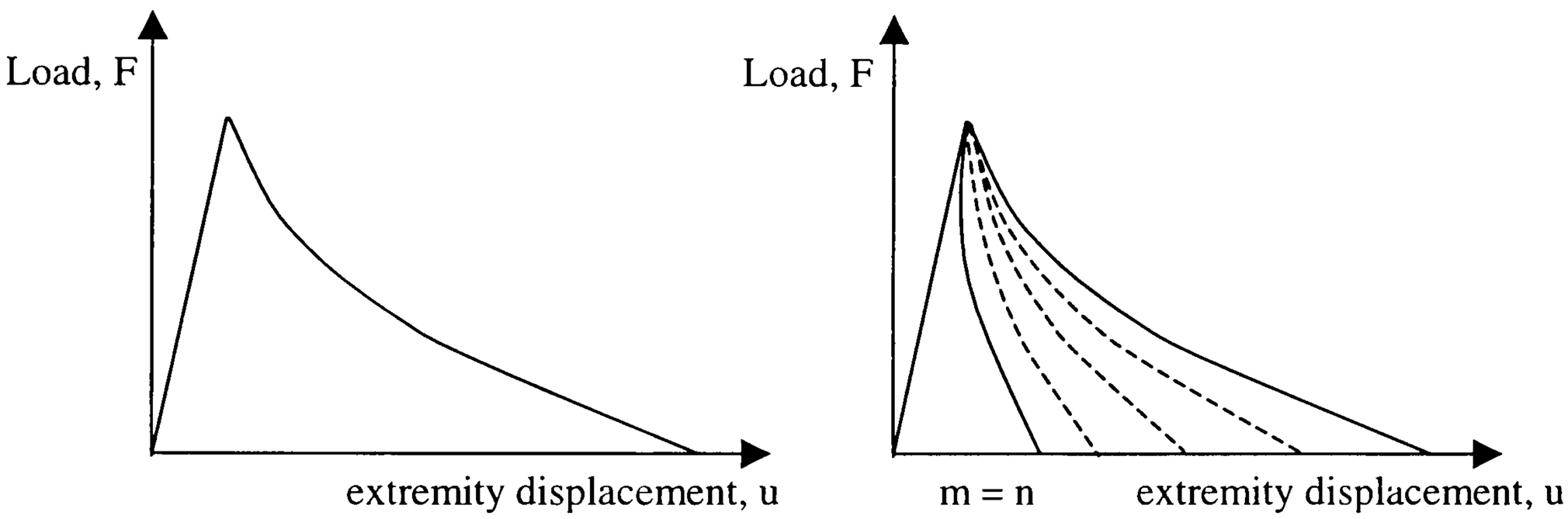

a) experimental response *b) possible finite element responses*

Fig. 2-21: Localisation of cracking in a plain concrete bar in tension

For the continuum formulation to be macroscopically equivalent to the real structure, the predicted load-displacement diagrams must be identical. This can only be achieved by choosing the crack band width equal to the element length multiplied by the number of softening elements, $h = m \, . \, L / n$, since only one localised crack is experimentally observed in the length of the bar. Consequently, the constitutive material model depends on the degree of localisation the finite element model will allow.

The bifurcation problem is a complex one and will be discussed further in section 2.2.4. The inability of the classical finite element formulation to solve the localisation problem is due to

the fact that the second law of thermodynamics is required to determine the appropriate bifurcated path, but the finite element formulation ignores this principle. This implies that beyond a certain level of softening, the governing set of partial differential equation changes regime, which is typical of bifurcation problems. In the static case, the elliptic character of the set of partial differential equations is lost, while, on the other hand, in the dynamic case, a change from a hyperbolic set to an elliptic set can be observed. In both cases, the rate boundary value problem becomes ill-posed and numerical solutions suffer from mesh sensitivity.

In practice, the bifurcation problem rarely arises as such in structural analysis. A non-uniform state of stress is usually present, which allows localisation in a single element to occur. Local bifurcation can also be avoided by the introduction of small stochastic imperfections throughout the structure, allowing the cracking strain to localise in the weaker elements. Consequently, if uniform fields of stresses and structural symmetries are kept at a minimum, the standard continuum formulation of strain-softening will tend to predict strain localisation in a band with the width of a single element, while the rest of the structure remains elastic. This implies that if the mesh is continuously refined so that the element size tends towards zero, the simulated crack band width will as well tend towards zero. For the prediction of the continuum formulation to tend towards the cohesive crack approach, the fracture energy dissipated in the crack band needs to remain a constant and not depend on the finite element discretisation. This can be achieved by setting the crack band width equal to the characteristic size of the finite elements used.

2.3.3. Bazant's crack band model

Bazant and Oh (1983)[59] refined the concept of smeared cracking to address the problem of localisation. Bazant's model, the crack band model, provides a solution to mesh size dependency by manipulating the crack band width so that the fracture energy dissipated remains constant upon mesh refinement. This does not constitute a regularisation method of the

boundary value problem as such, but it provides a useful method to render the smeared crack concept physically meaningful.

In the crack band model, two cases are distinguished:

1- The fracture is known to be physically distributed over the structure, with localised fracture planes spread at regular small intervals. This can be due to uniform stress fields in densely reinforced panels (e.g. shear walls), or to the presence of elastic structural elements restraining localisation (e.g. bonded steel plates).

2- The fracture is known to be physically localised in a fracture plane.

The following sections present the procedure recommended in each case.

Physically distributed fracture

It is assumed that, if the structure is properly modelled, the distributed nature of cracking will be reflected in the simulation in the form of a uniform field of cracking strains. The degree of softening is then independent of the mesh refinement. A single physical crack is smeared over an indeterminate number of finite elements displaying a constant distribution of cracking strain.

It must be emphasised that the finite element formulation is unable to predict the density of fracture energy consumed, which depends on the average crack spacing observed experimentally. Consequently, an extra parameter must be introduced in the form of a crack band width equal to the average crack spacing:

$$h = L_{av} \qquad \textit{(Eq. 2-74)}$$

Thus, in the case of distributed fracture, strain softening is defined by four parameters: three material parameters (f_t, G_f and the shape of the softening curve) and one structural parameter, h, depending on the structural elements responsible for crack distribution, e.g. the reinforcement grid. If experimental determination of the average crack spacing is not available, empirical formula must be resorted to. Usually, these formulae depend on the geometry of the elastic elements (e.g. diameter and spacing) and their elastic properties (e.g. elastic modulus).

Physically localised fracture

In the case of localised fracture, the crack band model assumes that localisation also arises in the smeared model, and consequently each smeared crack in the simulation corresponds to a single physical crack. For this condition to be satisfied, it must be ensured that any structural symmetry is destroyed. This can be achieved either by introducing small geometric or material imperfection in a random manner, or by introducing crack initiators, like notches, concentrated forces or material discontinuities.

In finite element analysis, the stress-strain behaviour at an integration point is considered to be representative for the area that belongs to it. Consequently, in the smeared crack approach, when fracture localises at an integration point, the area over which the cracking strain is smeared corresponds to the area belonging to the integration point. For the fracture energy consumed in the model to be equal to the fracture energy of a single crack, the crack band width must therefore be chosen equal to the width of the area belonging to the integration point. This width is proportional to the characteristic size of the element considered. It depends also on the number of integration points in the element, on the order of the shape functions and on the orientation of the crack inside the element.

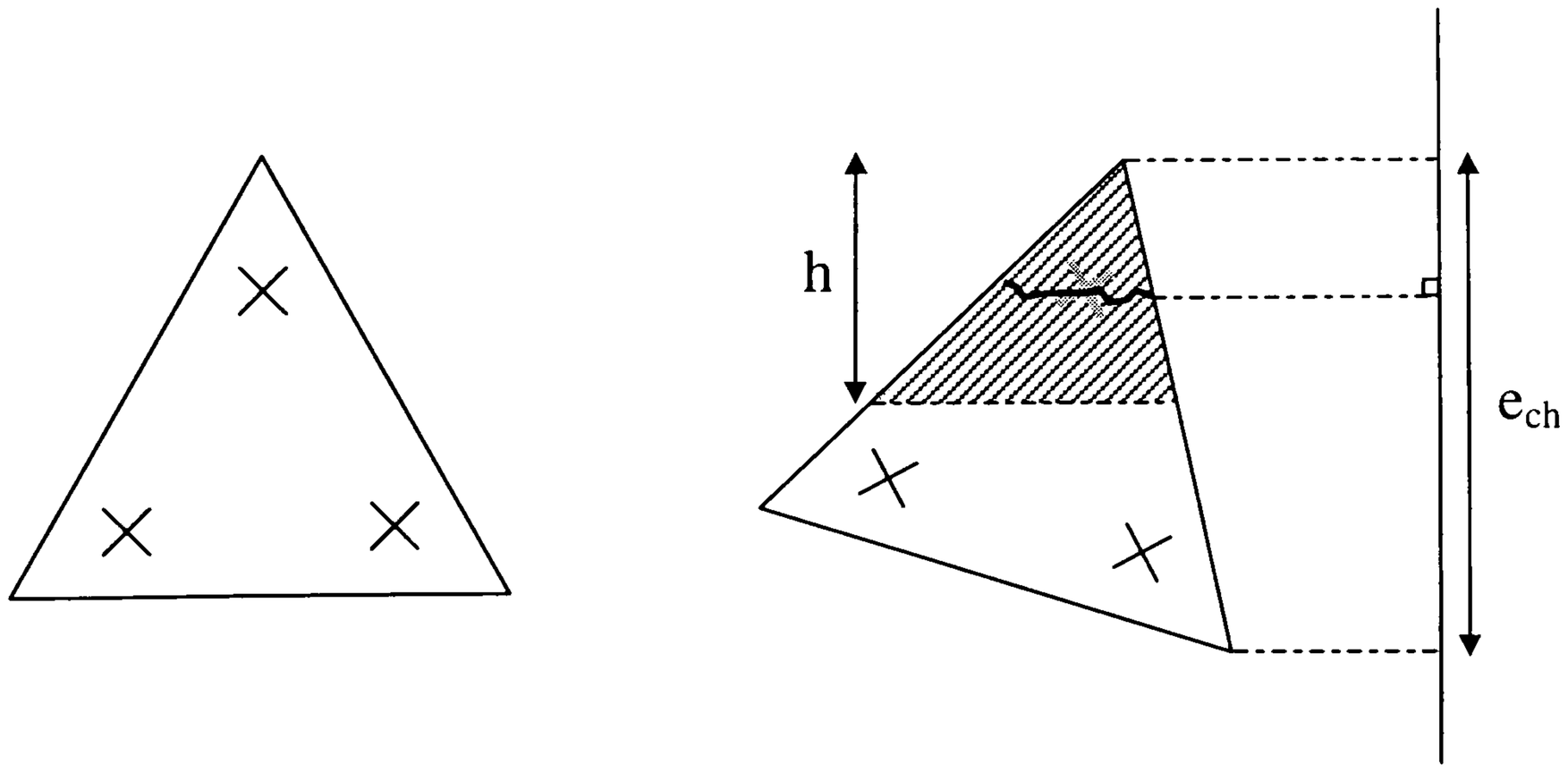

a) triangular element

b) smeared cracking localised in one integration point

Fig. 2-22: Definition of the crack band width, h

The general formula for the determination of the crack band width has the following form:

$$h = \alpha(p) \cdot \frac{e_{ch}(\theta)}{n(\theta)} \qquad \textit{(Eq. 2-75)}$$

where $\alpha(p)$ is a correction factor (with $\alpha(p) \leq 1$) depending on the order p of the shape functions, $e_{ch}(\theta)$ is the size of the element when projected on a line perpendicular to the cracking direction, and $n(\theta)$ is the number of rows of integration points when projected on the same line, Fig. 2-22. The value of $\alpha(p)$ is difficult to assess and is generally approximated to 1.

For instance, for a square element with linear shape functions and four integration points, if the orientation of cracking is parallel to the mesh lines, the crack band width is equal to half the element size, Fig. 2-23.

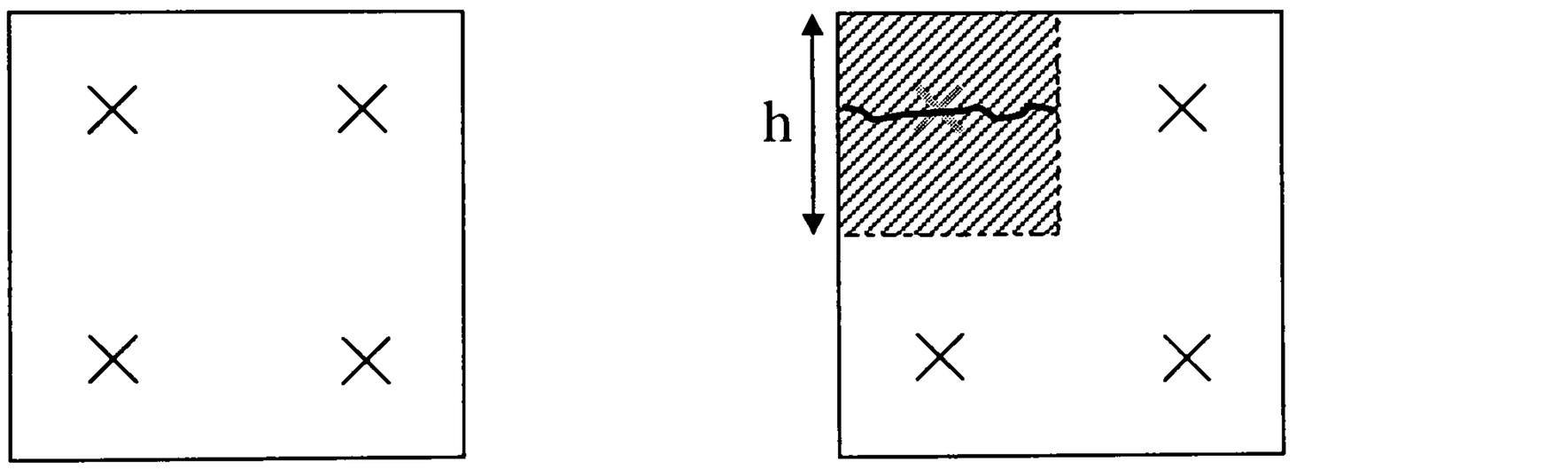

a) square element

b) smeared cracking localised in one integration point

Fig. 2-23: Example of crack band width determination

In elements large relatively to the structural size, elastic unloading displacements can become larger than the displacements due to cracking. The slope of the strain-softening curve at crack initiation is particularly critical. This slope results from the superimposition of the elastic modulus (positive) and the initial slope of the softening curve (negative), which depends on the degree of localisation, that is h. If h, which is proportional to the element size, becomes too large so that the initial slope of the strain-softening curve becomes positive, the element stiffness matrix becomes unstable with the presence of a local snap-back.

The critical crack band width is defined as follows:

$$\left[\frac{d\sigma_t}{d\varepsilon}\right]_{\varepsilon^{cr}=0} \leq 0 \qquad \textit{(Eq. 2-76)}$$

$$\therefore \left[\frac{d\sigma_t}{d\varepsilon^{cr}}\right]_{\varepsilon^{cr}=0} + E \leq 0$$

$$\therefore \left[\frac{d\sigma_t}{d(w^{cr}/h)}\right]_{w^{cr}=0} + E \leq 0$$

$$\therefore h \cdot \phi'(0) \leq -E$$

$$\therefore h \leq -\frac{E}{\phi'(0)} \qquad \textit{(Eq. 2-77)}$$

For linear strain-softening, $\phi'(0) = -f_t^2 / G_f$, which gives, $h_{max} = EG_f / f_t^2$.

For Hordijk's exponential softening curve, $\phi'(0) = -1.354 \cdot f_t^2 / G_f$, which gives, $h_{max} = 0.738 \cdot EG_f / f_t^2$.

It can be noted that h_{max} is of the general form: $h_{max} = \lambda \cdot EG_f / f_t^2$ where λ is a coefficient depending on the shape of the softening curve.

In this case, the non-linear finite element analysis will usually jump dynamically as shown on Fig. 2-24. This results in a larger fracture energy consumption than required, which remains constant upon variation of *h*. In this case, the general rules of the crack band model fail to resolve the localisation problem. Further steps needs to be taken to avoid mesh size dependency.

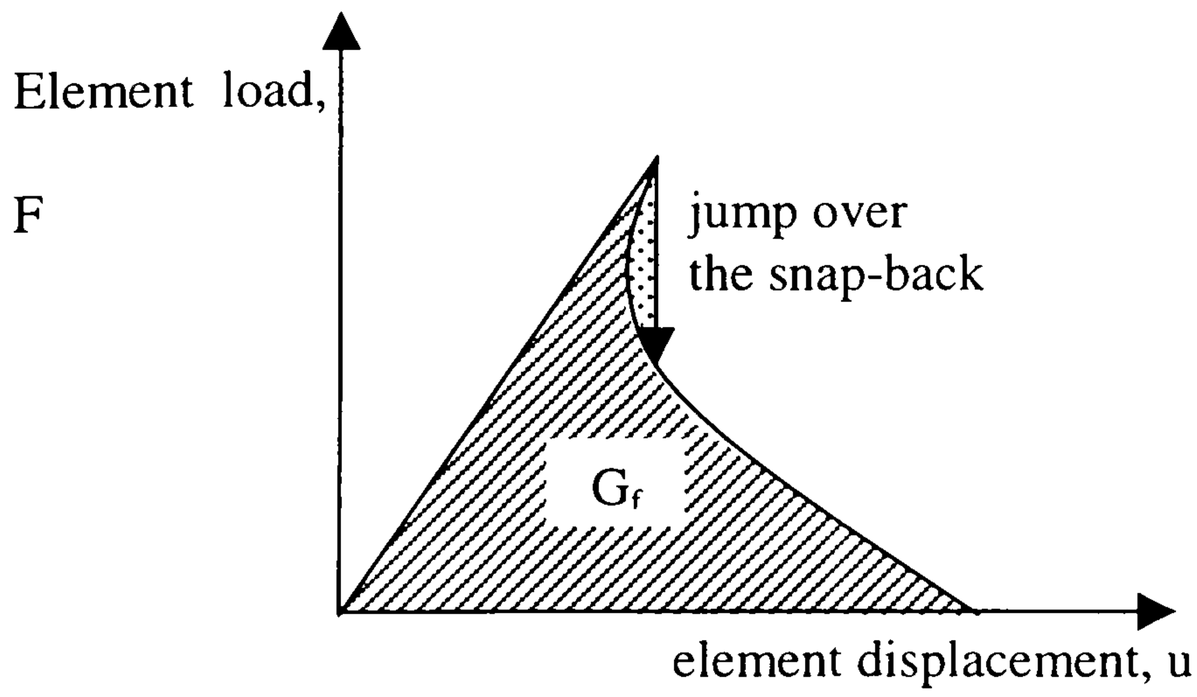

Fig. 2-24: Local snap-back in large elements

Alternative solutions are:

- limit the element size so that h is smaller than h_{max}.
- reduce the tensile strength so that the snap-back is avoided, conserving the same G_f:

$$f_{t,reduced} = \left(\frac{G_f E}{\lambda \cdot h} \right)^{1/2} \qquad \textit{(Eq. 2-78)}$$

Rots' fixed crack and multi-directional crack models

Rots (1985)[60] developed a crack band model with a formulation of the constitutive equations very similar to the damage model with stiffness degradation presented in section 2.3.1. This model is presented in more details in this section as this is the model chosen for subsequent finite element analyses.

The constitutive equations are formulated using an abridged matrix formulation. The physically meaningful cracking strains, $e^{cr} = \left(\varepsilon_{nn}^{cr}, \gamma_{nt}^{cr} \right)^T$, expressed in the coordinate system of the crack, are extracted from the cracking strain tensor using a transformation matrix N depending on $\vec{n}$, the orientation of cracking:

$$\varepsilon^{cr} = N \cdot e^{cr} \qquad \textit{(Eq. 2-79)}$$

$$e^{cr} = N^{-1} \cdot \varepsilon^{cr} \qquad \textit{(Eq. 2-80)}$$

The same treatment is applicable to the stresses:

$$\sigma = N \cdot s^{cr} \qquad \textit{(Eq. 2-81)}$$

$$s^{cr} = N^{-1} \cdot \sigma \qquad \textit{(Eq. 2-82)}$$

Accordingly, the secant formulation of (Eq. 2-61) and (Eq. 2-62) can be rewritten using a two-dimensional matrix:

$$\begin{Bmatrix} \sigma_{nn} \\ \tau_{nt} \end{Bmatrix} = \begin{bmatrix} D^I & 0 \\ 0 & D^{II} \end{bmatrix} \begin{Bmatrix} \varepsilon_{nn}^{cr} \\ \gamma_{nt}^{cr} \end{Bmatrix} \qquad \textit{(Eq. 2-83)}$$

$$s^{cr} = D^{cr} \cdot e^{cr} \qquad \textit{(Eq. 2-84)}$$

In these equations, mode I and the mode II cracking are once again assumed to be uncoupled.

In the simplest version of Rots' model, called the fixed crack model, the onset of cracking is caused by the maximum stress reaching the cracking strength, f_t. The direction of cracking is taken at normal to the principal stress at onset of cracking and supposed to remain constant. This corresponds to the following evolution rule for the internal parameter $\vec{n}$:

$$\vec{n} = \vec{n}_0 \qquad \textit{(Eq. 2-85)}$$

where $\vec{n}_0$ is the direction of the maximum principal stress at onset of cracking.

The general stress-strain equation is easily obtained from:

$$\sigma = D^e \cdot \left(\varepsilon - \varepsilon^{cr}\right) \qquad \textit{(Eq. 2-86)}$$

where D^e is the material elastic stiffness matrix.

Upon manipulation, the final equation is deduced from (Eq. 2-82), (Eq. 2-84) and (Eq. 2-86):

$$\sigma = \left[D^e - D^e N\left(D_0^{cr} + N^T D^e N\right)^{-1} N^T D^e\right]\varepsilon \qquad \textit{(Eq. 2-87)}$$

where D_0^{cr} is the initial D^{cr}.

If a non zero shear retention factor, β, is chosen, and if rotation of the principal axes occurs after onset of cracking, significant shear stresses are allowed to build up along the crack, which can cause the maximum principal stress to exceed once again the tensile strength in spite of strain softening. Although, the fixed crack concept makes physical sense, a number of authors[61-63] have reported it to produce over-stiff responses due to shear retention.

Consequently, the model has been modified to allow for multi-directional cracking. In the multi-directional crack model, after first cracking has occurred at an integration point, further cracking at the point is allowed to occur in a different direction based upon two criteria:

- the maximum principal stress is larger than the cracking strength,
- the direction of the principal stress is at an angle from existing cracking which is larger than a predefined threshold angle, θ_{cr}. A good choice for θ_{cr} is between 20 and 30 deg. to avoid over-stiffening and keep the level of complexity of the model reasonable.

Total strain is obtained by superposition of the contributions of all the cracks present in one point. To ease the formulation of the superposition of the cracking strains starting at different moment in the cracking history, an incremental approach is adopted where secant stiffness matrices are replaced by tangent matrices. For a complete presentation of the multi-directional crack formulation refer to Rots (1988)[61]. The multi-directional crack model is reported to yield softer responses than the fixed crack model. The simulated response is shown to fit better experimental behaviour.

Rots (1988)[61] demonstrated the equivalence to the limit of the multi-directional crack concept with the rotating crack concept for which no shear strains occurs in the crack as the axis of the crack is co-rotated with the principal stress axis. An example of purely rotating crack model is the elasto-plastic model with Rankine yield criterion presented in section 2.3.1. Simulations show that reducing the threshold angle, θ_{cr}, to zero renders the multi-directional crack model equivalent to the Rankine model.

Limitations

The main drawback pertaining to the crack band model is the directional bias introduced by the mesh topology. Due to the discontinuous representation of the strain field inherent to the finite element approach by element shape functions, strain discontinuities of the first or second order are introduced at the element interfaces. This artificially introduces preferential fracture directions along the mesh lines. A fracture plane supposed to form at small angles (10 to 30 deg.) to the mesh line will tend to be attracted by the element boundaries.

Consequently, a smooth fracture line is generally modelled by a rugged zig-zag crack band, which displays several linear portions following the mesh lines connected by kinks correcting in a discrete manner the deviation from the true fracture direction, Fig. 2-25.

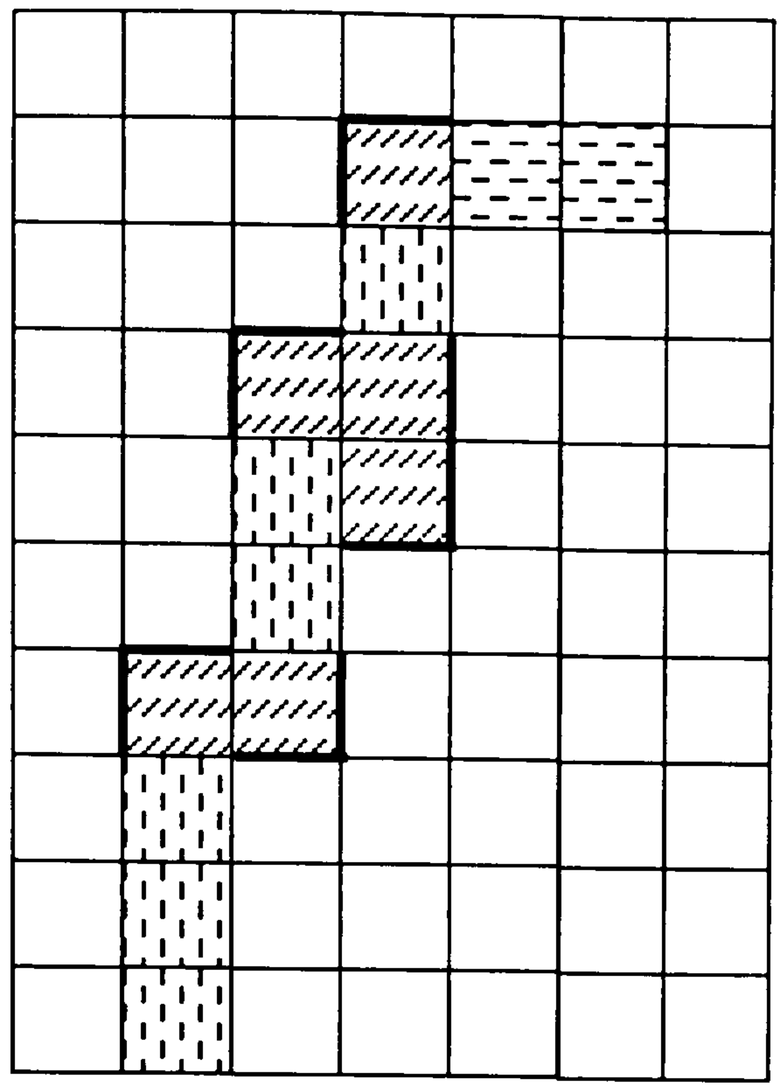

Fig. 2-25: Zig-zag cracking induced by directional bias

The objectivity of the method is therefore significantly compromised, as the cracking path predicted is mesh dependent. This leads usually to an over-stiff response of the model.

The effect of the directional bias is multiplied by the fact that the behaviours of the integration points inside an element are generally coupled, which leads to smearing the crack over the whole width of an element, contrary to the assumption of strain localisation in a single integration point. In addition, the existence of kinks along the cracking path renders the fracture plane discontinuous, forcing certain softening elements to be restrained by their neighbouring uncracked elements, as emphasised by bold lines in Fig. 2-25. The compatibility of displacements implies either further distribution of the crack in its width or spurious stiffening with high stress concentration in the elastic elements. This phenomenon is called stress locking.

To try to remedy the spreading of the crack band occurring in zig-zag crack propagation, Rots (1988)[61] suggested the following correction for the assumed crack band width. These results are valid for a crack propagating at an angle of 30 deg. to the mesh lines:

- linear triangular elements with one integration point, $h = e_{ch}$

- linear quadrilateral element with four integration point, $h = \sqrt{2} \cdot e_{ch}$
- quadratic triangular element with seven integration points, $h = \sqrt{2}/2 \cdot e_{ch}$
- quadratic quadrilateral element with nine integration points, $h = e_{ch}$

A second drawback of the crack band model is the appearance of spurious kinematic modes along the loading history. To the opinion of the author, these kinematic modes are not linked with the insufficiency of the integration scheme, but corresponds to local bifurcation phenomena that should be expected to arise due to the fundamental localisation indeterminacy of the smeared crack concept. While these spurious modes do not have significant influence on the structural response, they seriously impair the stability of the non-linear process resulting in insurmountable divergence in the iterative solution procedure.

In conclusion, the determination of the crack band width prior to the analysis proves to be a difficult task, especially if the direction of cracking relatively to the mesh topology is not known in advance. The crack band approach should therefore be seen as an approximate manipulation, through the determination of h, aimed at reducing mesh dependency. This does not however constitute a proper regularisation method of the boundary value problem.

However, Rots (1988)[61] demonstrates that the role of G_f is less important than the role of the two other material parameters (f_t and the shape of the softening curve). Since the size of the crack band width only influences G_f in the smeared crack model, this alleviates the consequences of the errors and questions involved in the determination of h. This is for this reason that the crack band method remains the most commonly used model for simulating fracture in quasi-brittle material.

2.3.4. Alternative models

As the drawbacks of the crack band model were discovered, the need for a more robust and more reliable model grew stronger and stronger. Two possible solutions were then available:

- Either imbed the discontinuous approach of the cohesive crack model into the continuum formulation of the classical finite element method, thus avoiding the fastidious introduction of strain-softening interface elements.
- Or enrich the continuum formulation of the crack band model by resorting to regularisation methods.

Inner softening band model

The inability of the inter-element discrete crack approach to predict the path of fracture prompted researchers to investigate the possibility of imbedding the discontinuous cracking displacement field within the elements. This is achieved by adding to the traditional finite element formulation a shape function including a jump discontinuity, which models an intra-element crack. The constitutive relationship is then expressed in term of stress and relative displacement as in the discrete crack approach.

This model originated with the modelling of shear bands in metal[64,65]. The concept was then applied to concrete at the Luleå University of Technology where it was defined as the inner softening band model[66-68]. In this model, the initial orientation of cracking is determined by the maximum principal stress. Subsequent rotation of the crack upon principal axis rotation is controlled by a parameter ζ, with $\zeta=0$ corresponding to the fixed crack concept, while $\zeta=1$ corresponds to the rotating crack concept.

The objectivity of the inner softening band model upon mesh refinement was shown, however the sensitivity of the mesh alignment remains a problem, even though it is not as pronounced as in the crack band model.

Enriched continuum models

An alternative solution is to maintain the crack band formulation but enriched with a regularisation procedure. Several regularisation procedures exist. Although they are very different in their formulation, they are all based on the introduction of an additional material parameter, namely an internal length scale.

The aim of the regularisation is to restore the well-posedness of the rate boundary value problem, thus remedying to the spurious mesh dependency and the localisation indeterminacy. The well-posedness of the boundary problem relies on three conditions. The first one is that the ellipticity of the equilibrium rate equation is maintained throughout the computation. The loss of ellipticity corresponds to the condition:

$$\det\left(n_j D_{ijkl} n_l\right) = 0 \qquad \textit{(Eq. 2-88)}$$

where D is the material tangential stiffness matrix and n the vector normal to the boundary.

For dynamic problems, this condition prevents the existence of spurious plane acceleration waves. The second condition is a boundary complementing condition excluding the emergence of stationary waves. The third condition is an interfacial complementing condition excluding the emergence of stationary interfacial waves.

The most commonly used regularisation method is the non-local continuum approach originally conceived for elastic material[69]. In this approach, the loss of ellipticity of the rate boundary value problem is remedied by using a non-local definition of the internal softening variable. While stresses and strains remain local variables, the value of the internal softening variable defined at a given point depends on the state of the material in the vicinity of this point. This can be understood mathematically as a localisation limiter, preventing the energy dissipation to vanish in a zone of zero volume upon mesh refinement. It can as well be understood physically as a way to model the interaction that exists between the microcracks. The formation or growth of one microcrack either promotes or inhibits the formation or growth of cracks at a distance (e.g. shielding effect).

Non-local models can be based on a plasticity or a damage formulation. The most common model is the scalar damage model developed by Bazant and Pijaudier-Cabot (1988)[70]. This model is an elasticity based model relying on a total stress-strain formulation:

$$\sigma = (1-\Omega)C \cdot \varepsilon \qquad \textit{(Eq. 2-89)}$$

where σ and ε are local tensors and Ω is a non-local damage parameter controlling strain-softening.

Ω is defined using a spatial averaging method:

$$\Omega(x) = \frac{1}{V_r(x)} \int_V g(s-x) \cdot \omega(s) \cdot dV \qquad \textit{(Eq. 2-90)}$$

where ω is the local damage,

$$V_r = \int_V g(s-x) \cdot dV \qquad \textit{(Eq. 2-91)}$$

and $g(s\text{-}x)$ is a weight function generally chosen as a Gaussian distribution:

$$g(r) = \exp\left(-k \left(\frac{r}{l_{ch}} \right)^2 \right) \qquad \textit{(Eq. 2-92)}$$

l_{ch} is assumed to be a material characteristic length with the same order of magnitude as the material inhomogeneities. Experiences carried out by Bazant and Pijaudier-Cabot (1989)[71] using unlocalised tension specimens showed that $l_{ch} \approx 2.7 \cdot d_{agg}$ for concrete.

An indirect method to unlocalise the formulation of the crack band model is to render the internal softening variable dependent on the gradient of the strain field. Such a formulation can be derived from the nonlocal model by expanding the strain field in the neighbourhood of a point into a Taylor series where the strain distribution in the vicinity of the point is approximated by the spatial partial derivatives of the strain tensor. A unidirectional formulation reduces to:

$$\bar{\varepsilon}(x) = \varepsilon(x) + \int_{-\infty}^{+\infty} g(s) \frac{s^2}{2l} ds = \varepsilon(x) + \left(\frac{\lambda}{2\pi} \right)^2 \cdot \frac{\partial^2 \varepsilon}{\partial x^2}(x) \qquad \textit{(Eq. 2-93)}$$

where λ is the characteristic length.

In a plasticity based model, $\bar{\varepsilon}$ can be used as the internal variable in lieu of $\tilde{\varepsilon}$.

These models are called grade-n continua (n corresponding to the degree of the Taylor expansion), or gradient models. This method results in the same regularised continuum formulation as the non-local approach. However, gradient plasticity has the distinct advantage that the consistency condition now yields a partial differential equation instead of an integro-differential equation.

The grade-n continuum approach can be considered as a generalisation of Cosserat's couple stress continuum or Eringen's micropolar elasticity. These methods were considered to be an alternative to achieve regularisation of the boundary value problem, but they have been superseded by fully non-local or high-gradient models, and will not be presented in here.

2.4. Non-linear Solution Techniques

When fracturing material models coupled with robust iterative solution procedures were introduced in non-linear finite element codes, it was expected ultimately that cracking patterns and failure mechanisms of reinforced concrete structures could be systematically simulated. However, after more than two decades of continuing refinement of the numerical techniques, calculations are repeatedly reported to be unstable and convergence is often lost before the failure mechanism is engaged. This can often be accounted for by the existence of singular points along the equilibrium path. At these points the customary continuation methods fail. More advanced numerical techniques based on bifurcation theory need to be implemented to continue the simulation past the singular point[72].

In non-linear static analysis, a singular point is characterised by the tangential stiffness matrix of the structure, K_t, becoming singular. This means that in the vicinity of a singular point, K_t^{-1} is ill-conditioned, and the convergence of the iterative method is lost. In order to solve this difficulty, two qualitatively different cases must be distinguished: limit points and bifurcation points. A limit point corresponds to a maximum in the load-displacement space along a single equilibrium path, and can be easily dealt with using indirect displacement control or the arc-length method[73-75]. On the other hand, a bifurcation point corresponds to a branch point, from which several alternative equilibrium paths emerge, and its investigation is generally not straightforward.

Much research has been devoted to the local bifurcation problem originating from the formulation of the material model for smeared cracking. This can be explained by the inability of the model to predict, in the case of a uniform stress field, how localised a crack band will be. The cracking point is thus a bifurcation point, after which each possible combination of crack band localisation constitutes an alternative equilibrium path. The solution to this problem is to

have recourse to an enriched continuum formulation, or to the discrete crack model.

Comparatively, little effort has been devoted to the more fundamental structural bifurcation problem. For this type of bifurcation, the alternative paths correspond to alternative softening mechanisms of the structure. Similarly to buckling, each softening mechanism leads to a different failure load and a different failure mode. This is the reason why it is crucial for design to make sure that every alternative path has been traced. This can be achieved using numerical bifurcation methods[72,76].

In this chapter, the customary continuation techniques will first be introduced. Then the mathematical definition of singular points will be provided along with a control method to deal with limit points, namely the arc-length method, presented as an extension of the Newton-Raphson continuation scheme. Eventually, the bifurcation theory is introduced theoretically, followed by an example of structural bifurcation.

2.4.1. Continuation techniques

In finite element analysis, equilibrium and compatibility are enforced by the fundamental equation:

$$K_s u - \lambda q = 0 \qquad \textit{(Eq. 2-94)}$$

where

K_s is the secant stiffness matrix (dimension n x n)

u is the displacement vector (dimension n)

λ is the load factor (scalar)

and q is the nominal load vector (dimension n)

In the case of material non-linearity, K_t, the tangential stiffness matrix is a function of u

and the loading history. The incremental equilibrium is iteratively enforced by minimising the out-of-balance forces, $g(x)$, given by:

$$g(x) = K_t \Delta u - \Delta\lambda q \qquad \textit{(Eq. 2-95)}$$

where

Δu is the incremental displacement

$\Delta\lambda$ is the incremental load factor

and $x = \begin{pmatrix} u \\ \lambda \end{pmatrix}$ is the augmented variable vector

Minimising $g(x)$ can be achieved using several iterative procedures:

- The linear stiffness method
- The quasi-Newton method
- And the Newton-Raphson Method

Linear stiffness method:

The linear method uses a constant stiffness matrix throughout the iterative process. This method potentially has the slowest convergence, but it costs the least time per iteration since the stiffness matrix needs to be set up only once. The linear stiffness method is usually very robust.

Using the foregoing notation, the iterative scheme can be formulated as follows:

$$u_{i+1} = u_i + \delta u_i \qquad \textit{(Eq. 2-96)}$$

with

$$\delta u_i = -K_0^{-1}.g(x_i) \qquad \textit{(Eq. 2-97)}$$

A one-dimensional representation of the linear stiffness method is presented in Fig. 2-26.

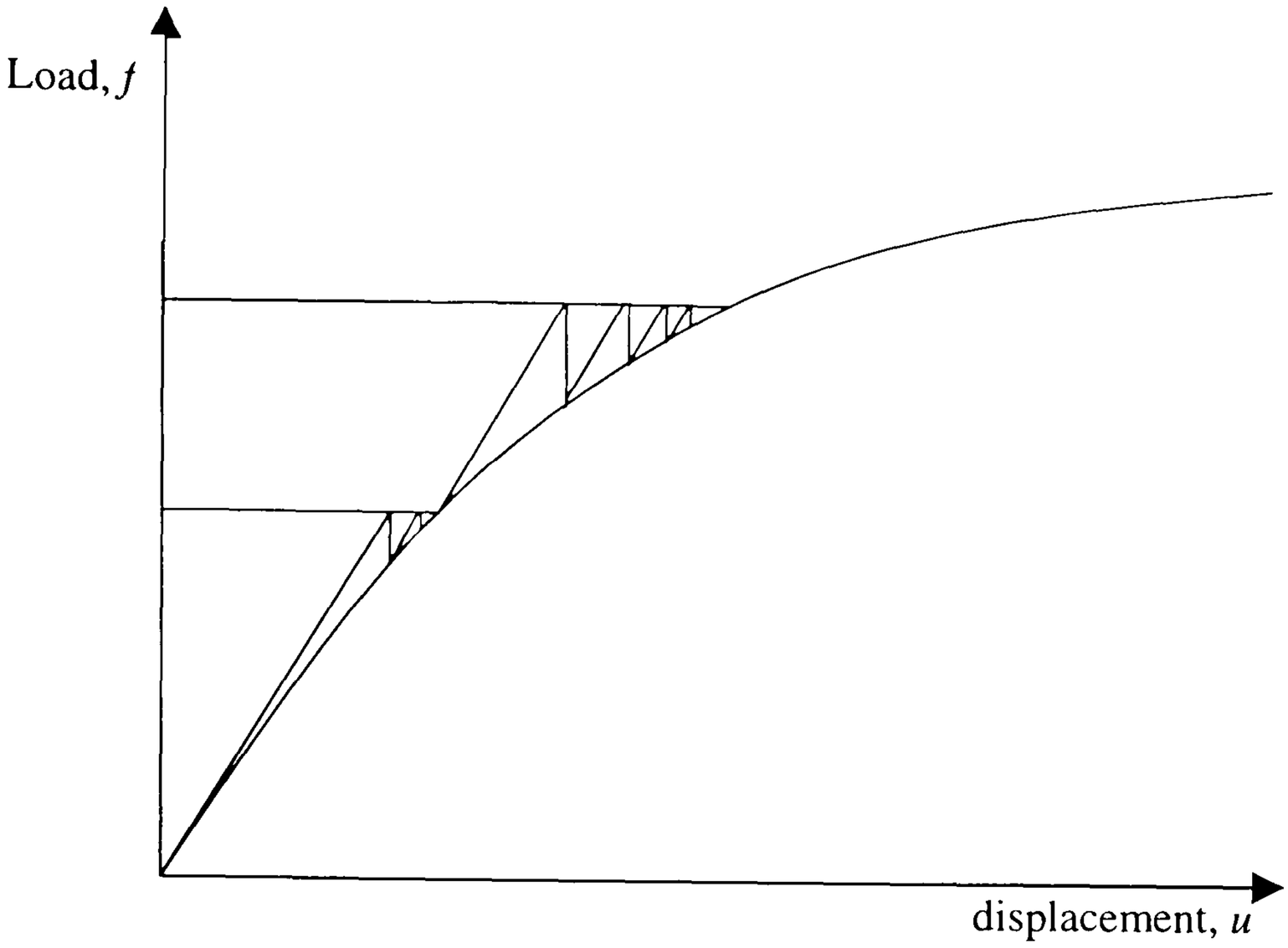

Fig. 2-26: Linear stiffness iterative method

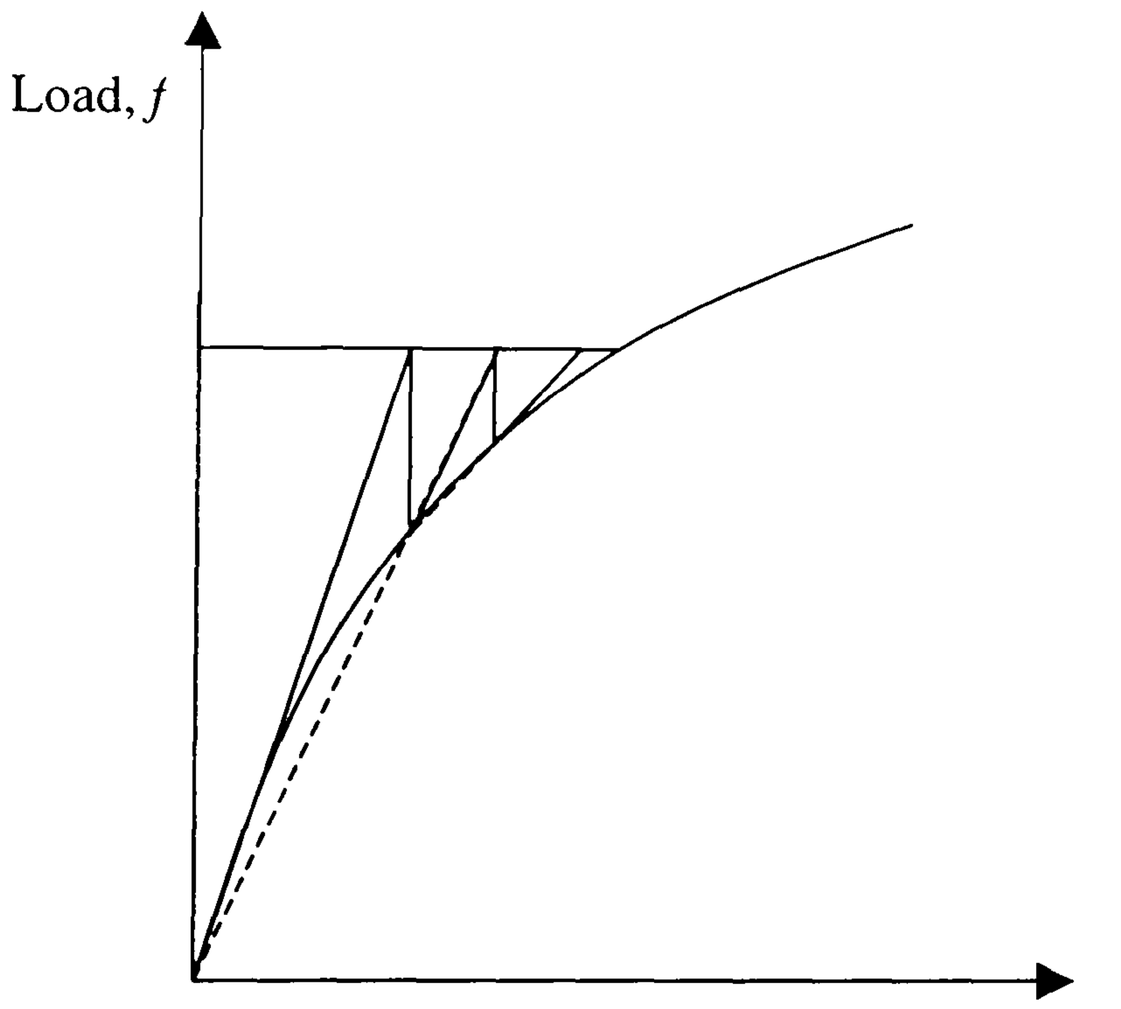

Fig. 2-27: Quasi-Newton iterative method

Quasi-Newton method:

The quasi-Newton method uses the information of previous solution vectors and out-of-balance force vectors during the increment to achieve a better approximation. The updated stiffness matrix is determined from the known positions on the equilibrium path.

Several quasi-Newton relations are available. The most common is the Broyden method, which writes:

$$\begin{cases} \text{For the first iteration :} \\ u_1 = u_0 + \Delta\lambda.\dot{u}_0 & \textit{(Eq. 2-98)} \\ \\ \text{followed by the iterative scheme :} \\ u_{i+1} = u_i + \delta u_i & \textit{(Eq. 2-99)} \\ \text{with} \\ \delta u_i = -K_i^{-1}.g(x_i) & \textit{(Eq. 2-100)} \\ \text{and} \\ K_i^{-1} = K_{i+1}^{-1} + \dfrac{\left(\delta u_{i-1} - K_{i+1}^{-1} g(x_i)\right)\cdot \delta u_{i-1}^T K_{i-1}^{-1}}{\delta u_{i-1}^T K_{i-1}^{-1} g(x_i)} & \textit{(Eq. 2-101)} \\ \\ \text{and preparing the next step after convergence :} \\ \dot{u}_n = K_t^{-1}.q & \textit{(Eq. 2-102)} \end{cases}$$

Alternative solutions are the Broyden-Fletcher-Godfarb-Shanno (BFGS) method and the Crisfield method. Both of them use a different definition for the iterative stiffness matrix K_{i+1}^{-1}.

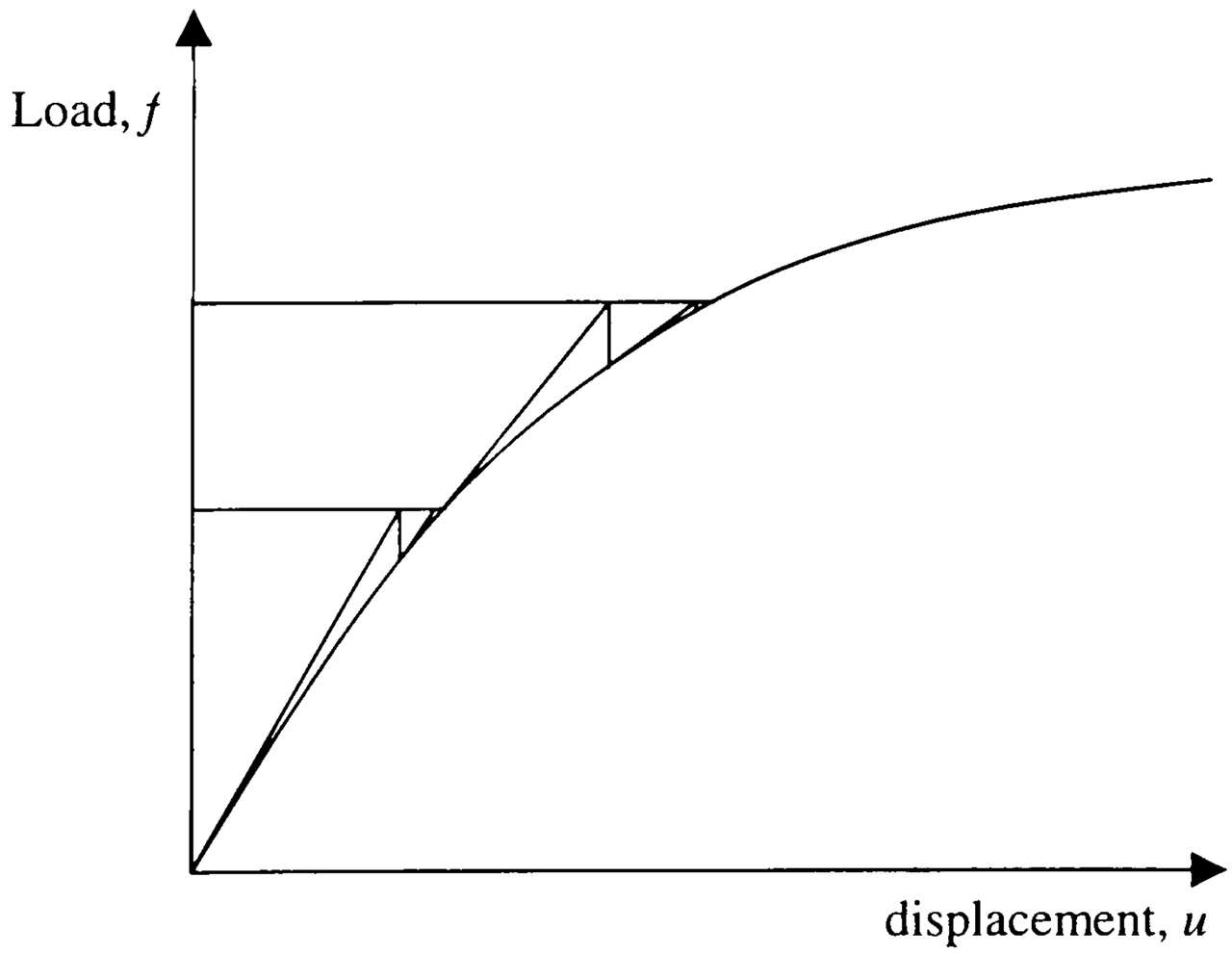

Fig. 2-28: Regular Newton-Raphson iterative method

Newton-Raphson Method

In the Newton-Raphson method, the stiffness matrix is updated at each iteration. This means that the prediction is based on the last known or predicted state, even if this is not an equilibrium state. The regular Newton-Raphson method, yields a quadratic convergence, i.e. the methods converges to the final solution within only a few iterations compared to the two other methods. A disadvantage of the method is that the stiffness matrix needs to be set up at every iteration and that the time consuming decomposition of the matrix needs to be repeated at every iteration as well. Moreover, if the initial prediction is far from an equilibrium state, the method easily fails because of divergence.

The formulation of the customary Newton-Raphson continuation technique is as follows:

For the first iteration :

$$u_1 = u_0 + \Delta\lambda . \dot{u}_0 \qquad \textit{(Eq. 2-103)}$$

followed by the iterative scheme:

$$u_{i+1} = u_i + \delta u_i \qquad \textit{(Eq. 2-104)}$$

with

$$\delta u_i = -K_{t(x_i)}^{-1} . g(x_i) \qquad \textit{(Eq. 2-105)}$$

and preparing the next step after convergence :

$$\dot{u}_n = K_t^{-1} . q \qquad \textit{(Eq. 2-106)}$$

It should be noted that this method is only valid when K_t is not singular.

2.4.2. Singular points

Singular points in non-linear finite element analysis

By definition, x^* is a singular point if K_t is singular. This means that, at x^*, K_t^{-1} does not exist

and K_t has an eigen-vector e_0 of zero eigen-value. It can then be deduced from the incremental equilibrium equation:

$$\Delta u^T K_t e_0 - \Delta\lambda \cdot q^T e_0 = 0 \qquad \textit{(Eq. 2-107)}$$

$$\therefore \quad \Delta\lambda \cdot q^T e_0 = 0 \qquad \text{at x*} \qquad \textit{(Eq. 2-108)}$$

Two different cases can be distinguished:

Case 1- (Eq. 2-108) is satisfied by:

$$\Delta\lambda = 0 \text{ and } \mathrm{q}^T e_0 \neq 0 \qquad \textit{(Eq. 2-109)}$$

$\Delta\lambda = 0$ around x^* means that x^* is a local maximum on the load-deflection curve. This corresponds to the physical definition of a limit point. From the condition $\dot{\lambda} = 0$ and the differential equilibrium equation $K_t.\dot{u} - \dot{\lambda}.q = 0$, it can be deduced that e_0 and $\dot{u}$ have the same direction, i.e. the eigen-mode corresponds to the differential displacement field at x^*.

Case 2- (Eq. 2-108) is satisfied by:

$$\Delta\lambda \neq 0 \text{ and } \mathrm{q}^T e_0 = 0 \qquad \textit{(Eq. 2-110)}$$

From $q^T.e_0 = 0$ it can be deduced that $q \in$ range(K_t). Therefore the rank of the augmented matrix $[K_t \quad -q]$ is equal to $(n - 1)$, i.e. whatever column is eliminated from this matrix, the determinant will still be zero.

This can be translated physically into: whatever the control provided (load or displacement control), the solution to the incremental equilibrium equation remains non-unique at x^*. This fundamental loss of uniqueness can be interpreted as the existence of several alternative paths emanating from x^*. This corresponds to the physical definition of a bifurcation point.

It can be noticed from $q^T.e_0 = 0$ that the eigen-mode, e_0, produces no work under q.

Continuation over limit points

Since the bifurcation algorithm to be presented in section 2.4.3 is a development of the arc-length method, the main concepts will be introduced here by showing how the use of the arc-length method allows the continuation over limit points.

K_t being singular at the limit point x^*, a bordered stiffness matrix, $G(x)$, is built, where:

$$G(x)=\begin{bmatrix} K_t & -q \\ \dot{u}^T & \dot{\lambda} \end{bmatrix} \qquad \textit{(Eq. 2-111)}$$

It will now be shown that G is not singular.

From (Eq. 2-109) it is deduced that $q \notin$ range(K_t), i.e. the rank of the augmented matrix $[K_t \quad -q]$ is equal to n.

The differential equilibrium equation can be rewritten as:

$$[K_t \quad -q].\dot{x}=0 \qquad \textit{(Eq. 2-112)}$$

with $\dot{x}=\begin{pmatrix} \dot{u} \\ \dot{\lambda} \end{pmatrix}$ the normalised branch direction vector

From (Eq. 2-112) it can be deduced that rank(G) = n+1. Therefore G is not singular and G^{-1} exists at x^*. An iterative method, similar to the Newton-Raphson technique, can then be implemented using G instead of K. This method is called arc-length continuation. The name is due to the extra equation introduced which constrains the arc-length of the incremental step to a prescribed value.

A variant is the pseudo arc-length continuation method based on the equilibrium equation and a

simplified incremental pseudo arc-length constraint:

$$\begin{cases} g(x) = 0 & \textit{(Eq. 2-113)} \\ \Delta x . \dot{x} = \Delta s & \textit{(Eq. 2-114)} \end{cases}$$

with Δs a prescribed arc-length

Newton-Raphson iterative scheme is then rewritten:

$$\begin{cases} \text{For the first iteration} \\ x_1 = x_0 + \Delta s . \dot{x}_0 & \textit{(Eq. 2-115)} \\ \textit{then} \\ x_{i+1} = x_i + \delta x_i & \textit{(Eq. 2-116)} \\ \textit{with} \\ \delta x_i = -G^{-1}_{(x_i)} \begin{pmatrix} g(x_i) \\ \Delta x_i^T . \dot{x}_i - \Delta s \end{pmatrix} & \textit{(Eq. 2-117)} \\ \Delta x_{i+1} = x_{i+1} - x_0 & \textit{(Eq. 2-118)} \\ \dot{x}_{i+1} = G^{-1} \begin{pmatrix} 0 \\ \vdots \\ 0 \\ 1 \end{pmatrix} & \textit{(Eq. 2-119)} \end{cases}$$

In the case of materials that fracture, the source of non-linearity, i.e. the set of cracks, is highly localised. The arc-length method is made more efficient if only the degrees of freedom displaying non-linearity are selected in the arc-length norm.

2.4.3. Bifurcation analysis

A bifurcation is a point where several equilibrium paths meet. The branch traced before reaching the bifurcation point is termed the fundamental path. This path usually extends continuously beyond the bifurcation point.

The branch that intersects the fundamental path is called the bifurcated path. In the general case, it is possible to trace the bifurcated branch in both directions from the bifurcation point. But it is possible for a fracturing material model, that only one side of the bifurcated branch exists due to the irreversible nature of fracture.

If the continuation method does not fail at the bifurcation point, the simulation usually continues on the fundamental path since the Newton-Raphson prediction assumes that the slope of the equilibrium path is continuous. Unfortunately, the fundamental path is not guaranteed to be the relevant one. In the common case where the bifurcation represents an alternative between a symmetric and a symmetry-breaking solution, the fundamental path (i.e. the symmetric solution) is always spurious.

As shown in section 2.4.2 from (Eq. 2-110), bifurcation is associated with a fundamental loss of uniqueness for the equilibrium equation. This singularity is opposed to the deterministic basis of mechanics and is due to the fact that the structure is modelled as being perfect. In the physical world, structures are never perfect, nor are the boundary and loading conditions. Bifurcation theory shows that, when imperfections are introduced in the model, the bifurcation point disappears, transforming the two intersecting branches into two distinct branches. This is called bifurcation unfolding, Fig. 2-29.

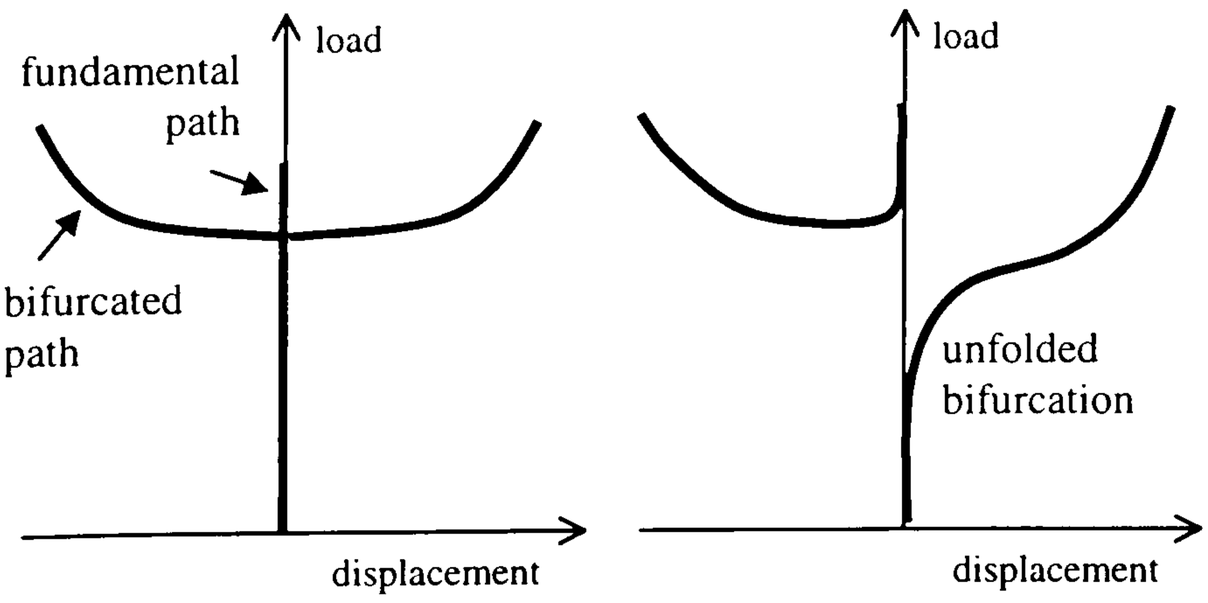

a- Perfect structure *b- Imperfect structure*

Fig. 2-29: Bifurcation unfolding.

Consequently, a full bifurcation analysis can be avoided by introducing imperfections into the model. However, when the two sides of the bifurcated branch are not identical (i.e. non-symmetric bifurcation), or when multiple bifurcated branches emerge from a single bifurcation point, the result of bifurcation unfolding may vary depending on the imperfection introduced. That is the reason why a complete bifurcation analysis carried out on the perfect model is desirable.

Bifurcation Point Detection

The first step in bifurcation analysis is to detect the presence of a bifurcation point. No bifurcation point should be passed unnoticed.

To that end, specific test functions can be designed. These functions have the properties that they change sign at the bifurcation point and they are continuous enough around it. Ideally, the determinant of the matrix G could be used as a test function. However, to save computing time, more readily accessible values are usually chosen, depending on the numerical method used to decompose G (see Seydel 1988[76]).

Once a bifurcation point has been detected between two converged states, its precise position can be determined by using a bisection or secant iteration scheme. These methods require many equilibrium points to be found around the bifurcation point. Alternatively, a less costly method using non-converged states has been designed by Crisfield (1994)[77].

If a less precise determination of the bifurcation point is sought, the monitoring of the number of negative pivots obtained from the decomposition of the stiffness matrix is often used. When this method is adopted, it is important to implement, at the same time, an algorithm distinguishing between limit points and bifurcation points, since both of them produce negative pivots. However, this is impracticable when a limit point and a bifurcation point lay very close to each other, which is common for fracturing material models.

Branch Switching Algorithms

The inertia of the continuation technique means that the simulation, if not too unstable to converge, automatically goes past the bifurcation and stays on the fundamental branch. In order to trace the other branches emerging from the bifurcation point, a branch switching algorithm needs to be implemented. The aim is to inject, at the bifurcation point, a perturbation in the displacement field so that the continuation method changes the equilibrium path.

To that end, the initial direction vector of the bifurcated branch, φ^*, needs to be determined. The exact determination of φ^* is theoretically possible using differentials of the tangent stiffness matrix, which are higher order terms than the ones traditionally required for static finite element analysis. However, the exact determination of φ^* is generally not necessary. A perturbation vector close to φ^* is sufficient to reroute the continuation.

φ^*, similarly to $\dot{x}$, satisfies the differential equilibrium equation: $[K_t \quad -q]\varphi^* = 0$

Therefore φ^* and $\dot{x}$ belong to the null space of $\begin{bmatrix} K_t^T \\ -q^T \end{bmatrix}$.

It has been shown that the rank of the augmented matrix $[K_t \quad -q]$ is equal to $(n-1)$, i.e. there are two vectors φ_1 and φ_2 so that the null space of $\begin{bmatrix} K_t^T \\ -q^T \end{bmatrix}$ is defined by span(φ_1,φ_2). Therefore φ^* can be written as a linear combination of φ_1 and φ_2: $\varphi^* = \alpha.\varphi_1 + \beta.\varphi_2$.

If $\dot{x}$ is chosen for φ_1, and φ_2 is chosen orthogonal to $\dot{x}$, then φ_2 belongs to the null space of $\begin{bmatrix} K_t^T & \dot{u} \\ -q^T & \dot{\lambda} \end{bmatrix}$, and φ_2 is easily obtained as the eigen-vector of the zero eigen-value of the square matrix G evaluated at the bifurcation point.

Instead of calculating the exact direction of φ^*, that is α and β, φ_2 only is injected in the first continuation step of the bifurcated branch. Thus the pseudo-arclength continuation method with the branch switching algorithm has the following formulation:

$$\begin{cases} \text{For the first iteration} \\ x_1 = x_0 + \Delta s.\varphi_2 & \textit{(Eq. 2-120)} \\ \text{then the iterative scheme based on :} \\ g(x) = 0 & \textit{(Eq. 2-121)} \\ \Delta x.\varphi_2 = \Delta s & \textit{(Eq. 2-122)} \end{cases}$$

Another method, proposed by de Borst (1987)[78], consists of considering the displacement vector, u, instead of the augmented variable vector, x.

From the differential equilibrium equation it can be shown that the differential displacement vector of the bifurcated path, $\dot{u}_2$, is a linear combination of $\dot{u}$ and e_0, with $\dot{u}$, the differential displacement vector of the fundamental path and e_0, the eigen-vector of zero eigen-value of K_t. The perturbation vector, $\dot{u}^*$, injected in the continuation scheme is built from $\dot{u}$ and e_0 so that it is orthogonal to $\dot{u}$.

The two methods are very similar. The formulation of the first one is however more general than the second one and should be preferred when used in conjunction with the pseudo-arclength method.

Criterion for Identifying the Relevant Path

Once all the potential equilibrium paths are determined, a criterion is required to identify the relevant path. The problem can be divided into two questions: (1) Which are the paths spuriously introduced by the inadequacy of the model to describe physical reality? (2) Amongst the physically acceptable paths, which is the one that should be regarded as the actual failure mode?

As a rule, if a branch cannot be reached using a model with imperfections, then this branch will not be followed by a real structure and it should be considered as a spurious behaviour introduced by the use of a perfect model. This is always the case for the fundamental path, past the bifurcation point. This means that only the bifurcated paths can be considered as physically acceptable.

As explained in the introduction to this section, the presence of imperfections can unfold the bifurcation on any of the bifurcated branches, depending on the geometry of the imperfections. It can be observed in the simulations that concentration of the imperfections on one side of the structure will induce one failure mechanism, while concentration of the imperfections on another side will induce a different failure mechanism. It could therefore be concluded that each of the bifurcated paths has, in practice, an equal chance of being followed. Consequently, for design purposes, the most adverse case should be chosen.

However, one can argue that the concentrated imperfection patterns are purposely introduced in the model to cause such and such effect, and that they are very unlikely to arise in practice, as actual material imperfection fields are randomly distributed. Moreover, it should not be overlooked that some bifurcated branches are much more sensitive to imperfections than others. For example, in the case of a non-symmetric bifurcation with the alternative between a softening and a hardening path, the bifurcation will be much more likely to unfold on the softening branch (i.e. catastrophic failure mode), than on the hardening branch (progressive failure).

To determine the most likely path, Bažant (1988 and 1991)[31,79] designed an energy-based criterion using the second law of thermodynamics, in the form stated in 1875 by Willard Gibbs: every system approaches equilibrium in such a manner that the internally produced entropy, ΔS_{in}, is maximised, among all reachable states. In the case of the simulation of concrete structures, the internal entropy is produced by cracking. In a finite element approach, ΔS_{in} can

be assessed from the second-order work (see Bazant 1988)[79]):

$$T.\Delta S_{in}^{i} = -\tfrac{1}{2}\Delta u.K^{i}.\Delta u \qquad \text{for displacement control,}$$

where T is the temperature in °K

K^i is the tangential stiffness matrix of the structure in the direction of path (i)

Δu is a prescribed displacement step

and $T.\Delta S_{in}^{i} = \tfrac{1}{2}\Delta q.C^{i}.\Delta q$ for load control,

with C^i the tangential compliance matrix of the structure in the direction of path (i)

Δq a prescribed load step

This criterion is particularly useful in material bifurcation, as it tends to choose the most localised solution. For structural bifurcation, the criterion will choose the mode of failure for which cracking is the most extensive in regard to the same step of the control parameter. Bažant showed that for a structure with a single load or a single control parameter, applying the criterion is equivalent to choosing the bifurcated path with either the smallest rising slope, the steepest softening slope or the most dramatic snap-back, in the load-displacement diagram. It is noted that these generally constitute the most adverse cases for design.

2.4.4. Symmetric bifurcation in a notched direct tension test

It will now be shown, using a plain concrete specimen, how structural bifurcation arises naturally in the non-linear simulation of softening material, even for very simple structures.

Description of the Test and Experimental Results

It has been noticed by others (Hordijk 1987[80], Rots and de Borst 1989[81]) that the direct-tension test, carried out on notched bars of plain concrete, displays a structural behaviour. In the following this behaviour is identified as a structural bifurcation.

The test was initially designed to investigate the softening behaviour of cracking concrete. This behaviour is known as strain-softening and is assumed to be a material characteristic. The test consists of subjecting a notched prism of plain concrete to a direct tensile load. It was expected that the structural response of such a simple specimen would directly provide the material constitutive law. However, it has been observed experimentally that the deformations are often not uniform over the cross-section, suggesting that a structural behaviour is occurring.

A detailed experimental investigation of the phenomenon revealed that, if the specimen is long enough, or if the extremities of the specimen are not constrained in rotation, a rotation with its axis orthogonal to the axis of the specimen will automatically arise, shortly after the onset of cracking. Thus, if the cracked cross-section is allowed to rotate, a symmetry-breaking displacement field replaces the initial symmetric type of cracking.

It is easy to see that continuing symmetric cracking constitutes an acceptable equilibrium solution. Therefore, the symmetry-breaking solution constitutes an alternative equilibrium path that must originate from a bifurcation point. Moreover, the bifurcated behaviour being similar whatever the sign of the rotation, we are in presence of a symmetric bifurcation.

Finite Element Model and Bifurcation Unfolding

In the first approach to simulate bifurcation, an accurate finite element model along with a simple bifurcation analysis method, i.e. bifurcation unfolding, has been used.

The specimen chosen is a prism of 205x100x50 mm^3. Two symmetric notches of 20 mm deep are inserted at mid-length. The upper extremity is left freely rotating and subjected to an evenly distributed tensile load. The lower extremity is built-in.

The 2D model developed is meshed with 812 quadrilateral 4-noded plane stress elements (Fig. 2-30-a). The material model is linear elastic, except for the twelve elements between the notches

for which smeared cracking is used. The material constants chosen are characteristic of concrete (Youngs modulus E=25 GPa, tensile strength f_t=4 MPa and fracture energy G=80 J/m^2). The exponential strain-softening curve from Hordijk (1992)[16] has been adopted for post-cracking material behaviour.

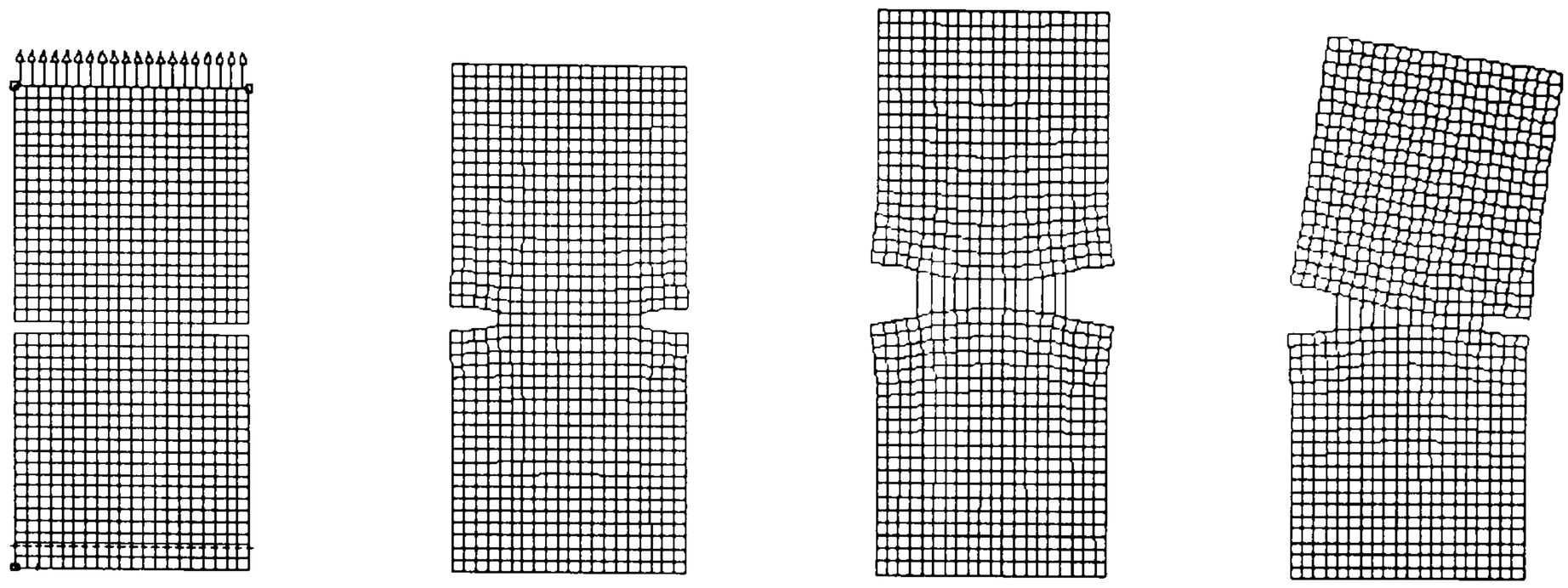

a) Mesh and loading *b) Elastic deformations* *c) Symmetric cracking fundamental path* *d) Asymmetric cracking bifurcated path*

Fig. 2-30: Finite element analysis of the notched direct tension test

The continuation analysis was carried out using the regular Newton-Raphson technique with the pseudo-arclength method. The range of the norm used for the arc-length was reduced to four crack mouth opening displacements measured at four points evenly distributed along the cracked cross-section. In total, 30 steps were carried out.

First, the simulation was performed on the perfect structure (perfectly symmetric specimen and boundary conditions). As expected the simulation continued all the way on the fundamental path, displaying symmetric deformations only. The deformed shapes of the elastic deformations and of the symmetrically cracked deformations are given respectively in Fig. 2-30-b and Fig. 2-30-c. Monitoring the appearance of negative pivots in the decomposition of the stiffness matrix indicated the presence of a bifurcation point at the 8th step, at a load level of 11 kN (a negative pivot appeared along a rising branch). When the analysis reached the limit point (17th steps, 11.6 kN), a second negative pivot appeared alongside the first one. The second negative pivot corresponds to the negative slope of the softening behaviour, Fig. 2-31.

In order to trace the bifurcated path signalled by the first negative pivot observed in the previous analysis, an imperfection was introduced in the structure in the form of a slightly weaker cracking strength in one element, on one side only of the specimen. The original cracking strength was reduced by 1 percent. This resulted in unfolding the bifurcation. As expected, no negative pivot was observed along the rising branch. The negative pivot corresponding to the limit point arose at the lower load level of 11.1 kN. This analysis produced a symmetry-breaking solution, Fig. 2-30-d and Fig. 2-31 to Fig. 2-33. The rotation obtained, Fig. 2-32, is identical to the behaviour observed experimentally[16,81].

In this simple case, the determination of the physical path is immediate. The fundamental path is not physical as the slightest imperfection directs the simulation on either of the two bifurcated branches. Then, the bifurcation being symmetric, the structure is equally likely to rotate in any of the two directions. It can be noticed that Bažant's criterion applies here. If the single control parameter version of the criterion is considered, then it is possible to check that the physical branch is the one with the steepest softening slope in the load-extremity displacement diagram, that is the bifurcated branch.

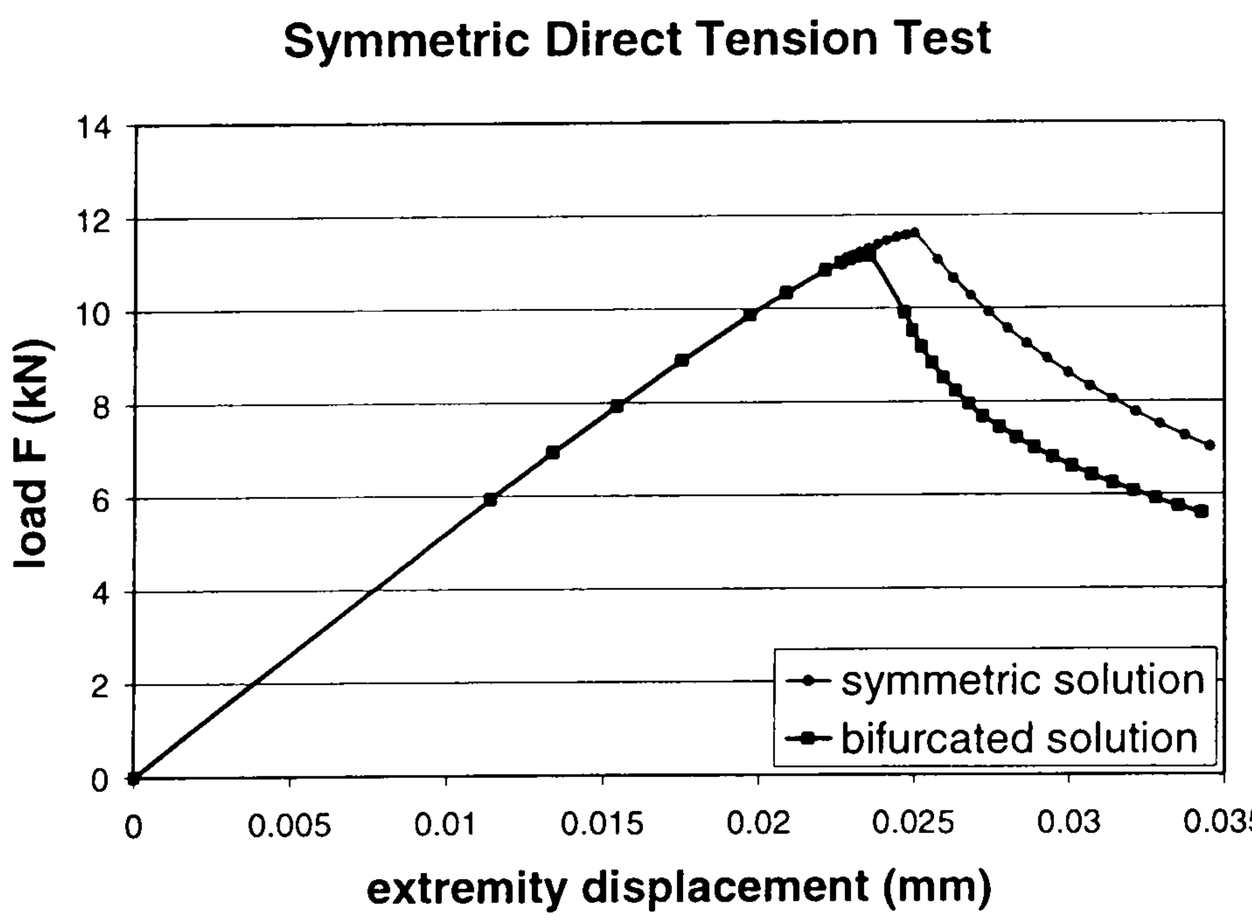

Fig. 2-31: Load-displacement diagram obtained from finite element analysis

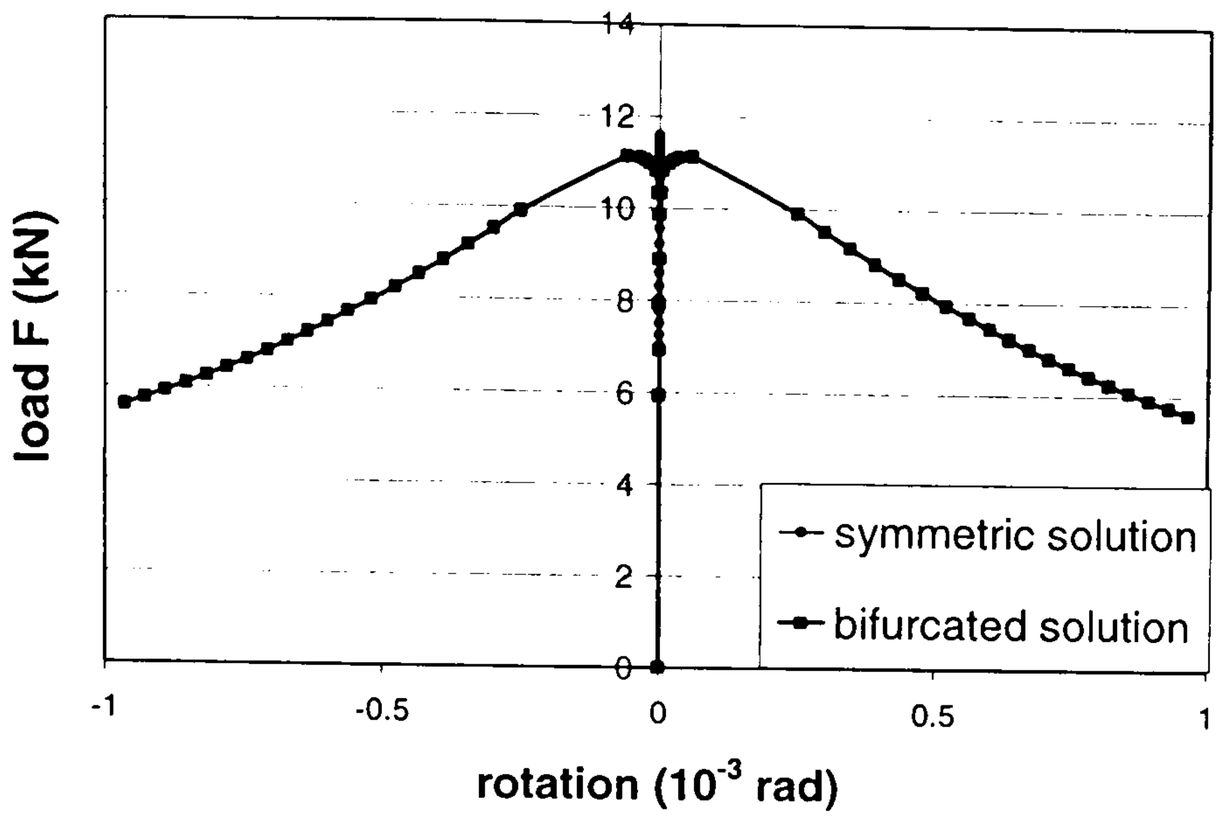

Fig. 2-32: Load-rotation diagram obtained from finite element analysis

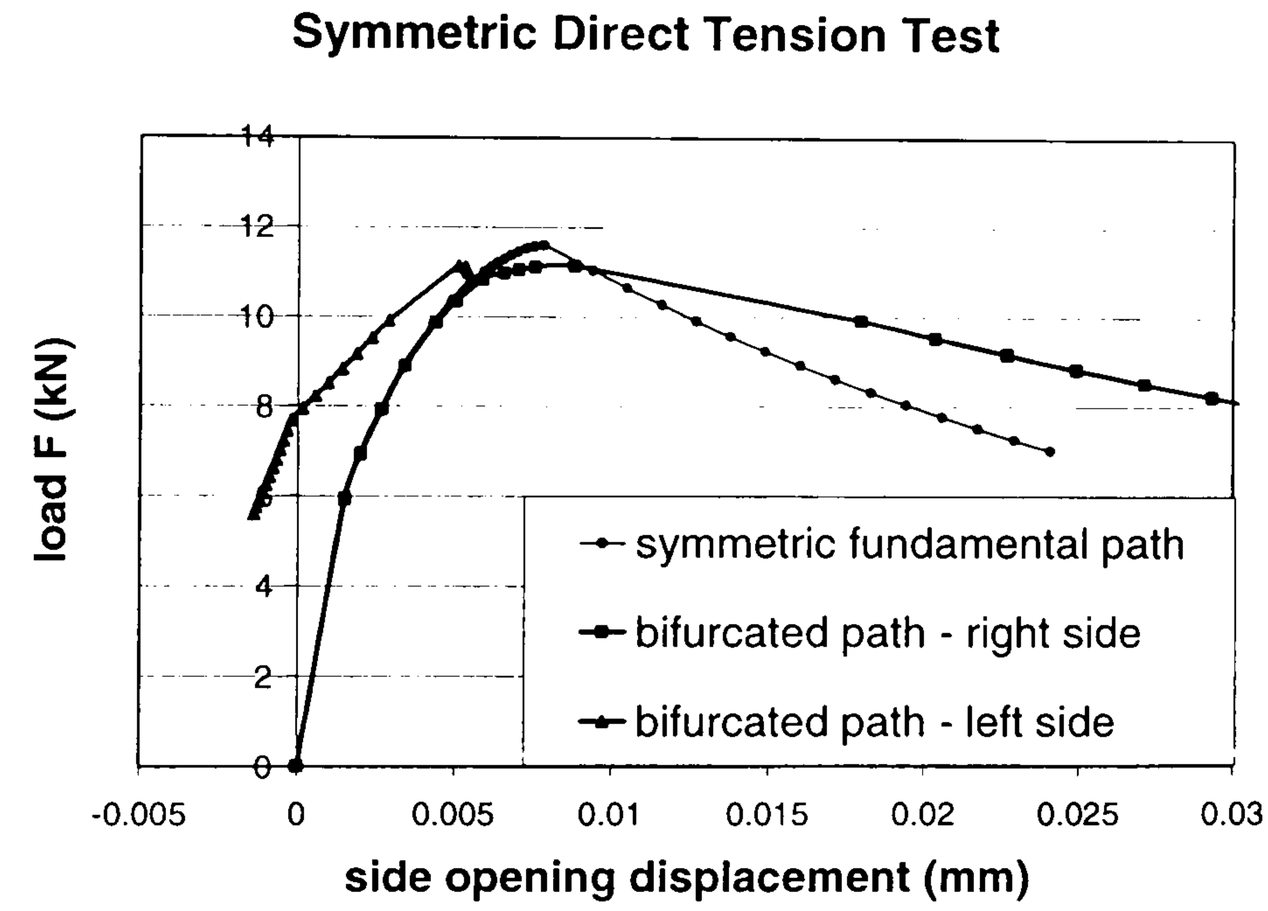

Fig. 2-33: Load-crack opening diagram obtained from finite element analysis

Simplified Kinematic model and Branch Switching

It is common sense to assume that a complex behaviour like the bifurcation described above can only be simulated using a complex model. However, it will be shown in the following that, when non-linearity is introduced, complex behaviours can spring up even from very simple mathematical models.

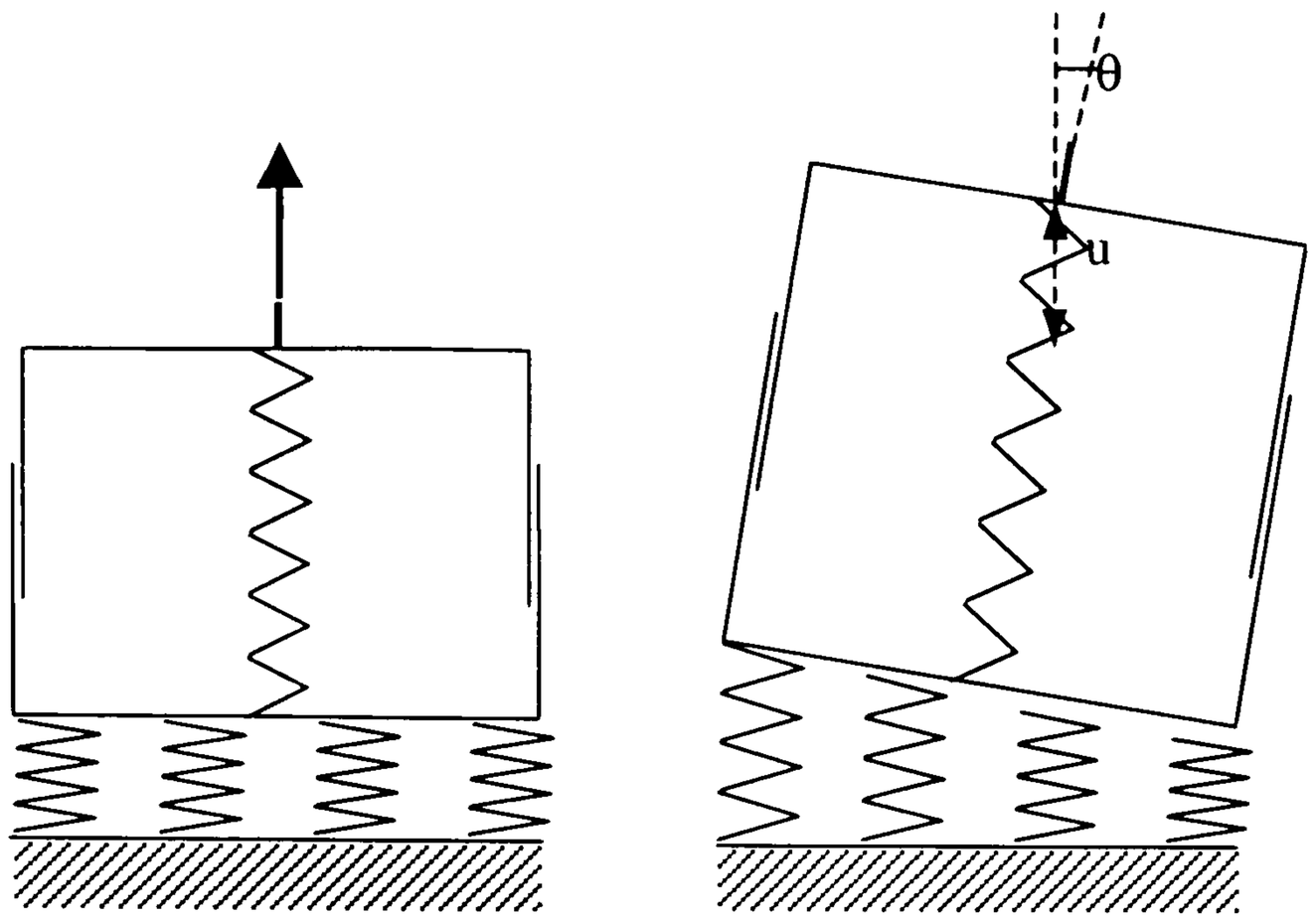

Fig. 2-34: Schematic drawing of the 2 DOF kinematic model

A simplified kinematic model of the same specimen, with only 2 degrees of freedom (DOF) has been designed, Fig. 2-34. The first DOF is the longitudinal displacement, u. The second DOF is the bifurcation variable, i.e. the rotation, θ. The two corresponding equilibrium equations written are: equilibrium of the vertical forces and equilibrium of the in-plane moments.

Only half the length of the specimen was modelled. The bulk of the concrete prism is assumed to deform longitudinally only and is modelled by a single linear spring with a stiffness deduced using E=25 GPa. The cracking interface is modelled by four non-linear springs. The load-displacement curve chosen for these springs has been built from the same exponential strain-softening curve than the one used for the finite element model (with f_t=4 MPa and G=80 J/m^2). However, since progressive cracking was not allowed with this lumped approach, the cut-off peak of the curve was smoothed using a parabolic curve. The cracking strength of the side springs was reduced by 25 percent to account for stress concentration due to the notches.

The simulation was carried out using the pseudo-arclength and the bifurcation analysis techniques described in section 2.4.3, including bifurcation point detection and branch switching. The whole non-linear analysis was driven automatically by the software

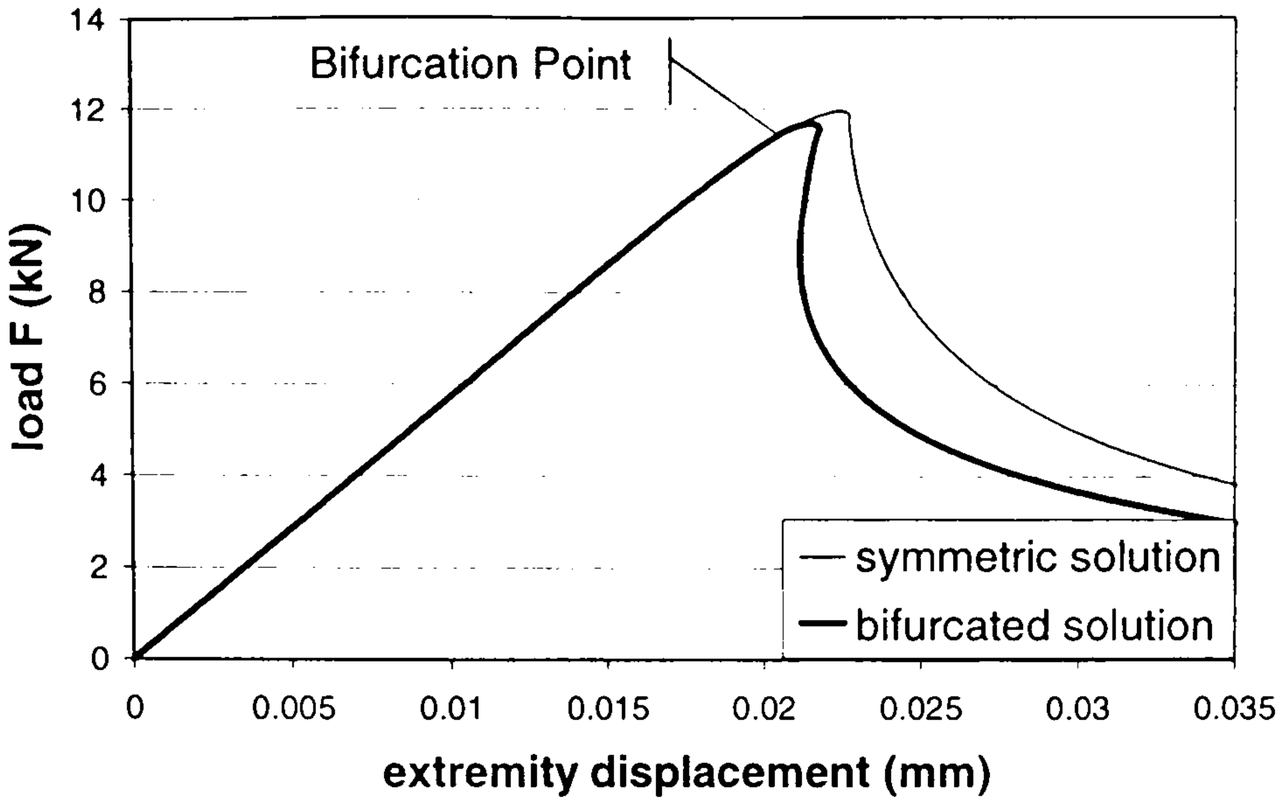

Fig. 2-35: Load-displacement obtained from 2 DOF model

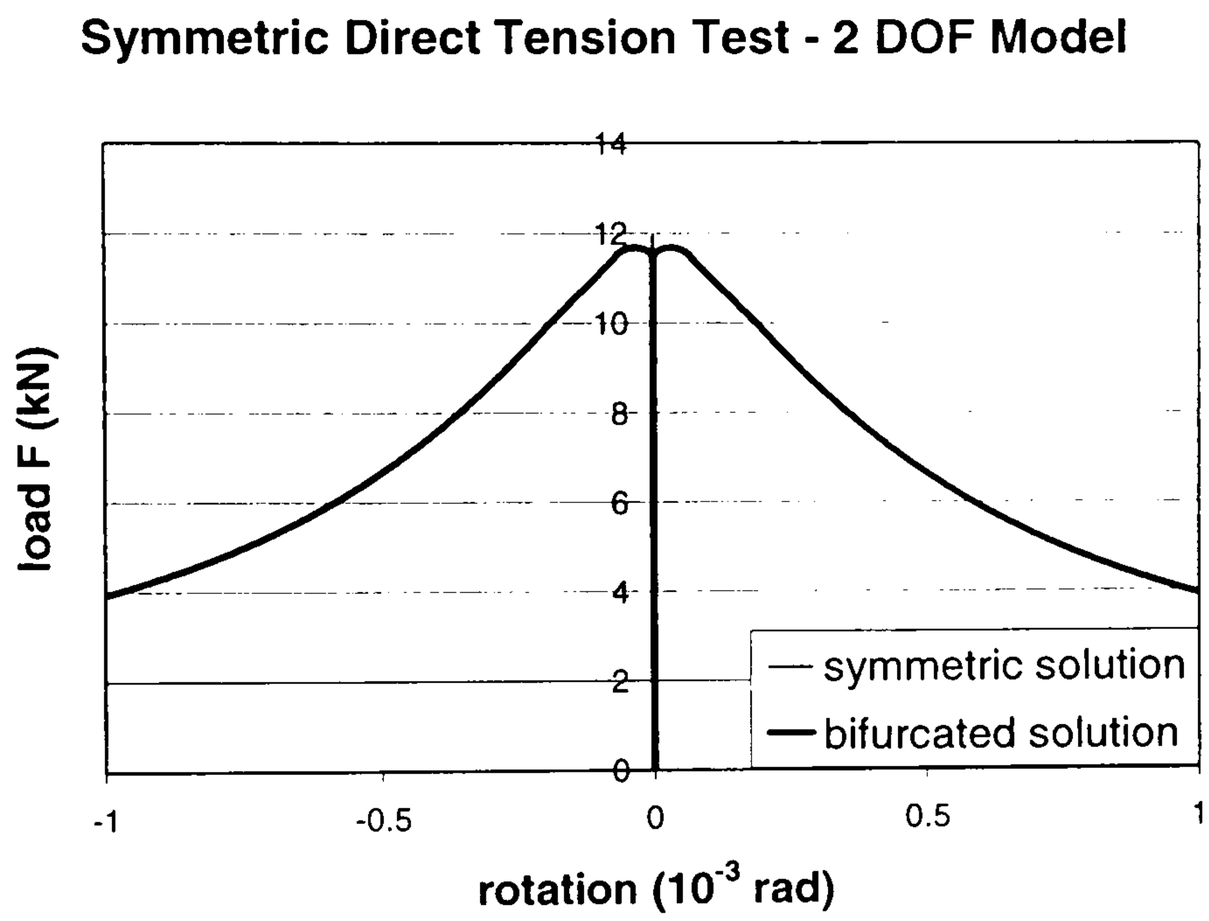

Fig. 2-36: Load-rotation diagram obtained from 2 DOF model

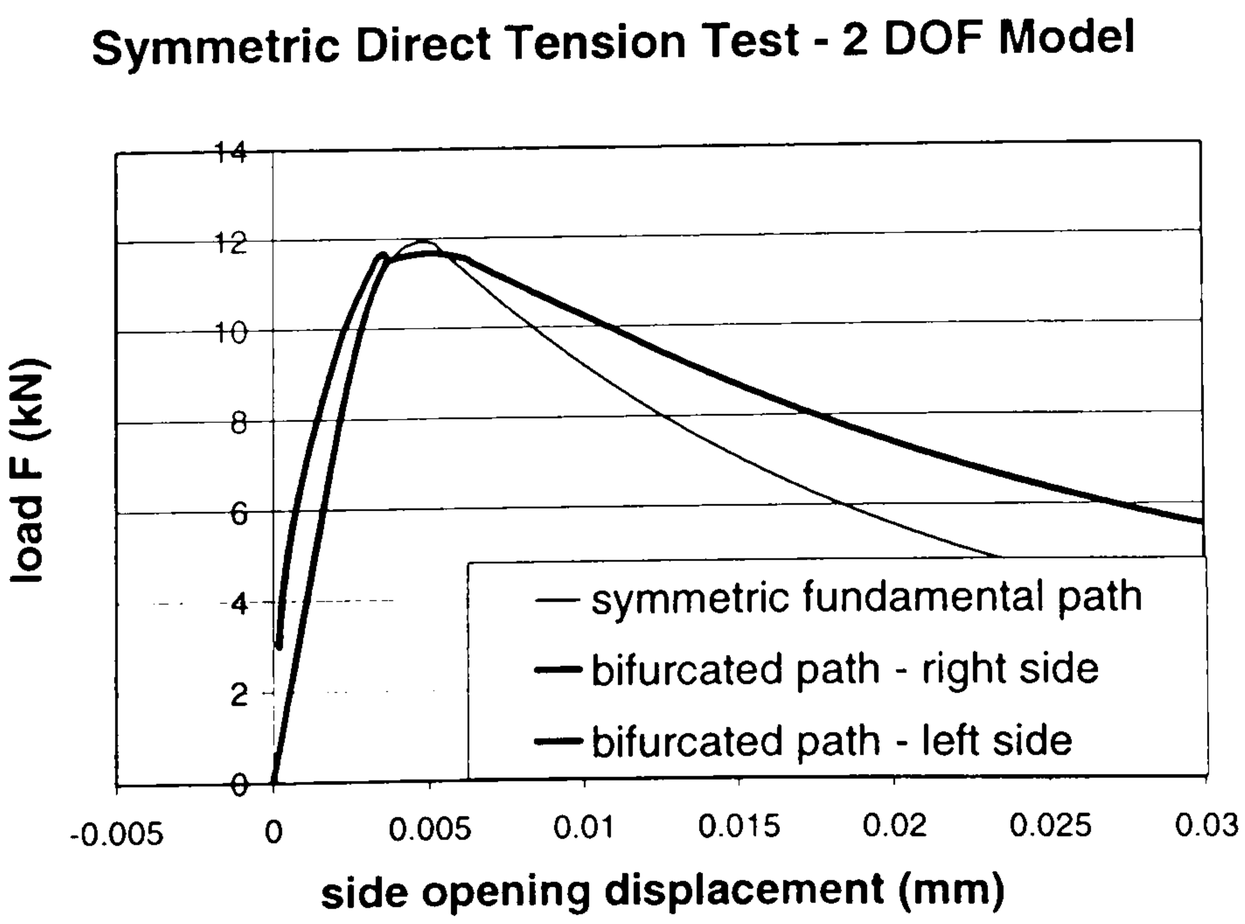

Fig. 2-37: Load-crack opening diagram obtained from 2 DOF model

AUTO[72]. A total of 300 steps were carried out on the fundamental path, and an extra 300 on the bifurcated branch.

The bifurcation point is automatically detected at a load level of 11.4 kN. The fundamental path is traced, with a limit point at 11.9 kN. Then the simulation is restarted automatically from the bifurcation point and, using the branch switching algorithm, the two bifurcated branches are traced, both with a limit point at 11.7 kN, Fig. 2-35.

The results of this simplified model compare well with the results from the finite element model, Fig. 2-35 to Fig. 2-37. The use of few-degree-of-freedom models allows the bifurcation analysis to be carried out in a reasonable amount of time. It shows that it can be advantageous, when tackling structural bifurcation problems, to make use of a simplified model in conjunction with powerful bifurcation analysis algorithms, since the core of the problem is not the exact determination of the structural strength, but rather the identification of the critical failure mode.

3. FRACTURE MECHANICS OF BOND IN REINFORCED CONCRETE

Predicting the response of reinforced concrete structures requires: (1) stable and robust computational methods which are able to trace the non-linear behaviour up to failure and beyond, (2) reliable constitutive models for steel and concrete, and (3) a physically sound model for the steel-to-concrete bond mechanism.

Much has been achieved in recent years in the field of numerical techniques for non-linear analysis to satisfy the first and the second requirement, as has been discussed in Chapter 2. However steel-to-concrete bond models have not undergone such a rationalisation. Although bond has been investigated since the birth of reinforced concrete, empirical models are still in general use today.

This chapter aims at gaining a better understanding of the bond mechanism in reinforced concrete using a three-step approach:

- identify the cracking mechanisms involved in bond by carrying out a phenomenological investigation,
- review the existing bond models,
- and understand the evolution of the load-carrying mechanisms, using a realistic finite element model and a simplified fracture mechanics model.

3.1. Phenomenological Approach

Considère[82], in 1899, observed the tensile response of steel wires encased in mortar. This was to be the first of a type of experiment, which has become standard for the study of bond properties

and is now known as the tension test. The most significant contributions to understanding bond using tension test are Lutz and Gergely[83] (1967), Bresler and Bertero[84] (1968), Goto[85] (1971), Nilson[86] (1972), Soretz and Hölzenbein[87] (1979), Mirza and Houde[88] (1979), and more recently Mitchell and Abrishami[89] (1996). Tepfers[90] (1979) and Noghabai[19] (1998) designed a modified version of the test using a shorter specimen in order to study more precisely the splitting effect.

The tests show that even after transverse cracks have appeared, the stiffness of the tension specimen is still higher than the steel bar alone. This is because, between adjacent cracks, tensile forces are transmitted from the steel to the surrounding concrete by bond stresses. One of the early models of this behaviour assumes that the contribution of the concrete could be considered as an increase of the steel bar stiffness. This has led to a number of empirical models for "tension stiffening" (see for example CEB-FIP Model Code 90[5] § 3.2.). The actual cracking mechanism is not considered in this type of model.

A better insight into the phenomenon of bond was gained when Goto[85] (1971) described the cracks appearing within a tension specimen, Fig. 3-1. Four crack patterns were identified:

- conical cracks radiating from the ribs of the steel bar, responsible for softening of the interface region and subsequent bond-slip,
- secondary crack developing from certain conical cracks, reaching out for the concrete surface and producing local transverse cracks,
- transverse (or primary) cracks normal to the bar axis, visible on the sides of the specimen,
- and splitting (or longitudinal) cracks in the plane of the bar axis, initiating at the face of the transverse cracks or at the specimen ends, and resulting locally in a total loss of bond.

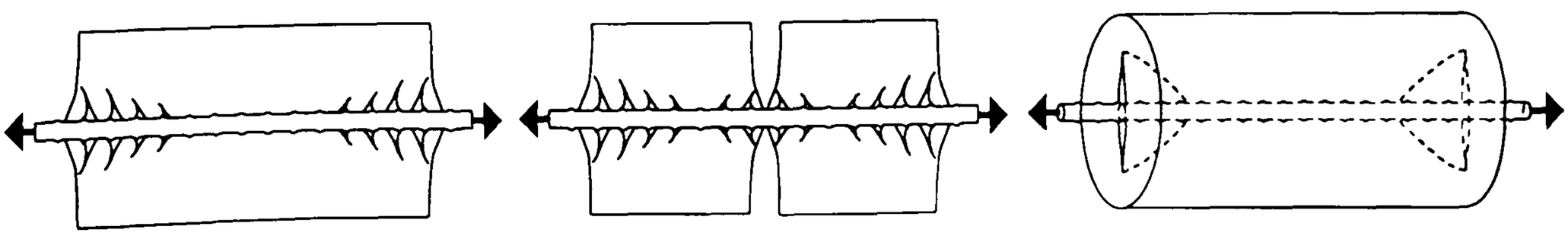

a) Conical cracks *b) Transverse or secondary crack and conical cracks* *c) Splitting cracks*

Fig. 3-1: Cracking mechanisms in tension tests

Up to date, the prediction of the average spacing of the transverse cracks has been empirical (see CEB-FIP Model Code 90[5] § 3.2.2. and § 7.4.3.). The main controlling parameter has been shown to be the bar diameter. It is important to note that the actual spacing, normally between L_{max} and 2 L_{max}, where L_{max} is the length over which slip between steel and concrete occurs[5], is typically subject to a large amount of scatter.

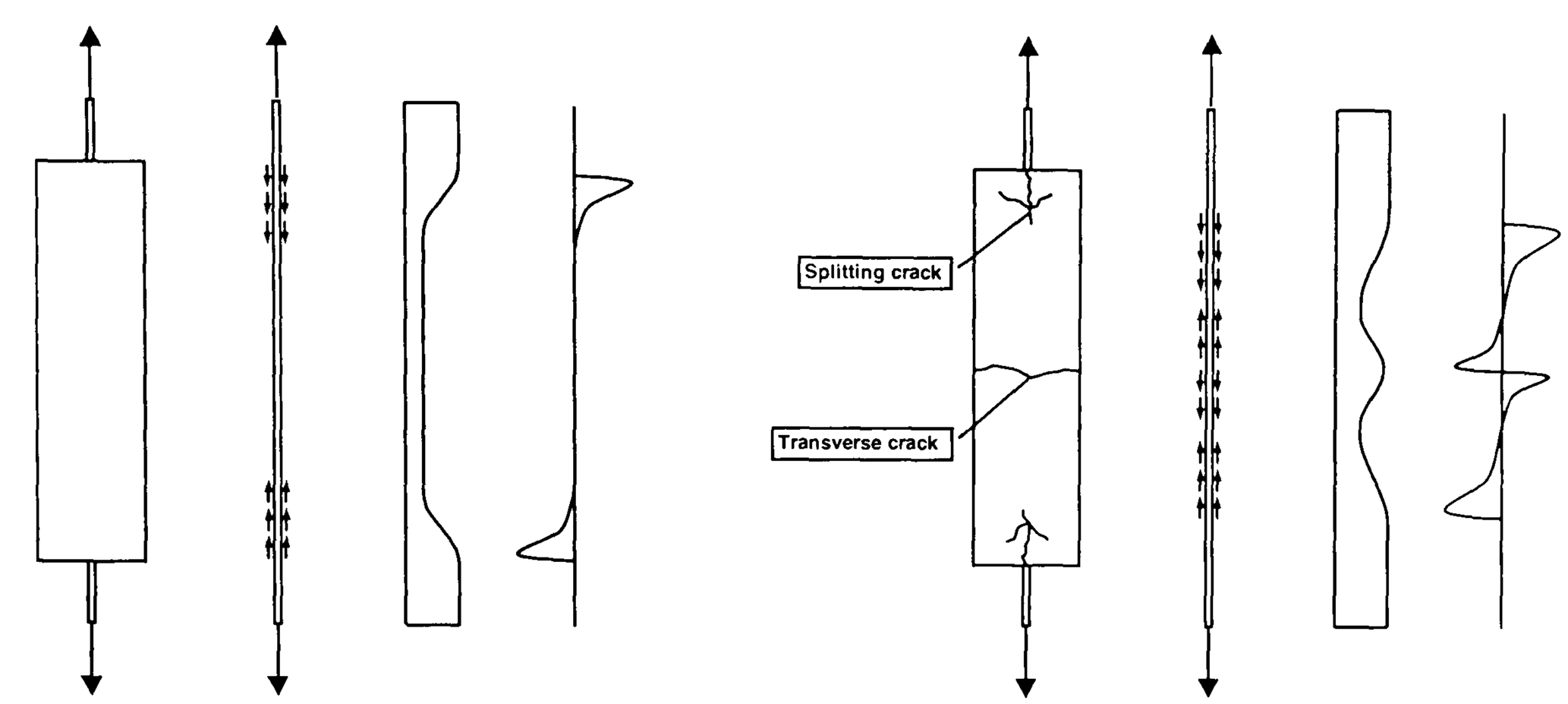

a) Uncracked Specimen *b) Specimen Cracked in Mixed Mode*

Fig. 3-2: Distribution of stresses along the steel bar for uncracked and cracked specimen (adapted from Mitchell and Abrishami)[9]

The fracture mechanics of the conical cracks is complex, and no reliable physical model has yet been developed. It has been shown by Soretz[87] (1979) and by Darwin[91] (1993) that the orientation, the distribution and the softening behaviour of conical crack depends on a number of parameters including the rib geometry (spacing, height, and rib pattern), the bar diameter, the proximity of other bars (longitudinal or transversal) and the concrete cover.

In order to understand the phenomena involved, the behaviour of the specimen under increasing load, Fig. 3-1 and Fig. 3-2, is considered. At the onset of loading, the specimen behaves elastically. Load is transmitted from the reinforcement to the concrete through a short transfer

length, which has locally high bond stresses. The load transferred to concrete is rapidly distributed to the whole concrete cross-section and the two materials act compositely. At a relatively low load level, the stress concentration induced by the presence of the ribs on the bar leads to the formation of conical cracks, first near the specimen end-face and then progressively along the bar. This results in an extension of the transfer length, local softening of the steel-to-concrete interface which accounts for the bond-slip, and formation of a comb-like structure, transmitting bond by a tapered spoke-hoop system (Goto[85] 1971). According to Tepfers,[90] local tensile hoop stresses are responsible for the onset of splitting. After the formation of the conical cracks, three main scenarios are possible.

In the first scenario, the longitudinal stress at some location in the concrete exceeds the tensile strength and transverse cracking occurs, localising at one or more cross-sections. At each of the faces of these cracks, a new set of conical cracks, identical to those at the extremities, appears. The maximum spacing of the transverse cracks is typically less than twice the transfer length. Therefore, full transfer is not achieved, and a smaller proportion of the load is transmitted to the concrete, which leads to a softening of the load-displacement relationship. This has the effect of reducing the concrete longitudinal stress to below the tensile strength. It is only after further loading that new transverse cracks, with a closer spacing, may appear.

In the second scenario, the crack initiated in front of the first rib becomes unstable before the tensile strength is reached elsewhere in the concrete cross-section, and develops into a splitting crack. At this load level, the structure becomes unstable. The splitting front advances quickly, destroying the steel-to-concrete bond. Secondary transverse cracks are usually observed along the path of the splitting crack. These can be considered as the ultimate state of conical cracks, which have eventually surfaced. This is consistent with Goto's observations.

In the third scenario, both transverse cracking and splitting occur, either simultaneously or one after the other. Thus any model should adopt initiation conditions for both transverse cracking

and splitting that do not prevent one starting if the other is already in progress. However, it should be noted that the two mechanisms are coupled, since in practice the splitting crack may be arrested by a transverse crack, which is on its path, or transverse cracking may be slowed down by structural softening due to splitting.

From this physical description of the phenomenon, it is possible to identify the components required for a physically sound model. Along the length of the specimen, cross-sections exhibiting different types of behaviour have been distinguished. These are: (1) cross-sections where splitting is present, that is where the steel takes all the load, (2) cross-sections within the transfer length, where bond-slip has occurred and where part only of the concrete section is loaded, (3) cross-sections beyond the transfer length, where plane cross-sections are assumed to remain plane, and (4) cross-sections within the crack-band-width of a transverse crack, where the concrete is softening. The basic requirement of a bond model is that the steel bar and the concrete cross-section act in parallel with a connection through their interface.

3.2. Review of Existing Models

Three approaches have been used by researchers to attempt to model steel-to-concrete bond. The first approach is empirical. Characteristic behaviour is described by parameterised empirical laws. In this type of approach, the actual cracking mechanisms involved are ignored. No understanding of the physical phenomena can be gained from empirical models. On the contrary, in the analytical approaches, information from phenomenological investigations is used to build a physically meaningful model. Bond-slip behaviour and ultimate strength are derived analytically. Eventually, in the last approach, general simulation of the physical phenomenon can be achieved using finite element methods. Finite element analyses provide a useful physical insight into the phenomenon investigated, thus complementing experimental observation and enhancing our understanding.

3.2.1. Empirical laws

Tension stiffening models

The first attempts to devise a bond-slip model looked at the structural load-displacement behaviour. It was observed, from tension tests, that the stiffness of reinforced concrete moves from that of the full composite action towards the stiffness of the steel bar alone which occurs after extensive cracking of concrete. Four regimes were identified. The quasi-linear, the crack formation stage, the stabilised cracking regime and the steel yielding phase. Each regime is generally modelled by a linear curve. The empirical law is thus completely defined by the parametrised coordinates of the vertices of the multi-linear load-displacement diagram, Fig. 3-3.

Such load-versus-elongation responses are called tension-stiffening models. A typical example is the tension-stiffening curve provided by the CEB Model Code 1990[5]. In the following, a steel bar is assumed to influence an equivalent area of concrete A_c, e.g. the total concrete area of an axially loaded reinforced concrete specimen or approximately half of the area under the neutral axis in the beam bending case. With this assumption the equations of the CEB-FIP Model Code are rearranged and written in a simpler form.

$$\begin{cases} \text{In the uncracked linear regime:} \\ \sigma_s^e = \left(\dfrac{A_c E_c + A_s E_s}{A_s} \right) \varepsilon_s^e \qquad \textit{(Eq. 3-1)} \\ \\ \text{In the crack formation phase} \\ \text{For short term loading:} \\ \sigma_s^e = \left(\dfrac{A_c E_c + A_s E_s}{3A_s E_c + A_s E_s} \right) \left(E_s \varepsilon_s^e + 3 \dfrac{A_c}{A_s} f_t \right) \qquad \textit{(Eq. 3-2)} \\ \\ \text{For long - term or repeated loading:} \\ \sigma_s^e = \left(\dfrac{A_c E_c + A_s E_s}{3.5A_s E_c + A_s E_s} \right) \left(E_s \varepsilon_s^e + 3.5 \dfrac{A_c}{A_s} f_t \right) \qquad \textit{(Eq. 3-3)} \end{cases}$$

In the stabilised cracking regime

for short term loading :

$$\sigma_s^e = E_s \varepsilon_s^e + 0.4 \frac{A_c}{A_s} f_t \qquad \textit{(Eq. 3-4)}$$

for long - term or repeated loading :

$$\sigma_s^e = E_s \varepsilon_s^e + 0.25 \frac{A_c}{A_s} f_t \qquad \textit{(Eq. 3-5)}$$

In the post yielding regime

for short term loading :

$$\varepsilon_s^e = \varepsilon_s^y - 0.4 \frac{A_c}{A_s} f_t + 0.8 \left(\frac{f_y - f_t}{E_s} - \frac{f_t}{E_c} \right) \qquad \textit{(Eq. 3-6)}$$

for long - term or repeated loading :

$$\varepsilon_s^e = \varepsilon_s^y - 0.25 \frac{A_c}{A_s} f_t + 0.8 \left(\frac{f_y - f_t}{E_s} - \frac{f_t}{E_c} \right) \qquad \textit{(Eq. 3-7)}$$

where ε_s^e and σ_s^e are the equivalent strain and stress in the steel bar alone, A_s is the steel area, E_c and E_s are the concrete and steel moduli of elasticity, and f_y is the steel yield strength.

It should be noted that in the first linear stage, the effect of conical cracking is ignored and, more importantly, in the crack formation stage, no difference is made between regular transverse cracking and brittle splitting crack propagation. In conclusion, tension-stiffening models are good approximations of the behaviour of steel encased in concrete, which can be included in larger models of reinforced concrete structures.

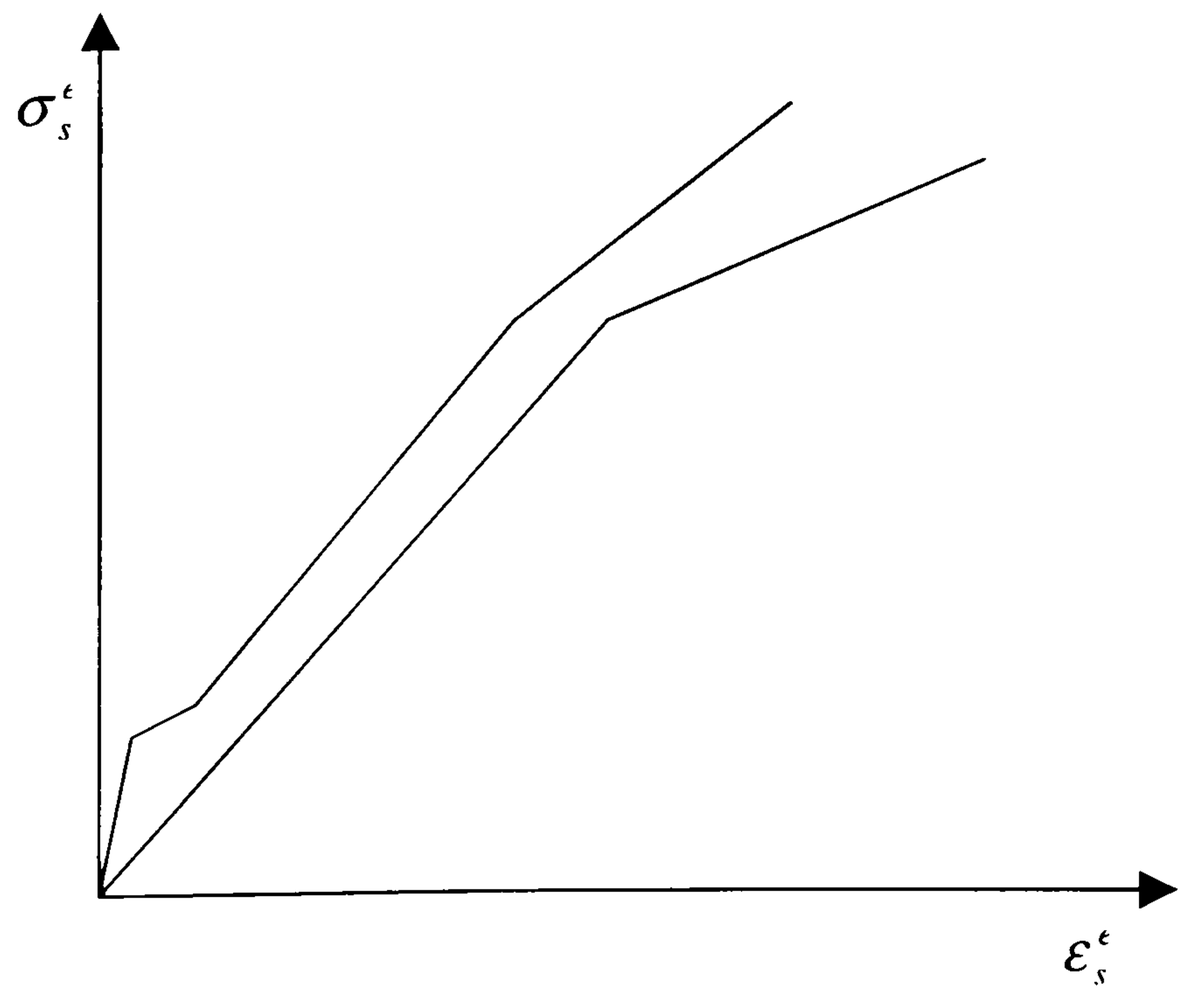

Fig. 3-3: CEB-FIP tension-stiffening model[5]

Transverse crack spacing

An important factor in the assessment of the remaining stiffness in the stabilised cracking range is the average transverse crack spacing. It has already been mentioned that this type of distributed cracking is mainly controlled by the characteristics of the steel bar. However, different empirical laws have been designed to predict the average transverse crack spacing using a number of parameters, ranging from the bar diameter to the concrete cover. The material parameters have been shown to have a lesser influence than the geometric parameters[92].

In the CEB-FIP Model Code 1990[5] the transverse crack spacing is predicted to be typically between L_{max} and 2 L_{max}, where L_{max} is the length over which bond-slip occurs, i.e. the transfer length. The transfer length is assumed to depend on two parameters only, namely the bar diameter and the reinforcement ratio, $\rho_s = A_s/A_c$:

$$L_{\max} = \frac{d_b}{3.6\rho_s} \qquad \textit{(Eq. 3-8)}$$

Bond-slip laws

A more physical approach is to consider the steel and concrete separately. The structural non-linear behaviour is then considered a consequence of non-linear bond-slip interface behaviour. It has been believed for a long time that the bond-slip behaviour could be considered as a constitutive law of reinforced concrete in addition to steel and concrete material laws.

It was shown however that the bond-slip law depends not only on the material parameters but also, to some extent, on the topology of the problem. Therefore, general bond-slip laws including no parameter besides the slip or only material parameters must be considered as mere approximations of the actual bond-slip behaviour. This is the reason why much discrepancy is observed between the bond-slip laws formulated by different researchers, Fig. 3-4. The bond slip laws presented below are derived from tension transfer tests.

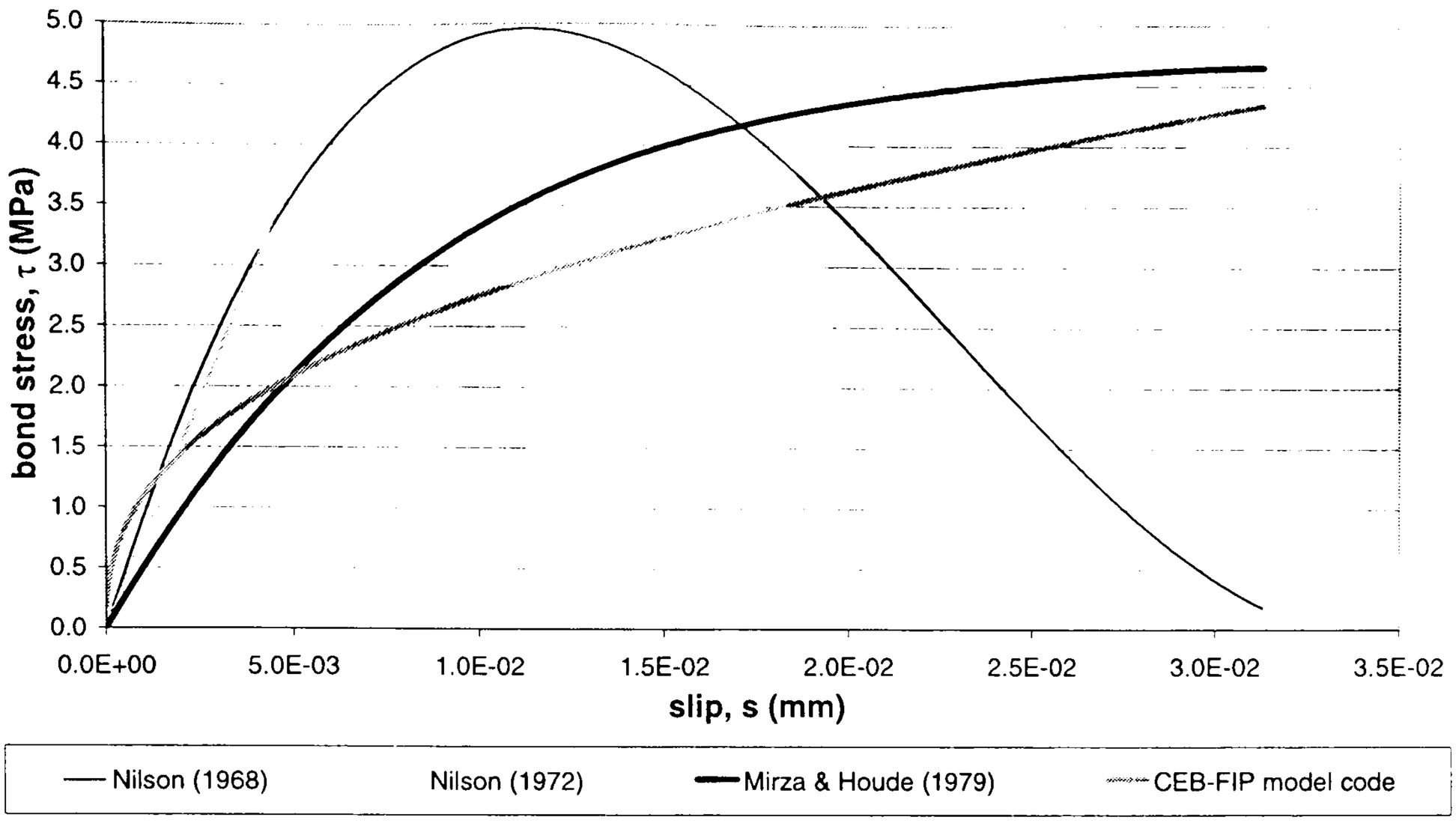

Fig. 3-4: Empirical bond-slip laws

Nilson (1968)[93] used the experimental data of Bresler and Bertero (1966)[84] to formulate a general bond-slip law. In spite of the significant scatter of experimental data, the following law was proposed:

$$\tau = .9788 \cdot 10^6 s - 57.24 \cdot 10^6 s^2 + 0.8356 \cdot 10^9 s^3 \qquad \textit{(Eq. 3-9)}$$

τ in MPa and s in mm

Later on, in 1972, Nilson [86] carried out a set of experiments, measuring the slip indirectly using strain gages imbedded in the concrete. From there, a law was formulated for the initial slope of the bond slip curve depending on the concrete tensile strength, f_t, and the longitudinal distance from concrete surface, c_l :

$$\tau = 122.1 \cdot (0.0563 \cdot c_l + 1.5) \cdot s \cdot f_t \qquad \textit{(Eq. 3-10)}$$

for $s < 8 \cdot 10^{-3}$ mm

Mirza and Houde (1979)[88] conducted an experimental investigation including 62 tension specimens. Fitting a fourth order polynomial to the experimental data produced a curve somewhat different from Nilson's curve:

$$\tau = 0.5293 \cdot 10^6 s - 25.11 \cdot 10^6 s^2 + 0.5848 \cdot 10^9 s^3 - 5.466 \cdot 10^9 s^4 \qquad \textit{(Eq. 3-11)}$$

τ in MPa and s in mm

The most recent bond-slip curve available is the empirical formula given in the CEB-FIP Model Code 90[5]. Although the initial part of the curve seems over-stiff, the later part of the curve agrees well with Mirza and Houde's curve. The CEB-FIP Code defines an ultimate bond stress, τ_{max}, after which a descending branch is proposed. This corresponds to an assumed softening behaviour of the bond failure mechanism. It is believed that this descending branch describes a phenomenon of different nature than the bond-slip phenomenon. Consequently, it is not presented here.

The ascending branch of the CEB-FIP formula has the following form:

$$\tau = \tau_{max}\left(\frac{s}{0.6}\right)^{0.4} \qquad \textit{(Eq. 3-12)}$$

where s is the slip in mm and $\tau_{max} = 2\sqrt{f_c}$ is the ultimate bond stress (τ_{max} and f_c in MPa).

3.2.2. Analytical models

Empirical models are mainly concerned with modelling the effects of conical and transverse cracking, which can be described with a limited number of parameters. Splitting cracking however depends strongly on the topology of the specimen making the development of empirical laws difficult. Consequently, physical models have been sought to explain the mechanics of splitting.

Splitting with strength criterion

Tepfers (1979)[90] suggested a model based on the assumption that tensile hoop stresses occur in the concrete to equilibrate the diagonal compressive stresses generated, between the conical cracks, by the bond forces. Once conical cracking occurs, the bond stresses are no longer transferred through direct shear stresses, but are transferred through inclined compressive struts between adjacent conical cracks. These inclined compression forces can be decomposed into a longitudinal component responsible for the longitudinal stressing of the concrete, and a radial

component that must be equilibrated in the cross-sectional plane. Considering the problem as a plain stress analysis, the radial component is equivalent to an inner radial pressure in a thick cylinder. Elastic analysis reveals that tensile hoop stresses develop within the cylinder wall, with a maximum stress at the inner surface, Fig. 3-5.

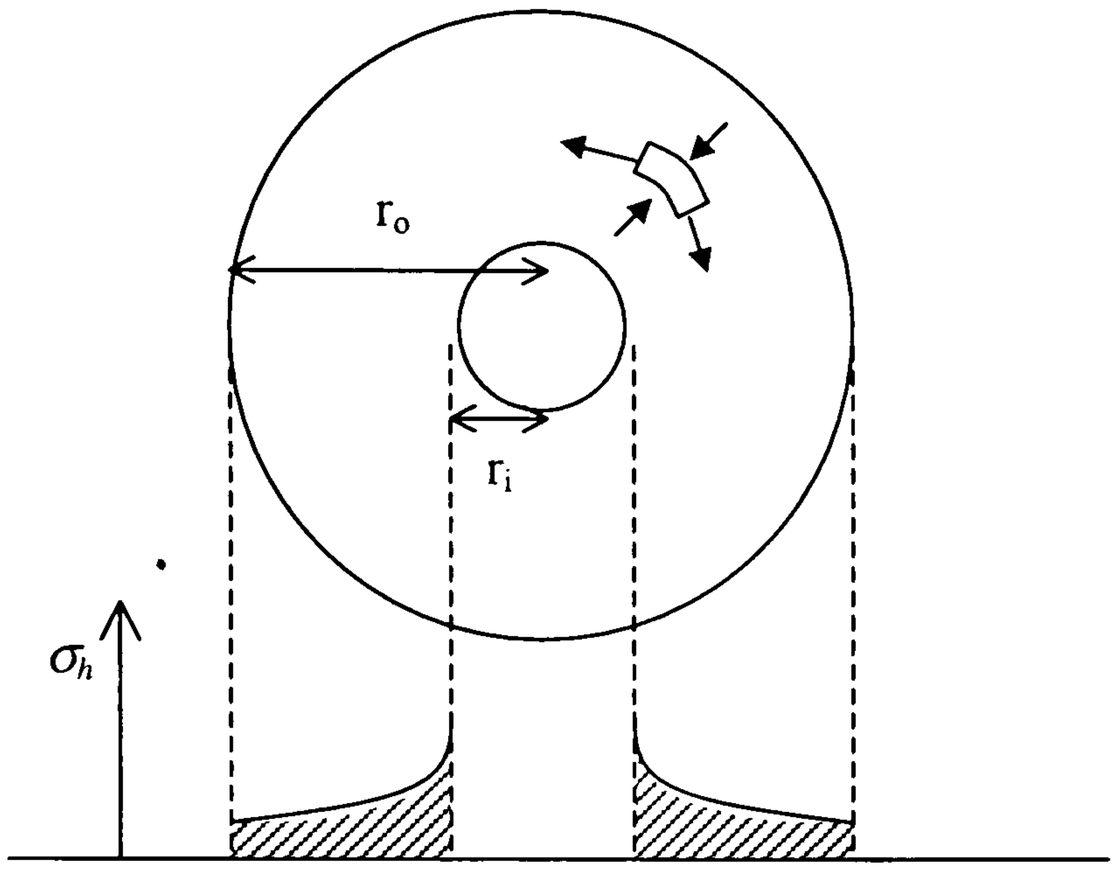

Fig. 3-5: Hoop stresses distribution in an elastic thick cylinder

The solution of the stress distribution in an elastic thick-walled cylinder[94] subjected to inner radial pressure, p_i, is given in the following:

$$\begin{cases} \text{Compressive radial stress:} \\ \sigma_r = \dfrac{p_i r_i^2}{r_0^2 - r_i^2}\left(1 - \dfrac{r_0^2}{r^2}\right) \end{cases} \qquad \textit{(Eq. 3-13)}$$

$$\begin{cases} \text{Tensile hoop stress:} \\ \sigma_h = \dfrac{p_i r_i^2}{r_0^2 - r_i^2}\left(1 + \dfrac{r_0^2}{r^2}\right) \end{cases} \qquad \textit{(Eq. 3-14)}$$

Assuming that the diagonal compressive struts replacing uniform direct shear stresses are inclined at an angle α_{cc}, the relation between radial pressure and bond stress is easily deduced:

$$p_i = \tan\alpha_{cc} \cdot \tau \qquad \textit{(Eq. 3-15)}$$

Equating the maximum hoop stress in the ring with the concrete tensile strength yields the maximum acceptable bond stress:

$$\tau_{max} = \frac{f_t}{\tan\alpha_{cc}} \frac{r_0^2 - r_i^2}{r_0^2 + r_i^2} \qquad \textit{(Eq. 3-16)}$$

In the case of a reinforcing bar embedded in a rectangular section, r_i is the diameter of the bar and r_0 is to be taken as the concrete cover from the centre of the bar. This model, however, only predicts the onset of conical cracking. The actual maximum bond stress is reached when conical cracking extent reaches a critical radius, e_c. Thus Tepfers developed a partly-cracked elastic model, where the concrete is assumed to be cracked radially (by distributed splitting) up to a radius e. The elastic thick-walled cylinder analysis is then applicable to a cylinder of inner radius e, since no hoop stresses are allowed within radius e, Fig. 3-6.

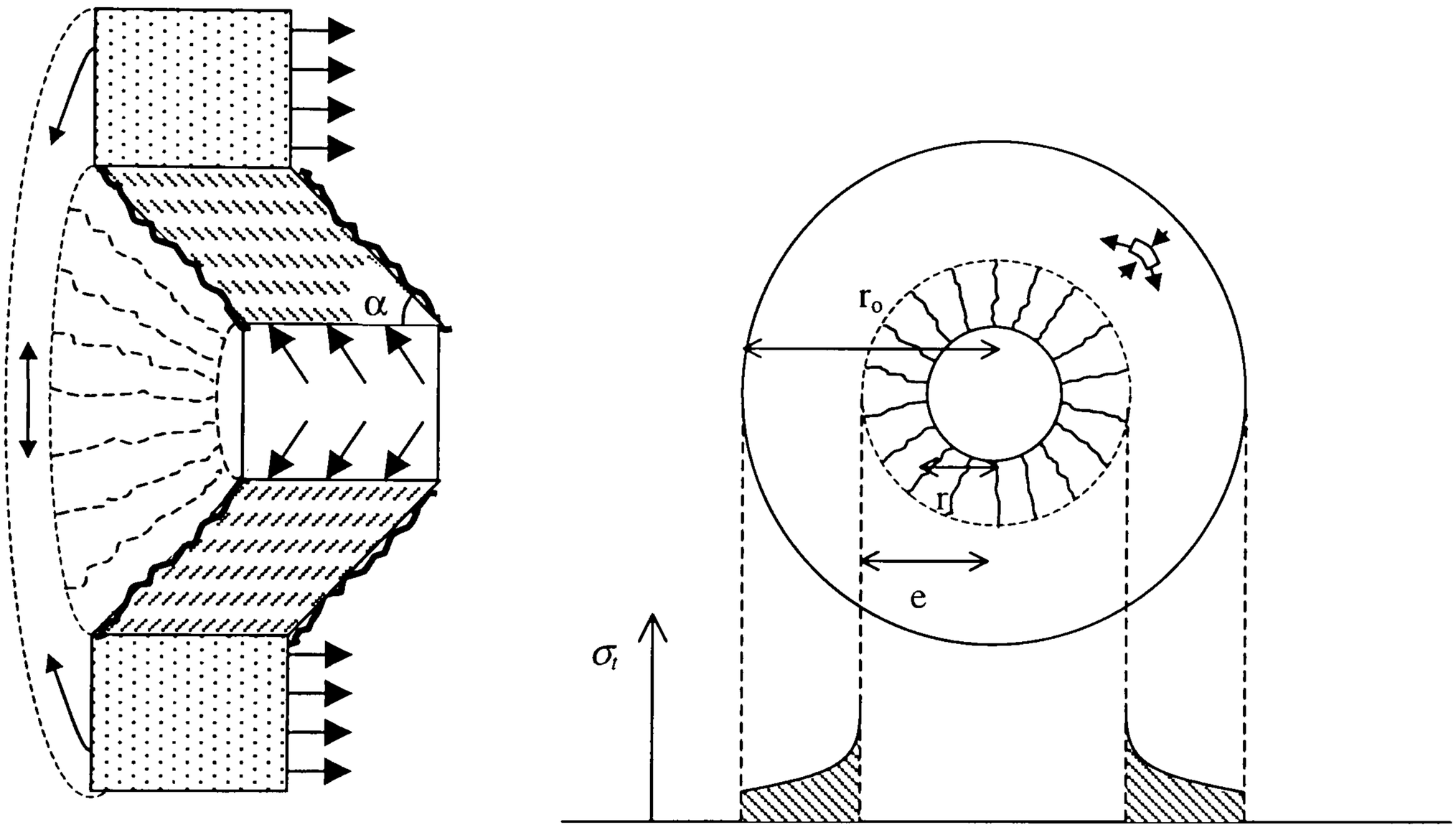

a) 3D view of a longitudinal cut *b) hoop stress distribution*

Fig. 3-6: Stress distribution in a partly-cracked elastic thick cylinder

The hoop stress distribution is then given by:

$$\sigma_h = \frac{(r_i/e)p_i e^2}{r_0^2 - e^2}\left(1+\frac{r_0^2}{r^2}\right) = \frac{p_i r_i e}{r_0^2 - e^2}\left(1+\frac{r_0^2}{r^2}\right) \qquad \textit{(Eq. 3-17)}$$

The maximum sustainable bond stress is obtained by differentiation for the critical crack extent $e_c = 0.486\ r_0$:

$$\tau_{max}^{sp} = 0.3\frac{r_0}{r_i}\frac{f_t}{\tan\alpha_{cc}} \qquad \textit{(Eq. 3-18)}$$

Tepfers[90] showed that the partly-cracked model under-estimate the bond capacity. This is mainly due to the fact that crack-bridging stresses remain in the cracked concrete and

that ongoing splitting is not really distributed. Therefore, Tepfers proposed an upper bound in the form of a plastic model, where tensile hoop stresses are constant over the wall thickness and equal to the concrete strength, Fig. 3-7.

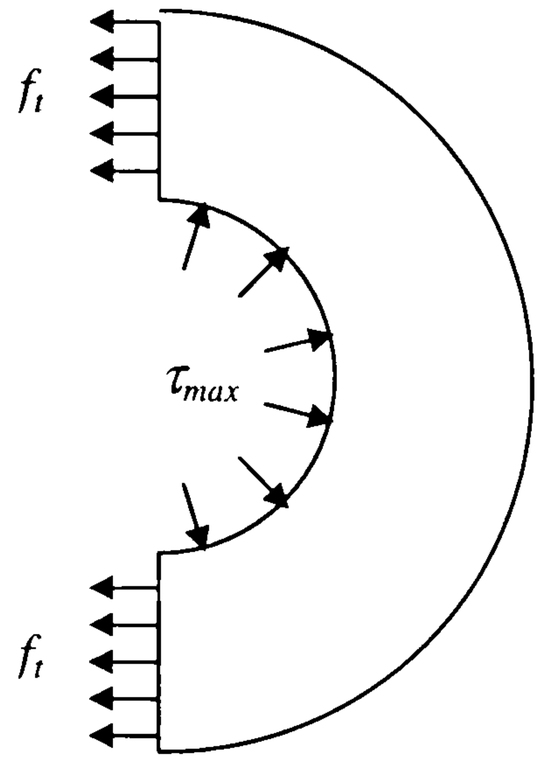

Fig. 3-7: Thick-walled cylinder plastic model

The formula for the maximum bond stress is readily derivable:

$$\tau_{\max} = \frac{r_0 - r_i}{r_i} \frac{f_t}{\tan \alpha_{cc}} \qquad \textit{(Eq. 3-19)}$$

Tepfers showed that most of the experimental data lie between the two boundaries provided by the partly-cracked elastic and the plastic model. This approach enhanced greatly the understanding of splitting crack formation, however, the model is not truly predictive as the two boundaries typically take values with difference of at least 50%.

Tepfers was only concerned with splitting. However, it is possible to extend the partly-cracked elastic model to predict the branching out of conical cracking towards the concrete surface, i.e. the secondary cracking. For that purpose, the longitudinal stress at the tip of conical cracking is checked against the concrete strength. A few simplifying assumptions were necessary:

- The extent of conical cracking is given by the critical radius, e_c,
- the longitudinal stress concentration between two adjacent ribs is linear and proportional to the radius, r,
- the longitudinal stresses due to the ribs in front of the cross-section considered are evenly distributed in the cross-section over an area A_c,

- and the bond stresses are assumed to be uniformly distributed over the length of the bar in front of the cross-section considered.

With these assumptions, the condition for secondary cracking is:

$$\begin{cases} \sigma_n + \dfrac{\sigma_l}{2} + \sqrt{\dfrac{\sigma_l^2}{4} + \tau_e^2} = f_t & \textit{(Eq. 3-20)} \\ \textit{with} & \\ \sigma_n = \dfrac{2\pi r_i r_s}{A_c} n & \textit{(Eq. 3-21)} \\ \textit{and} & \\ \sigma_l = \dfrac{r_s}{(r_0 - e)} \tau_e \approx 2\dfrac{r_s}{r_0} \tau_e & \textit{(Eq. 3-22)} \\ \textit{and} & \\ \tau_{\max} = \dfrac{e}{r_i} \tau_e = \dfrac{0.486 r_0}{r_i} \tau_e & \textit{(Eq. 3-23)} \end{cases}$$

where σ_n is the longitudinal stress due to n ribs in front of the considered cross-section, σ_l is the longitudinal stress due to the rib considered at the tip of the conical crack, τ_e is the shear stress at the tip of the conical crack, and r_s is the rib spacing.

Assuming a typical rib spacing r_s = 1.6 r_i as defined by various national and international standards, e.g. ISO 6935-2[95], BS 4449:1997[96] and ASTM A 615[97], and rearranging (Eq. 3-20) with e_c = 0.486 r_0, the following maximum bond stress for secondary cracking is obtained:

$$\tau_{\max}^{sc} = \frac{r_0^2 / r_i^2}{10n\dfrac{r_i^2}{A_c} + 3.2 + \sqrt{10.25 + 4.23\dfrac{r_0^2}{r_i^2}}} \frac{f_t}{\tan \alpha_{cc}} \qquad \textit{(Eq. 3-24)}$$

A typical example can be used to determine the distance at which the secondary cracking becomes more critical than splitting. Goto[85] observed conical crack angles of α_{cc} = 60 deg. Assuming a standard flexural design, the following relations can be chosen: $r_0 = 4\ r_i$ and $A_c = 7.25\ r_0^2$. In these conditions, the criterion for secondary cracking to arise before splitting:

$$n \geq 8 \qquad \textit{(Eq. 3-25)}$$

This agrees fairly well with Goto's experiments which displayed secondary cracking at the 6^{th} or 7^{th} rib from transverse cracking, for a bar of 9 mm radius and a cover of 40 mm.

Splitting with LEFM criterion

As Tepfers lower and upper bound models provide a wide range of possible bond capacity, it was considered that a fracture mechanics approach would produce a more accurate prediction. The simplest fracture mechanics model is the LEFM model for the propagation of a single radial crack in a ring, a configuration studied by Bowie and Freese (1972)[98].

The energy criterion for splitting crack propagation is expressed in term of stress intensity factors:

$$\begin{cases} K_I = \tau \tan \alpha_{cc} \sqrt{\pi a} \cdot \dfrac{2r_0^2}{r_0^2 - r_i^2} \cdot F_I & \textit{(Eq. 3-26)} \\ \text{with} \\ F_I = f\left(r_i / r_0, a/(r_0 - r_i)\right) & \textit{(Eq. 3-27)} \end{cases}$$

$$\begin{cases} \textit{cracking criterion :} \\ K_I = K_{IC} & \textit{(Eq. 3-28)} \\ \text{with} \\ K_{IC} = \sqrt{E_c G_f} & \textit{(Eq. 3-29)} \end{cases}$$

The function F_I can be found in most fracture mechanics text books, Fig. 3-8.

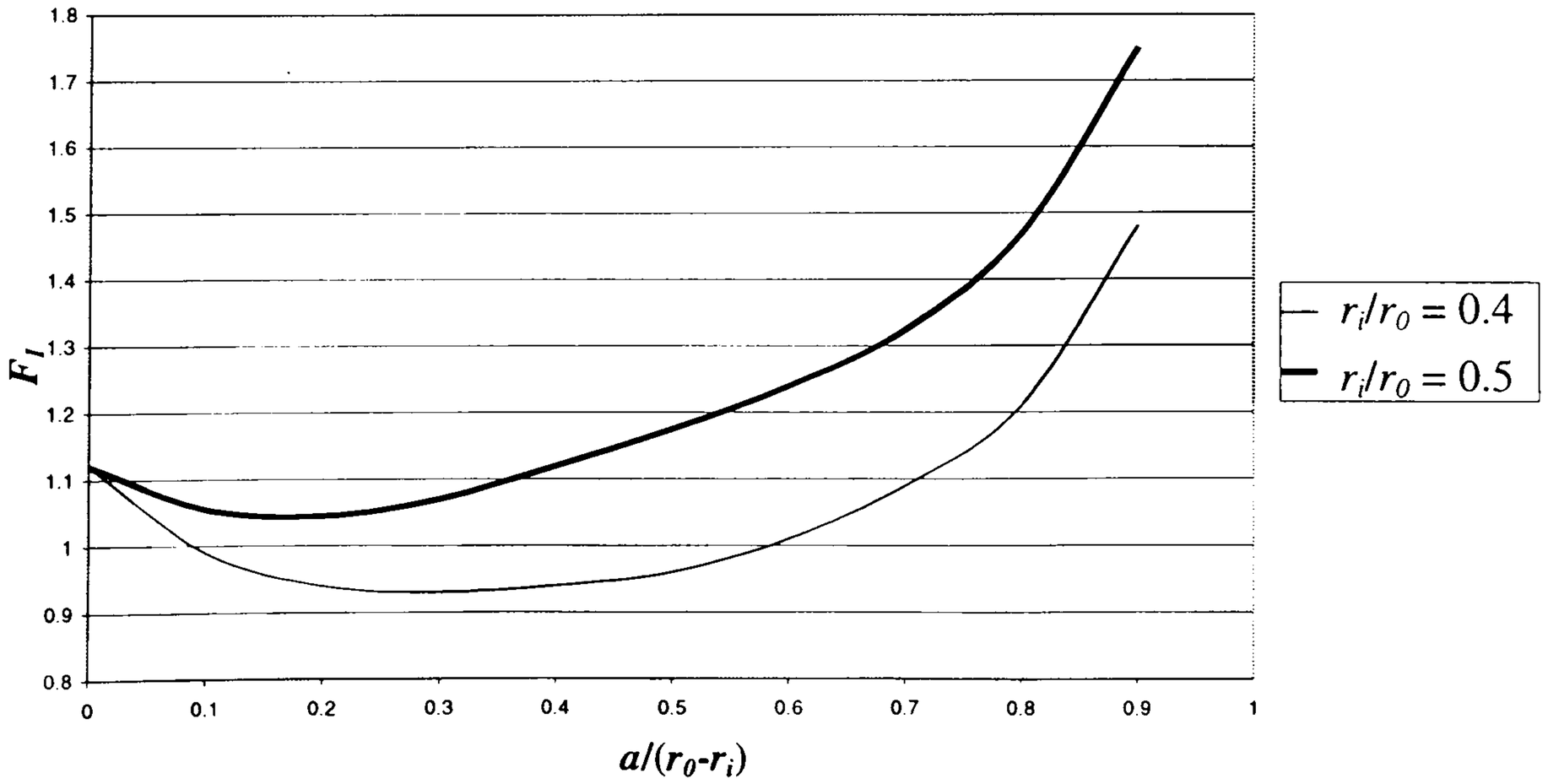

Fig. 3-8: LEFM analysis of a ring with a single crack

The maximum bond stress predicted by LEFM is obtained graphically by plotting the bond-to-crack extent diagram. A very large bond capacity is predicted for a small extent of cracking. Bond capacity then decreases monotonically with increasing crack extent. Consequently, it is necessary to adopt both the partly-cracked elastic criterion and the LEFM criterion to produce a physically realistic model. Maximum bond stress is generally obtained where the two curves meet. In the case where the LEFM curve is always above the partly-cracked elastic one or if the LEFM crosses the partly-cracked elastic one after the peak load, then the energy criterion is not prominent/applicable, Fig. 3-9.

Splitting with NLFM criterion

A more realistic approach is the use of a non-linear fracture mechanics model. Reinhardt (1992)[99] improved Tepfers' partly-cracked elastic model by inserting softening stresses in the cracked part of the ring. Reinhardt used Hordijk's exponential softening curve, (Eq. 2-47),and worked out the additional bond capacity provided by softening stresses for a crack extent e.

$$\tau = \frac{f_t}{r_i \tan\alpha_{cc}}\left[e\frac{r_0^2 - e^2}{r_0^2 + e^2} + \frac{1}{6.93\beta}\left(1 - e^{-6.93\beta(e-r_i)}\right) - \frac{\beta(e-r_i)^2}{73} + \frac{1}{14.24\beta} \right.$$

$$\left. -3.896\beta^2 e^{-6.93\beta(e-r_i)}\left[(e-r_i)^3 + \frac{(e-r_i)^2}{2.31\beta} + \frac{e-r_i}{8\beta^2} + \frac{1}{55.47\beta^3} \right] \right] \qquad \textit{(Eq. 3-30)}$$

with

$$\beta = \frac{2\pi \cdot \varepsilon_{ct}}{n \cdot w_{ult}^{cr}} = \frac{1.223 f_t^{\,2}}{n E_c G_f} = 3.19 f_t^{\,0.45} \qquad \textit{(Eq. 3-31)}$$

The maximum bond stress is obtained by plotting the bond-to-crack extent diagram.

Van der Veen[54] devised a similar model using Van der Veen's power law for the softening behaviour, (Eq. 2-46). It resulted in a quite simpler equation:

$$\tau_{max} = \frac{f_t}{r_i \tan\alpha_{cc}}\left[e\frac{r_0^2 - e^2}{r_0^2 + e^2} + \frac{e-r_i}{1.248}\left[1 - \beta(e-r_i)\right]^{0.248} \right] \qquad \textit{(Eq. 3-32)}$$

with

$$\beta = \frac{2\pi \cdot \varepsilon_{ct}}{n \cdot w_{ult}^{cr}} = \frac{1.223 f_t^{\,2}}{n E_c G_f} = 3.19 f_t^{\,0.45} \qquad \textit{(Eq. 3-33)}$$

The maximum bond stress is equally obtained by plotting the bond-to-crack extent diagram.

Worked example

In order to give a better understanding of the different models, a typical example is worked out.

The chosen problem data are the following:

- the bar diameter, $d_b = 24$ mm ($r_i = 12$ mm)
- the concrete cover, $c = 18$ mm ($r_0 = 30$ mm and $r_i/r_0 = 0.4$)
- the concrete tensile strength, $f_t = 4$ MPa, and the maximum aggregate size, $d_{agg} = 16$ mm,
- the conical crack angle, $\alpha_{cc} = 60$ deg.
- G_f is deduced from f_t and d_{agg} using (Eq. 2-37) and (Eq. 2-39),
- E_c is derived using the following formula from the CEB-FIP Model Code 1990:

$$E_c = 2.15 \times 10^4 \left(\frac{f_c}{10} \right)^{1/3} MPa \qquad \textit{(Eq. 3-34)}$$

The evolution of the bond capacity with the crack extension is then obtained using (Eq. 3-17), (Eq. 3-19), and (Eq. 3-27) to (Eq. 3-33), see Fig. 3-9.

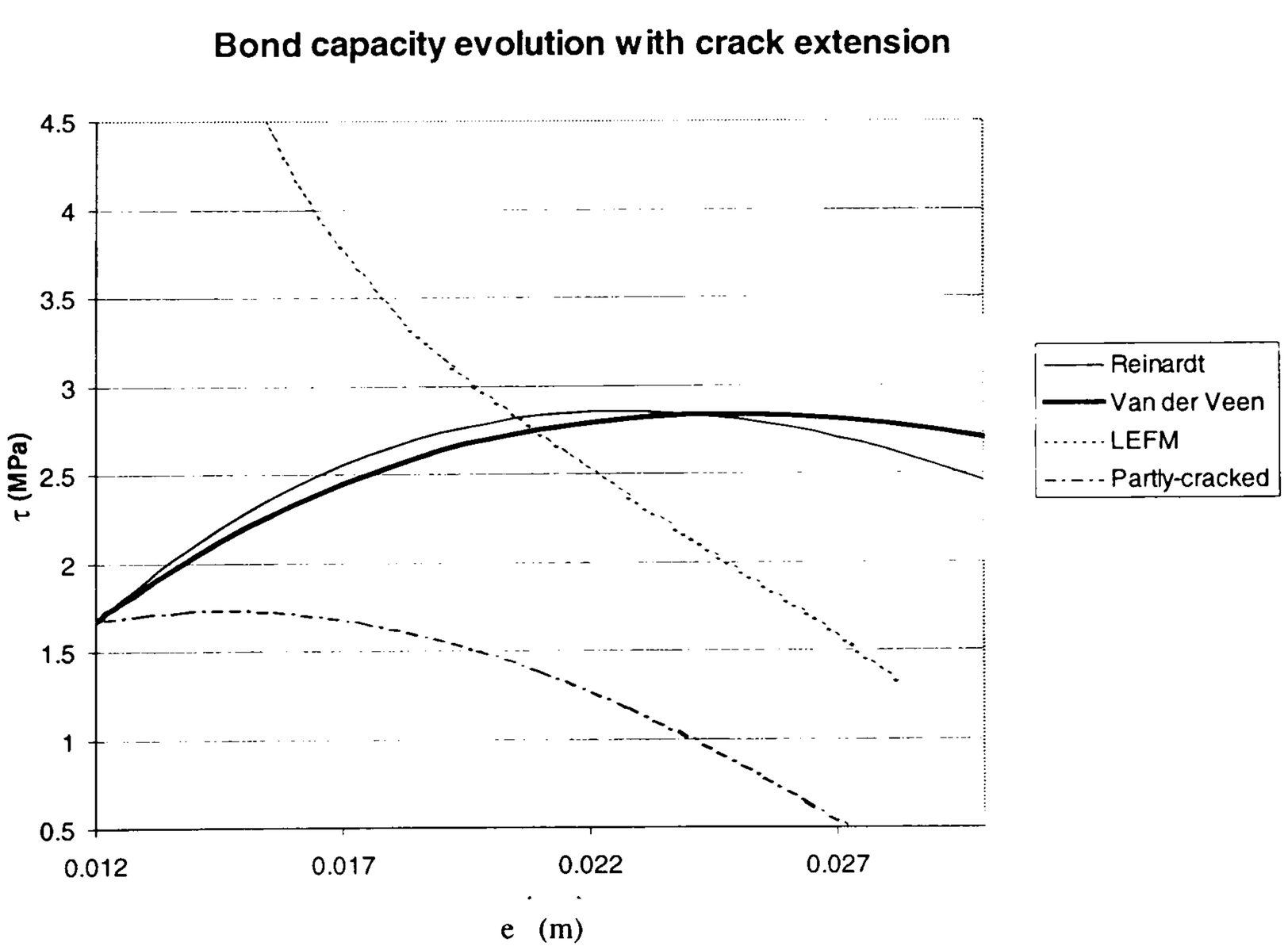

Fig. 3-9: Comparison of the different splitting models

Maximum bond stress is directly read on the diagram. Final results are summarised in Table 3-1.

Table 3-1: Comparison of maximum bond stress and critical crack extension.

Model	Partly-cracked elastic	Plastic	LEFM + Partly-cracked elastic	NLFM (Reinhardt)	NLFM (Van der Veen)
τ_{max} (MPa)	1.732	3.464	1.732	2.85	2.83
e critic (mm)	14.6	_	14.6	23	24

As expected, plastic and partly-cracked elastic models give very different results (50% difference). The LEFM curve remains above the partly cracked elastic model, therefore it is not the critical criterion for this example. It can be noted that Reinhardt's and Van der Veen's models give very similar results, and lie between the lower and the upper bounds of the partly-cracked elastic and the plastic models respectively.

In conclusion, if a simple model is required, the partly-cracked elastic model can be used safely as the LEFM criterion is generally not critical. For a more accurate model, Reinhard's or Van der Veen's model can be used with equal reliability.

3.2.3. Axi-symmetric finite element models

Fig. 3-6 shows that if the three-dimensional problem is considered, conical cracks and hoop stresses responsible for splitting interact. Analytical models are not able to describe this interaction. That is the reason why axi-symmetric non-linear finite element models have been developed by several researchers to simulate the three-dimensional cracking behaviour.

Avoiding the complexity of a fully three-dimensional model, all the finite element analyses encountered in the literature opt for axi-symmetric models. Generalisation of the results obtained to bond-slip behaviour in beams requires the assumption that the behaviour of a cylindrical reinforced concrete tension specimen is close enough from the behaviour of a rectangular tension specimen with equivalent concrete cover.

The first to simulate the full tension-stiffening curve of a reinforced concrete tension specimen was Ingraffea et al.[43,100]. Using the assumption that conical cracking is a local phenomenon, hence it is independent from overall geometry, an axi-symmetric model was used in which the steel bar was modelled with elastic elements. Connection between steel and concrete was achieved by full bond in the longitudinal direction at every second steel element. Cracking, including strain-softening, was simulated using a discrete-crack approach with progressive remeshing, allowing for the proper crack direction to be modelled. Conical cracking was successfully simulated and was shown to be responsible for the non-linear bond-slip behaviour.

Pijaudier-Cabot and Mazars (1991)[101] designed an axi-symmetric model with full bond between steel and concrete. A scalar non-local damage model with a sophisticated mode II constitutive law was chosen to simulate cracking. The model was shown to be mesh insensitive and to simulate appropriately the distribution of damage along the reinforcing bar contrary to a local approach. However, the scalar nature of the model along with the somewhat arbitrary mode II constitutive law removes much of the interest inherent to non-linear finite element analysis since the cracking patterns are not simulated.

Rots (1992) [102] achieved better results by using the rotating smeared crack concept for conical cracking, the fixed smeared cracking concept for splitting and the fixed discrete cracking concept for transverse cracking. Strain-softening was included in the material model. Connection between the steel and the concrete was achieved discretely by connecting them at every second node, at the actual location of the ribs, Fig. 3-10-a). Rots manages to simulate successfully conical cracking, splitting and transverse cracking, Fig. 3-10-b) and Fig. 3-10-c), including the softening branches of the loading curve. The model was not benchmarked against experimental data, but bond-slip curves were produced and are compared in Fig. 3-11 with empirical bond-slip laws. The initial part compares well with Nilson (1968), while the ultimate stage compares better with Mirza and Houde (1979). It is not known if the discrepancy is due to the empirical laws depending on very few parameters, or on the finite element model yielding an over-stiff response.

a)

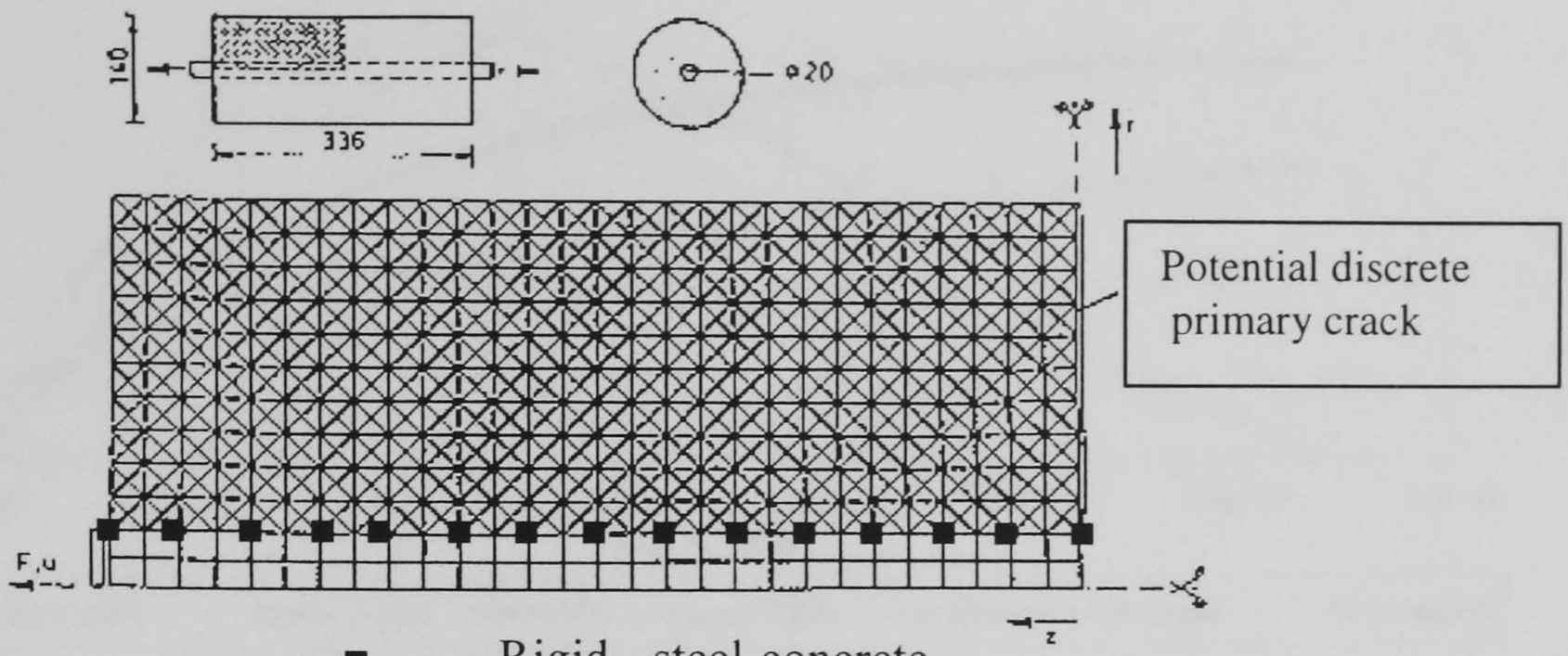

b)

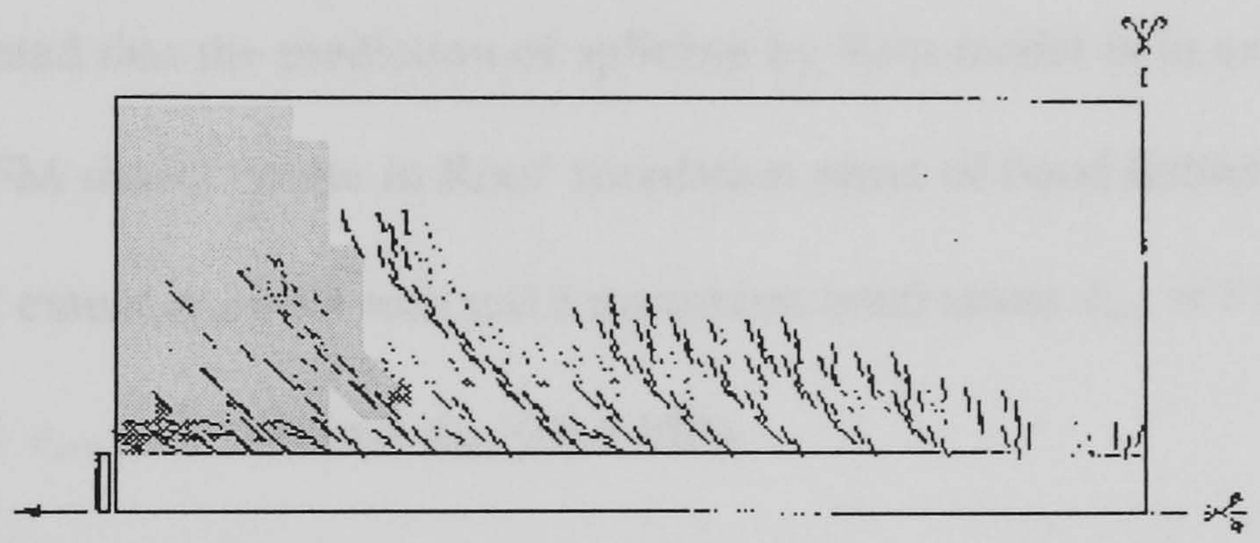

c)

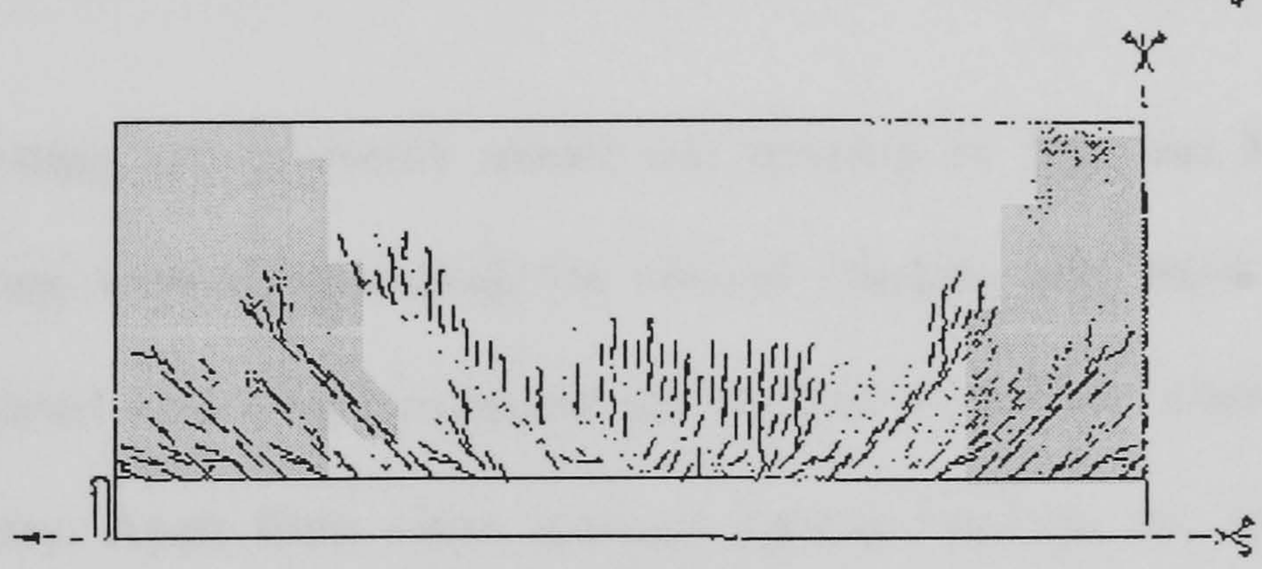

Fig. 3-10: Rots' axi-symmetric model of the bond-slip problem
Adapted from Rots (1992)[102]

a) mesh definition, b) cracking pattern at impending transverse crack formation, c) cracking pattern at final stage (dark areas correspond to the propagation of splitting cracks).

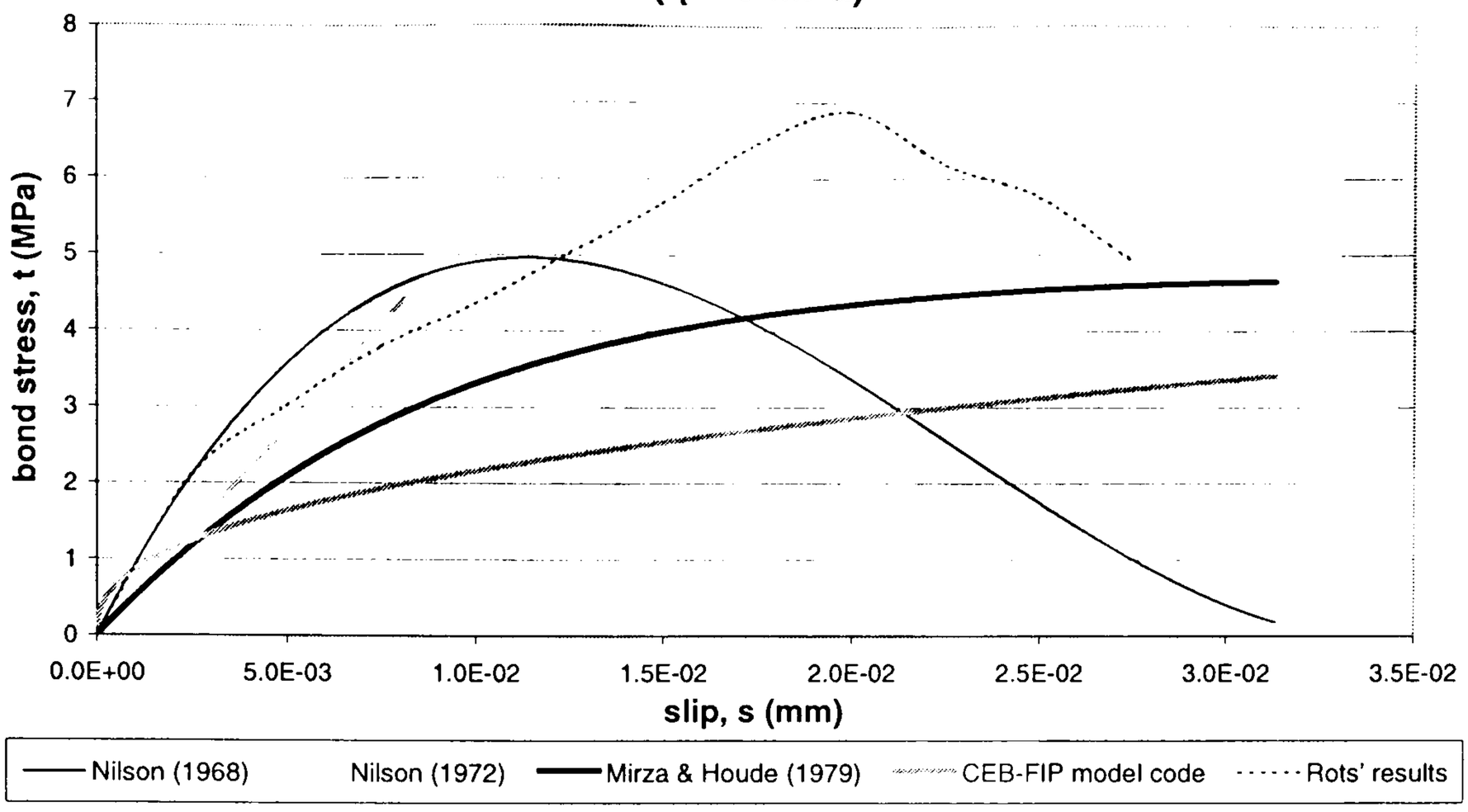

Fig. 3-11: Rots' simulated bond-slip curve compared to empirical laws

It should be noted that the prediction of splitting by Rots model is in excellent agreement with Reinhardt NLFM model: while in Rots' simulation onset of bond failure by splitting occurs for a critical crack extent e_{crit} = 44 mm and a maximum bond stress τ_{max} = 7 MPa, Reinhardt NLFM model predicts e_{crit} = 42 mm and τ_{max} = 6.6 MPa.

Another interesting axi-symmetric model was develop by Yao and Murray (1995)[103] using discrete cracking without remeshing for conical cracking and fixed smeared cracking for splitting. A refined model was introduced for the steel to concrete connection, which included the rib geometry. Apart from some spurious zig-zag cracking due to the discrete cracking technique, conical cracking and splitting were satisfactorily simulated. The main conclusion from this work was to emphasise the importance of splitting on the bond-slip behaviour of reinforced concrete, as had already been observed in Rots' model. It was also concluded from the two analyses that no single valued functional exists between bond stress and slip, challenging the concept of a constitutive relationship for bond-slip. Indeed, this relation was shown to change with the position relative to the closest transverse crack and the onset of splitting, i.e. the three phenomena are coupled. However, it was shown in Fig. 3-11 that in the absence of splitting crack an average bond-slip law is still acceptable.

3.3. Mechanics of Crack Formation

Further investigation of the mechanics of crack formation involved in the steel-to-concrete bond behaviour requires a three-dimensional non-linear finite element model. Axi-symmetric models provided realistic results for axi-symmetric specimens. However, the customary reinforced concrete flexural design does not generally result in an axi-symmetric geometry. Since the bond phenomenon is fully three-dimensional, it is expected that the lack of symmetry in the concrete boundaries will influence the bond response.

A highly refined 3D model was developed to simulate conical cracking, secondary cracking, splitting cracks and transverse cracking as realistically as possible. The aim was to investigate the influence of the concrete cover notably on the onset of secondary cracking, the interaction of the different cracking mechanisms, and to determine the limitation of the non-linear finite element method in simulating the propagation of unstable cracks.

Eventually, the shortcomings of the finite element model to predict the onset of splitting propagation were compensated for by the development of a fracture mechanics model adopting a different approach to these of Tepfers and Reinhard. The entire system of the concrete and the reinforcing bar was included in the energy balance rather than considering the action of the bar on the concrete as an external load.

3.3.1.3D Finite element model

Definition of the specimen

A standard flexural design has been adopted for the specimen. In order to limit the complexity of the structural behaviour, whilst retaining the characteristics of the bond behaviour under the neutral axis, a four bar tension test was chosen. It was assumed that the tensile stress

distribution of the tension specimen is approximately equivalent to the stress distribution occurring in the tensile zone of a flexural member.

The load was applied symmetrically to all four bars. The test was assumed to be conducted with displacement control and crack mouth opening displacement control.

The characteristic features of the specimen were:

- 4 high yield ribbed steel bars of 16 mm diameter,
- rib spacing of 10 mm ($r_s = 0.625\ d_b$),
- rectangular concrete cross-section 125 x 240 mm,
- and 20 mm horizontal and vertical concrete cover,
- total length, L, of 372 mm.

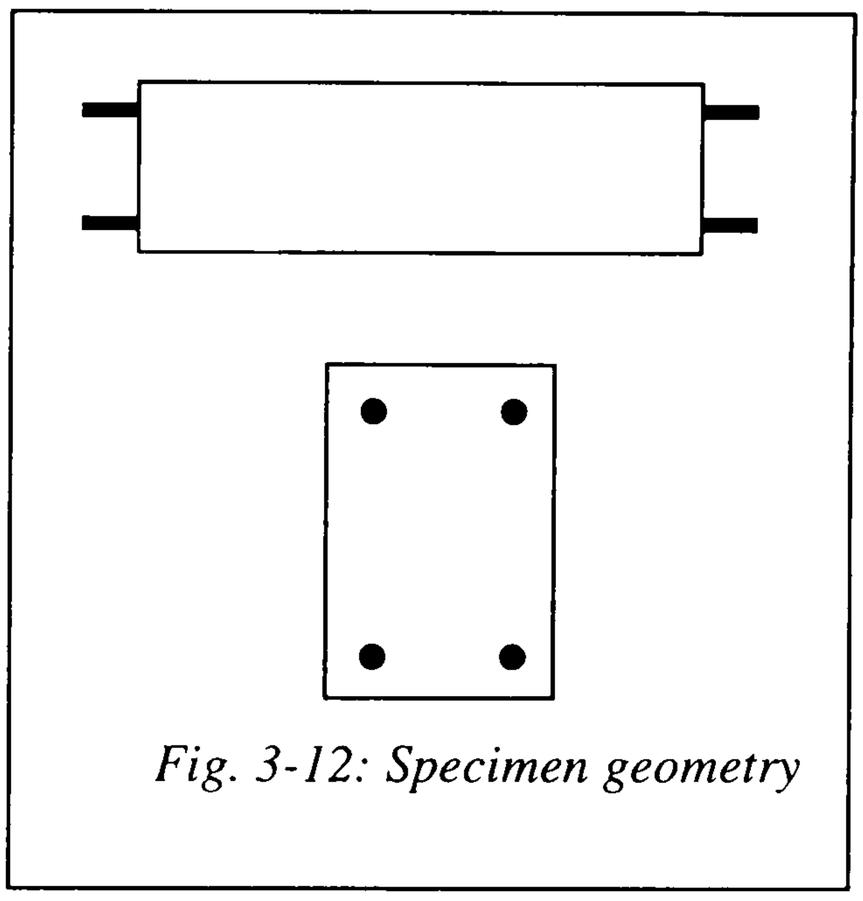

Fig. 3-12: Specimen geometry

L was chosen to be longer than twice L_{max}, as defined by the CEB-FIP model code 1990 to allow for the bond stress to develop fully: $L_{\max} = \frac{d_b}{3.6\rho_s} = 161$ mm

Material properties used were:

- steel material property : $E_s = 205$ GPa
- concrete material properties : $E_c = 25$ GPa

  $f_t = 4.1$ MPa

  $G_f = 80$ J/m^2

According to the CEB-FIP model code 1990, this corresponds approximately to a concrete compressive strength, f_c, of 50 MPa, and a maximum aggregate size, d_{agg}, of 8 mm. The value of 8 mm for d_{agg} is slightly underestimated. However, the value 80 J/m^2 from which d_{agg} is derived was chosen close to the typical specific fracture energy obtained for normal concrete mixes. It is believed that this choice has only little effect on the outcome of the simulation.

Presentation of DIANA model

To reduce computational cost, three-fold symmetry was used so that an eighth only of the specimen, i.e. half a bar, was modelled, Fig. 3-13. Boundary conditions were used to satisfy symmetry conditions, i.e. restraints normal to the planes of symmetry are provided. Only one load was applied at the extremity of the steel bar.

The reinforcing bar was modelled by 1D bar elements. The discretisation was chosen to correspond to the rib spacing. Concrete was modelled by 3D 20-noded brick elements, Table 3-2. Conical cracking and secondary cracking were simulated using smeared cracking. The cracking strength was assumed to be 4.1 MPa. Because of the preference of smeared cracking to form parallel to mesh lines, the mesh topology was chosen so that mesh orientation corresponded to the more likely cracking orientation. Thus, around the bar, prismatic elements were inclined at an angle of 60 deg. from the bar axis in a cone-like shape to follow potential conical cracking. Everywhere else the meshing was orthogonal to concrete surfaces.

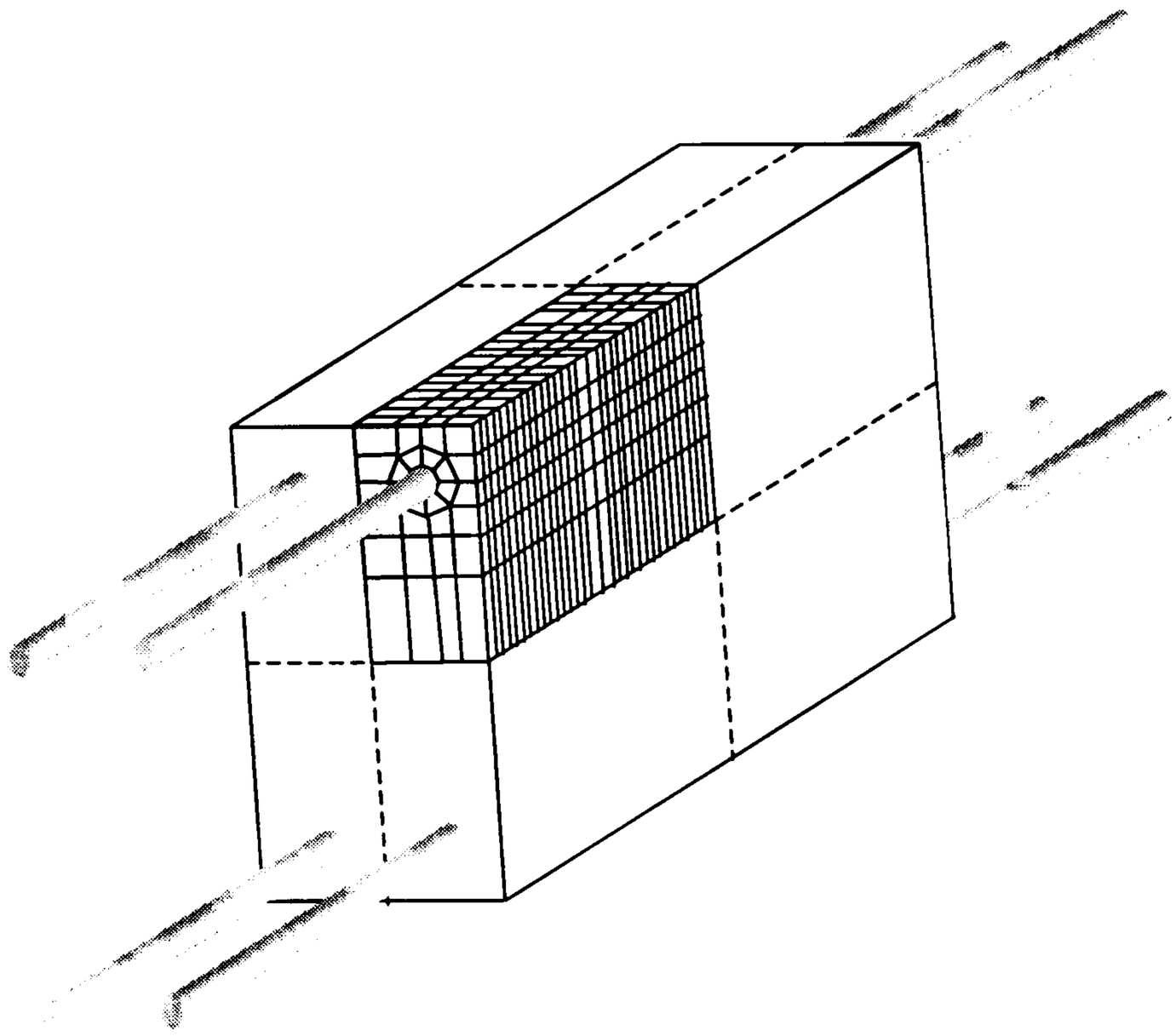

Fig. 3-13: Threefold symmetry and mesh topology

Particular attention was given to the connection between steel and concrete, as it does strongly influence the bond behaviour. The model was intended to be as realistic as possible within the

limits of finite element analysis. Connection between the steel bar and a first layer of interface elements was achieved through rigid links, Fig. 3-14. At the nodes corresponding to the ribs rigid connection in the radial and the longitudinal direction was enforced. At the mid-nodes, between rib locations, only radial rigid connection was enforced. This was intended to model the mechanical connection achieved between steel and concrete through the ribs in the longitudinal direction, and the incompressibility of the steel bar in the radial direction.

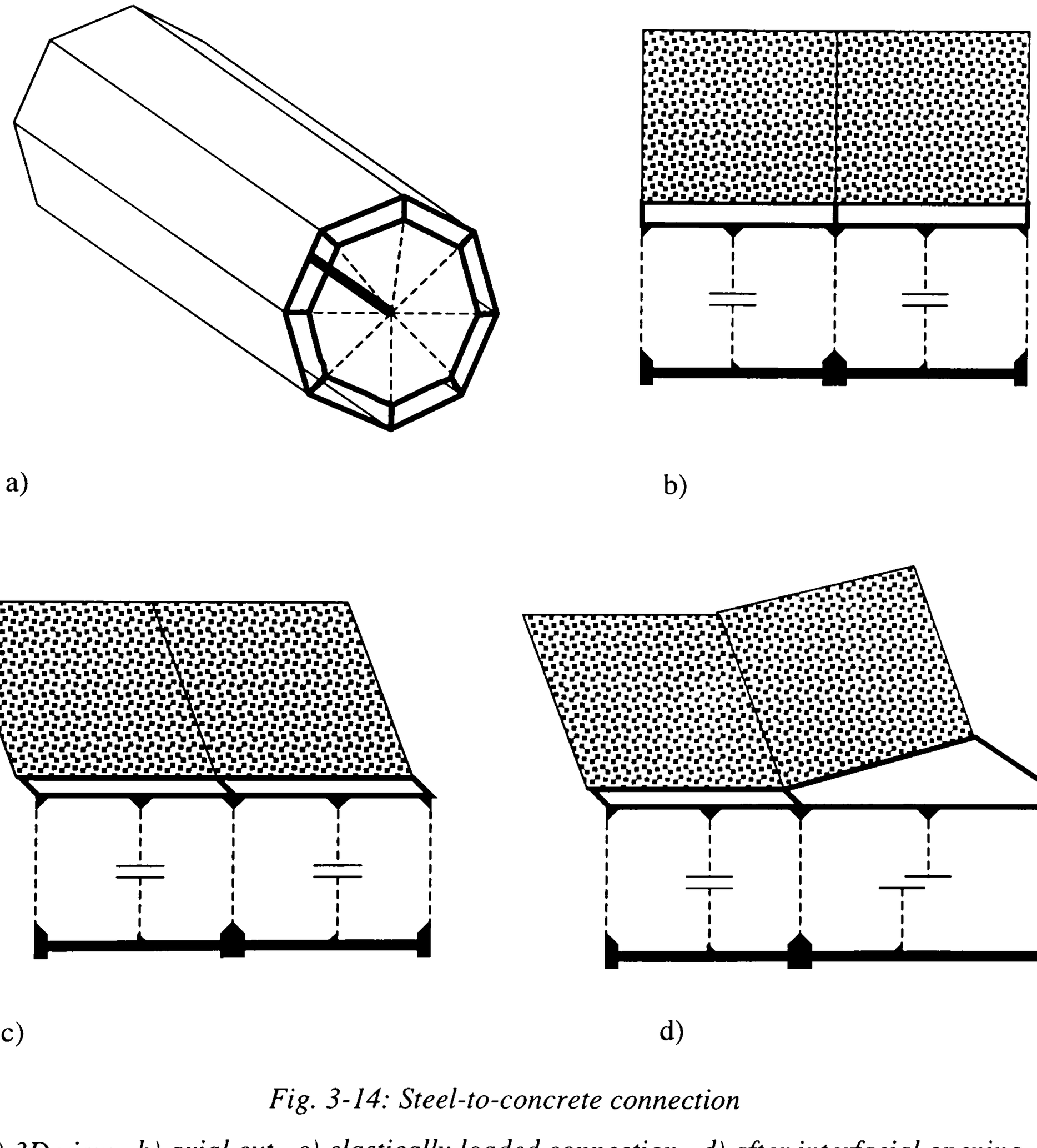

Fig. 3-14: Steel-to-concrete connection

a) 3D view, b) axial cut, c) elastically loaded connection, d) after interfacial opening

The possibility of the loss of this mechanical connection was modelled by interface elements. Below a given normal traction, the interface was infinitely rigid in normal and tangential directions. Once this normal strength was reached, the interface normal and tangential stiffness was reduced to zero. Although the actual normal strength of the steel-to-concrete interface due

to chemical and mechanical bond is low compared to the corresponding stresses obtained in the simulation, a strength of 1 MPa was arbitrarily chosen to avoid early instability to set in the simulation.

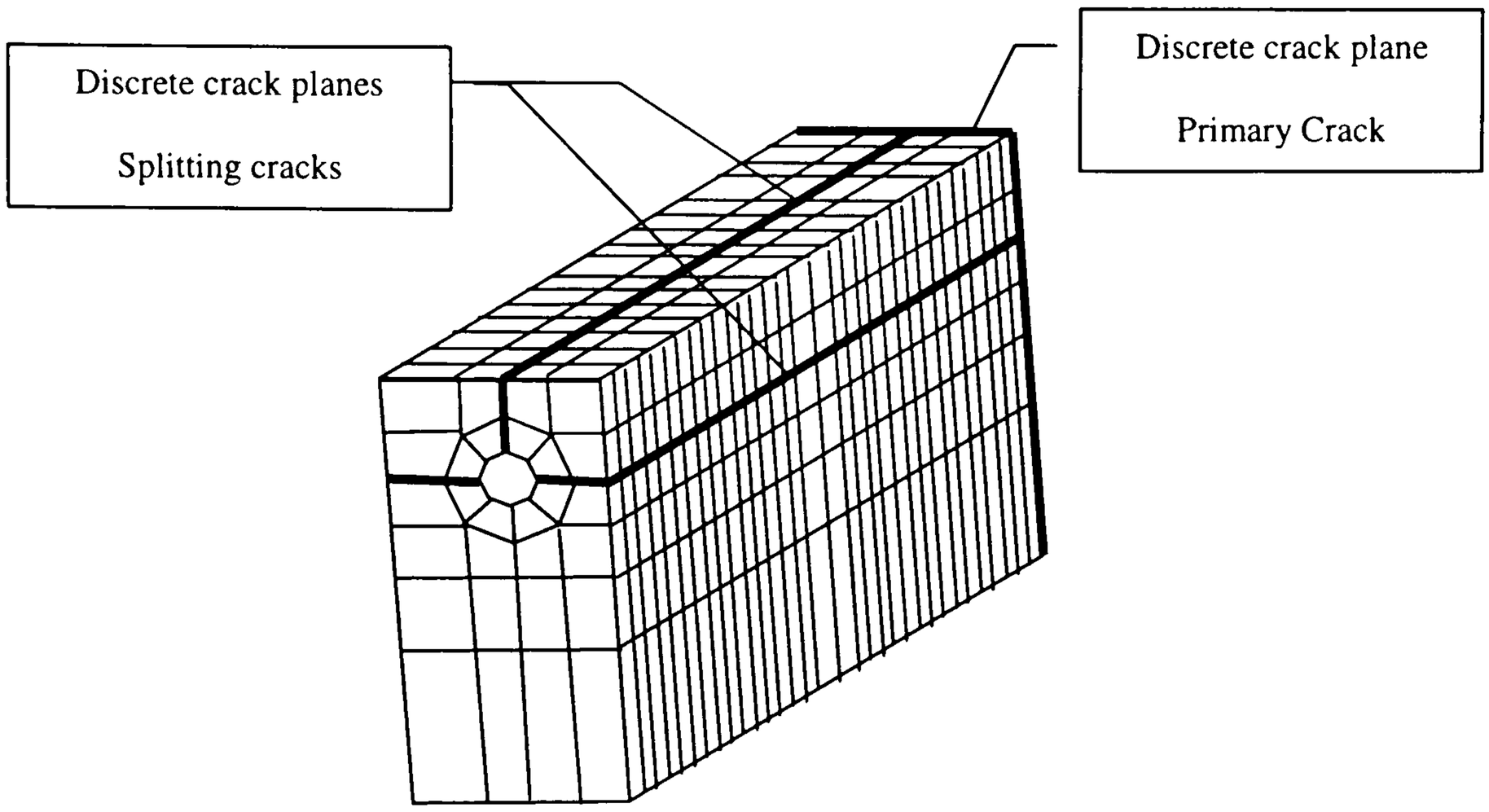

Fig. 3-15: Position of the discrete crack interfaces

Additional interface elements were inserted in the transverse symmetry plane to model transverse cracking in a discrete way. Interface elements were also inserted horizontally and vertically along the reinforcing bar to simulate potential splitting, Fig. 3-15. In both of these cases, a slightly lower tensile strength was implemented (4 MPa) to avoid smeared cracking arising first in adjacent elements.

The steel elements were considered to behave linear elastically throughout the simulation. After the simulation, it was checked that the yield strength had not been reached. The concrete material model was elastic behaviour up to the tensile strength f_t and Hordijk et al. strain softening curve was implemented for the cracking behaviour, Eq. 2-47. Smeared cracking was used for conical and secondary cracking. The constitutive model chosen was Rots' multidirectional crack model with a threshold angle of 60 deg. The size of the crack band width was chosen according to Eq. 2-75. Cracking was assumed to propagate along mesh lines, and the 3x3x3 integration scheme was adopted, which yielded a crack band width, h = 2.9 mm for

the conical cracks and h = 3.3 mm for secondary cracks. Consequently, an average crack band width of 3 mm was adopted everywhere. The appropriateness of such a choice will be assessed later.

Table 3-2: Model size

brick elements	bar elements	interface elements	nodes	integration points
1 168	37	536	8 630	36 656

The solution procedure adopted was the regular Newton-Raphson iteration scheme complemented with the line search algorithm. Convergence was tested using an energy norm criterion. Convergence was assumed to be achieved for a relative energy variation of 0.5‰.

Load control was implemented up to a load of 27.2 kN. Then indirect displacement control was enforced using a selective arc-length method on the crack mouth opening of the splitting cracks and the secondary cracks. Appearance of negative pivots was monitored throughout the simulation.

In total, 53 steps were carried out, each requiring between 2 and 4 iterations, Table 3-3. No negative pivot was encountered throughout the simulation up to step 53. At step 53 a negative pivot corresponding to the negative load step appeared. Convergence was lost after step 53 at the onset of transverse cracking.

Table 3-3: Simulation figures

steps	iterations	CPU time
53	129	23 h

Presentation of the results

Before any cracking occured in the specimen, linear stiff behaviour was observed, $K \approx 440$ kN/mm. Stress was transmitted rapidly from the bar to the surrounding

concrete with shear stress concentrations at the location of the ribs. Beyond the transfer length, the tensile longitudinal stresses were distributed uniformly over the concrete cross-section and the steel stress dropped to 18 % of its value, at the point of application of the load. 90 % of the longitudinal force transferred occurs over a length $t_f = 65$ mm, Fig. 3-16.

Hoop stresses in front of the first rib built up very rapidly, to an approximate level of 15 % of the steel stress. So did the shear stresses at the first rib, to an approximate level of 12 % of the steel stress. It can be deduced that local splitting in front of the first rib occurs at steel stresses as low as 27 MPa (5.5 kN for a bar of 16 mm), and the first conical cracking occurs at a steel stress level of 34 MPa (6.8 kN for a bar of 16 mm). This was verified at the third step for the onset of splitting (6 kN) and at the fourth step for first conical cracking (8 kN).

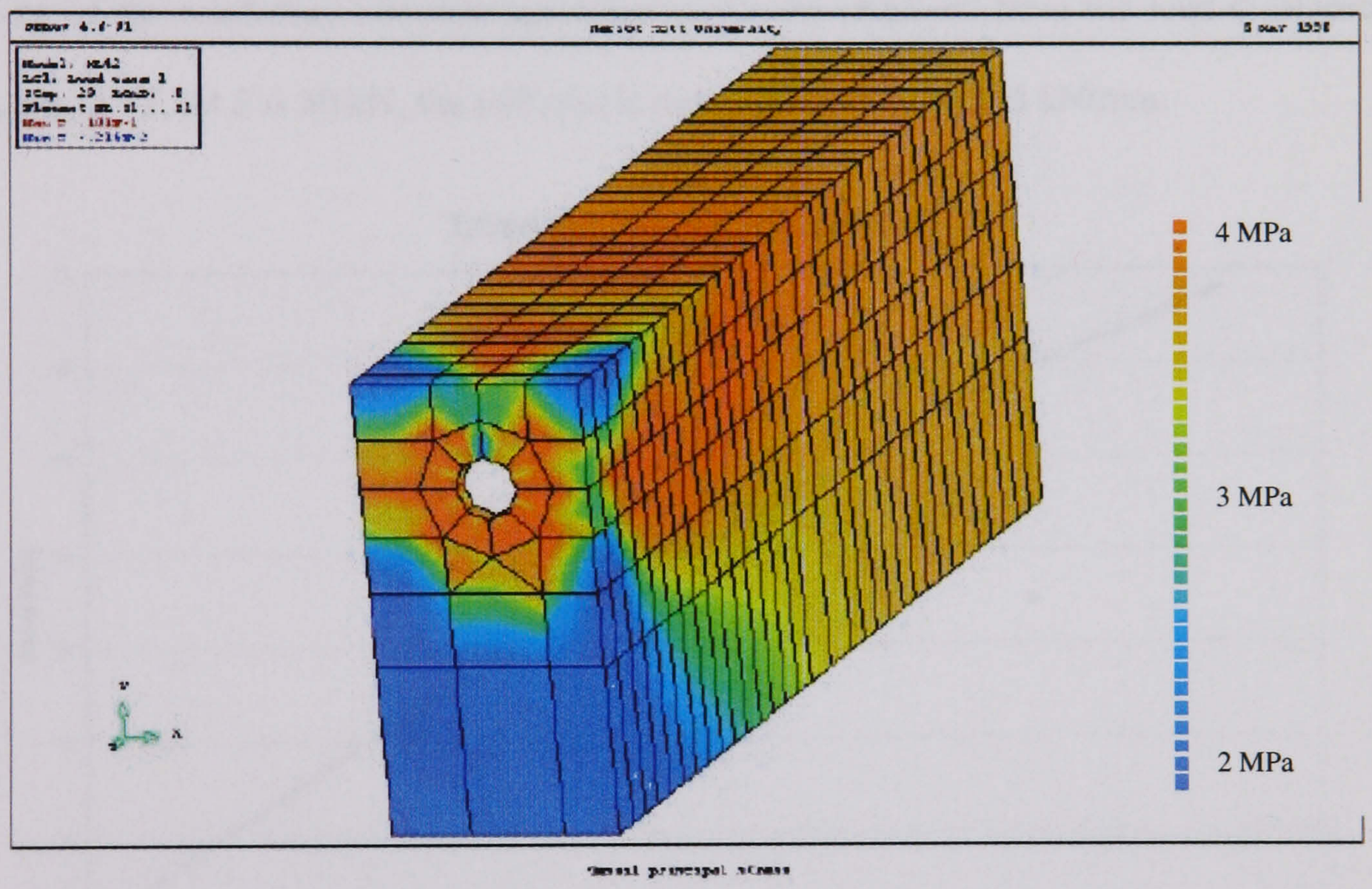

Fig. 3-16: distribution of principal tensile stress on the surface of the specimen, F = 28.5 kN

If cracks openings below 1 μm are ignored (corresponding to a stress drop of less than 10% of the concrete strength), conical cracking progressed along the bar at the following pace, Fig. 3-18:

- second rib at 13 kN
- third rib at 16 kN
- fourth rib at 20 kN

- fifth rib at 22.4 kN
- sixth rib at 26.4 kN

This corresponds, approximately, to a new rib cracking at every 3 kN increment, i.e. for an increase of 15 MPa in the steel stress. It should be noted that the conical crack pattern was not symmetric about the bar axis. More extensive cracking took place on the underside of the bar, away from the concrete cover. The inner block of concrete provided more confinement to the bar and tended to draw a more concentrated bond stress flow, resulting in more extensive damage on the underside of the bar.

The progressive softening of the bond interface and the subsequent slip resulted in a structural softening of the reinforced concrete specimen as can be observed from the load-displacement curve, Fig. 3-17. At $F = 30$ kN, the stiffness is reduced by 12 % to 385 kN/mm.

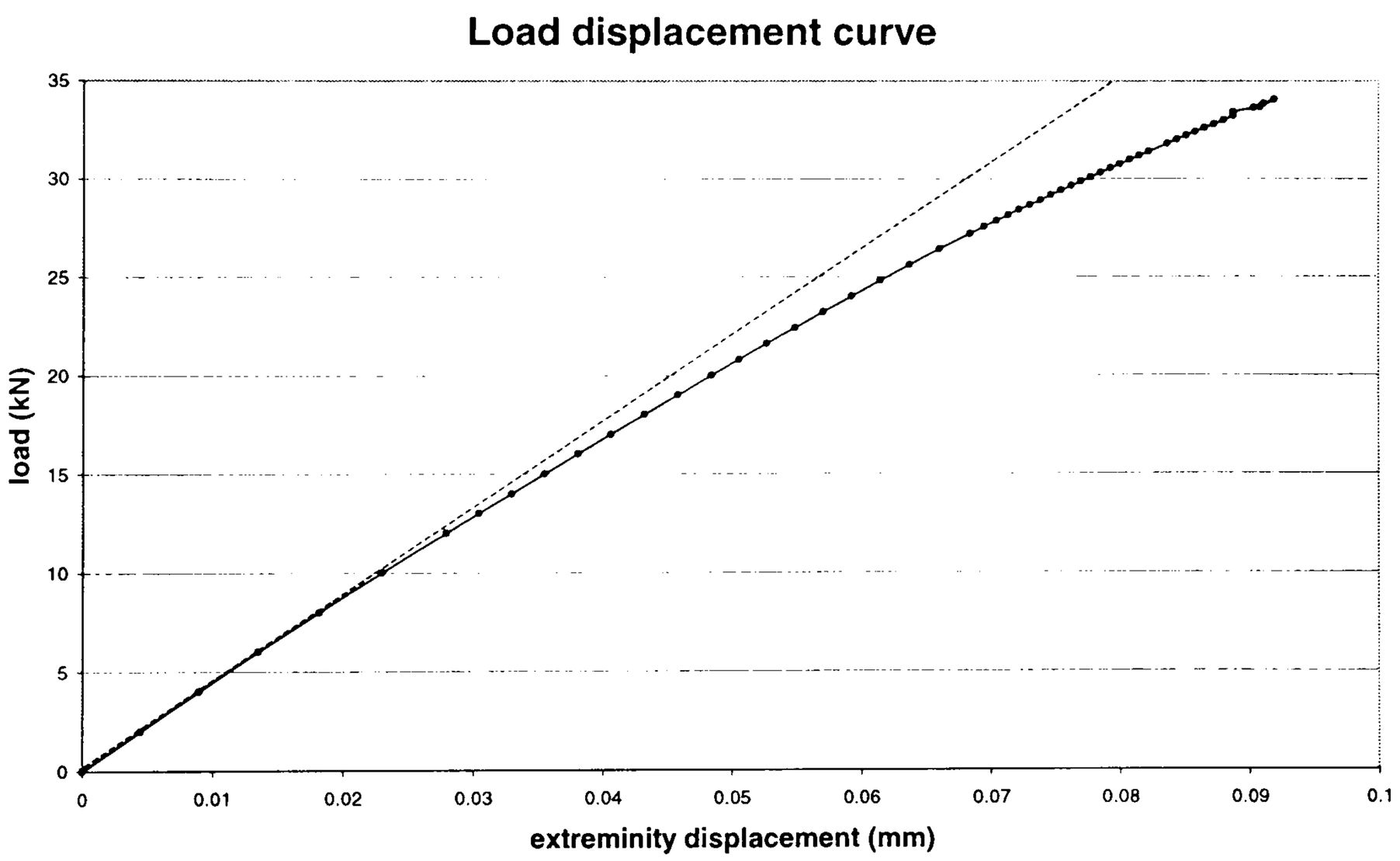

Fig. 3-17: Load-displacement curve of the reinforced concrete specimen

Conical cracks developed along the mesh lines at 60 deg. from the bar axis. Even at high steel stresses (e.g. 170 MPa) the conical cracks did not radiate more than 10 mm from the bar, Fig. 3-18. The maximum conical crack opening was not more than 8.5 μm, which corresponds to a stress drop of 44 %.

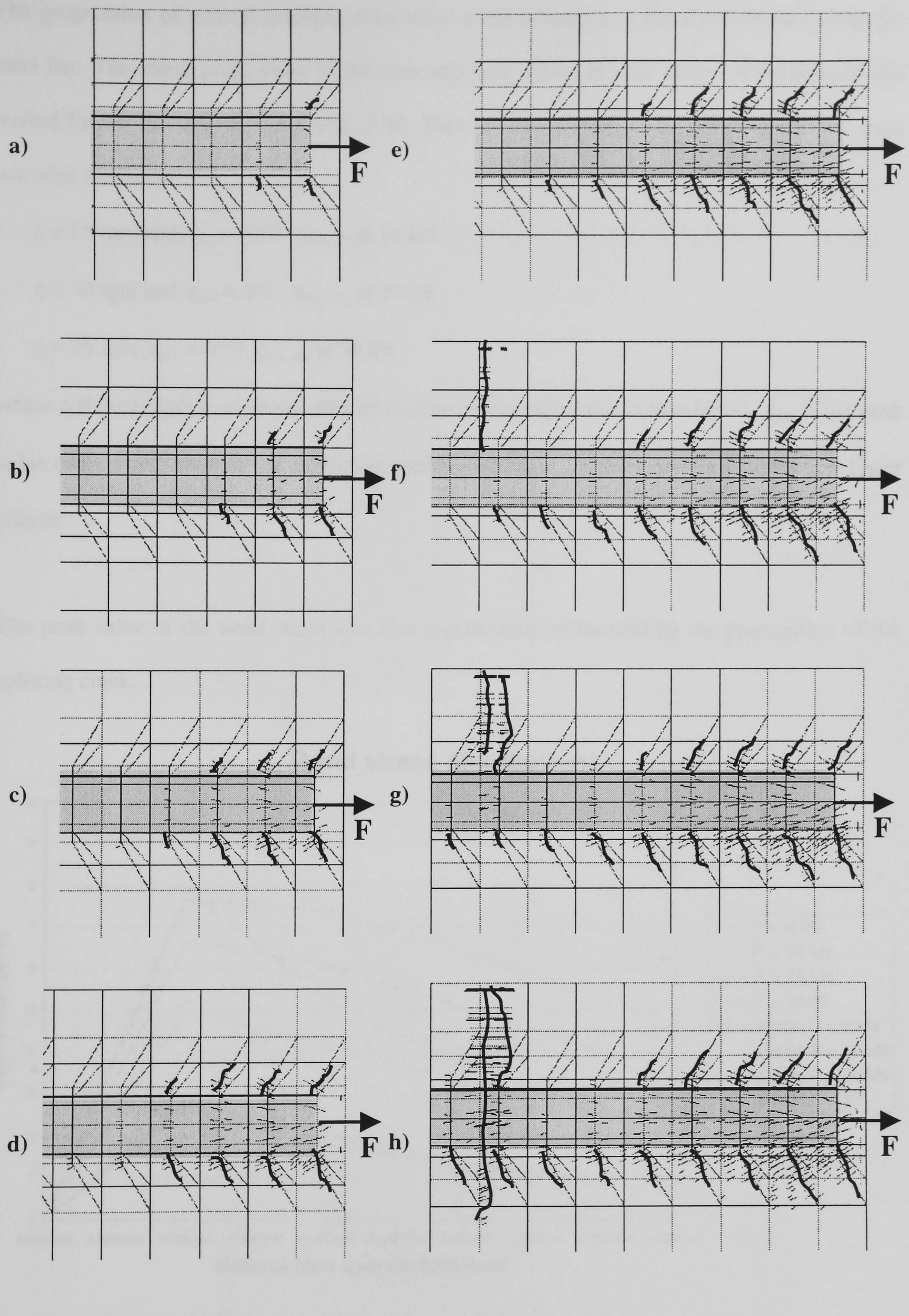

Fig. 3-18: progression of conical and secondary cracking along the bar

a)F = 12 kN, b) F = 16 kN, c) F = 20 kN, d) F = 24 kN,
e) F = 28 kN, f) F = 30 kN, g) F = 31.4 kN, h) F = 33.4 kN

The progression of conical cracking resulted in a redistribution of the bond stresses along the steel bar. The stress peak, close to the concrete face where the bar enters, was flattened and moved further into the concrete, Fig. 3-19. Thus, as the load was increased, the transfer zone was also increased:

- $t_f = 65$ mm and $\tau_{max} = 0.98\ \tau_{max,\ lin}$ at 10 kN
- $t_f = 70$ mm and $\tau_{max} = 0.91\ \tau_{max,\ lin}$ at 20 kN
- $t_f = 75$ mm $\tau_{max} = 0.75\ \tau_{max,\ lin}$ at 30 kN

where t_f if the length over which 90% of the concrete tensile force is transferred, τ_{max} is the peak value of the bond stress in the non-linear analysis and $\tau_{max,\ lin}$ is the value predicted by the linear anlysis.

The peak value of the bond stress was also significantly influenced by the propagation of the splitting crack.

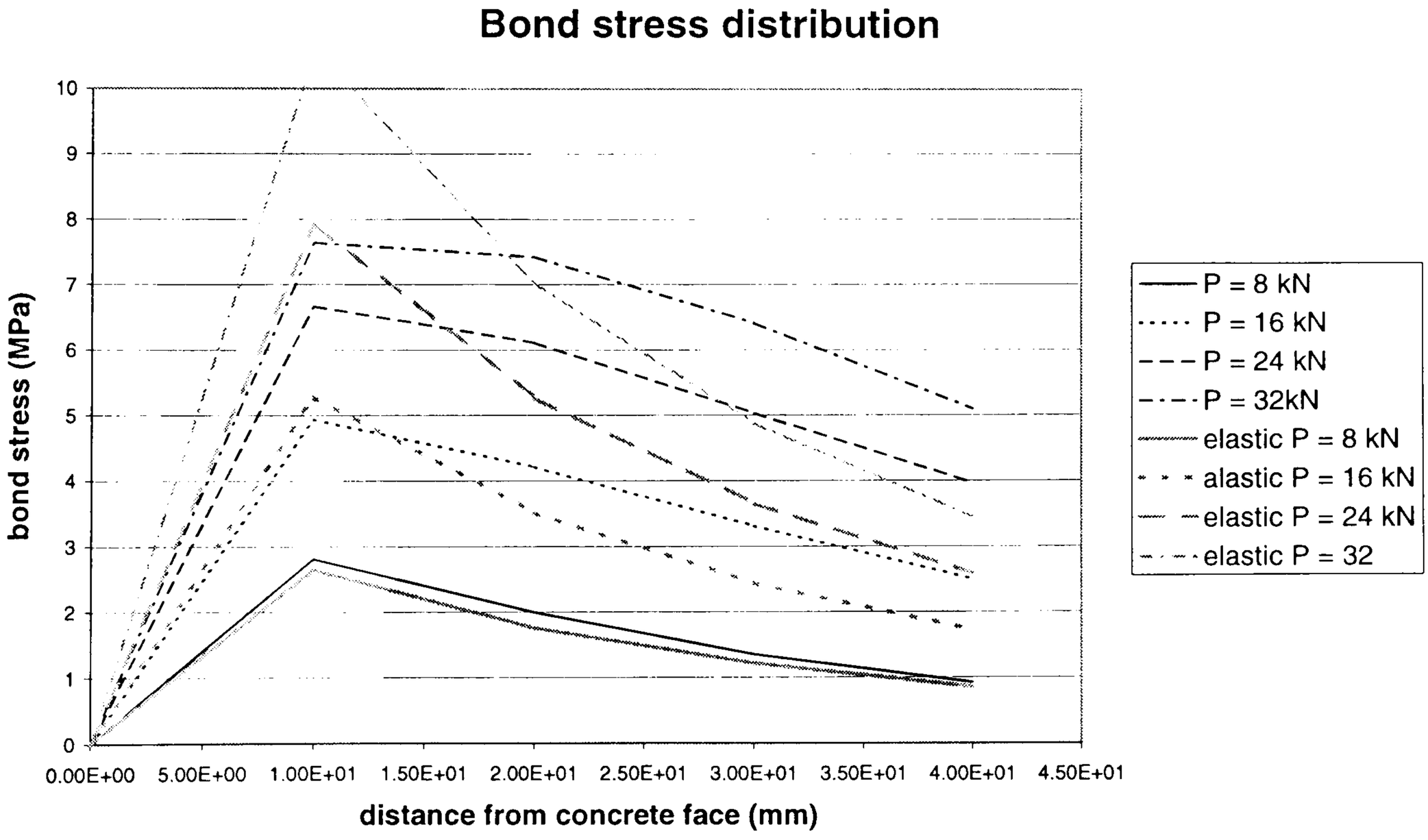

Fig. 3-19: Evolution of the bond stress distribution along the steel bar

The conical cracks transformed the bond transfer mechanism from a direct shear bond to a discrete set of compressive diagonal struts balanced by horizontal tensile stresses, i.e.

transferred longitudinal stress, and circular hoop stresses responsible for splitting, Fig. 3-20 and Fig. 3-21. The mechanism occurring in the simulation corresponded exactly to Tepfer's model. Although the interface elements simulating splitting opened satisfyingly, the interface elements between steel and concrete did not open, that is the concrete never lost longitudinal connection with the steel bar. This may be due to the normal strength chosen for these interface elements, 1 MPa. The relevance of such a normal strength will be discussed later.

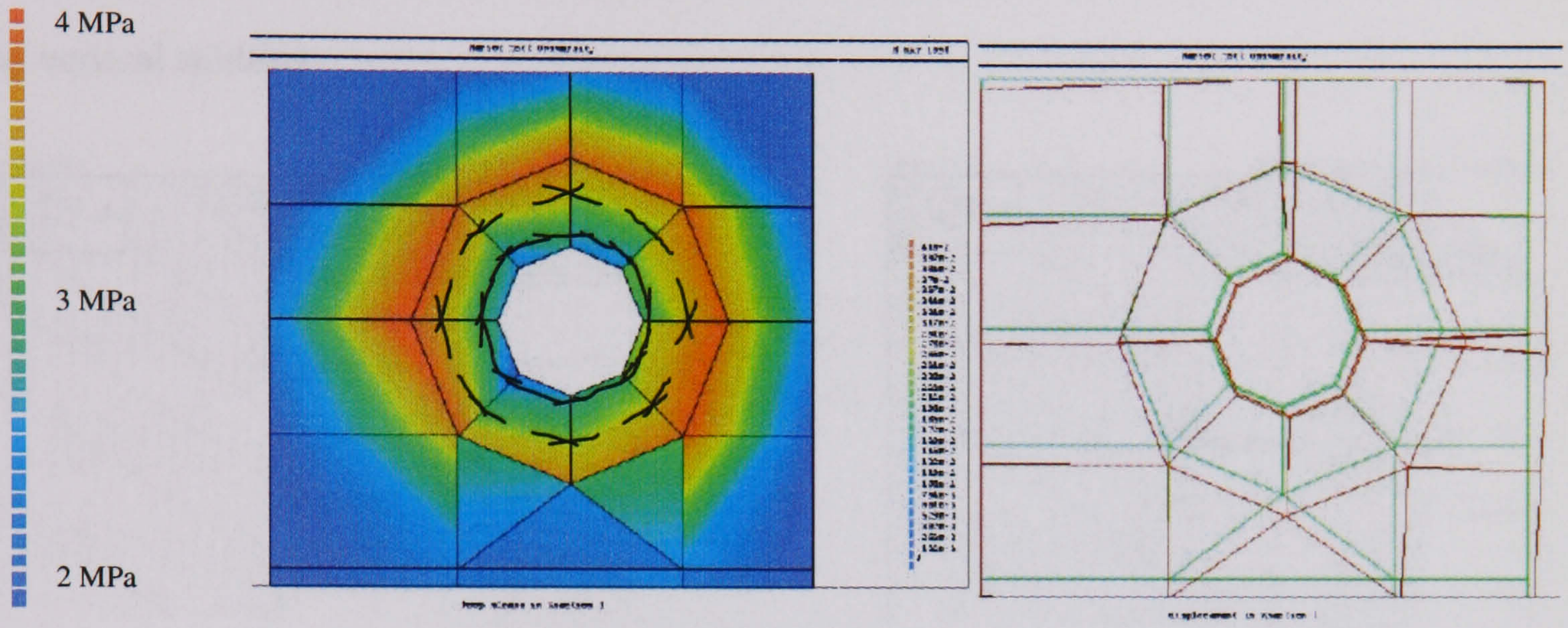

Fig. 3-20: Hoop stresses and splitting crack opening between the first and the second rib, the vectors correspond to the direction of displayed stress intensity, F = 28.5 kN

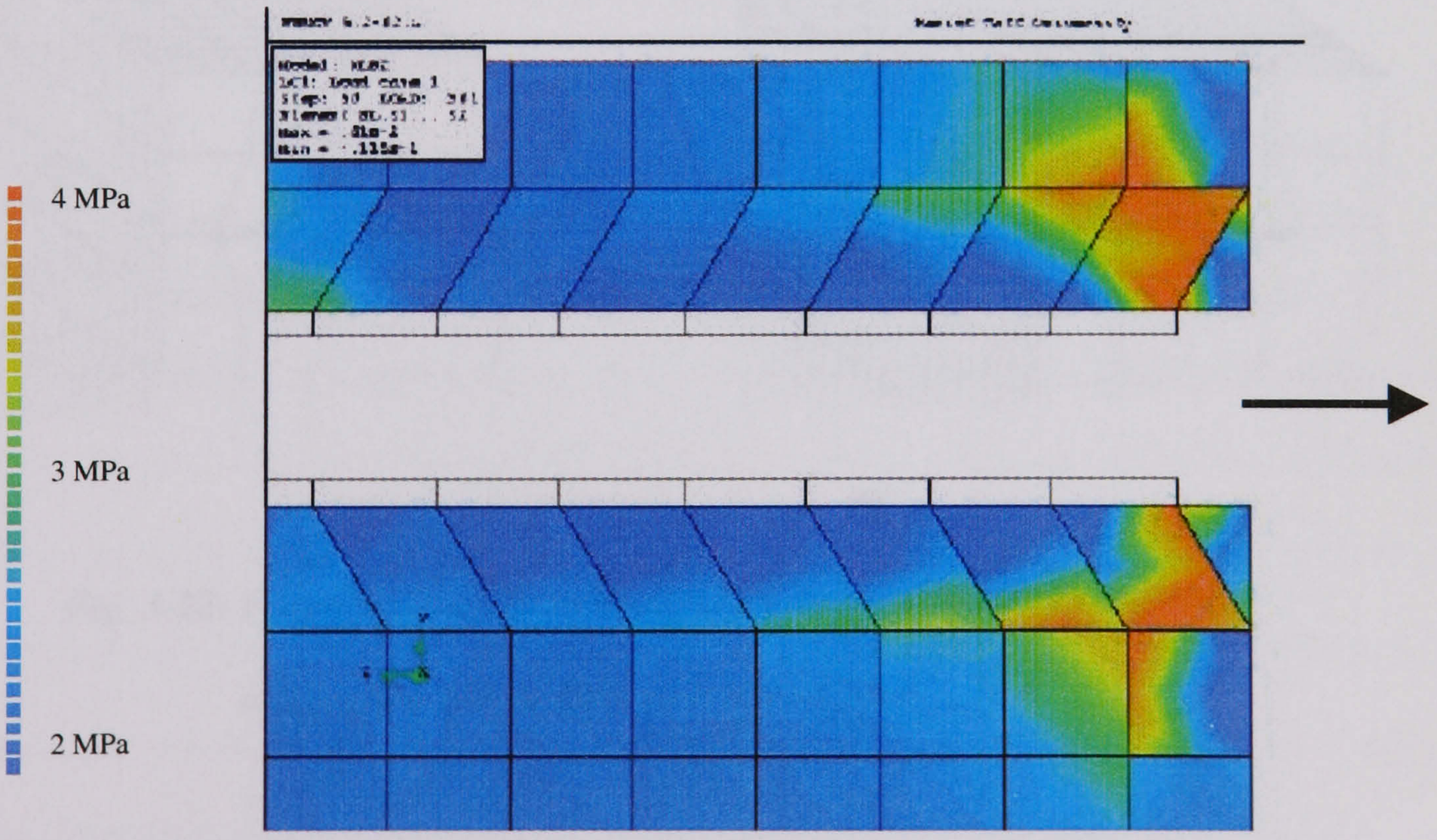

Fig. 3-21: Hoop stress distribution at F = 33.4 kN, longitudinal cut.

The conical cap in front of the first rib failed at a relatively low load (6 kN) under splitting hoop stresses due to the lack of concrete confinement. Slices of concrete between further ribs had a higher splitting capacity. The onset of splitting between the first and the second rib arised at 14 kN, i.e. 4.4 MPa of average bond stress between the two first ribs, and thorough splitting does not occur before 24 kN, i.e. 6.7 MPa of average bond stress between the two first ribs. Splitting proceeded towards the concrete surface using the shorter paths, i.e. horizontal and vertical cracking through the concrete cover, Fig. 3-22. Horizontal splitting arose first, closely followed by vertical splitting.

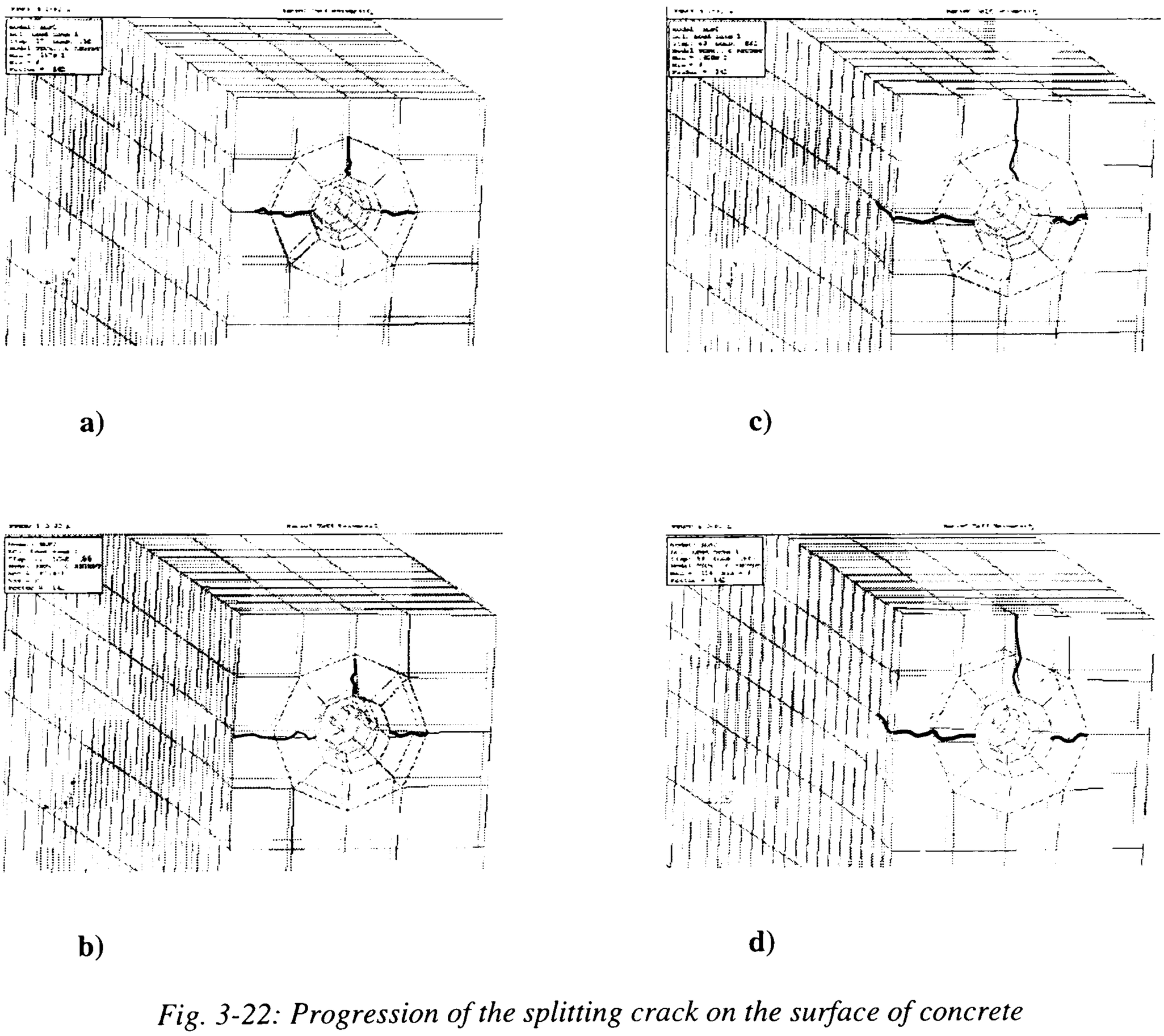

Fig. 3-22: Progression of the splitting crack on the surface of concrete

a) F =22.4, b) F = 26.4, c) F = 31.4, d) F = 33.4

The onset of secondary cracking occurred at 27.6 kN, at the eighth rib, i.e. 80 mm from specimen's extremity. Starting from the concrete surface, the secondary crack worked its way down towards the reinforcement, thus meeting conical cracking, Fig. 3-18. The crack reached

the reinforcement level at 30 kN, i.e. 150 MPa of steel stress. At 170 MPa of steel stress, the mouth opening of the secondary cracking reached approximately 8 µm.

Even after extensive conical and secondary cracking, 82 % of the force was still transferred to concrete, as in the linear analysis, Fig. 3-23. This predicts the onset of transverse cracking at 35 kN. When this value was approached, the convergence of the iterative process is lost with the opening of the transverse crack and the analysis is unable to proceed further. Several indirect displacement controls have been tried and failed. It was not possible to trace the descending branch of the transverse crack softening.

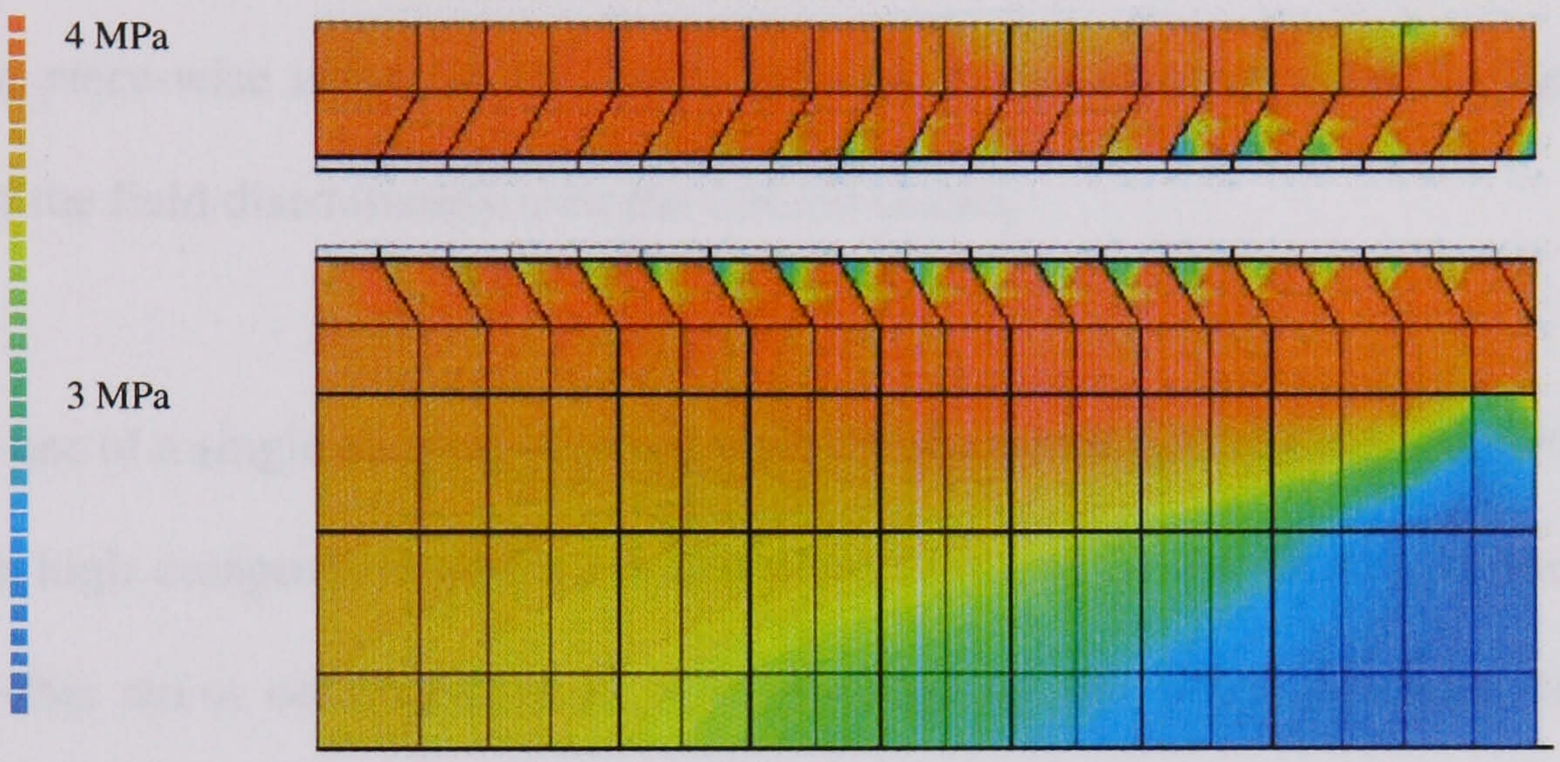

Fig. 3-23: Principal tensile stress distribution at F = 31.4 kN, longitudinal cut

Discussion and comparison with empirical models

The model produced very satisfying results for the evolution of conical cracking, the mechanism of secondary cracking and the onset of splitting. However, the steel-to-concrete connection interface failed to model adequately the sudden and complete loss of bond at splitting crack opening, which prevented the splitting crack propagating. It is believed that this spurious behaviour is due to the arbitrarily chosen normal connection strength of 1 MPa. However, this strength was intentionally introduced to avoid early instability and loss of convergence in the simulation. The solution procedure used, the Newton-Raphson iterative scheme, is designed to follow continuous non-linear phenomena. Obviously, the sudden release

of the steel bar by concrete splitting is a discontinuous dynamical phenomenon and cannot be followed statically by decreasing, appropriately, the load. Consequently, it is believed that no realistic simulation of splitting can be achieved through finite element modelling.

The level of mesh refinement, the use of higher order elements and the choice of full integration scheme insured a good overall approximation field for the stress and strain distribution. The inclined mesh around the steel bar in the form of a cone turned out to be a particularly good choice as it presented two advantages:

- reduction of the mesh bias on the cracking direction, assuming that the cracking direction is approximately known from experiments,
- use of the piece-wise nature of the finite element stress and strain fields to facilitate the modelling of the field discontinuity over the conical cracks.

However, the use of a single element between each rib is a minimum requirement. Once conical cracks open a high compressive stress concentration develops in the vicinity of the rib. It is possible that this stress concentration is ill-represented by the shape functions of a single element. Although it was first thought by several experimental investigators that bond failure could occur by local compressive failure at the ribs, it was shown later that no such failure could be observed.[43] That is the reason why no compressive failure criterion was introduced in the model, and that the inaccuracy of the assessment of the compressive stress concentration at the ribs is not considered a critical issue.

As mentioned in chapter 2, the choice of an appropriate crack band width is important. Shear locking due to zig-zag cracking and the coupling of the integration points behaviour in each element usually result in wider crack bands than the one derived from Eq. 2-75. In this analysis, however, zig-zag cracking was successfully avoided by orientating the mesh lines with the potential cracking direction and integration point coupling was limited to a minimum by using higher order elements. As a result, for the conical cracking, each physical crack was modelled

by one smeared crack in its width. Localisation is not a problem in this model as discontinuous crack initiators were introduced in lieu of the ribs to force the cracking to localise.

For secondary cracking, no crack initiator is present which resulted in a crack band of two integration points width, Fig. 3-18. This constituted an undesired effect since only one secondary crack would form in reality. However, the consequences are limited as the crack plane eventually localises in one of the two integration points in its width.

The bond-slip curves were obtained using the following method:

- Average bond stress between ribs is obtained dividing the drop of force in the steel bar with the surface area of the bar between two ribs, $\tau = \Delta F/(\pi.d_b.rs)$.
- Slip is obtained as the difference of displacements between the steel bar cross-section and the corresponding point in concrete, 10 mm away from the bar surface.
- The bond-slip behaviour is measured for points in the concrete cover (outer measures) and for points towards the bulk of concrete (inner measures), for the four first ribs.

The resulting curves are plotted and compared with the empirical bond-slip curves, Fig. 3-24. The outer measures display more or less the same trend whatever the rib, as do the inner measures. The discrepancy between the two sets may be explained by the fact that slip is plotted against average bond and not against local bond. This would mean that less bond is actually transferred to the concrete cover than towards the bulk of concrete, which is intuitively understandable as the bulk of concrete is stiffer and resists more the pulling of the bar than the concrete cover. If this is the case, it is possible that the discrepancy observed between the inner behaviour and the outer behaviour may only be due to the local variation of the bond stress around the bar. It is therefore possible that if the average bond stress were replaced by the local bond stress, all the bond-slip curves would superimpose. Consequently, although the bond slip curve is certainly dependant to some extent on the geometry of the concrete section, the diameter of the bar and the material properties, it can be concluded that for a given topology and a given set of materials, the bond-slip curve does not seem to vary along or around the steel bar.

Comparing the bond-slip curve of the simulation with the experimental curves yields a satisfying result, Fig. 3-24. The rising branch of Nilson (1968) corresponds nearly exactly with the behaviour of the inner measures. The CEB-FIP curve and Mirza and Houde curve seem far too soft compared to the simulation. An acceptable approximation is obtained if the maximum slip allowed in the CEB-FIP curve is reduced from 0.6 mm to 0.1 mm.

It should be noted that these curves reflect the effects of conical cracking only as splitting propagation is prevented in the model, due to the nature of the connection between steel and concrete. The gradual softening of the curves corresponds to the progressive extension and opening of the conical cracks.

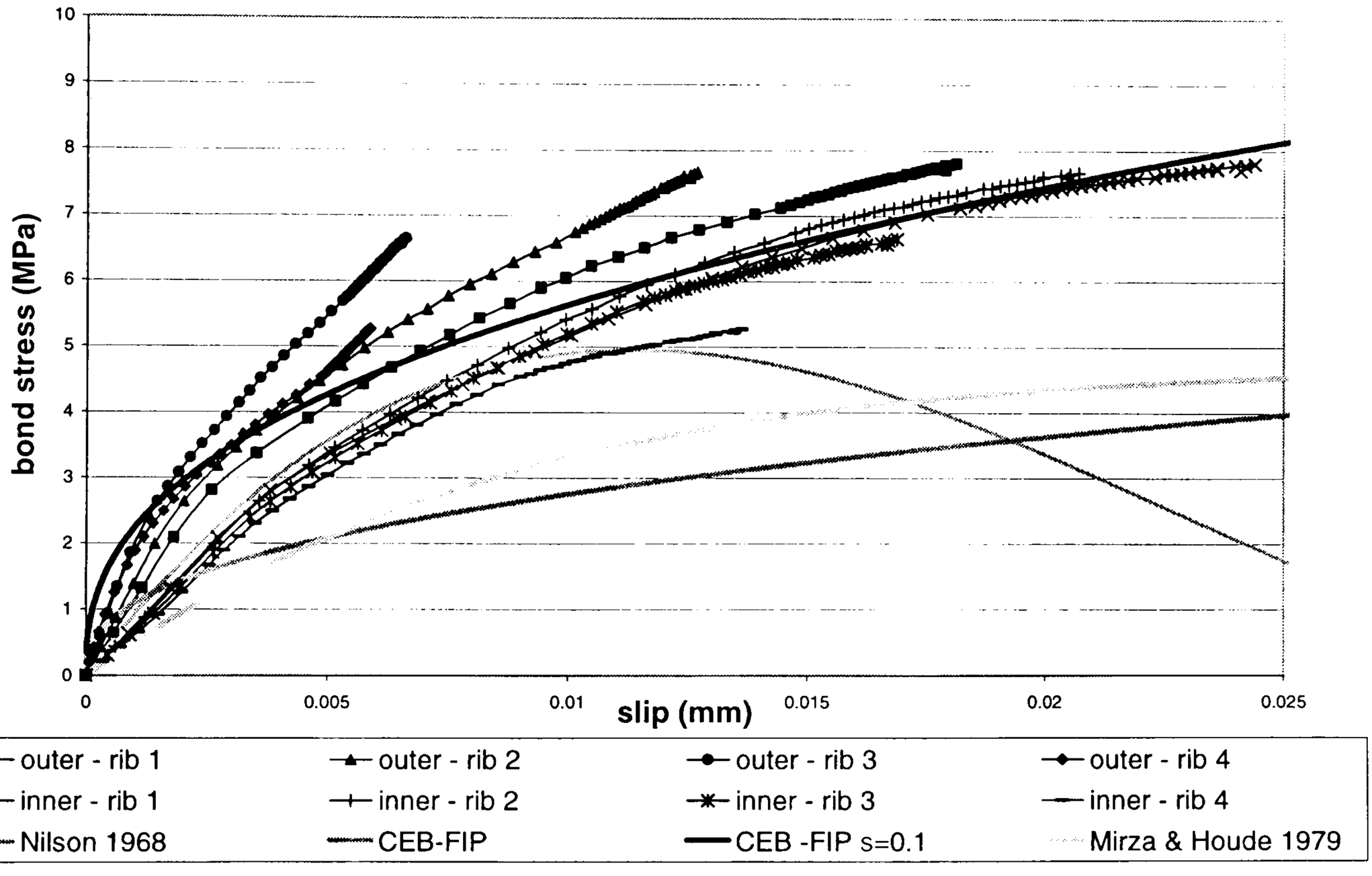

Fig. 3-24: Bond-slip law derived at rib locations, bond stress is averaged over the rib spacing

The model is unable to simulate the propagation of the splitting crack, however the onset on splitting was predicted at 14 kN, for a bond in the first rib of 4.4 MPa. This can be compared to the onset of splitting predicted by the different analytical models:

- Tepfers' partly-cracked elastic model predicts e_c = 13.6 mm, τ_{max} = 2.485 MPa, F = 7 kN,
- Tepfers' plastic model predicts τ_{max} = 5.92 MPa, F = 20 kN,
- Reinardt's NLFM model predicts e_{cx} = 20 mm, τ_{max} = 4.7 MPa, F = 15 kN,

- and Van de Veen's NLFM model predicts $e_{cx} = 23$ mm, $\tau_{max} = 4.8$ MPa, $F = 15.5$ kN.

Reinardt's and Van der Veen's models compare very well with the prediction of the finite element model. It is therefore concluded that the assumption of axi-symmetry used in these models is acceptable: for a standard rectangular section, hoop stresses develop as if the bar was encased in a cylinder of concrete with the thickness of the actual concrete cover, Fig. 3-20.

It should be noted that the numerical results show that the analytical model presented in section 3.2 for the onset of secondary cracking is irrelevant. In this model the secondary cracking was assumed to stem from the tip of a conical crack, while the finite element model predicts that the secondary crack starts at the concrete surface and then develops downwards to meet conical cracking. The analytical model will not be used in the following analyses.

The results from the finite element analysis lead to the following conclusions:

- The pattern of the simulated conical cracks confirms Goto's experimental observations.
- The stress distribution resulting from conical crack formation and the onset of the splitting crack confirm the mechanism of bond transfer postulated by Tepfers.
- The role of secondary cracking in the softening behaviour of the steel-to-concrete interface is highlighted in this analysis.
- Moreover, the onset of splitting predicted by Reinhard's or Van der Veen's NLFM models is confirmed by this simulation.
- The bond-slip curve proposed by Nilson (1968) appears to be the closer to the simulated bond-slip behaviour than those proposed by others.
- The maximum bond capacity is not determined by the local mechanics of the conical cracks, but rather by the overall fracture mechanics of the system. Therefore, a bond-slip curve with high or no maximum bond complemented by a separate splitting model is recommended.
- The inability of either the FEA or the NLFM model to predict propagation of splitting suggests that a fracture mechanics model based on the energy balance of the bar-concrete system should be considered.

3.3.2. Fracture mechanics model for bond failure by splitting

Like post-buckling analysis, the study of unstable crack evolution requires an energy approach.[104] Fracture mechanics models based on the energy balance of concrete only, like Reinhard's and Van der Veen's models, are able to predict the onset of splitting, but not the critical threshold of splitting propagation. Consideration of the fracture mechanics of the steel bar and the concrete is necessary to predict this threshold. Such a LEFM model is presented in the following.

Presentation of the model

Consider a reinforced concrete tie subjected to a tensile force at its extremity. Beyond the transfer zone, the reinforced concrete cross-section acts compositely with an overall stiffness $(A_s E_c + A_c E_c)$ where A_s and A_c are the cross-sectional areas of steel and concrete, and E_s and E_c are the elastic moduli of steel and concrete.

The propagation of a splitting crack on a length δe results in the steel bar being released for a length δe. From a structural point of view, this is equivalent to a shortening of the section of reinforced concrete by a length δe and an extension of the steel bar by a length δe. The new topology of the problem is identical locally to the previous one, as long as the specimen remains longer than the transfer length. Consequently, the splitting propagation is a critically unstable phenomenon occurring at constant load.

The distribution of bond stresses, Fig. 3-19, shows that the bond stress rapidly dies away along the bar away from the concrete surface. The splitting hoop stresses, which develop only in the presence of conical cracks, are proportional to bond stresses. Consequently, no large area of damaged concrete can exist ahead of the splitting crack, and strain softening does not play a significant role in the propagation of splitting. That is the reason why it is believed that LEFM is applicable to the problem of splitting propagation.

Assuming that stable splitting occurs before the critical threshold of splitting propagation, a splitting initiator is present in the structure. Noting that the transformation arises at constant load, it is then possible to enforced an energy balance by using Eq. 2-16.

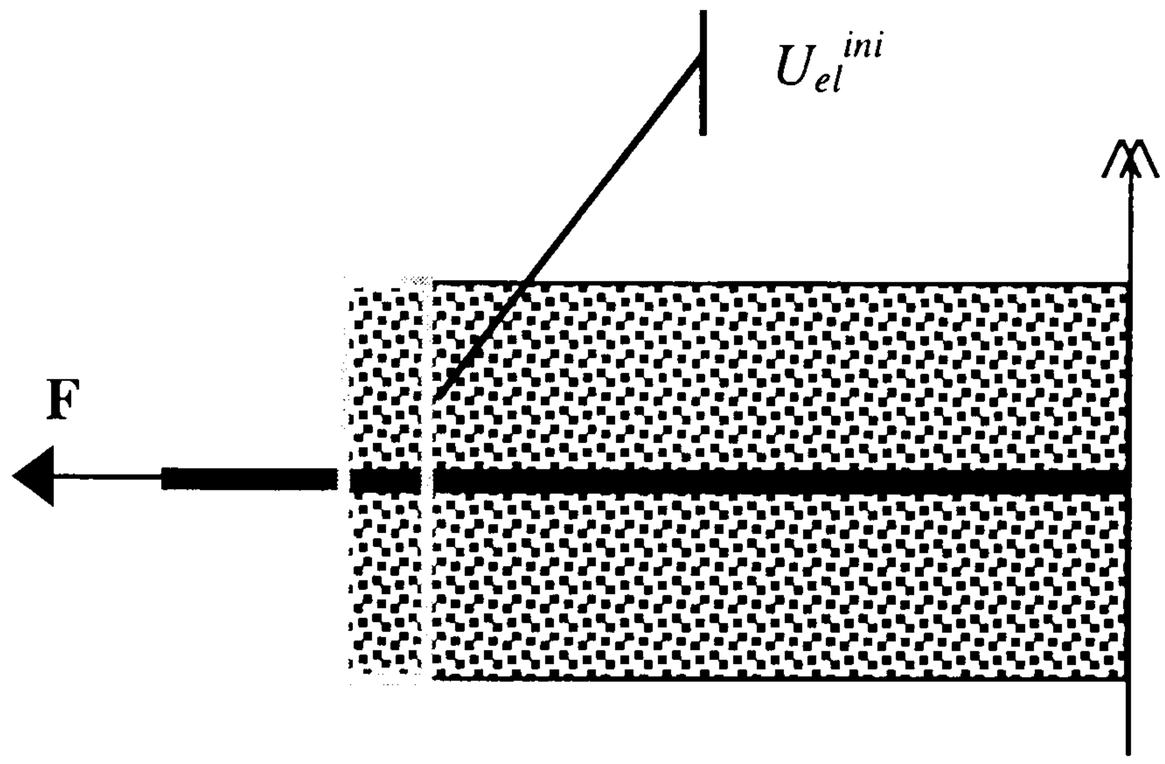

Fig. 3-25: Reinforced concrete tie before splitting

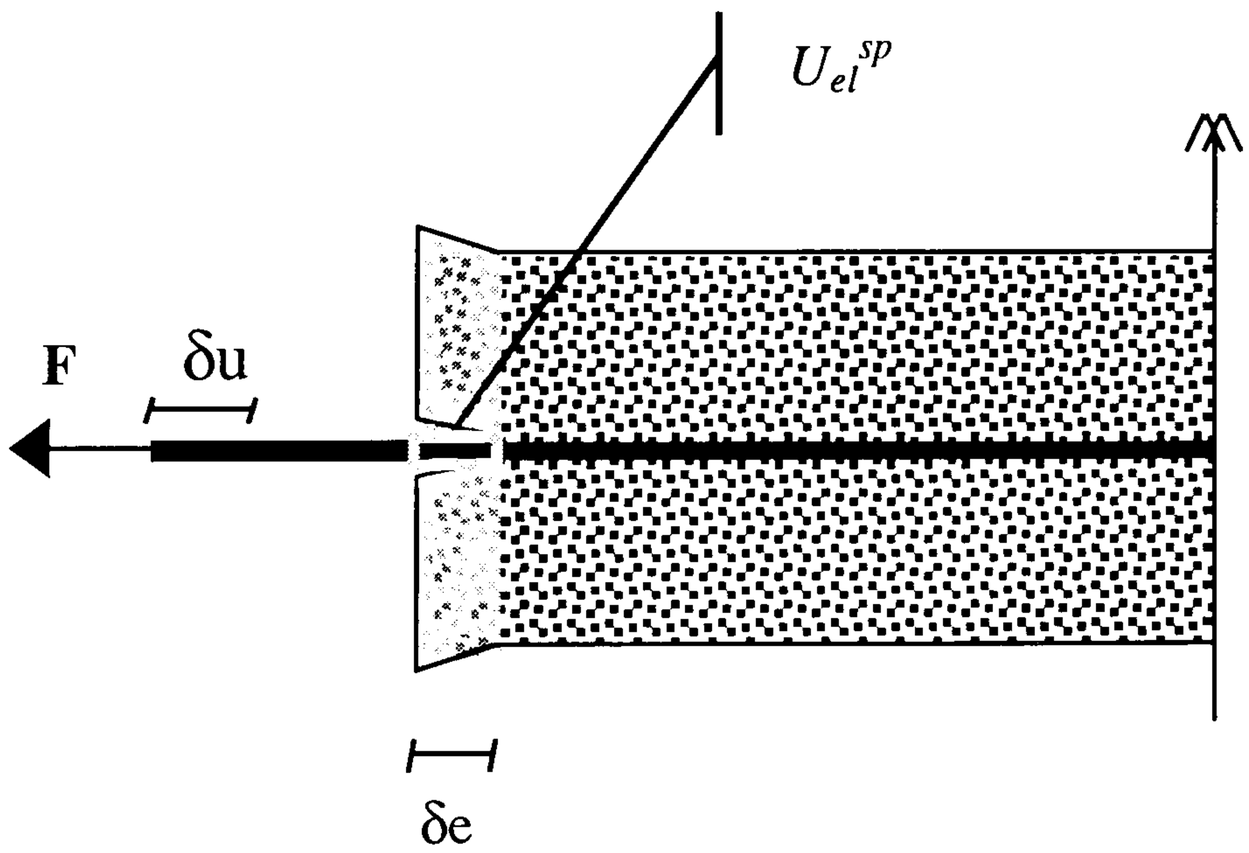

advance of splitting

Fig. 3-26: Reinforced concrete tie after splitting

The variation in strain energy is due to the shortening of the section of concrete and to the extension of the exposed steel bar, Fig. 3-25 and Fig. 3-26:

$$\delta U_{el} = U_{el}^{sp} - U_{el}^{ini} \qquad \textit{(Eq. 3-35)}$$

$$= \frac{1}{2} F^2 \left(\frac{1}{E_s A_s} - \frac{1}{E_s A_s + E_c A_c} \right) \qquad \textit{(Eq. 3-36)}$$

The work of external force on the extremity displacement δu is due to the softening of the structure:

$$\delta W_{ext} = F \cdot \delta u \qquad \textit{(Eq. 3-37)}$$

$$= F^2 \left(\frac{1}{K_{sp}} - \frac{1}{K_{ini}} \right) \delta e = F^2 \left(\frac{1}{E_s A_s} - \frac{1}{E_s A_s + E_c A_c} \right) \delta e \qquad \textit{(Eq. 3-38)}$$

It can be verified that $\delta W_{ext} = 2\, \mathrm{d}U_{el}$.

The consumption of fracture energy is proportional to the splitting crack extension:

$$\delta G = G_f b \cdot \delta e = \Gamma \cdot \delta e \qquad \textit{(Eq. 3-39)}$$

The energy balance is enforced by applying Eq. 2-16:

$$\delta G = \delta U_{el} = \tfrac{1}{2} \delta W_{ext} \qquad \textit{(Eq. 3-40)}$$

which yields the following expression for the critical load level:

$$F_{cr} = \sqrt{\frac{2\Gamma}{\frac{1}{E_s A_s} - \frac{1}{E_s A_s + E_c A_c}}} \qquad \textit{(Eq. 3-41)}$$

Application to the tension specimen

The application of the fracture mechanics model to the specimen simulated by finite element analysis is straightforward. The only contentious point is the determination of Γ. The difficulty is in determining the failure regime. Since the splitting propagation is a case of critical equilibrium, a slightly higher load will result in a dynamic failure. In this case, equilibrium is not maintained during splitting propagation and the conical cracks will not shift along with the progression of the splitting. On the contrary, in the case of a quasi-static propagation of splitting, which requires the critical splitting load to be maintained throughout the process, conical cracks will develop together with the progression of splitting. From a structural point of view, it is equivalent to a shift of the set of pre-existing conical cracks with the splitting propagation.

The consequence for the determination of Γ, recalling that the fracture energy G_f is assumed to be 80 J/m^2, is the following:

- if the failure regime is dynamic, the fracture energy consumption results only from the opening of the splitting crack, $\Gamma = 2 \times 20 \times 10^{-3} \times 80 = 3.2$ J/m,
- if the failure regime quasi-static, the energy necessary to open the conical crack must be considered besides the opening of the splitting crack, $\Gamma = [40 + \pi(18^2-8^2)/10] \times 10^{-3} \times 80$ J/m

  $\Gamma = 9.7$ J/m

This is a significant difference and more should be learn from experimental results to conclude on this point.

The other components of the Eq. 3-41 are derived easily:

$E_s A_s = 41.22$ MN

$(E_s A_s + E_c A_c) = 224.29$ MN

which yields for the critical splitting load,

in the dynamic regime: $F_{crit} = 18$ kN, $\tau_{max} = 5.4$ MPa

in the quasi-static regime: $F_{crit} = 31.4$ kN, $\tau_{max} = 9.4$ MPa

It can be checked that both the above critical loads are higher than the onset of stable splitting predicted by the analytical and the numerical models, 15 kN and 14 kN. Splitting in the dynamic regime is predicted to arise shortly after the onset of splitting, while quasi-static splitting is predicted to arise at a load nearly twice as large as the onset of splitting.

4. APPLICATION AND VERIFICATION OF THE BOND MODEL

The mechanics of bond cracking have been investigated in previous chapters. Existing empirical laws and analytical models have been checked against a refined finite element model although divergence in the analysis prevented simulation of the opening of the transverse crack. A new fracture mechanics approach, which has been developed for the propagation of splitting, was described. It is now possible to design a simpler non-linear model incorporating the different non-linear constitutive laws identified:

- non-linear bond-slip due to conical and secondary cracking along the transfer length,
- strain-softening opening of the transverse crack,
- and the fracture mechanics criterion for splitting.

The model has been developed and checked against experimental results for tension specimens, which soften by transverse cracking, by splitting or by a combination of both. The splitting model has then been applied to a structural problem, i.e. the shear failure of reinforced concrete beams without stirrups. The predictions were compared with the empirical formula proposed in the CEB-FIP model code 1990.

4.1. Model for the Simulation of the Behaviour of Tension Tests

Since a detailed finite element analysis seeking to simulate all bond related fracture processes has to be very complex and time consuming, it is believed that a better understanding of the structural

behaviour including interaction between the different cracking mechanisms can be gained by developing a simple non-linear model, for which the non-linear constitutive behaviours of each component is provided and not derived.

4.1.1. Model components

The model was formulated as a set of non-linear equations enforcing static equilibrium of the different components acting on each other and equilibrium of the structure under the external load. If splitting propagation is ignored, the model is an eight degrees-of-freedom system made up of linear springs and non-linear sliders, Fig. 4-1. The structure of the system was based on the different cross-sectional behaviours identified in the conclusions of section 3.1. By using symmetry, only half of the total length of the specimen had to be modelled.

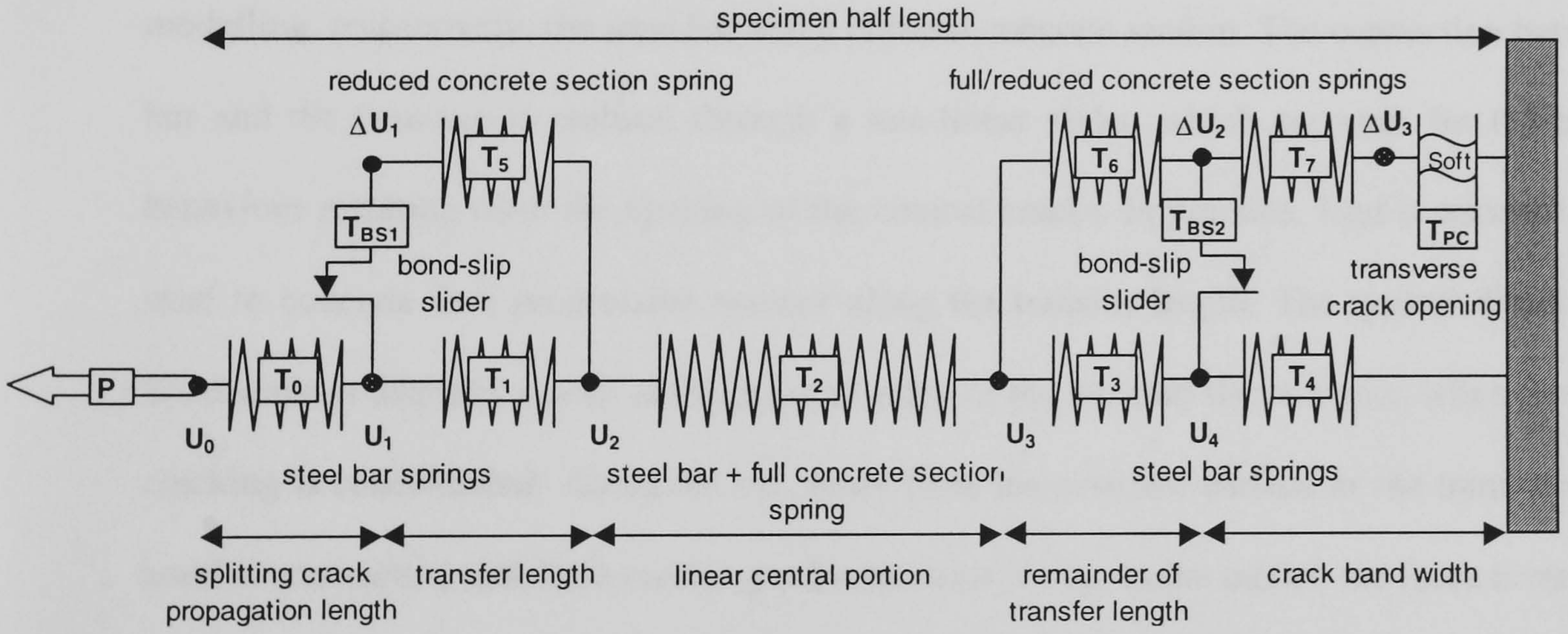

Fig. 4-1: 8 DOF , springs and sliders system

Breakdown of the model

The physical meaning of each spring and slider is detailed in the following, Fig. 4-2. The specimen was divided in portions along its length. Each portion comprises components modelling the steel bar and components modelling the concrete.

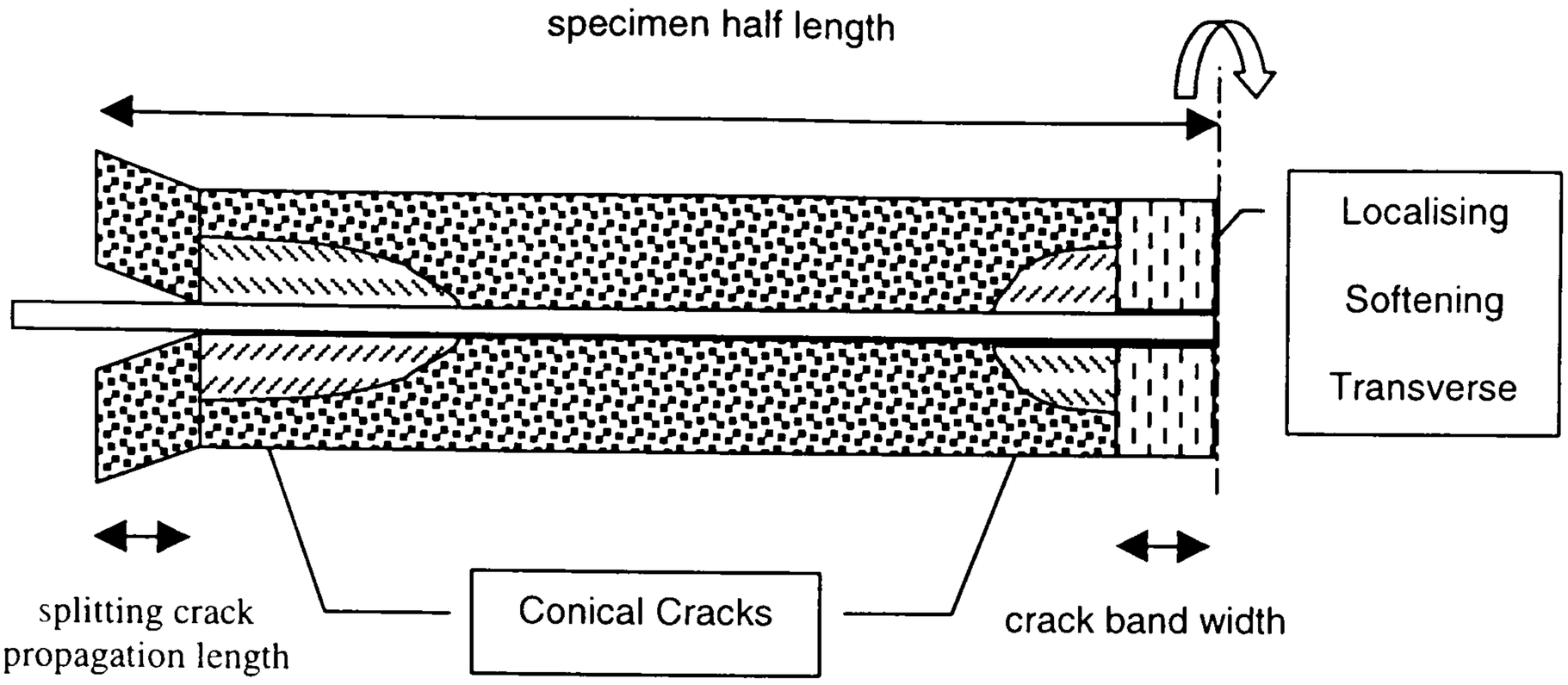

Fig. 4-2: Physical meaning of the 8 DOF system

The first portion, which models the splitting crack propagation length, consists of a linear spring with the stiffness of the reinforcing bar only.

The second portion models the transfer length. It is made up of two linear springs in parallel, modelling, respectively, the steel bar and a reduced concrete section. The connection between the bar and the concrete is realised through a non-linear slider, which accounts for the bond-slip behaviour resulting from the opening of the conical cracks. In practice, load is transmitted from steel to concrete in a progressive manner along the transfer length. The typical distribution of bond stresses displays a peak at the point of entry of the bar into the concrete, where the conical cracking is concentrated. Along the bar, away from the concrete surface or the transverse crack, bond is transmitted with little cracking at lower stress levels. In the model, the force is transmitted to the concrete discretely through a slider, which amounts to replacing the stress distribution curve by a constant mean stress. In order to reduce levelling off of the peak stress, only half of the transfer length is modelled by the bond-slip slider. The rest of the bond force, which is assessed to be approximately 30% of the total bond force in the linear range, is transmitted to the concrete by a rigid link.

The third portion comprises a single linear spring, modelling the composite section.

The fourth portion is designed so that its response is similar to the third portion until the transverse crack opens. Then, from the onset of transverse cracking up to the ultimate transverse crack opening, its response becomes progressively similar to the first transfer length. This corresponds to the set of conical cracks appearing at the face of the newly formed transverse crack.

The last portion models the cross-section where the transverse crack occurs. In addition to the steel and concrete springs in parallel, it comprises a non-linear slider modelling the softening behaviour of a crack opening in concrete.

Components definition

The stiffness of each linear spring was determined from the modulus of elasticity of steel or concrete. For concrete, the formula from the CEB-FIP Model Code 90[5], given in (Eq. 3-34), has been used.

The average length between adjacent transverse crack, L_{max}, was calculated using the empirical rule in the CEB-FIP Model Code 90, given in (Eq. 3-8). As explained above, the modelled transfer zone was taken as a quarter of L_{max} :

$$t_f = \frac{L_{\max}}{4} = \frac{d_b}{14.4\rho_s} \qquad \textit{(Eq. 4-1)}$$

The bond-slip law used for the non-linear sliders is the empirical formula from the CEB-FIP Model Code 90, given in (Eq. 3-12), where the nominal slip 0.6 mm was replaced by 0.1 mm, in agreement with the results of the finite element model, section 3.3.1. Using a single-degree-of-freedom bond-slip slider amounts to considering a constant bond stress along the transfer length. Therefore the bond force was obtained by multiplying the bond stress by the surface area of the reinforcing bar in the modelled transfer length.

The concept of a crack band was used to smear the opening of the transverse crack over the length of the fifth portion of the model. The width of this crack band was progressively reduced as the crack opened. In this way, crack localisation was simulated. A linear relation between the crack band width and the crack opening was adopted. An a priori initial width of 50 mm was chosen.

The strain softening law adopted for the opening of the transverse crack is the exponential law proposed by Hordijk et al.[22] , given in (Eq. 2-47).

G_f is the specific fracture energy of concrete determined from the empirical formula from the CEB-FIP Model Code 90, given in (Eq. 2-39) and (Eq. 2-40).

4.1.2. Static equilibrium of Forces

Each constitutive equation provides a relation between forces and displacements. The model was then formulated in term of equilibrium of forces, where the real unknowns were the displacements at the extremities of the components.

The eight degrees of freedom of the system, i.e. the eight nodal displacements, are governed by the following static equilibrium equations, Fig. 4-1:

$$\begin{cases} T_0 - F = 0 & \textit{(Eq. 4-2)} \\ T_1 + T_5 - F = 0 & \textit{(Eq. 4-3)} \\ T_2 - F = 0 & \textit{(Eq. 4-4)} \\ T_3 + T_6 - F = 0 & \textit{(Eq. 4-5)} \\ T_4 + T_7 - F = 0 & \textit{(Eq. 4-6)} \\ T_5 - T_{BS1} = 0 & \textit{(Eq. 4-7)} \\ T_3 + T_{BS2} - T_4 = 0 & \textit{(Eq. 4-8)} \\ T_7 - T_{PC} = 0 & \textit{(Eq. 4-9)} \end{cases}$$

where F is the applied load, T_0 is the force carried by the steel bar protruding from concrete, T_2 is

the force carried by the central part of the reinforced concrete tie, T_1 and T_3 are the forces carried by the steel bar in the transfer zones, T_5 and T_6 are the forces carried by the concrete in the transfer zones, T_4 and $T_7 = T_{PC}$ are the forces carried respectively by the steel bar and by the concrete in the transverse crack band, and T_{BS1} and T_{BS2} are the bond forces transferred from steel to concrete.

4.1.3. Fracture mechanics model for splitting

For this simulation, a model for splitting propagation similar to the one presented in section 3.3.2 was proposed. However, considering that a numerical analysis rather than an analytical model was to be used, a more general approach was adopted. The criterion for splitting propagation was derived from the fundamental principal of LEFM, (Eq. 2-4): $R = G_f$. For numerical convenience, the partial derivative present in the definition of R was replaced by an incremental formulation.

Test for the onset of splitting

In the model, the possible onset of splitting, $R = G_f$, was tested as follows. At a given load level, a small splitting crack extent, de, was introduced, and the corresponding variation of the potential energy, $d\Pi$, was calculated. Splitting was allowed to occur if:

$$d\Pi > dG \qquad \textit{(Eq. 4-10)}$$

where $dG = \Gamma de$ is the fracture energy consumed, with Γ the fracture energy consumed per unit length of splitting crack extent. $d\Pi$ is deduced from a system similar to (Eq. 4-2) to (Eq. 4-9) where the total forces are replaced by increments of force. In order to check equilibrium following the introduction of the crack, the system was linearised using the tangent stiffness of the structure at the load level considered. This system introduced eight additional linear equations, along with eight unknowns, i.e. the small variations of the displacements caused by de.

Incremental energy equation for splitting propagation

A further degree of freedom was introduced to account for the actual splitting crack length, e, which corresponded to the length of the first portion of the model. The splitting crack was allowed to propagate only if (Eq. 4-10) was satisfied. The incremental increase in the splitting crack length, Δe, was calculated using the energy conservation principle:

$$\Delta\Pi + \Delta G = 0 \qquad \textit{(Eq. 4-11)}$$

with the fracture energy increment $\Delta G = \Gamma \Delta e$

and the total energy increment $\Delta\Pi = \Delta U_{el} - \Delta W_{ext}$

where ΔU_{el} is the sum of the increments of the elastic energy stored in the springs and ΔW_{ext} is the work done by the external load, F, due to the end displacement.

(Eq. 4-11) constituted the seventeenth equation of the non-linear system.

When assessing the fracture energy, Γ, required, per unit length, for the splitting crack to propagate, two cases had to be distinguished. Either the crack propagates dynamically, or the process occurs quasi-statically. In the first case, the fracture energy necessary to open the splitting crack only is required. In the second case, development of the conical cracks resulting from a shift of the bond transfer zone must be considered in the calculation of Γ. This type of cracking cannot generally be neglected as it absorbs a significant amount of energy. Assessing its value was however difficult as the exact area of conical cracking was not known and no experimental data were available. An approximate assessment has been achieved assuming conical cracks radiating 20 mm from the reinforcing bar surface.

In the following simulations, the fracture processes were assumed to take place quasi-statically, satisfying the equilibrium equations at all time. Consequently, conical cracking was included in the derivation of Γ.

In a typical simulation, splitting commenced with a stable progression phase before reaching the instability threshold given in (Eq. 2-12). At this level, splitting occurred at constant load. This load level could not be exceeded since the second variation of the energy release rate became positive beyond this point.

4.1.4. Continuation and bifurcation analysis

Due to the discontinuous nature of cracking mechanisms and to the bifurcation nature of the stability problem, strongly discontinuous non-linearities were to be expected. Therefore robust continuation methods and post-bifurcation numerical techniques were required.

The proposed numerical model reduces to the solution of a system of non-linear algebraic equations. The continuation and bifurcation software, AUTO,[72] offers the numerical tools necessary to carry out such analyses. The source code was modified to extend the capabilities of AUTO so that history dependency and incremental solution of equations could be implemented.

As advocated in section 2.4.4, full bifurcation analysis techniques are desirable to tackle highly non-linear phenomena in a completely general way. The regular Newton-Raphson iteration scheme was adopted along with the bifurcation point detection technique and the branch-switching algorithm presented in section 2.4.3. This solution method resulted in an entirely automated simulation with tracing of all possible branches. The choice of the relevant bifurcated branch was left to the analyst. For that purpose, Bažant's thermodynamics criterion was used. Since the structure was subjected to a single external load only, this criterion reduced to choosing the branch with either the smallest rising slope, the steepest softening slope, or the most dramatic snap back.

4.2. Benchmarking of the Model against Experimental Data

In order to benchmark the numerical model, experimental tests carried out by Mitchell and Abrishami[89] (1996) have been simulated. These tests had a wide variation of the parameters and suitable data was provided to carry out the analysis.

4.2.1. Description of Mitchell and Abrishami's tests

In the tests, prismatic specimens were axially loaded by applying tension forces directly to the steel bar protruding from the concrete encasement. The total elongation of the reinforced concrete specimen was measured by two LVDTs, clamped to the steel reinforcing bar just outside the concrete. The applied load versus the average member elongation was plotted and a precise cracking history was provided for each specimen.

All the specimens had a length of 1500 mm. Two different concrete strengths were used: a normal strength concrete, UC (with f_c = 34.9 MPa and $f_t = 0.9f_{sp}$ = 2.79 MPa) and a high strength concrete, HUC (with f_c = 90 MPa and $f_t = 0.9f_{sp}$ = 5.67 MPa). An average free shrinkage strain of about $-0.3\text{x}10^{-3}$ was measured. Four steel bar diameters were used, along with four corresponding concrete cross-sections. Table 1 presents the details of the ten specimens tested.

Table 4-1: Details of the pulled specimens (adapted from Mitchell and Abrishami)

Specimen	Rectangular cross-section b x H (mm)	Bar diameter d_b (mm)	Steel yielding stress f_y (MPa)	Type of crack *	$\frac{F_{sp}}{A_s f_y}$ **	Average transverse crack spacing s_a (mm)	Maximum transverse crack spacing s_{max} (mm)
UC-10	90 x 90	11.3	420	T	–	167	200
UC-15	95 x 170	16	490	T-S	1.00	214	295
UC-20	100 x 245	19.5	440	T-S	0.37	375	430
UC-25	105 x 387	25.2	440	S	0.22	–	–
UC-30	110 x 515	29.9	530	S	0.19	–	–
HUC-10	90 x 90	11.3	420	T	–	167	300
HUC-15	95 x 170	16	490	T-S	0.42	500	750
HUC-20	100 x 245	19.5	440	S	0.36	–	–
HUC-25	105 x 387	25.2	440	S	0.26	–	–
HUC-30	110 x 515	29.9	530	S	0.18	–	–

*Note : T = transverse crack; S = splitting crack

**Note : F_{sp} = applied load at onset of visible splitting crack

$A_s f_y$ = force in reinforcing bar while yielding

4.2.2. Simulation of the tests

The ability of the computer code AUTO to identify bifurcations and the continuation facilities are sophisticated enough to find, easily, the converged path. A small load step was initially specified, AUTO was then able to carry out the simulation without any external intervention. Small load steps were also chosen to reduce the order of the numerical approximations as much as possible. This was particularly important when tracing the post-bifurcation branches. A typical simulation required several thousands steps.

The simulation produced the history of the displacements versus the applied load, the evolution of the splitting crack and the opening of the transverse crack. In order to compare the predicted

response with the experimental data, the extremity displacement versus the applied load has been plotted, Fig. 4-3, for the ten specimens.

As discussed in section 4.1.3, the assessment of the conical cracking contribution to the fracture energy consumption is only approximate and some tuning is necessary. In these simulations, the assessed conical crack area was multiplied by a tuning factor of 1.5 to fit the splitting failure of HUC-15. This factor was then kept equal to 1.5 for all the other specimens.

Shrinkage has an effect on the tensile response of the specimens. Radial shrinkage could be responsible for a decrease in the load of first conical and splitting cracking, but has no effect on the onset of unstable splitting crack propagation and will be ignored. The effect of longitudinal shrinkage has been taken into account in the following way. It was assumed that the restraint provided by the steel bar was small enough for the shrinkage of the specimen to be equal to the free shrinkage (-0.3×10^{-3}). Thus, in the unloaded shrunk specimen, the stress of the reinforcing bar was assumed to vary along the bond transfer length from zero outside the concrete, to the compressive stress corresponding to a strain of -0.3×10^{-3}. The concrete was subjected to the tensile forces that were required to balance the compressive force in the bar. Because the steel bar was assumed to behave linearly, it was noted that the previously described state of stress is equivalent to applying a pull-out force which would result in the same stress drop in the steel to the one caused by shrinkage. Consequently, simulation has been carried out without adding initial stresses, but the origin of the axes has been shifted to the point of the curve for which the stress drop in question was obtained in the reinforcing bar.

Softening could be due to transverse cracking, splitting or both simultaneously, termed mixed-mode. The mode observed experimentally is indicated on each graph. The visually observed onset of splitting has been indicated by a dot on the experimental curves.

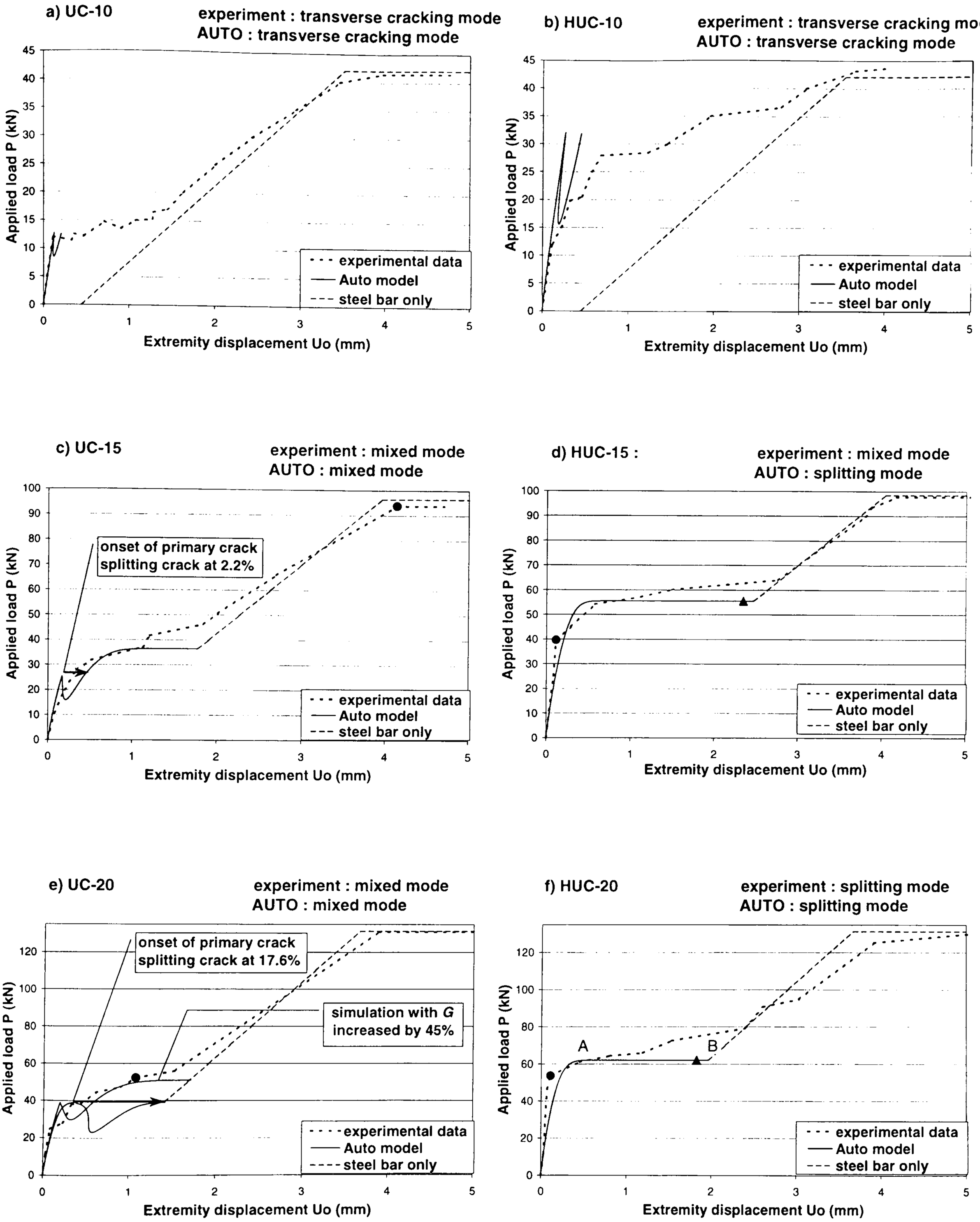

Fig. 4-3: Comparison of test results and predicted response

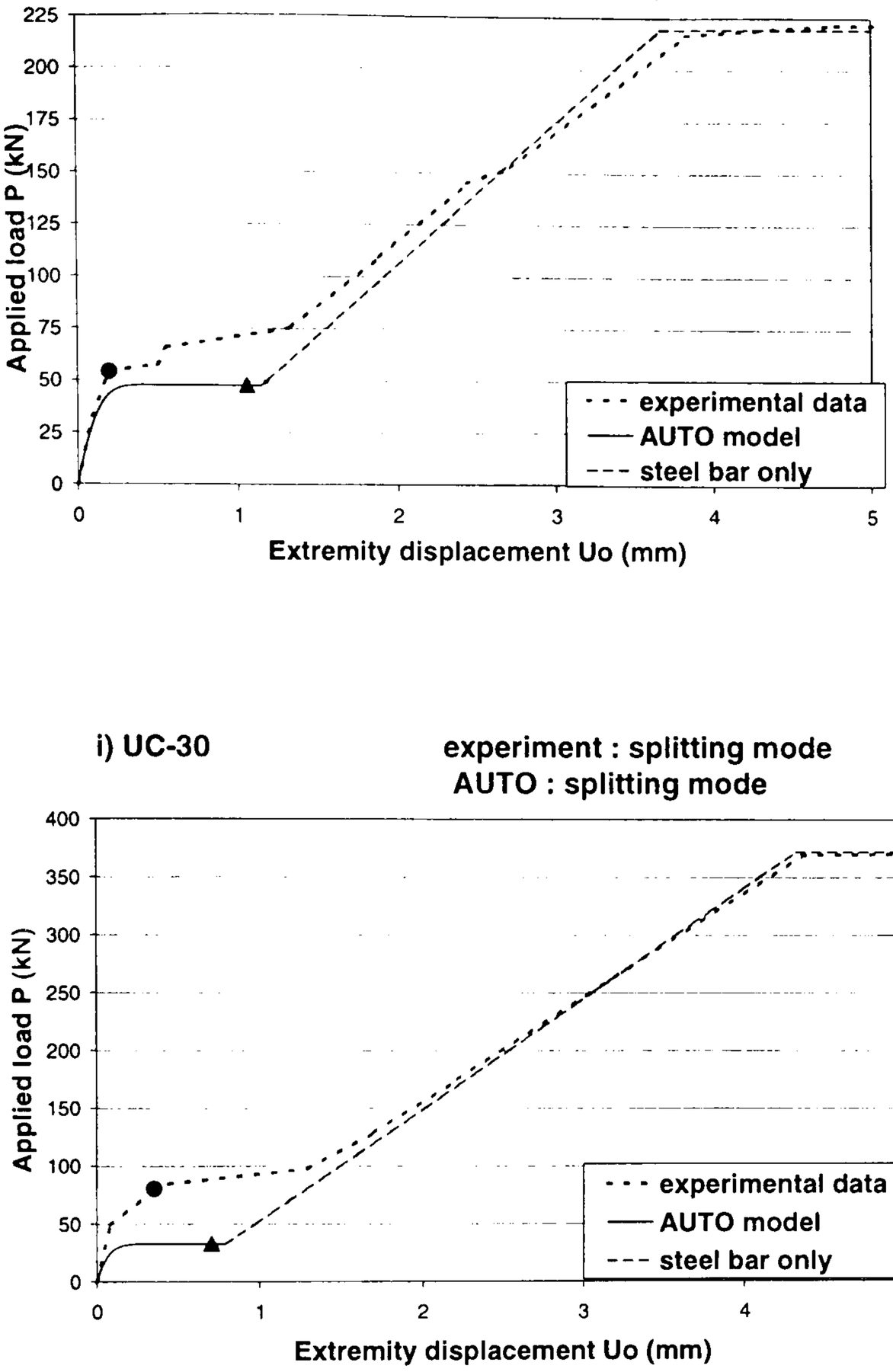

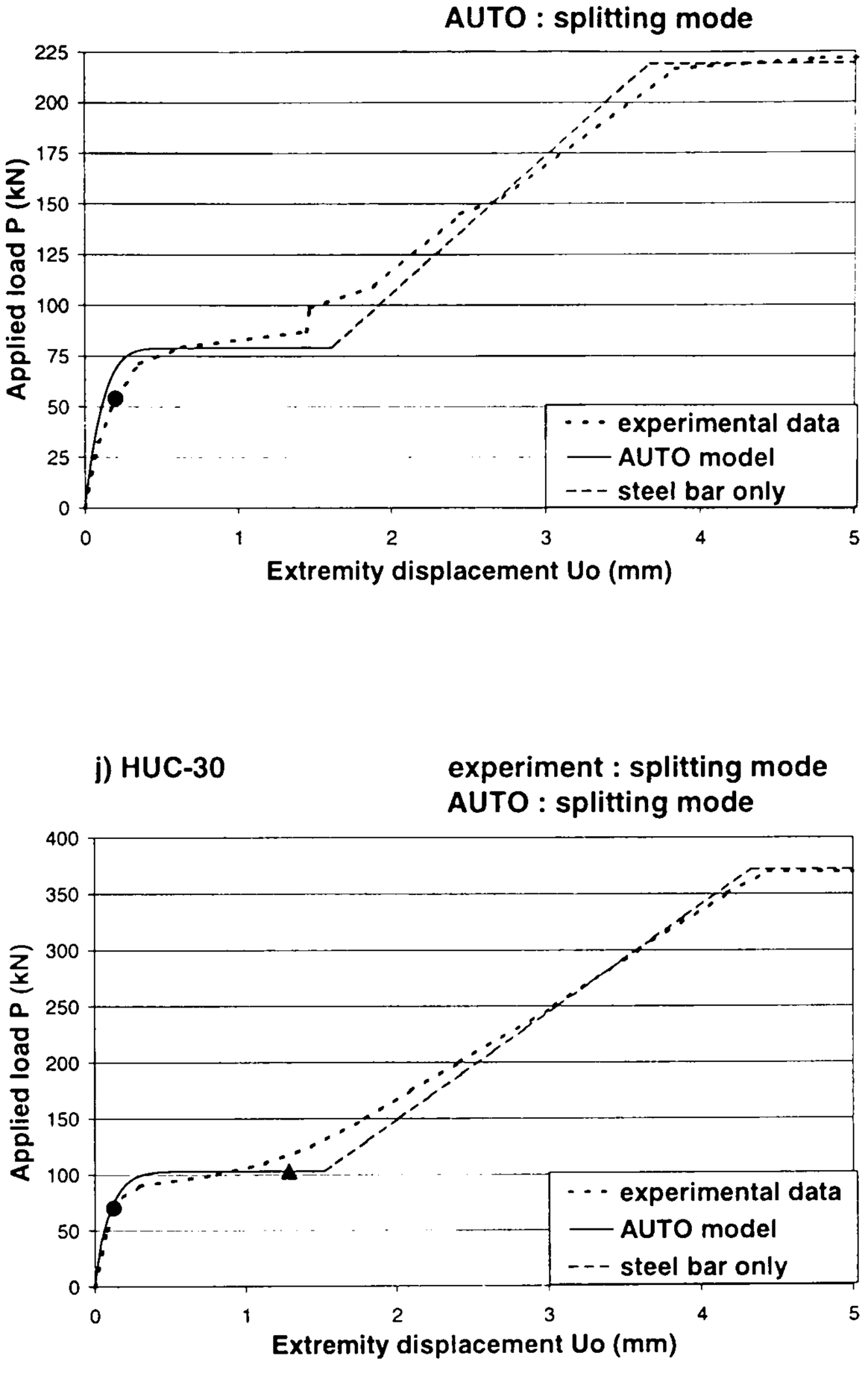

Fig. 4-3: Comparison of test results and predicted response (continued)

The present model is limited to the prediction of three transverse cracks (this is due to the limited number of degrees of freedom used, and could be easily extended). Therefore, for the specimens in which transverse cracking mode dominated, the simulation was stopped at an early stage, at the beginning of softening. When splitting occurred, the behaviour could be traced up to the total loss of bond between steel and concrete throughout the entire length of the specimen. Once full splitting was achieved, the behaviour was the response of the reinforcing bar alone.

When transverse cracking occurred after splitting had begun, the extent of the splitting crack is given as a percentage of the total length. At these points, horizontal arrows have been drawn to mark the possibility of "snap-through" for a test realised under load-control, Fig. 4-3 (c) and (e).

This is due to the fact that, while the simulation followed the static path of the system, the actual experimental response may have jumped dynamically over the "valleys" of the predicted path.

4.2.3. Discussion

The plots, Fig. 4-3, comprise the following, the experimental data obtained from the paper by Mitchell and Abrishami,[89] the response of the steel bar only deduced from the steel bar properties, and the numerical prediction. It can be seen from the plots of the results that the proposed numerical model is able to accurately predict the load-deflection response up to the onset of cracking and to a varying degree beyond first cracking.

In tests UC-10 and HUC-10, Fig. 4-3 (a) and (b), the failure occurred due to the yielding of the reinforcement, following the development of a number of transverse cracks. As explained previously, the current model allows for the development of only three transverse cracks in the specimen length. It can be seen that the prediction of the onset of transverse cracking compares favourably with the experimental results for UC-10, however, the prediction for HUC-10 is not so good.

In the splitting mode failures, the onset of splitting is accompanied by a development of the crack at constant load, e.g. A-B, Fig. 4-3 (f). The numerical predictions beyond point B have been ignored because, at this stage, the load would be carried by the reinforcement alone. In fact, in some cases, the numerical model predicts that the zone between the transfer zones has zero length just prior to reaching B. The point at which this occurs is shown by a triangle on the splitting plateau. The discrepancies between the predictions and the experimental results at, for example, point B are considered to be due to the simplified modelling of the transfer zones. In the model, the zones are shorter than in the specimen and therefore the interaction between the zones, when they begin to overlap each other is postponed in the model.

The average value of longitudinal shrinkage was used in all the analyses because no detail of its variation was given in the experimental data. This may explain the discrepancy between the computed load and the experimental load at onset of splitting for specimen UC-30, Fig. 4-3 (i). In all the other tests in which splitting occurred, Fig. 4-3 (f) to (h) and (j), it can be seen that the model predicted the load-displacement, the mode of behaviour, and the onset of cracking accurately.

In the analysis of the mixed mode failures, specimens UC-15 and UC-20, the splitting crack appeared first and propagated some way along the specimen before a transverse crack formed. In the case of UC-15, it had propagated along 2.2% of the length of the specimen, before the transverse crack formed. The splitting crack continued to form with increasing load until it reached a stage at which it propagated under constant load. When the crack was fully formed, the load was carried by the reinforcement. In the case of HUC-15, Mitchell et al. stated that it was a mixed mode failure even though the splitting crack appeared at a relatively low load and displacement. The analysis predicted a splitting failure. It should be noted that the longitudinal tensile stress in the concrete during the splitting failure is approximately 80% of the concrete tensile strength, so it is possible that transverse cracks would appear in a physical test.

In conclusion, the proposed model proved to be successful, especially the adoption of the LEFM criterion for splitting propagation. Consequently, the analytical formula derived from the similar approach, presented in section 3.3.2, can be used further in structural models with a good level of reliability. The only point to remain unclear is the assessment of the fracture energy consumed by conical cracking. More experimental data are needed to determine the parameters influencing its variation.

4.3. Shear Failure of Reinforced Concrete Beams without Stirrups

Confidence has been gained in the fracture mechanics model for splitting propagation. It is now possible to apply the model to a structural problem for which failure is triggered by splitting. The flexural shear failure of slender beams has been modelled analytically by many authors with little success. In each case, an erroneous failure mechanism was assumed. Starting from the phenomena observed experimentally, a fracture mechanics model is designed where failure is triggered by splitting. The model is checked against an empirical formula.

4.3.1. Phenomenological approach

Leonhardt and Walther (1962)[105] have shown that, if the reinforcement ratio, ρ, is kept constant, the mode of failure of rectangular reinforced concrete beams without stirrups depends on the shear span-to-depth ratio, a_s/d. For a reinforcement ratio of 1.88%, shear failure is more critical than flexural failure for shear span-to-depth ratios between 1 and 7. Two types of shear failures have been identified:

- web shear failure for $a_s/d < 2.5$, characterised by a compression failure under the application point of the load after diagonal shear cracks have appeared in the web,

- flexural shear failure for $a_s/d > 2.5$, characterised by flexural cracks extending into diagonal shear cracks, ultimately developing through the concrete compression zone, which results in failure.

While the failure mechanism of the web shear failure is known to correspond to the ultimate capacity of the arching mechanism taking place in short beams, the failure mechanism of the flexural shear failure has not been clearly identified. Kani (1964)[106] proposed a model based on a comb analogy, where "teeth" of concrete between adjacent shear cracks are considered to act as cantilever beams subjected to a point load at their extremity by the main reinforcement. In this model, structural failure results from flexural failure at the root of the tooth. Kani's model is known to underestimate significantly the shear capacity. This is the reason why many researchers have carried out experimental investigations to try to identify the failure mechanism involved in the flexural shear failure.

Based on experimental results, the following major shear transfer mechanisms have been identified:

- shear stresses in the uncracked compression zone of concrete,
- inclined compression force in the compression zone corresponding to arching action,
- interface shear transfer along the diagonal shear crack through aggregated interlock,
- residual normal stresses across the diagonal crack due to strain softening,
- dowel action of the longitudinal reinforcement.

The concrete contribution to shear (the four first components) can be measured to carry most of the shear force. Therefore the dowel action was usually ignored in early models. However, it was shown by Chana (1986)[107] that the longitudinal reinforcement controls the capacity of the other mechanisms inasmuch as it prevents the diagonal crack from opening, which controls aggregate-interlock and strain softening, and inasmuch as the longitudinal reinforcement controls the extent of the diagonal crack into the compressive zone, which would result in a reduction of the area of uncracked concrete carrying shear.

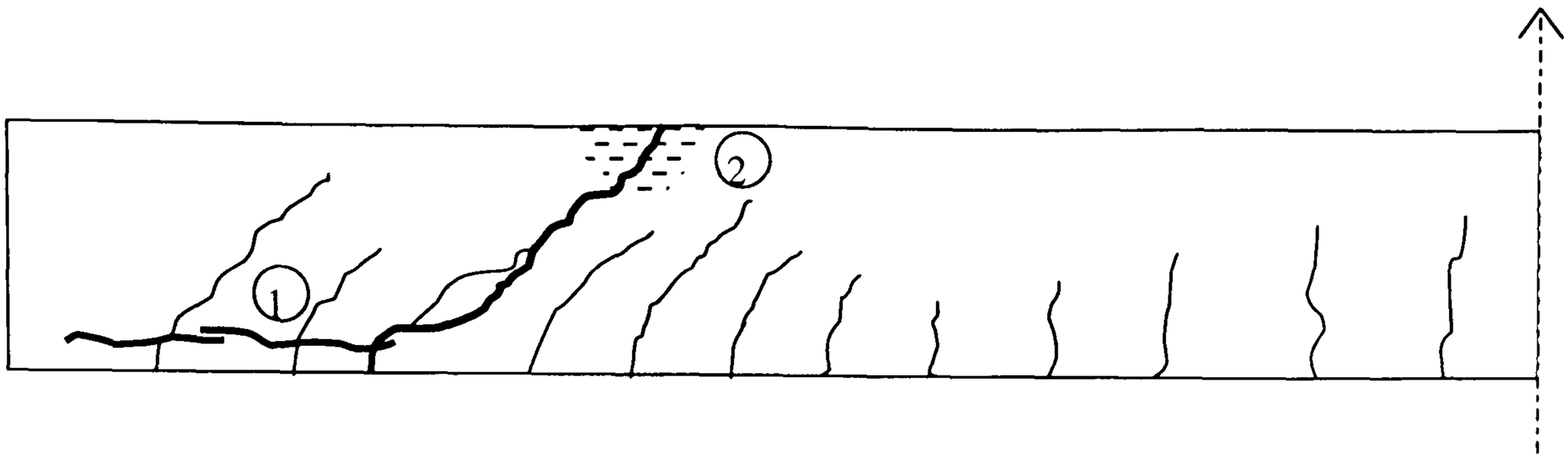

Fig. 4-4: Cracking pattern of a reinforced concrete beam failing in flexural shear

Chana (1988)[108] used high speed photography and continuous recording of crack widths at critical locations to investigate the history of the mechanisms occurring in the flexural shear failure. A typical cracking pattern of a slender beam without shear reinforcement failing in flexural shear is shown in Fig. 4-4. Chana showed that the first crack to open is the horizontal splitting of concrete at the level of the main reinforcement, closely followed by the opening and the extension of the pre-existing diagonal shear crack, resulting in the failure of the concrete compression zone under a combination of compression and shear stresses. It was concluded that the compression zone is intact at the onset of failure, and that the flexural shear failure is triggered by dowel cracking, i.e. splitting cracking.

4.3.2. Review of existing models

Flexural shear failure has been extensively studied over the years, leading to the development of many empirical laws and analytical models. For slender beams, however, no analytical model yields satisfactory results. Consequently, design code approaches are still based on empirical formulae.

Empirical methods

The first empirical formula to be developed is due to Zsutty (1968)[109] and (1971)[110] who derived two formulae from a dimensional and a regression analysis. Using the experimental data for 86 slender beams led to the formula:

$$V_{cr} = 2210 \cdot \left(f_c \rho \frac{d}{a_s} \right)^{1/3} bd \qquad \textit{(Eq. 4-12)}$$

with V_{cr} in kN, f_c in MPa, b and d in m.

Based on the experimental data for 108 short beams, Zsutty developed the slightly different formula:

$$V_{cr} = 5430 \cdot (f_c \rho)^{1/3} \left(\frac{d}{a_s} \right)^{4/3} bd \qquad \textit{(Eq. 4-13)}$$

with V_{cr} in kN, f_c in MPa, b and d in m.

The British design code for the structural use of concrete, BS 8110[111], adopted a similar equation, probably adapted from Zsutty's formula, where an extra term is added to reflect the size effect:

$$V_{cr} = \frac{790}{\gamma_m} (100\rho)^{1/3} \left(\frac{0.4}{d} \right)^{1/4} \left(\frac{f_c}{25} \right)^{1/3} bd \qquad \textit{(Eq. 4-14)}$$

with V_{cr} in kN, f_c in MPa, b and d in m,

where $100\rho < 3$, $400/d > 1$, $f_c < 40$ MPa, and γ_m is a safety factor equal to 1.25.

The ACI building code (1963)[112] adopted a formula based on a different approach. The shear capacity of a beam without stirrups is divided into a concrete contribution and a longitudinal reinforcement contribution:

$$V_{cr} = \left(0.16\sqrt{f_c} + 17\rho \frac{Vd}{M} \right) \times 10^3 bd \qquad \textit{(Eq. 4-15)}$$

$$\leq 290 \cdot \sqrt{f_c} bd$$

with V_{cr} in kN, f_c in MPa, b and d in m.

For a number of reasons this equation is now considered inappropriate.

An alternative, simplified, formula is proposed in the ACI building code (1989)[113], ACI 318-89, where the shear capacity is assumed to be entirely dependent on the concrete contribution:

$$V_{cr} = 170 \cdot \sqrt{f_c}\, bd \qquad \textit{(Eq. 4-16)}$$

with V_{cr} in kN, f_c in MPa, b and d in m.

More recently, Okamura and Higai (1980)[114] and Niwa et al. (1986)[115] have developed a new empirical formula from experimental data. They obtained the same power laws for the concrete strength and the reinforcement ratio as (Eq. 4-12). A size effect term similar to the BS 8110 was also derived. However, the approach produced a completely different term to take account of the role of the shear span-to-depth ratio:

$$V_{cr} = 200 \frac{(100\rho)^{1/3}}{d^{1/4}} f_c^{1/3} \left(0.75 + \frac{1.4d}{a_s} \right) bd \qquad \textit{(Eq. 4-17)}$$

with V_{cr} in kN, f_c in MPa, b and d in m.

The CEB-FIP model code (1990)[5] suggests the most sophisticated formula. Zsutty's power laws are adopted and an extra size effect term is added:

$$V_{cr} = 150 \cdot \left(1 + \sqrt{\frac{0.2}{d}} \right) \left(\frac{3d}{a_s} \right)^{1/3} (100\rho)^{1/3} f_c^{1/3} \cdot bd \qquad \textit{(Eq. 4-18)}$$

with V_{cr} in kN, f_c in MPa, b and d in m.

Simple strut-and-tie models

Simple strut-and-tie models, derived from the lower-bound theorem of plasticity, predict the failure of deep beams where most of the shear force is carried by arch action. For these models the tensile strength of concrete is neglected and the concrete contribution is assumed to be carried by a single inclined strut. The longitudinal reinforcement is assumed to be anchored well behind the support. Two failure mechanisms are considered:

- failure of concrete in bi-axial compression over the support or under the load,
- yielding of the reinforcement.

Nielson et al. (1978)[116] worked out the ultimate shear capacity from this model. Defining the mechanical reinforcement ratio as follows:

$$\omega = \rho \frac{f_y}{f_c} \qquad \textit{(Eq. 4-19)}$$

For $\omega < 2/3$, the beam fails by steel yielding:

$$V_{cr} = \frac{f_c b H^2}{a_s} \frac{\omega(1-\omega/2)}{1+\omega/2} \qquad \textit{(Eq. 4-20)}$$

For $\omega > 2/3$, the beam fails by concrete crushing:

$$V_{cr} = \frac{f_c b H^2}{4 a_s} \qquad \textit{(Eq. 4-21)}$$

More sophisticated patterns of the force flow may be envisaged by incorporating the general tools of stress field analysis: models including fans, arches and bands allow for a proper consideration of distributed loads.

Truss models with concrete ties

Several authors have tried to generalise the strut-and-tie model to shear failure of slender beams. Marti (1980)[117] extended the plasticity approach by using a Mohr-Coulomb yield criterion for concrete that includes tensile stresses. Al-Nahlawi and Wight (1992)[118] proposed a truss model with concrete compression struts inclined at either 45 deg. or 35 deg. and concrete tension ties perpendicular to the struts. Reineck (1991)[119] showed that these truss models with concrete ties comply fully with Kani's tooth model.

However, it appears clearly that a different approach is needed to capture the shear failure of slender members without stirrups, for which the failure mechanism differs significantly from the ones assumed in the truss models.

Modified compression field theory

Collins and Mitchell (1996)[120] developed a more general approach to shear, the modified compression field theory, which is used as the basis for a unified approach to shear in reinforced concrete. This theory can be implemented in different ways with varying levels of complexity, from a full non-linear finite element analysis, to a multi-layered sectional analysis, to the simplest case where only the crack width at the level of the longitudinal reinforcement is considered. The latter case, that is the most suitable for design, is analogous to a variable-angle truss model with diagonal concrete ties.

The crack pattern is idealised as a series of parallel cracks all occurring at an angle θ to the longitudinal reinforcement. In lieu of following the complex stress variations in the cracked concrete, only the average stress state and the stress state at the crack are considered. As these two states are statically equivalent, the loss of tensile stress in the concrete at the crack must be replaced by increased steel stresses, or, after yielding of some of the reinforcement at the crack, by shear stresses along the crack interface. The shear stress transmitted across the crack will be a function of the crack width, w. Thus, the shear resistance of a diagonally cracked member is given by:

$$V_{cr} = \frac{0.18\sqrt{f_c}bd}{0.3 + \frac{24w}{d_{agg} + 16}} \qquad \textit{(Eq. 4-22)}$$

where w is the crack width in mm and f_c the compressive strength in MPa.

w is derived from the calculated crack spacing and the crack inclination. The inclination of the diagonal cracks is calculated using a strain compatibility procedure involving average stresses and average strains.

The failure mechanism considered in the modified compression field theory is the yielding of the steel, the crushing of the concrete and the loss of the concrete contribution due to aggregate

interlock along diagonal cracks. However, the dowel action and the splitting crack being ignored in this approach, the failure mechanism described by Chana cannot be predicted.

Fracture mechanics approach

The existence of a size effect observed in the experimental results, prompted several researchers to applied fracture mechanics to the shear failure. Gustafsson and Hillerborg (1988)[121] investigated the diagonal shear strength using the cohesive crack concept, with the objective to show that a size effect can be predicted theoretically. The Gustafsson-Hillerborg model assumes that a single polygonal cohesive crack with linear softening is formed, while the bulk of the concrete remains linear elastic. The behaviour of the steel is assumed to be linear elastic all the time. An elastic-perfectly plastic law is adopted for the bond-slip curve. The failure criterion adopted is the crushing of the concrete.

Different cracking patterns were investigated numerically. Using the foregoing approach, Gustafsson and Hillerborg analysed the influence of the size, the steel ratio and the shear span-to-depth ratio. They concluded that a size effect law with the form $\frac{k}{d^{1/4}}$ could be adopted.

Bazant and Kim (1984)[122] and Bazant and Sun (1987)[123] developed a set of phenomenological equations to describe the dependence of the diagonal shear strength on the size, shape and steel ratio of beams failing in diagonal shear. Once again the analysis focused on the size effect, using a size effect correction approach introduced by Bazant. The shear strength is assumed to result from the combination of the arching action and the composite beam action. The summation of the two components yielded a formula similar to the ACI building code empirical law. This equation, however, gives little explanation of the structural behaviour and the experimental data display a large scatter around the predicted failure load.

A more physical approach was adopted by Jenq and Shah (1989)[124] who applied their two-parameter NLFM model to the shear failure. The non-linear fracture mechanics of the diagonal crack is investigated. The ultimate shear capacity is supposed to be obtained as the summation of the contributions from steel and from concrete. The concrete contribution is derived using the fracture mechanics model while the steel contribution is estimated considering the average ultimate bond stress, assumed to be proportional to the embedded length.

Later on, So and Karihaloo (1993)[2] pointed out that this approach was over simplified as it ignores the influence of reinforcement on the fracture behaviour of concrete, which was confirmed by the large discrepancy between the predicted and the measured shear capacity. Thus, Karihaloo was the first to introduce a failure criterion for longitudinal splitting, where the maximum bond stress is derived from Van der Veen's model. Karihaloo concluded that by taking into account the bond-slip relationship, the dowel action and the aggregate interlock, it would appear that the modified Jenq-Shah technique predicts the shear capacity accurately.

This result emphasises the importance of modelling the correct failure mode. Karihaloo is the only one to adopt a failure criterion, i.e. splitting by dowel action, in agreement with the failure mechanism described by Chana, and, as a matter of fact, Karihaloo's model is the only one to yield satisfactory results for the shear capacity of slender beams. With this conclusion in mind, the fracture mechanics model developed for splitting propagation is applied to the flexural shear failure of slender beam and is compared with the CEB-FIP empirical formula.

4.3.3. Fracture mechanics model for flexural shear failure by splitting

Identification of the critical failure mechanism

From Chana's experimental observations, it is clear that the release of the main reinforcement by splitting controls the opening and the extension of the diagonal crack. As long as no splitting has occurred, the unbonded length of the longitudinal steel is limited, thus preventing the opening of the diagonal crack. Once splitting has begun, the steel bar is released from its concrete encasement. The drastically reduced stiffness in tension allows the diagonal crack to open and extend, while a rotation about the tip of the diagonal crack occurs, Fig. 4-5. Ultimately, the remaining concrete ligament is strained to the crushing limit, resulting in the structural failure.

This failure mechanism is the most likely for the flexural shear mode. Splitting cracks appearing at the level of the longitudinal reinforcement and extending towards the support can be observed on many structures that failed in flexural shear. However, it is possible, if a low reinforcement ratio is used that a similar yet different type of failure occurs.

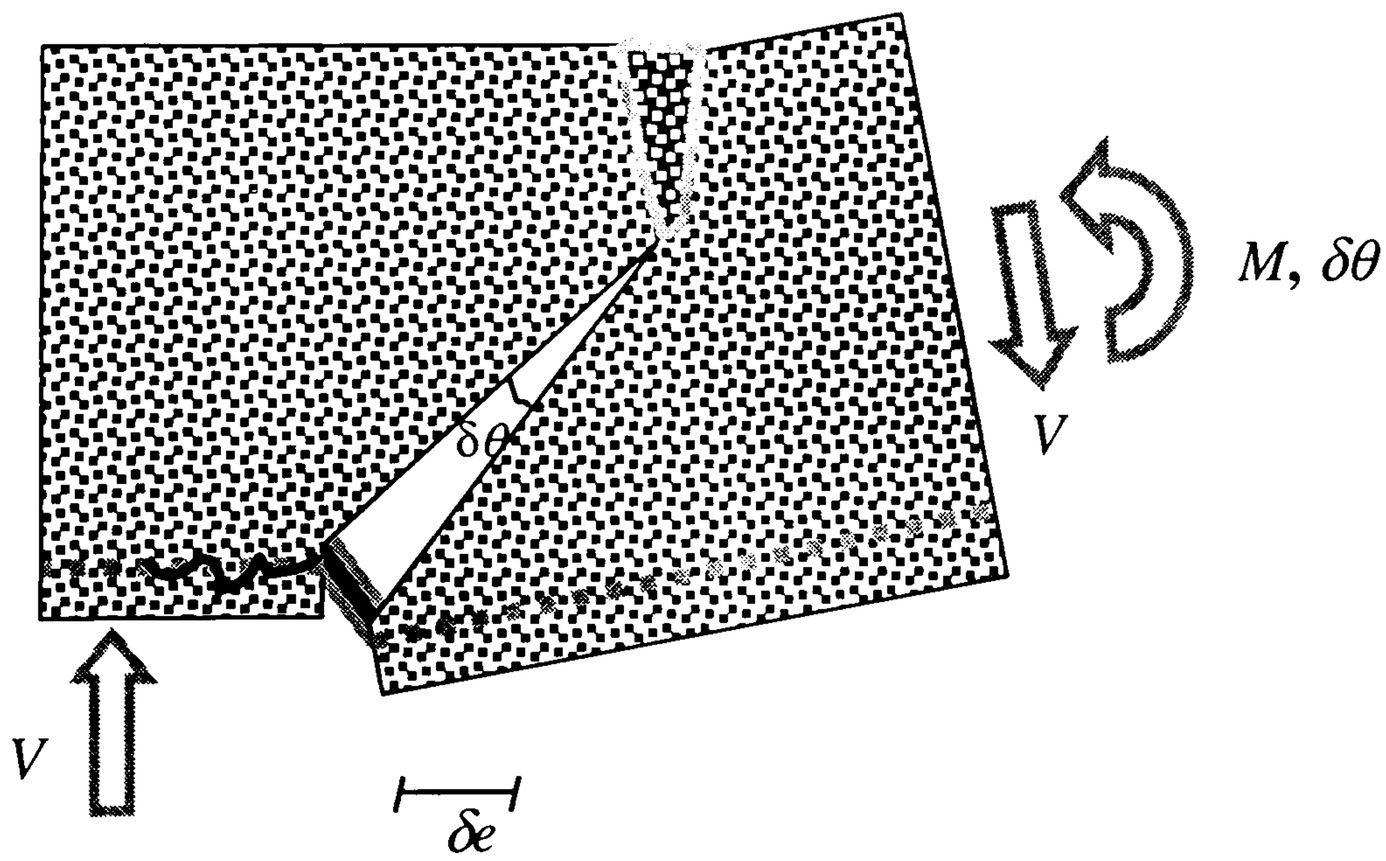

Fig. 4-5: Failure mechanism for flexural shear failure by splitting

While most of the time splitting is more critical than the yielding of the steel bar, it can happen that the steel yields before splitting, resulting in the same opening of the diagonal crack and the same ultimate crushing of the concrete after rotation. In this case, the use of plasticity theory would be appropriate. This study, however, is limited to the modelling of the shear failure by splitting.

Formulation of the fracture mechanics model

The formulation of the model is based on the fundamental relation of fracture mechanics, $\delta G = \frac{1}{2}\, \delta W_{ext}$, as deduced for the failure load of a structure, (Eq. 2-16). The mechanism producing the external work is the rotation under constant load about the tip of the diagonal crack. In order to calculate the energy release, the rotational stiffness of the beam needs to be determined. To that aim, the bulk of uncracked concrete and the embedded reinforcement are considered to behave as a rigid body. The rotational stiffness depends on the axial and the dowel stiffness of the longitudinal reinforcement, itself depending on the extent of splitting releasing the reinforcing bar. The stiffness is worked out considering the free body diagram, Fig. 4-6.

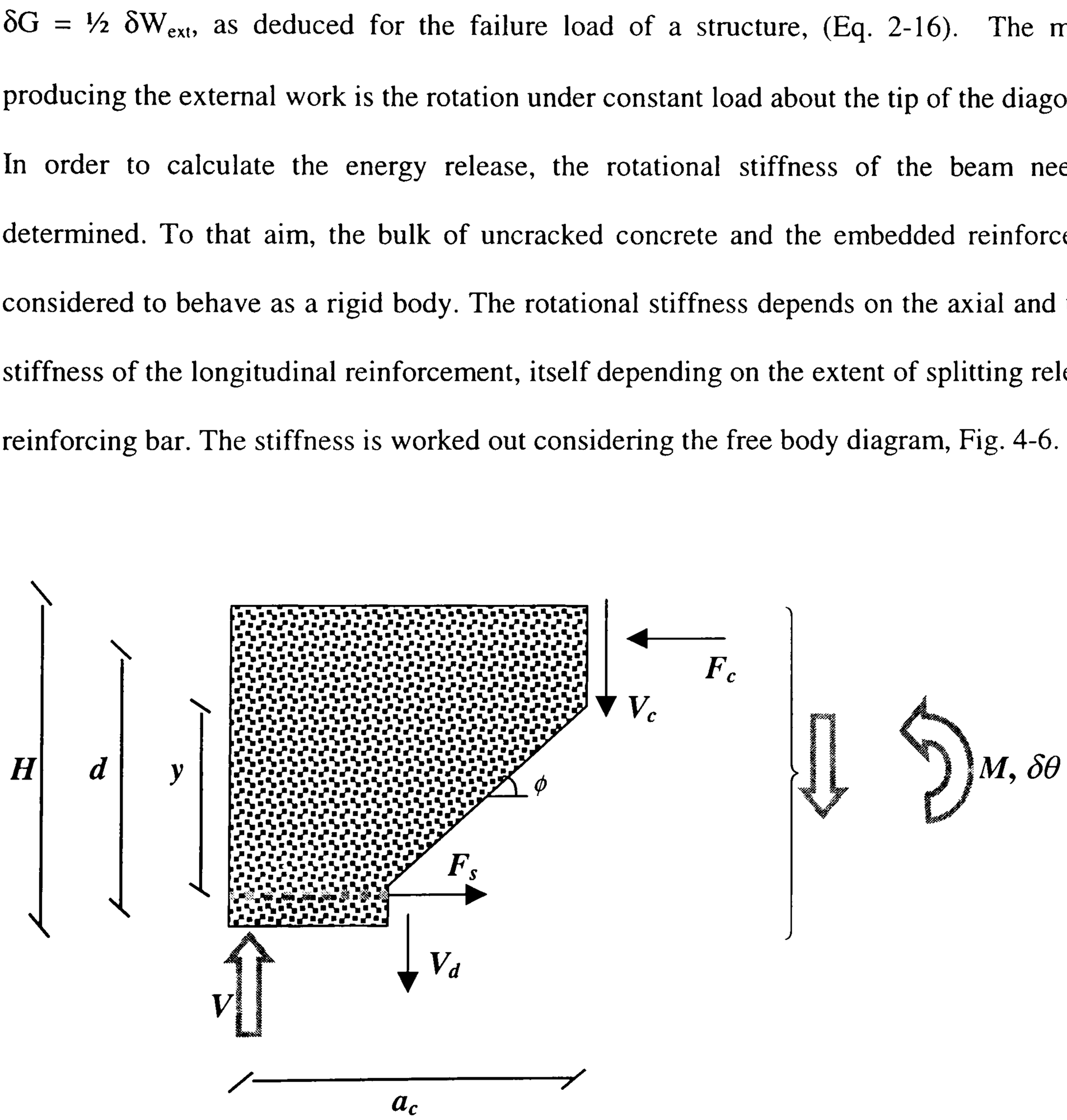

Fig. 4-6: Free body diagram and notation definition

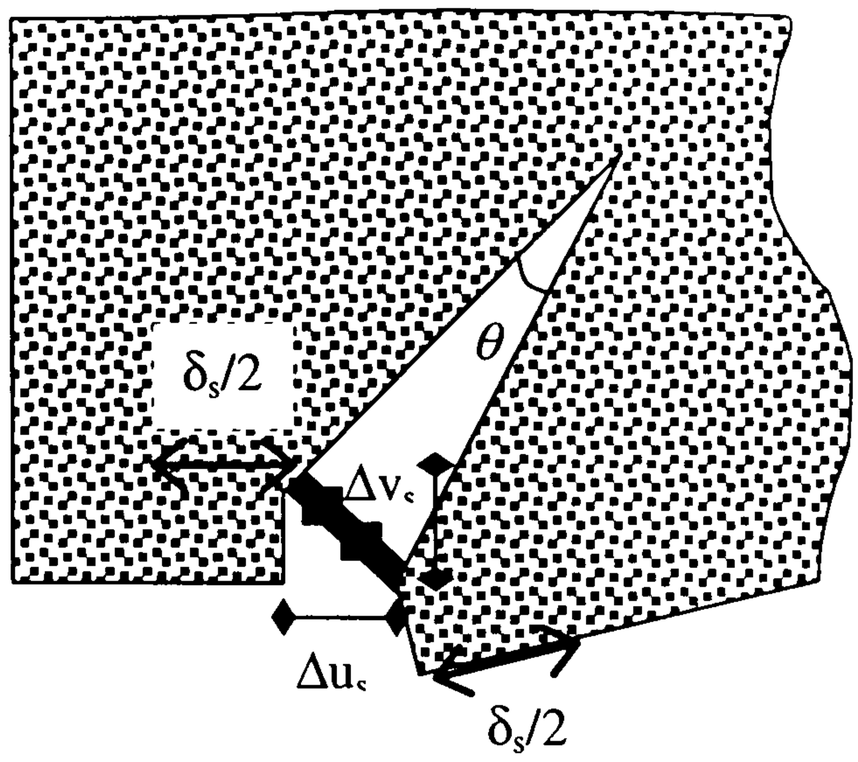

$$\Delta u_s = \theta \cdot y$$

$$\Delta v_s = \frac{\theta \cdot y}{\tan \phi}$$

Fig. 4-7: Reinforcing bar deformation – geometric considerations

The axial and shear force in the steel bar crossing the diagonal crack can be linked to the angle of rotation, θ, using the elastic properties of the bar and some geometric considerations, Fig. 4-7, and assuming the angle of the diagonal crack, ϕ, to be 45 deg.:

$$\begin{cases} F_s = \dfrac{E_s A_s}{\delta_s} \Delta u_s = \dfrac{E_s A_s}{\delta_s} y\theta & \textit{(Eq. 4-23)} \\ V_d = \dfrac{G_s \Sigma_s}{\delta_s} \Delta v_s = \dfrac{9}{26} \dfrac{E_s A_s}{\delta_s} y\theta & \textit{(Eq. 4-24)} \end{cases}$$

where G_s is the shear modulus of steel, Σ_s is the reduced cross-section of the bar and δ_s is the unbonded length of the reinforcement. In (Eq. 4-24) the well-known results from the engineer's beam bending theory, for a circular cross-section, are used:

$$\Sigma_s = 0.9 \cdot A_s \qquad \textit{(Eq. 4-25)}$$

$$G_s = \frac{E_s}{2(1+\upsilon_s)} = \frac{9}{26} E_s \qquad \textit{(Eq. 4-26)}$$

The equilibrium of the free body is given by the following set of equations:

$$\begin{cases} F_s = F_c & \textit{(Eq. 4-27)} \\ V_c + V_d = V & \textit{(Eq. 4-28)} \\ V \cdot a_c = V_d \cdot y + F_s \cdot d & \textit{(Eq. 4-29)} \end{cases}$$

The diagonal crack extent, y, and the effective depth, d, are assumed to be proportional to the height of the beam, H: $y = \beta H$ and $d = \gamma H$.

(Eq. 4-29) can then be rewritten using (Eq. 4-23) and (Eq. 4-24):

$$V \cdot a_c = \beta\left(\frac{9}{26}\beta + \gamma\right)\frac{E_s A_s}{\delta_s} H^2 \theta \qquad \textit{(Eq. 4-30)}$$

which provides a formula for the rotational stiffness.

Differentiating this expression about the unbonded length, δ_s, yields:

$$\delta\theta = \delta\left(a_c \frac{\delta_s}{A_s E_s} \frac{V}{\beta\left(\frac{9}{26}\beta + \gamma\right)H^2}\right) = \frac{a_c}{A_s E_s} \frac{V}{\beta\left(\frac{9}{26}\beta + \gamma\right)H^2} \delta e \qquad \textit{(Eq. 4-31)}$$

where δe is the variation of the unbonded length, i.e. the variation of the extent of the splitting crack.

It is now possible to write the fundamental relation of fracture mechanics as a criterion for splitting failure:

$$\delta W_{ext} = 2\delta G \qquad \textit{(Eq. 4-32)}$$

$$a_c V_{cr} \cdot \delta\theta = 2\Gamma \cdot \delta e \qquad \textit{(Eq. 4-33)}$$

where G is the fracture energy necessary to extent the splitting crack by one unit length.

Substituting (Eq. 4-31) into (Eq. 4-33) gives the expression for the critical shear load:

$$V_{cr}^2 = \left(\frac{\beta h}{a_c}\right)^2 \left(\frac{9}{13} + 2\frac{\gamma}{\beta}\right) A_s E_s \Gamma \qquad \textit{(Eq. 4-34)}$$

$$V_{cr} = \sqrt{\frac{9}{13} + 2\frac{\gamma}{\beta}} \cdot \frac{\beta \cdot h}{a_c} \cdot \sqrt{\Gamma A_s E_s} \qquad \textit{(Eq. 4-35)}$$

with V_{cr}, Γ, A_s and E_s in S.I. or alternatively, V_{cr} in kN, Γ in kN.m/m, A_s in mm^2 and E_s in GPa

It is possible to make a certain number of assumptions without loosing much generality of the formula:

$$d = \gamma \cdot H = 0.9H$$
$$y = \beta \cdot H = 0.8H$$
$$d_{agg} = 20 \text{ mm}$$

The two first assumptions are motivated by experimental observations, and the third assumption corresponds to the concrete mix commonly used. Using the CEB-FIP formula for the assessment of the fracture energy, (Eq. 2-40), and assuming a dynamical mode of failure, i.e. only the fracture energy from the splitting crack is required, it is possible to simplify the formula:

$$V_{cr} = 4.517 \cdot \frac{H}{a_c} \cdot f_c^{0.35} \cdot \sqrt{A_s E_s b} \qquad \textit{(Eq. 4-36)}$$

with V_{cr} in N, f_c in MPa, A_s in m^2, E_s in N/m^2, and b in m or alternatively, V_{cr} in kN, f_c in MPa, A_s in m^2, E_s in GPa, and b in mm

The difficulty resides in the determination of the position of the critical diagonal crack, a_c. Kim and White (1991) postulated the same failure mechanism and adopted a mixed approach, half physical, half empirical, to predict the flexural shear cracking and the position of the critical diagonal crack. The point of first shear cracking is obtained considering that a diagonal crack forms from a flexural crack when the tensile strength of concrete is reached due to bond stress concentration at the steel bar level, near the flexural crack. Kim and White determined two curves varying along the beam length, which are conditions for diagonal cracking. The first one is the existence of a flexural crack. This capacity decreases monotonically along the length of the beam:

$$V_{fl} = \frac{M_{cr}}{a_c} = k_1 \frac{\sqrt{\rho_s f_c} b d^2}{a_c} \qquad \textit{(Eq. 4-37)}$$

where k_1 is an empirical factor.

The second condition is the bond stress reaching the tensile strength of concrete. This capacity increases monotonically along the beam length:

$$V_b = k_2 \left(1 - \sqrt{\rho_s}\right) \sqrt{\frac{f_c a_c}{a_s}} bd \qquad \textit{(Eq. 4-38)}$$

where k_2 is an empirical factor.

The point of critical diagonal cracking is then found at the intersection of the two curves. By equating the two formula:

$$a_c = k_3 a_s \left[\frac{\rho_s \left(\frac{d}{a_s} \right)^2}{\left(1 - \sqrt{\rho_s}\right)^2} \right]^{1/3} \qquad \textit{(Eq. 4-39)}$$

Few experimental data are available to check the position of the critical diagonal crack. However, Kim and White found 14 experimental results in the literature, which they used in a statistical analysis to determine the coefficient k_3. The numerical value suggested, although a large scatter was observed, is 3.3.

Substituting (Eq. 4-39) into (Eq. 4-36) provides a predictive analytical formula for the flexural shear capacity:

$$V_{cr} = \frac{1.109}{\sqrt{H}} \cdot \left(\frac{H}{a_s} \right)^{1/3} \left(1 - \sqrt{\rho}\right)^{2/3} \rho_s^{1/6} f_c^{0.35} \sqrt{E_s} \cdot bH \qquad \textit{(Eq. 4-40)}$$

The first term corresponds to the size effect, as expected from a linear elastic fracture mechanics analysis. The second term takes into account the slenderness of the beam. The third and fourth terms of the equation reflect the reinforcement ratio influence and the fifth term the influence of the concrete strength.

4.3.4. Benchmarking of the Model Against an Empirical Formula

It is important to check the analytical formula against experimentally derived data. Agreement between the formula and the experimental data will help confirm the assumed failure mode. Since experimental flexural shear failure loads are typically largely scattered, the model was

benchmarked against an empirical formula rather than directly against the experimental results. It is believed that the large scatter is mainly due to the variation in the fracture energy required per unit length of splitting crack extent, as the mode varies between dynamic and quasi-static failure. The empirical formula of the CEB-FIP provides a lower bound of the flexural shear failure, and as such, it should correspond to the dynamical mode of failure.

Comparison

To allow the comparison with the CEB-FIP formula, the elastic modulus of steel, E_s, is set to 205 GPa in (Eq. 4-40). Rearranging the equation and adopting the format of the CEB-FIP formula, (Eq. 4-40) becomes:

$$V_{cr} = 150 \cdot \frac{1.183}{\sqrt{d}} \cdot \left(\frac{3d}{a_s}\right)^{1/3} (100 \cdot \rho_s)^{1/6} \left(1 - \sqrt{\rho_s}\right)^{2/3} f_c^{0.35} \cdot bd \qquad \textit{(Eq. 4-41)}$$

[kN] [m] [MPa] [m].[m]

where the following assumptions have been made: $\phi = 45°$, $\gamma = 0.9$, $\beta = 0.8$, $d_{agg} = 20$ mm, $E_s = 205$ GPa and the failure is triggered by unstable dynamic splitting.

This formula has to be compared with the CEB-FIP formula, recalled here:

$$V_{cr} = 150 \cdot \left(1 + \sqrt{\frac{0.2}{d}}\right)\left(\frac{3d}{a_s}\right)^{1/3} (100 \cdot \rho_s)^{1/3} f_c^{1/3} \cdot bd \qquad \textit{(Eq. 4-42)}$$

[kN] [m] [MPa] [m].[m]

It is remarkable that the slenderness term and the concrete strength term correspond nearly exactly (the slight discrepancy between the power of f_c is due to the approximate power, 0.7, used in the assessment of the fracture energy, G_f).

The discrepancy in the size effect term can be due to two reasons. Either the LEFM approximation does not yield a realistic size effect on the whole range of variation of the size of the structure, and in this case a non-linear size effect correction procedure as proposed by Bazant and Planas (1998) could be adopted. Or the size correction term inserted in the CEB-FIP formula

is not realistic, as already pointed out by Bazant. As a matter of fact, the size effect term of the CEB-FIP formula displays a curvature opposed to the one predicted by the NLFM theory. Nevertheless, when the two terms are allowed to depart from ±10%, the range of variation of the structural size is within the range of practice:

$$\frac{1.183}{\sqrt{d}} \underset{\pm 10\%}{\approx} 1+\sqrt{\frac{200}{d}} \qquad \text{for} \qquad 375 < d < 760 \text{ mm.}$$

The complex form of the reinforcement ratio term derived analytically may explain the discrepancy with the empirical term. Once again, when the two terms are allowed to depart from ±10%, the range of variation of the reinforcement ratio is within the range of practice:

$$(100 \cdot \rho_s)^{1/6}\left(1-\sqrt{\rho_s}\right)^{2/3} \underset{\pm 10\%}{\approx} (100 \cdot \rho_s)^{1/3} \qquad \text{for} \qquad 0.4 < \rho_s < 1.2\ \%$$

Discussion

It is remarkable that the two formulae compare so well, not only in their form but also in the numerical constants. This is probably due to the fact that few simplifying assumptions have been made to obtain the analytical formula, and that when assumptions have been made, either they are very close to the experimentally observed behaviour ($\phi = 45^o$), or their value is reliably determined (d_{agg} = 20 mm and E_s = 205 GPa), or their variation has little effect on the final result. As a matter of fact, the initial value of the unbonded length δ_{s0} has no effect on the final result, and the ratio of γ to β has a small effect: changing the ratio from 1.125 to 1.5, i.e. a variation of 33%, results in a variation of 12% to the final result.

Only two parameters in the analytical model have a significant effect and are not very well defined. The first one is the empirical coefficient derived by Kim and White based on only 14 experimental results. The final result is inversely proportional to this coefficient. A better assessment of this coefficient should be achieved. This would involve carrying experiments on a wide range of variation of parameters, noting the position of the critical diagonal crack.

The second critical parameter is the value of the fracture energy required per unit length of splitting crack extent. It seems that most of the flexural shear failures observed experimentally happen dynamically, therefore requiring only the fracture energy to open the horizontal splitting crack. However, it is not clear if the onset of the failure does not happen in a stable quasi-static way, therefore requiring extra fracture energy for the displacement of the set of conical cracks. This could explain the wide variation observed experimentally. The indeterminacy would therefore be inherent to this mode of failure. In any case, the assumption of dynamic failure is a safe assumption and any design formula based on this model should adopt this assumption.

Conclusions

It should be concluded that the mode of failure assumed, i.e. rotation about the tip of the diagonal crack triggered by splitting, is the correct failure mechanism. This conclusion emphasises the importance of carrying a rigorous phenomenological investigation prior to any model development. The proper failure mechanism must first be identified. Then a model of the phenomenon can be designed, taking into account the significant parameters.

It is believed that an analytical formula is more satisfactory than an empirical formula, as it provides physical insight into the phenomenon. From this improved understanding of the failure mechanism the design of appropriate strengthening techniques can be envisaged.

5. PREMATURE FAILURE OF EXTERNALLY PLATED REINFORCED CONCRETE BEAMS

5.1. Presentation of the Strengthening Method

The rapid deterioration of the infrastructure is a challenge facing engineers and owners of concrete structures and bridges world-wide[10,125]. Traditional structural rehabilitation methods such as external post-tensioning and concrete overlays often suffer from inherent disadvantages ranging from difficult application procedures to lack of durability, leaving the growing repair and rehabilitation market in need of cost-effective, efficient and durable retrofit techniques.

The causes of the deterioration of reinforced concrete structures are manifold[126]. Corrosion of the inner reinforcement can be due to the application of de-icing salts or the exposure to an aggressive environment. The continual upgrading of service loads including the increase of the volume of traffic on bridges has resulted in a large number of bridges requiring retrofitting. In addition, many other structures require strengthening for various reasons, for example faulty design. These considerations illustrate the great importance of effective renovation techniques for existing structures. An appropriate strengthening method must aim at improving both the behaviour under service loading and the ultimate capacity. Improving the serviceability of a structure includes reduction of the deflections and reduction of the crack widths. Considerations for the ultimate state include strength upgrading, ductility and durability improvement. Few retrofit methods meet all these requirements.

Presentation of the plate bonding strengthening technique

Strengthening of existing structures by gluing steel plates to their tension face has been used world-wide for over thirty years and proved to be both an economical and an efficient retrofit

technique. Its practical advantages range from the simplicity of application, the minimal effect on the structural size and the possibility of application with little disruption to the use of the structure. A report on this method was presented at the RILEM symposium 1967[127]. Following this, there were numerous publications and the plate bonding technique found its way into practice relatively quickly. More recently, after a significant price decrease of carbon fibre, it has been considered that steel plates should be replaced by Fibre Reinforced Plastics (FRP) plates or flexible carbon fibre fabrics. The ease of handling the material on construction sites, due to the light weight of the FRP composites, helped to reduce, further, the labour cost. The first practical use of FRP for the retrofitting of a concrete structure dates from 1992[128]. Since then many other structures have been strengthened with FRP plates or carbon fibre fabrics in Europe, Japan and North America. It was shown that the plate bonding technique is a structurally sound and a cost-effective method[10]. The only drawbacks are the need in certain cases for expensive fire protection and the unsuitability of steel plates for installation on chloride contaminated structures.

The strengthening performance of the technique is impressive both at serviceability and ultimate loading[129]. The first crack load can be doubled and the crack width reduced by 50%, while the deflection at a given load can be decreased by 40% at least. In the case of an under reinforced beam the bending strength can be doubled, and in the case of an over reinforced beam the bending strength can be increased by 50%. However, the improvement in ductility is generally not significant. If failure is due to the plate yielding the ductility is satisfying. But, if the failure is caused by plate separation or by fracture of composite plate material, the structure is actually made more brittle by the strengthening technique.

Arduini, Di Tommaso and Nanni (1997)[130] carried out experiments on reinforced concrete beams strengthened with FRP plates. Although the beams did not fail in the flexural mode but by plate separation, an increase in the flexural capacity of up to 60% was achieved. Significant stiffening was also observed. The strengthened beams displayed a much more brittle failure with a sudden falling branch only arrested by the yielding plateau of the unstrengthened beam.

The load-deflection curves of Fig. 5-1 show that doubling the thickness of the FRP plate resulted in a decrease of the flexural capacity. It can therefore be concluded that over-dimensioning is ineffective in avoiding failure by plate separation.

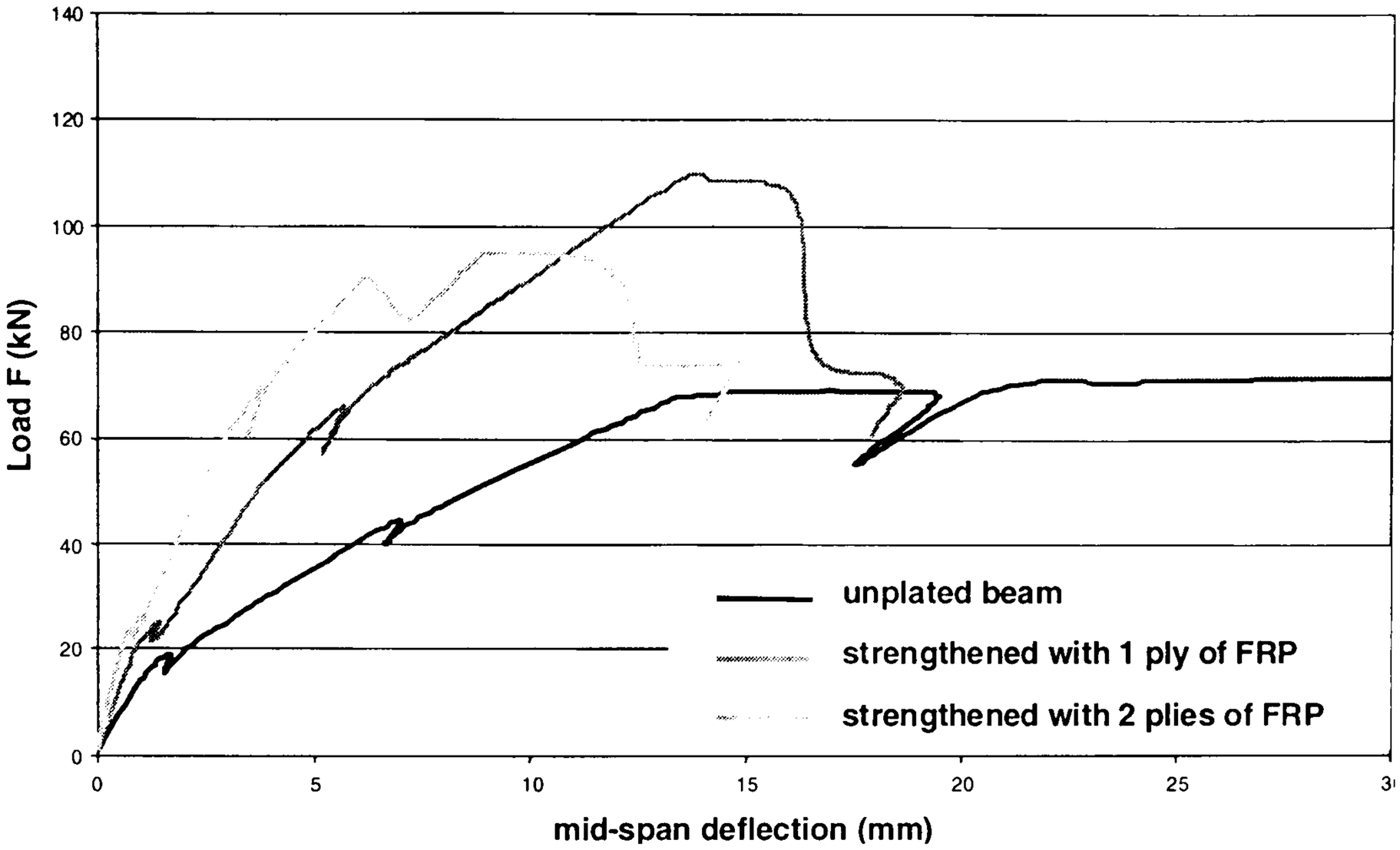

Fig. 5-1: *Influence of plate gluing on the load-deflection curve*

Details of the plate bonding technique are explained in the following. Before strengthening, the condition of the existing structure must be ascertained. The plate bonding work starts with preparation of the tension face of the existing structure by sand blasting, to remove the weak and greasy top layer. The surface preparation is important as an appropriate level of roughness must be obtained to achieve a good adhesion with the epoxy glue, and the surface must be made plane enough to match the plate. Subsequently, the clean and primed steel plate or FRP plate is placed on a wooden installation beam and the freshly mixed high strength epoxy is poured on the inner side of the plate. Then, the wooden supporting beam is mechanically pressed against the existing concrete structure. Immediately, the beam and the plate are fixed in place by temporary scaffolding. Also, when the scaffolding is applied, pressure is put on the epoxy layer and the excess epoxy is pushed aside and removed. An epoxy layer of about 1 to 2 mm is preferable. After a minimum hardening time for the epoxy of about 24 hours, the supporting scaffolding is removed and the plate acts as external reinforcement. To obtain satisfactory composite action between the plate and the concrete, the quality of the workmanship is very important.

The characteristics of the various materials used for the plate are summarised in Table 5-1. The glue usually used is a two components cold hardening epoxy with very high cohesion and adhesion strength, far above concrete tensile strength.

Table 5-1: Characteristic material properties for the plate

	Mild Steel	Carbon	Aramid	E-glass
f_t (MPa)	240 / 360	3650	3600	2700
E (GPa)	205	231	130	72
fatigue behaviour	good	excellent	good	adequate
Density, ρ (kg/l)	7	1.76	1.45	2.5
ν	0.2	-0.2	0.35	0.2
corrosion resistance	Protection needed	Excellent corrosion resistance		
price	Very good	adequate	adequate	good

Strengthening by plate bonding has been applied to various types of structures including flat slabs, ribbed slabs, hollow box post-tensioned bridges, tunnel linings and doubly curved precast shells. Details of such applications can be found in Rostasy (1993)[131], Dereymaeker (1993)[126], Meier (1995)[10], Nanni (1995)[132] and Barboni et al. (1997)[133].

Failure modes

Analysing the results of many experimental data, Arduini and Nanni in 1997[134] and Buyukozturk and Hearing in 1998[125] identified five different possible failure modes for externally plated reinforced concrete beams. These can be classified into three groups, flexural modes of failure, tensile failure of concrete and adhesive failure of epoxy resulting in delamination.

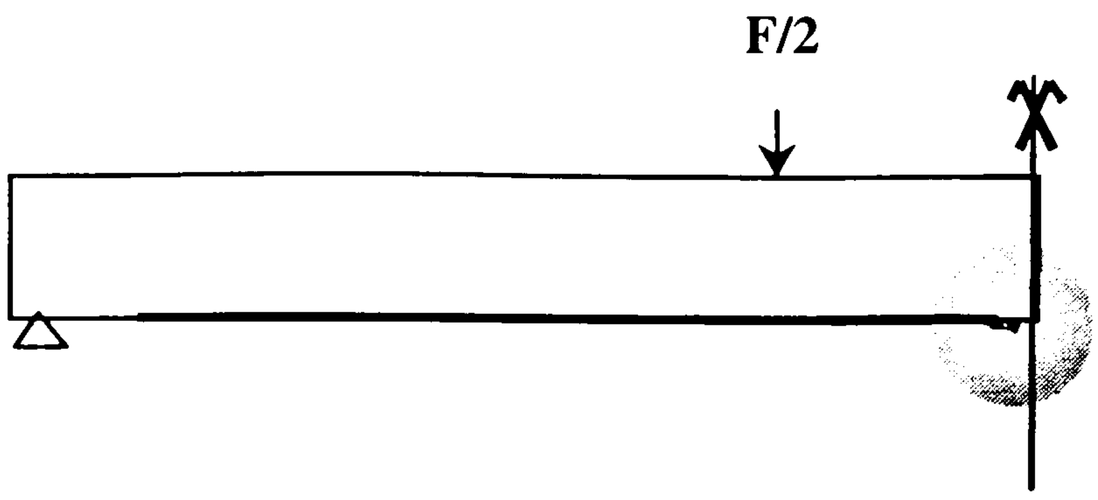

a) **plate tensile failure,**

rupture of FRP plate or yielding of steel plate

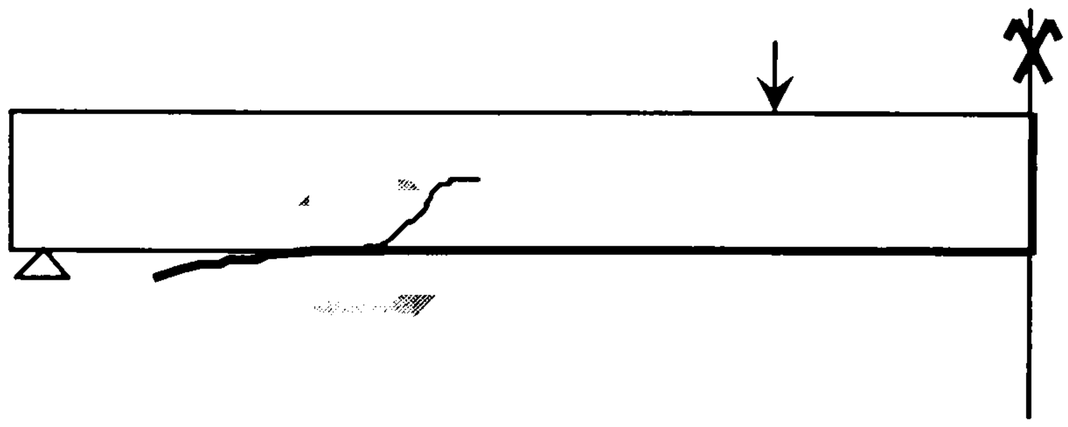

b) **debonding at plate/concrete interface by reverse peeling**

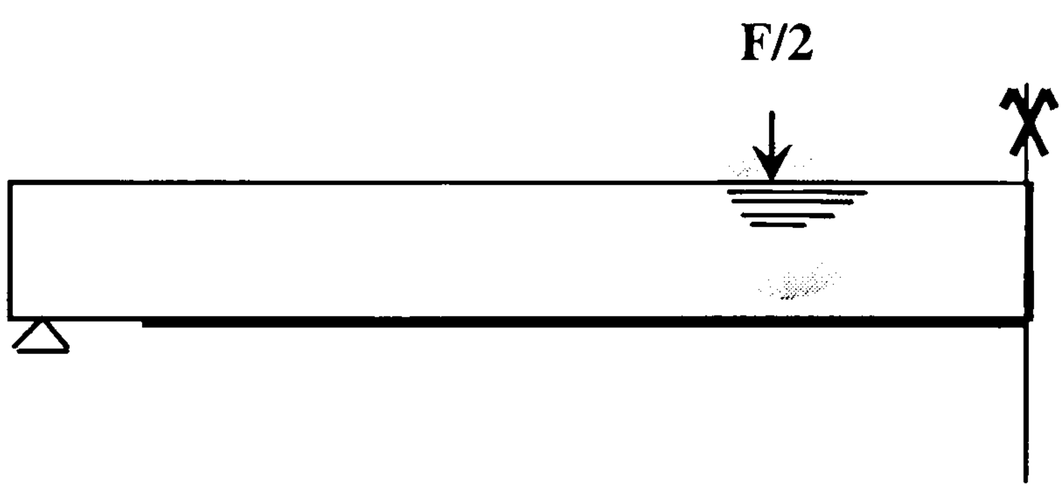

c) **concrete crushing**

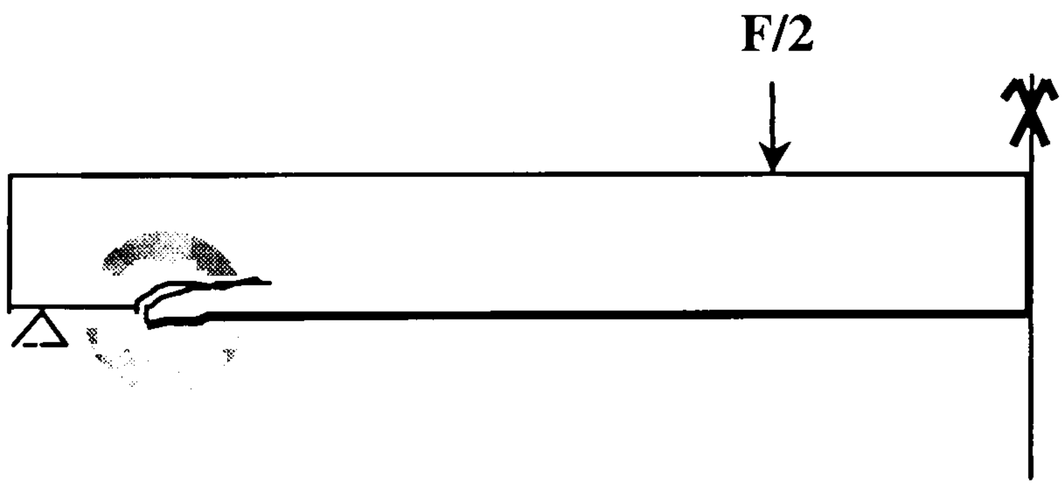

d) **advancing peeling failure in the plane of the inner reinforcement**

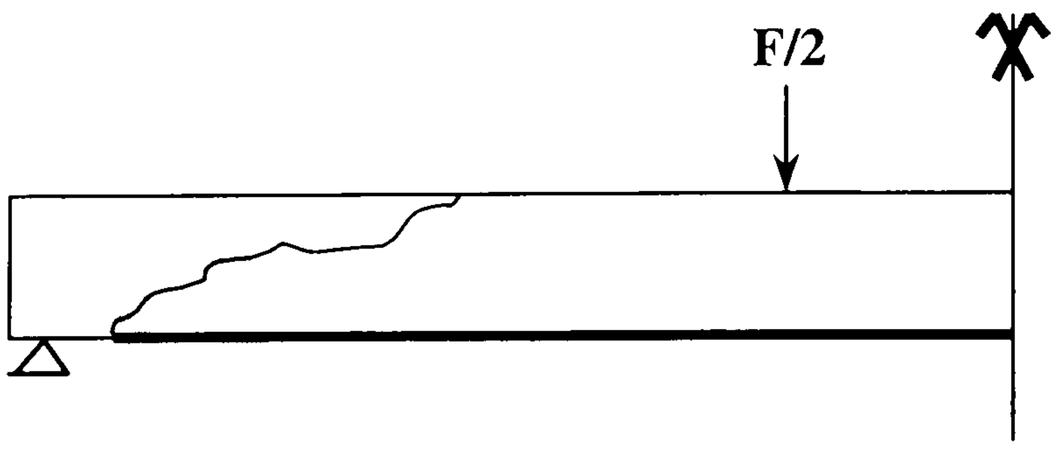

e) **shear failure**

Fig. 5-2: Classification of the failure modes of externally plated reinforced concrete beams

In the first group, two types of failures are distinguished. The flexural failure is due either to concrete compression failure under the external load, Fig. 5-2-c, or to the tensile failure of the plate, i.e. yielding for a steel plate or rupture for a FRP plate, Fig. 5-2-a. In both cases the failure is adequately ductile, although the tensile failure is preferable. When the plated beam fails in this mode, very high flexural strength increases are observed. These failure mechanisms should consequently be adopted as the preferred design modes of failure, if possible.

The second group of failure modes includes shear failure of the beam initiated by diagonal cracking from the plate end, Fig. 5-2-e, and debonding of the concrete layer resulting in plate separation, Fig. 5-2-d. Shear failure is generally triggered either by yielding of the inner reinforcement or by splitting of concrete at the level of the inner reinforcement. The debonding failure mechanism is characterised by splitting of concrete at the level of the inner reinforcement. Splitting either starts from the transverse crack present at the plate end and progresses towards the middle of the beam resulting in plate peeling or is triggered by a flexural crack and progresses backwards with extensive transverse cracking towards the end of the plate, with the same result. All these failure mechanisms are extremely brittle and should be avoided, if possible, to achieve safe design.

The last group of failure modes involves the failure of the epoxy glue, either by loss of cohesion or by loss of adhesion. The loss of cohesion is relatively rare and is generally due to poor workmanship. The loss of adhesion is more common, especially for FRP fabrics, within which fibres are subjected to debonding stresses with uneven concrete surface. The debonding can be initiated either from a discrete shear or flexural crack somewhere along the plate, Fig. 5-2-b), or from the plate extremity. In both cases, debonding results in the delamination of the entire plate.

The prediction of the flexural type of failure is relatively straightforward. Several researchers[135,136] have concluded that stress equilibrium of the section is applicable in the analysis of the flexural failures at an ultimate moment M_u. Using the customary assumptions of

the engineer's bending theory, and assuming that the inner reinforcement is yielding, the ultimate moment given by the tensile failure of the plate is formulated:

$$\frac{M_u}{bd^2 f_c} = \frac{f_y}{f_c}\frac{A_s}{A_c}\left(1-\frac{\bar{y}}{d}\right)+\frac{f_p}{f_c}\frac{A_p}{A_c}\left(\frac{H}{d}-\frac{\bar{y}}{d}\right) \qquad \textit{(Eq. 5-1)}$$

where $\bar{y}$ is the distance from the centroid of the concrete compressive stress distribution to the top fibre.

The ultimate moment given by the compression failure of concrete has a similar formulation:

$$\frac{M_u}{bd^2 f_c} = 0.85\beta_1 \frac{c_n}{d}\left(\frac{H}{d}-\frac{\beta_1 c_n}{2d}\right)-\frac{f_y}{f_c}\frac{A_s}{A_c}\left(\frac{H}{d}-1\right) \qquad \textit{(Eq. 5-2)}$$

where c_n is the depth of the neutral axis from the top fibre, β_1 is an empirical constant depending on the concrete strength, and $\beta_1 c_n$ is the depth of the equivalent rectangular compressive stress block.

Several analytical models have been developed by Jones et al. (1988)[137] and by Roberts et al. (1989)[138,139] to attempt to predict the debonding failure, also called peeling failure. These models are all based on the linear local stress concentration at the plate end, assumed to be responsible for the peeling of the plate. However, this approach was not conclusive, as the material behaviour is highly non-linear in this area. Nanni and Arduini (1997)[134] concluded that "this stress concentration is never activated, nor does it control the failure mechanism." Consequently, this approach will not presented here.

The design engineer has various means of ensuring that the externally plated beam will fail in the ductile flexural mode. Delamination can be prevented by achieving a better surface preparation, especially checking the levelness of the concrete surface, by ensuring better workmanship and by choosing a stronger epoxy glue. To avoid the shear failure, it is possible to improve the shear capacity of a beam by gluing plates on its sides[140,141]. This solution is however not available for slabs. The most difficult premature failure to prevent is the peeling failure. It is possible to bolt or anchor the plate at its extremity but the improvement is generally

not significant except if the bolts are anchored very deep inside the concrete beam[142]. The additional work required by the anchoring method increases dramatically the overall labour cost and makes the technique less attractive.

As peeling is the only undesired failure mechanism that cannot be easily prevented, it is of the utmost importance to achieve safe and ductile design that the peeling failure is better understood and that a predictive method is developed. Thus the following sections are devoted to the study and the modelling of peeling failure.

5.2. Phenomenological Approach to Peeling Failure

The first step to a better understanding of peeling failure is to try and make sense of the various experimental observations collected by others. Many researchers have carried out experimental tests on plated beams, but only a few have provided valuable phenomenological observations of the cracking mechanisms.

5.2.1. Experimental observations

Oehlers (1990)[143] and Oehlers (1992)[144] was the first to investigate more specifically peeling failure. Two types of peeling failure were identified: flexural peeling and flexural-shear peeling. The first one can be observed in plated beams with the plate ending in a constant bending moment region for which a peeling crack associated with a flexural crack causes plate separation. The second type of peeling failure is observed in plated beams with the plate ending in the shear span. In this case, failure occurs by the sudden propagation of a peeling crack associated with a diagonal flexural-shear crack, Fig. 5-3.

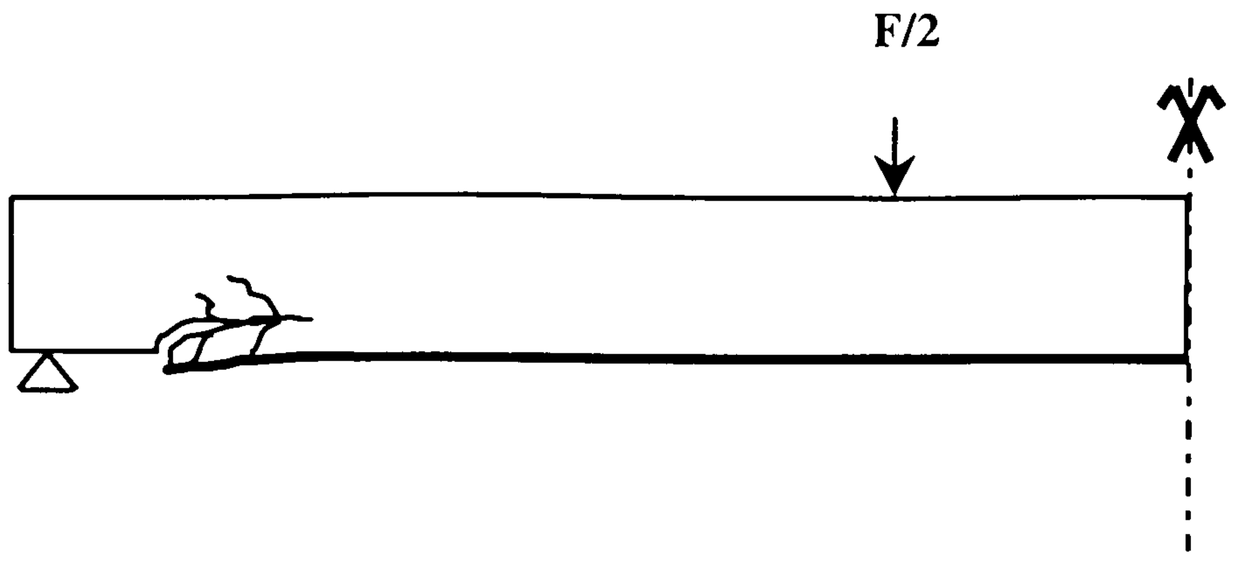

Fig. 5-3: Peeling failure of plated beam

Oehler (1992) described the typical flexural failure in these terms, Fig. 5-4: " Flexural cracks, which were almost vertical, first occurred adjacent to the plate end and these induced a

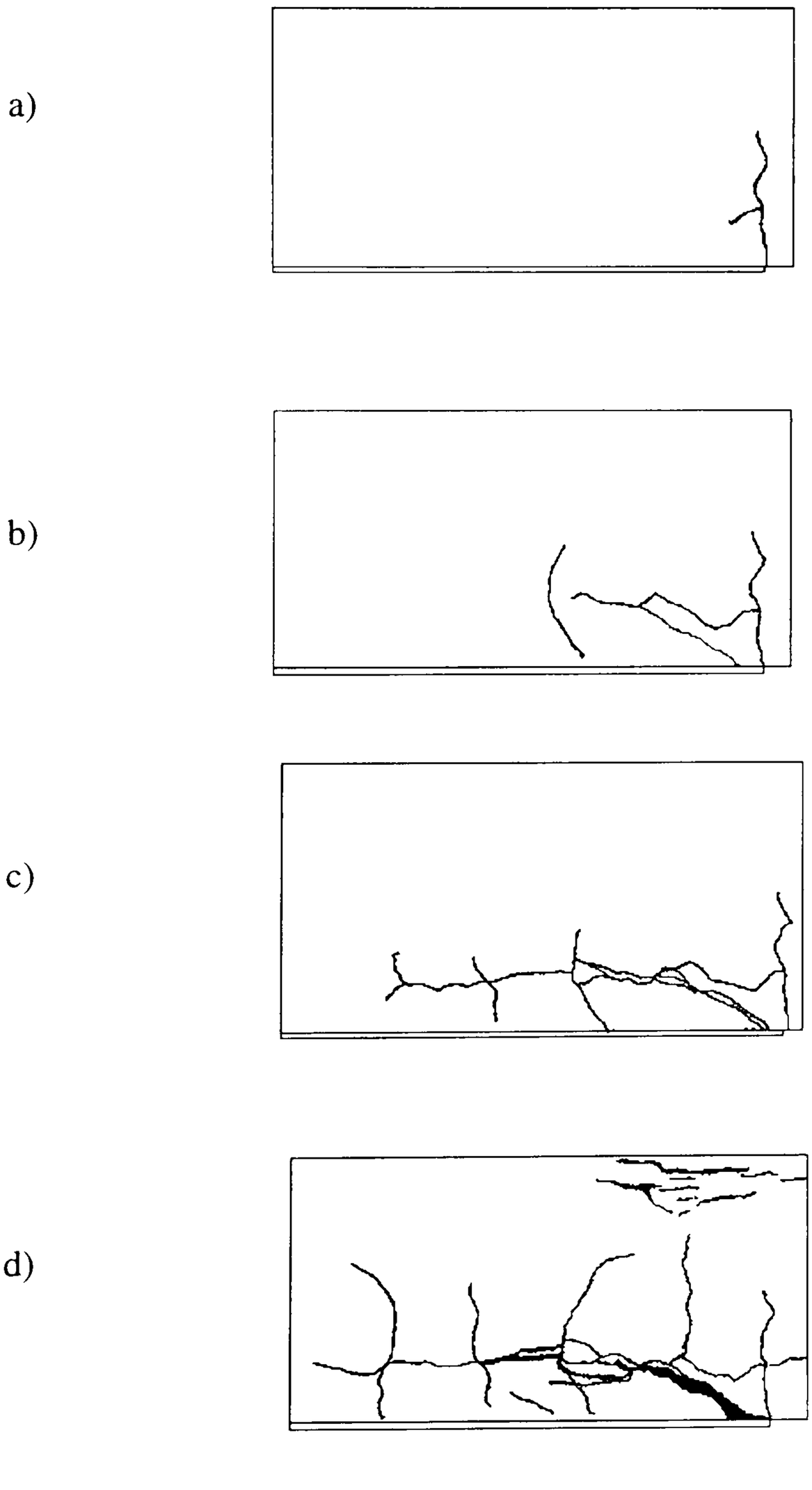

Fig. 5-4: Evolution of the cracking pattern in the flexural peeling failure of plated beams

a) flexural crack and initiation of peeling crack, b) propagation of peeling crack and opening of flexural crack in front of the peeling crack, c) further propagation of the peeling crack, d) ultimate load.

horizontal peeling crack at the end of the plate and at the level of the bottom reinforcement. The horizontal peeling crack then progressed gradually to cause debonding [...]. The debonding caused the flexural strength of the plated beam to reduce to that of the reinforced concrete beam so that further increases in the applied load then led to flexural failure of the beam." The important points in this description are the fact that flexural cracking takes place prior to peeling, and that peeling occurs due to a horizontal crack propagating at the level of the inner reinforcement. These observations are very similar to the cracking mechanism of splitting in tension specimens or in the flexural-shear failure of beams without stirrups. The hypothesis that the peeling crack is actually a splitting crack should then be investigated further.

Oehlers (1992) described a similar mechanism for flexural-shear peeling, Fig. 5-5: " The first crack to form was the diagonal crack [...]. A further small increase in the load induced a horizontal peeling crack at the level of the bottom reinforcement that only propagated slightly as the applied load was increased. Shear failure of the beam propagated the peeling crack very rapidly, which, in turn, caused the plate to debond as indicated in the test [...]. Therefore, in this specimen, shear failure of the reinforced concrete beam and debonding due to shear peeling

a)

b)

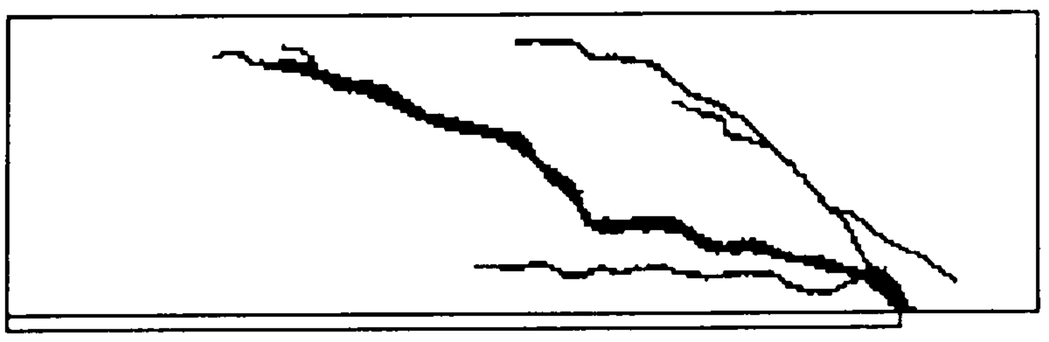

Fig. 5-5: Evolution of the cracking pattern in the flexural-shear peeling failure of plated beams

a) onset of peeling, b) ultimate load

coincided and it is also worth emphasising that both shear failures were very rapid." It is not clear in Oehlers' account if the peeling crack caused the shear failure or if the shear failure provoked the propagation of the peeling crack. However, it is clear that the diagonal crack appears first and that the shear failure coincides with the unstable propagation of the peeling crack at the level of the inner reinforcement. Again, this cracking pattern looks very similar to the flexural-shear failure of beams without stirrups, and further analysis should consider the possibility of a mode of failure triggered by splitting propagation.

Several other researchers reported similar cracking mechanism for the peeling failure. Ritchie et al. (1991)[145] carried out experimental tests on sixteen plated beams and noted that "many plated beams failed through the concrete, with cracking initiating from the end of the plate, then propagating at about a 45 deg angle up to the internal longitudinal steel, then continuing horizontally through the concrete at the level of the reinforcing steel. Swamy et al. (1987)[146] observed that some of the beams tested "failed by shearing of the concrete along the level of the internal reinforcement, effectively ripping off the cover." And most importantly it was noted that "there was no sign of debonding of the glue and concrete or plate prior to failure, nor was there any sign of cracking in the glue. The steel bars had not begun to yield either." This confirm that peeling is an extremely brittle failure displaying no warning signals. The absence of steel yielding excludes the possibility of flexural-shear failure by yielding and confirms the hypothesis of splitting along the inner reinforcement as the cause of flexural-shear failure.

It is remarkable that all the observations were pointing towards splitting at the level of the inner reinforcement as the critical cracking mechanism, and that most of the analytical and numerical investigations still concentrated on the interface stresses between the plate and the concrete. It is believed that the complex bond stresses arising at the level of the inner reinforcement, including the usual bond stresses in the transfer length and the extra tensile stresses transferred from the steel bar to the plate, are more critical than the stress concentration at the interface between the plate and the concrete.

5.2.2. Mechanism of crack formation

In order to gain more physical insight into the cracking mechanisms involved in the peeling failure, a 2D non-linear finite element model was developed. The flexural type of peeling failure was chosen to limit the complexity of the model. The aim of this simulation is to prove that the critical area for peeling is located at the level of the inner reinforcement and not at the plate-concrete interface. Analogy with the splitting mechanism will be closely examined.

Limits of the study

First of all, it is important to state clearly the scope covered by this analysis. The limits adopted are as follows:

- It has been chosen to investigate the flexural type of peeling failure only. That is the reason why a portion of a plated beam subjected to a constant bending moment will be considered.
- In order to provide insight into the failure mechanism, the model will be highly refined near the area at the end of the plate and particular attention will be paid to the modelling of the connection between the concrete and the inner reinforcement.
- It is assumed that the global phenomenon can be adequately simulated by a 2D model.
- The non-linear simulation will be carried out up to the load level causing the onset of the peeling crack, termed the serviceability load by Oehlers. The aim is to identify the mechanism causing peeling, but not to simulate the failure up to the ultimate load, as it is believed that a more complex model is needed to account for the 3D effects involved in the progress of the peeling crack.

Within these limits, the model boundaries adopted for the non-linear analysis remain valid: only a portion of the plated beam, delimited by two assumed flexural cracks, is considered. The position of the first flexural crack, precisely at the end of the plate is not controversial, as it is always observed experimentally. However, the position of the second one, further along the plate, was not founded on experimental evidence as the stitching effect of the plate prevents the

flexural crack from becoming visible to the naked eye. Consequently, it has been chosen to place the second flexural crack far enough from the plate end not to interfere with the phenomenon arising on the face of the first flexural crack. This point is further emphasised by the following observation. Assuming that the cross-sections remain plane, that the normal compressive stress distribution is triangular, and ignoring the tensile contribution of concrete, it can be calculated using the engineer's bending theory that the tensile strain in the plate would be lower than the concrete cracking strain at up to 70% of the serviceability load, as defined by Oehlers[143] regarding the onset of peeling. It is therefore strongly advisable to place the second flexural crack as far as possible from the plate end since it does not actually arise until a late stage in the simulation.

Using (Eq. 3-8) for the calculation of the transfer length, a minimum distance of 150 cm is calculated for the specimen considered. Consequently, a length of 200 mm has been chosen for the length of the portion.

It should be noted that the following simplifying assumptions have been made for the definition of the normal loading on the two boundary cross-sections:

- The flexural cracks are assumed to extend up to the neutral axis, and, accordingly, no tensile contribution of the concrete is considered.
- The concrete is assumed to have a linear elastic behaviour in compression.
- The local bending moments arising in the reinforcing bars and in the steel plate (due to their thickness) are assumed not to be significant and will be ignored.

Description of the specimen chosen for the analysis

The modelled specimen was chosen to correspond to four of the beams tested in pure bending by Oehlers. The geometric features of the specimen are summarised in Table 5-2.

Table 5-2: Geometrical features of the specimen

Unplated depth	150 mm
Plate thickness	5 mm
Beam breadth	125 mm
Concrete cover	20 mm
Tensile reinforcement	2 ϕ16
Compressive reinforcement	2 ϕ10

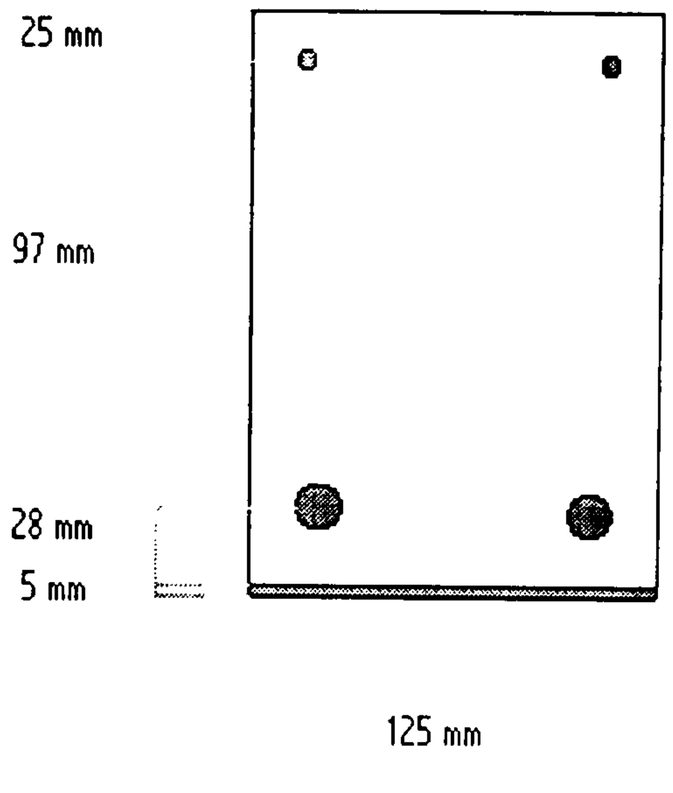

The material properties are the following:

- Concrete modulus of elasticity, E_c = 25 GPa.
- Concrete tensile strength, f_t = 4.1 MPa.
- Steel modulus of elasticity, E_s = 205 GPa.

Oehlers reported a serviceability bending moment varying between 4.5 and 6.8 kN.m and an ultimate bending moment between 12.6 kN.m and 14.4 kN.m. The average value for the serviceability bending moment was 5.5 kN.m.

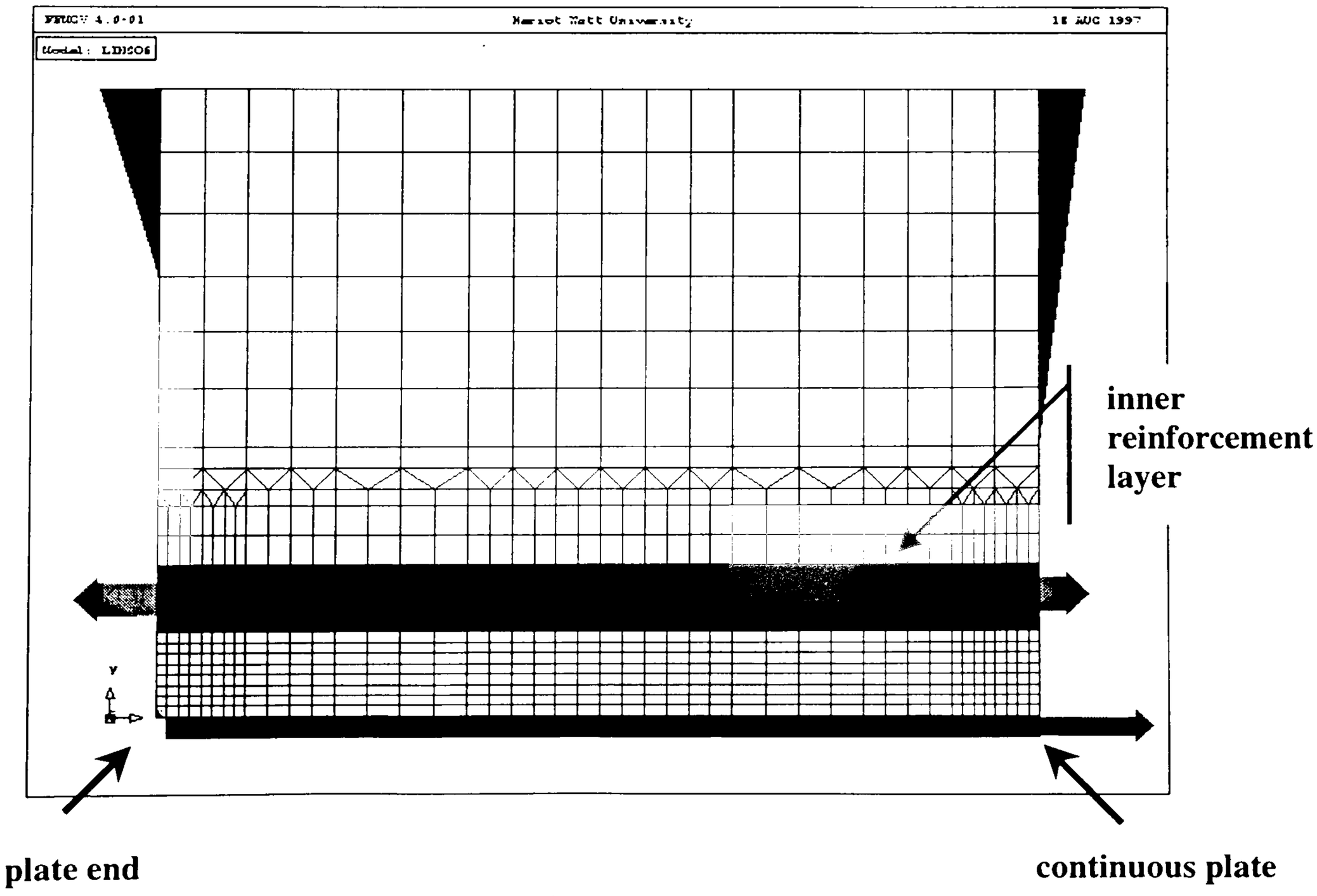

Fig. 5-6: 2D finite element model of a plated beam

Description of the finite element model

The mesh was made up of three different types of elements, Fig. 5-6:

- Quadrilateral 8-noded isoparametric plane elements (8x2 DOF) for the concrete.
- Triangular 6-noded isoparametric plane elements (6x2 DOF) for the concrete.
- Linear 3-noded beam elements (3x3 DOF) for the steel bars.

The concrete region subjected to compressive stress was modelled by a relatively coarse mesh of quadrilateral elements (squares of 20x20mm and rectangles of 10x20mm). The region under the neutral axis was modelled by a fine mesh of quadrilateral elements (ranging from 2.5x2.5mm to 5x5mm). The transition between the two regions was achieved by using triangular elements. Special care was devoted to keeping an acceptable aspect ratio for all the 2D elements, as it is known that distorted finite elements yield an over-stiff response. The triangular elements were placed outside the regions of stress concentration, as earlier linear models proved that the triangular elements were consistently introducing perturbations in the stress field because of the inevitable difference of directional bias between the rectangular and the triangular elements. Full integration scheme was adopted for all elements.

Cracking was simulated using smeared cracking along with Hordijk's exponential softening curve, (Eq. 2-47). A threshold angle of 90 deg. was chosen for the multi-directional crack model. The crack band width was calculated for the elements near to the tensile reinforcement layer using (Eq. 2-75).

The plate thickness may play an important role in the peeling failure. It was therefore decided that the plate should not be reduced to linear finite elements: 2D plane elements were used. The plate is curtailed at the left end of the model, while it is continuous at the right end. That is to say that no external load is applied to the left end steel element, while the right end steel element is subjected to a normal tensile force corresponding to the one calculated on the assumption that full transfer is achieved, Fig. 5-6.

Experimental results, Swamy et al. (1987)[146] and analytical studies, Jones et al. (1988)[137] showed that the thickness of the epoxy layer had little or no influence on the peeling failure. This is mainly due to the great difference between the values of the modulus of elasticity of steel and epoxy. It was therefore decided to ignore the epoxy layer in the model. Since debonding of the plate is not considered in this study, no ultimate bond criterion was introduced: full bond was assumed throughout the simulation. This is achieved by direct connection between steel elements and concrete elements.

A sophisticated model of the reinforcement was designed. Link elements were used to tie the 1D steel elements to the 2D concrete elements. Link elements are linear finite elements, with fictitious cross-sectional properties, aimed at connecting different part of a finite element mesh. The link elements used in the non-linear model have the following properties:

- An infinitely small cross-sectional area was chosen (10^{-10} m^2), so that no axial forces may be transmitted through these elements.
- A high inertia in bending is chosen, so that the elements remain straight throughout the simulation.

The link elements were introduced in the mesh, perpendicularly to the beam elements modelling the reinforcing bars, at the location of the ribs, every 10 mm along the bars. They were rigidly clamped to the beam elements and were connected to the surrounding concrete elements, in a band corresponding to the actual bar diameter, Fig. 5-7.

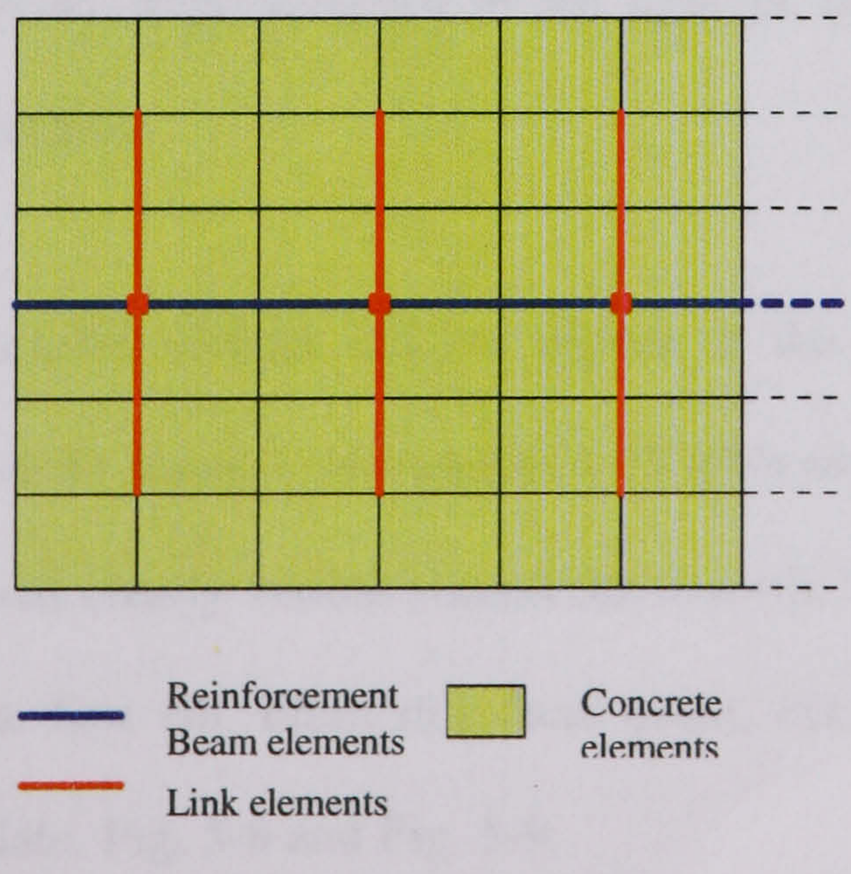

Fig. 5-7: Reinforcement modelling by introduction of link elements

This modelling technique has the following characteristics:

- It allows axial tensile forces to be transmitted from the reinforcing bars to the surrounding concrete.
- The steel does not carry any stresses in the vertical direction.
- The cross-sections of the reinforcing bars are free to rotate.
- The actual diameter of the bars is taken into account.

The drawback of this model is that 2D behaviour was assumed, i.e. the concrete lying at the same level as the reinforcing bars was assumed to exhibit the same horizontal displacement as the bars, throughout the breadth of the beam. It is obvious that this is not what actually happens, since the concrete a few millimetres away from the bar is less influenced than the concrete directly in contact with it. However it was assumed that the effect of this 3D behaviour is negligible and it has little influence on the overall mechanism.

The simulation was carried out using the regular Newton-Raphson method. A total of 50 steps were performed. Most of the steps had a size of 0.025 times the experimental average serviceability load. For convergence the internal energy variation was checked. Convergence was reached at each step up to 1.1 times the average serviceability load, M_s.

Interpretation of the results of the model

The outcome of this simulation provides a valuable insight into the phenomenon up to the serviceability load. The results were analysed in the light of the experimental observations presented in the preceding section.

As expected, the critical tensile stresses did not appear at the interface between plate and concrete, where the peak tensile stress at M_s reached 1.75 MPa only. However, a concentration of vertical tensile stresses was clearly visible around the first rib. The core of the tensile region was located just behind the first rib. From this focal point, the tensile region branched and radiated towards the steel plate, Fig. 5-8 and Fig. 5-9.

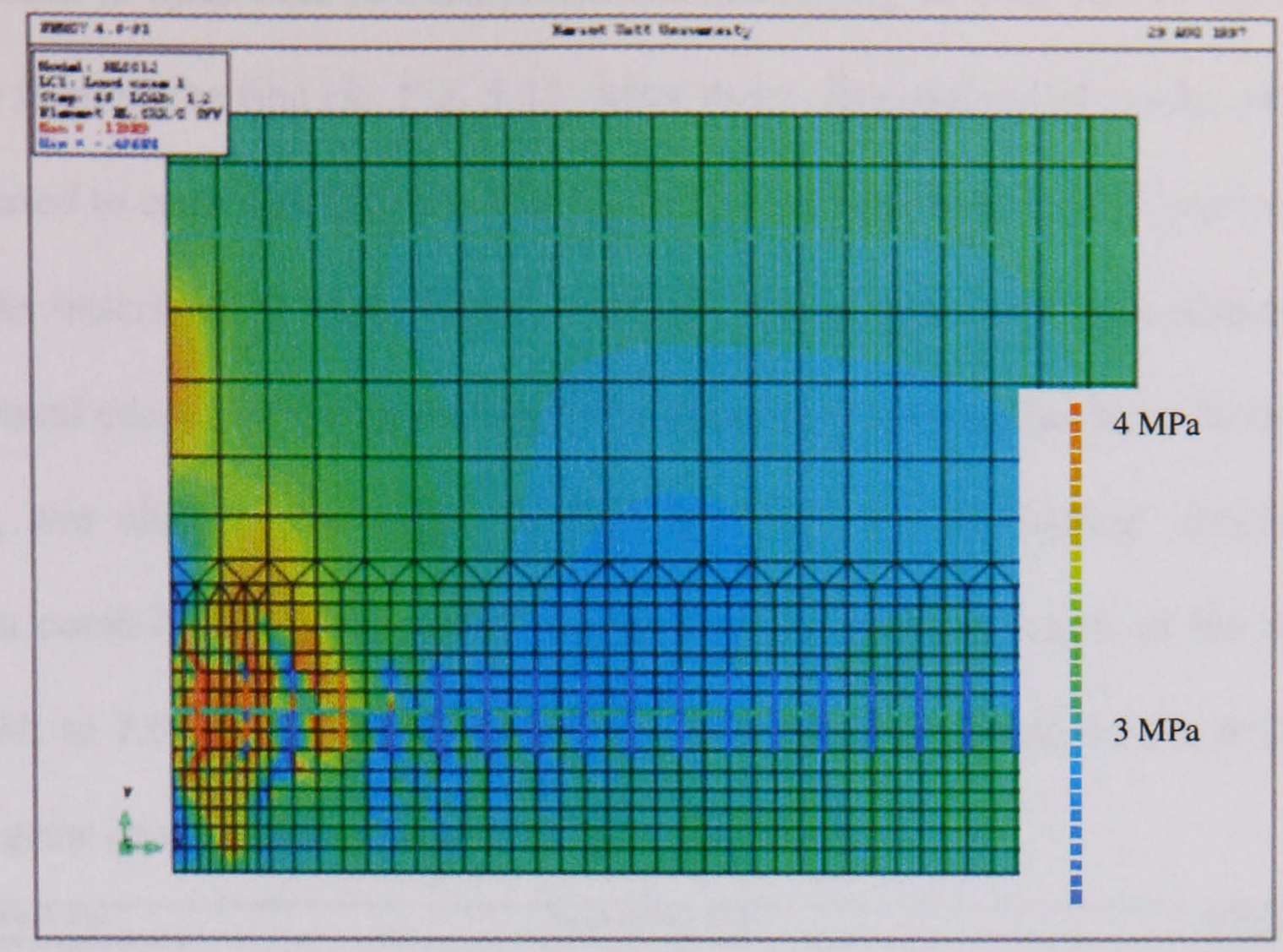

Fig. 5-8: Distribution of vertical stresses – tensile hoop stresses concentration

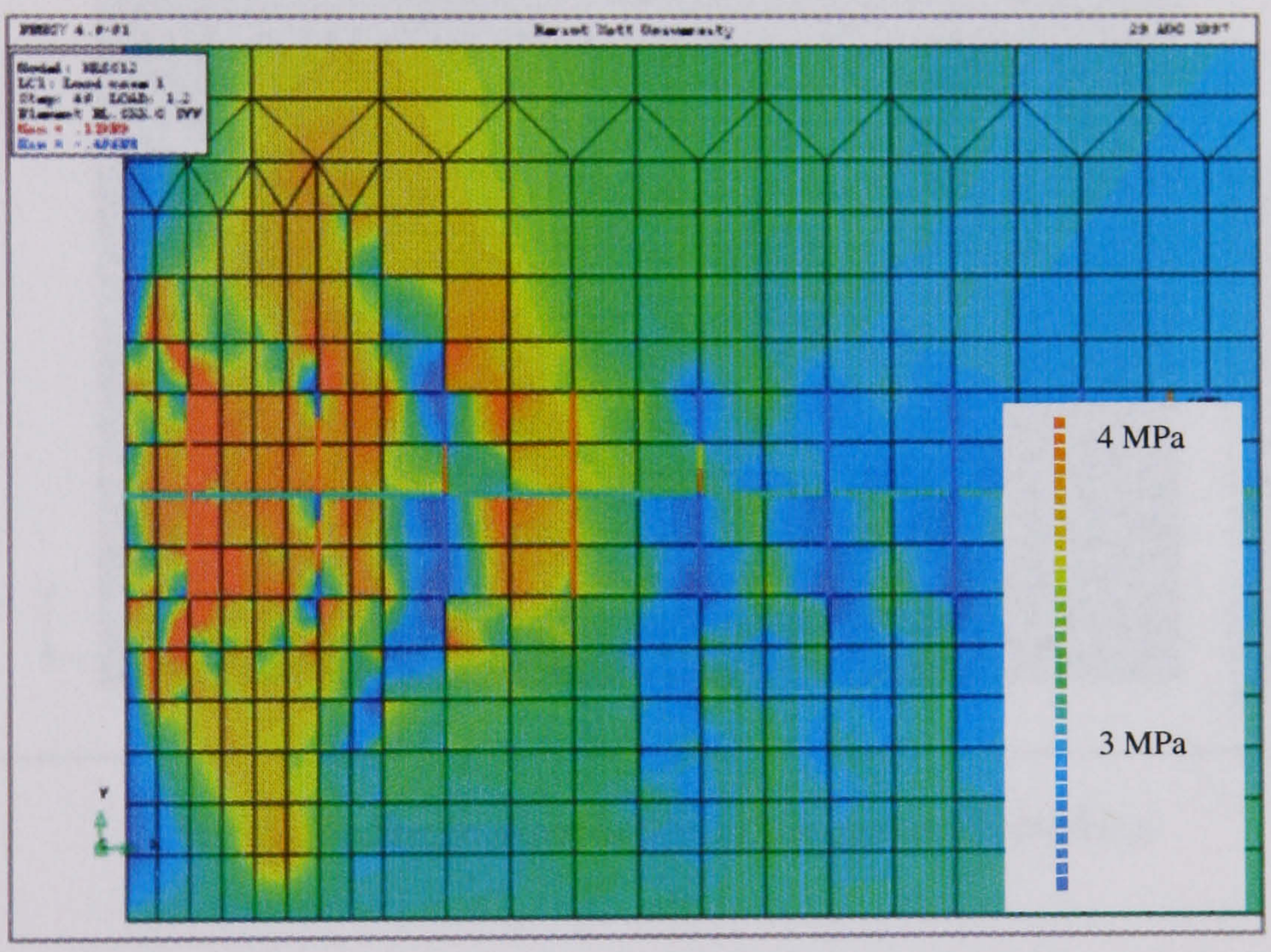

Fig. 5-9: Vertical stresses - zoom on the hoop stress concentration

Considering the shape of the σ_y distribution, and the small value of the tensile interface stresses, it becomes difficult to justify the development of the peeling crack by the bending of the steel plate, as suggested in analytical models developed by several researchers[137,139]. On the other hand, the outcome of this analysis clearly pointed out the prominent role played by the bond mechanism of the inner reinforcement in the peeling failure.

The first cracks to open were two horizontal notches arising on each side of the bar and rapidly stopping in front of the first rib, Fig. 5-11. After these, diagonal radial cracks, at the location of the ribs, started to open significantly, Fig. 5-10. These cracks were the 2D version of the conical radial cracks described by Goto. These V-shaped cracks had their bases directed towards the nearest flexural crack and the angle they form with the reinforcement axis, 50 to 60 deg. in the simulation, was close to the angle observed by Goto. As in Tepfers' model, these cracks generated a comb-like structure aimed at resisting the pull-out action of the reinforcing bar. From 0.7 M_s to 1.0 M_s, the conical cracks lengthened. The conical cracks at the third rib, in particular, grew quicker and opened wider than the others.

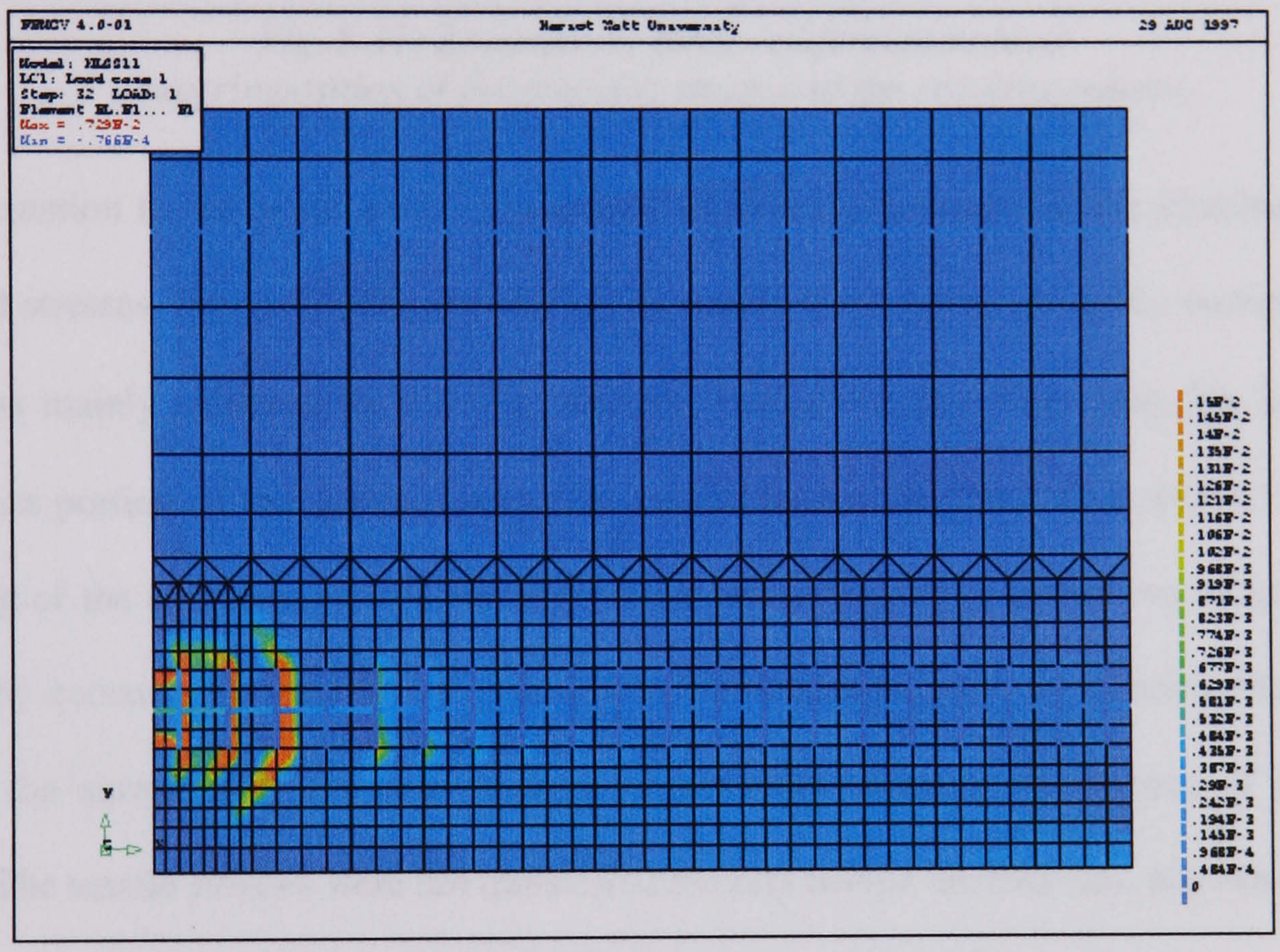

Fig. 5-10: Strain distribution of the smeared cracking

The load level 1.0 M_s marked the start of new phenomena: a flexural crack began to form 160 mm away from the plate end, and the initial horizontal notches, formed at the face of the first flexural crack, began suddenly to propagate up to the second rib, thus marking the onset of stable peeling. The final stage, from 1.0 M_s to 1.2 M_s, was characterised by the two following features:

- The third conical crack reached the steel plate at the location of the tensile σ_y stress peak.
- The conical cracks emerging from the 10th and 11th ribs met the newly formed flexural crack.

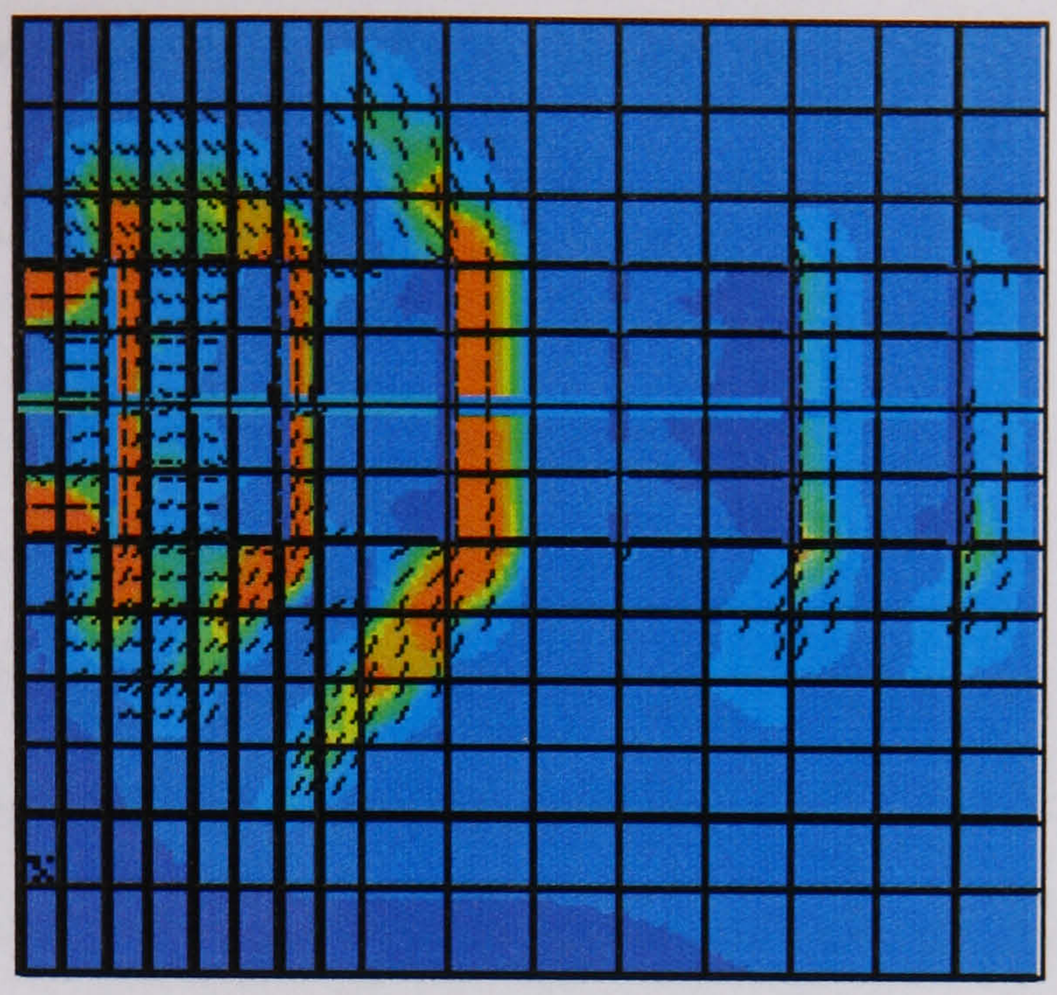

Fig. 5-11: Zoom on the inner reinforcement level
superimposition of the cracking strain and the cracking pattern

An explanation to the crack patterns described above can be sought in the distribution of the principal stresses, Fig. 5-12. The transfer of the tensile force in the bar to the concrete and the plate was mainly achieved by direct σ_x stresses, behind the first three ribs. Up to 0.5 M_s, a significant portion of the tensile forces was carried by the concrete. From 0.5 to 0.7 M_s, the softening of the concrete, located just behind the ribs, reduced the proportion of tensile forces carried by concrete. Beyond 0.7 M_s, the way in which tensile forces were transmitted from the bars to the surrounding concrete changed significantly with the appearance of the conical cracks. The tensile stresses were not transferred directly behind the first ribs, anymore, but, were rather spread in a plume-like shape on either side of the reinforcement layer. This different mechanism of transfer was achieved due to the comb-like structure created by the emergence of the conical cracks. The pull-out force was transmitted in compression through the teeth of the comb, acting like diagonal struts, then, slightly away from the bar-to-concrete interface, this diagonal compression was transformed into horizontal tension and tensile hoop stresses around the bar (represented here by σ_y).

The opening of the conical cracks around the first three ribs occurred with the shift of the uncracked type of transfer to the fifth and sixth ribs. This can be interpreted as a progression of the softening process. It can therefore be deduced that, in the case of the unplated beam, conical

cracking alone is effective enough to reduce dramatically the bond, thus decreasing significantly the transfer of tensile forces. However, this does not infer global failure, since the transfer is not needed for the global equilibrium of the beam. On the contrary, in the case of the plated beam, the transfer of tensile forces to the concrete is necessary to allow the plate to take up part of the global bending moment. As a matter of fact, at least the fixed portion of tensile forces, that has to be carried by the plate after transfer (determined by the characteristics of the plated cross-section), must transit through concrete. Consequently, while the magnitude of the tensile force increases, softening near the face of the first flexural crack implies that a longer and longer section of reinforcement is needed to achieve the amount of transfer required.

It is now possible to understand why the analysis cannot converge beyond 1.2 M_s. The emergence of a new flexural crack 16 cm away from the plate end reduced the transfer length available (initially of 20 cm). In the same time, the cracking pattern shows that 16 cm at least were already required to transfer the tensile forces towards the plate. Consequently, the plated beam could not take any increase of load. The failure by exhaustion of the anchoring capacity was inevitable.

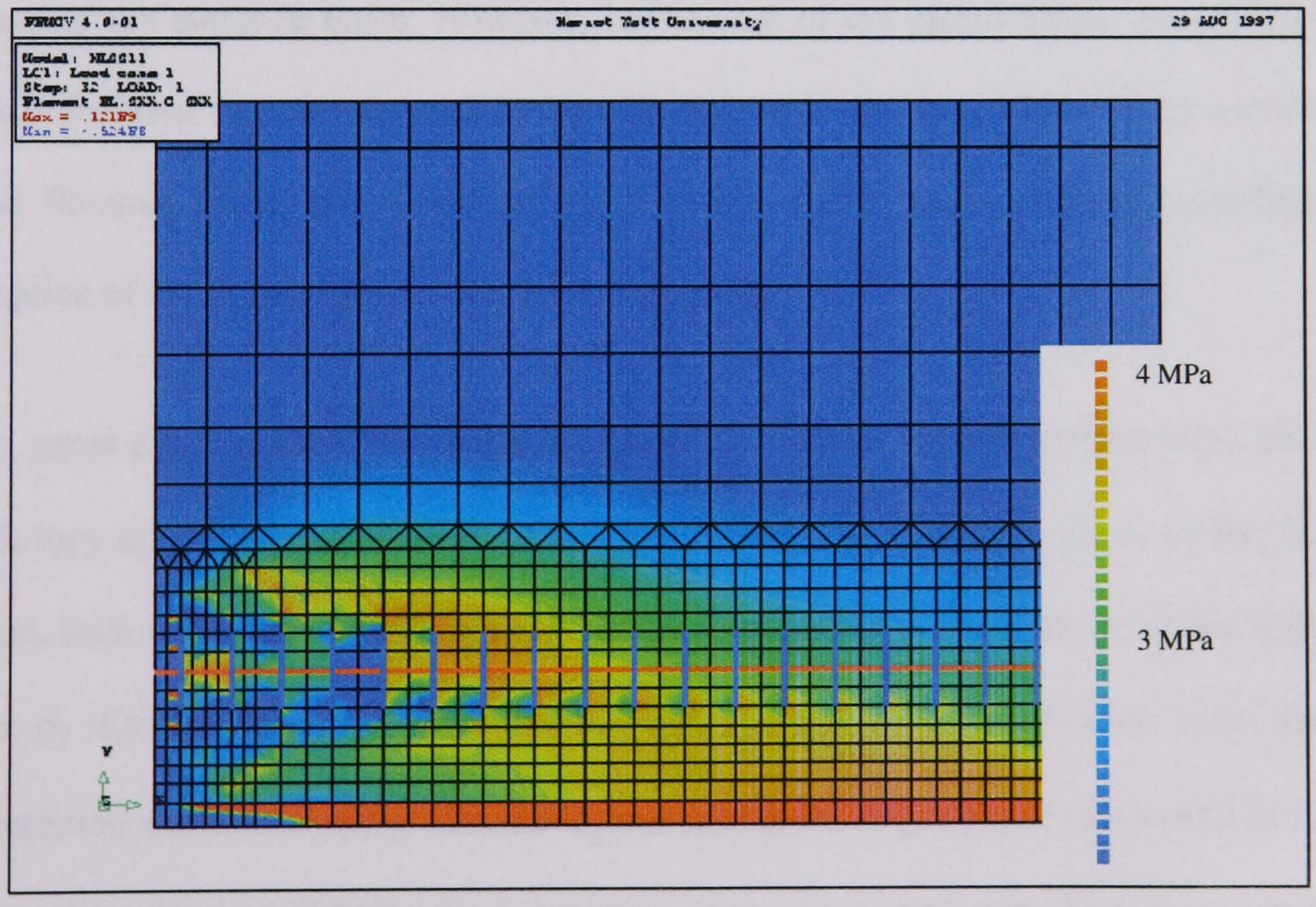

Fig. 5-12: Principal tensile stress – transfer of longitudinal tensile forces to the plate

From the distribution of principal stresses, Fig. 5-12, it is possible to draw schematically the

stress path along the beam, Fig. 5-13. The diagram explains how the tensile stresses redistributed from the unplated section to the plated one.

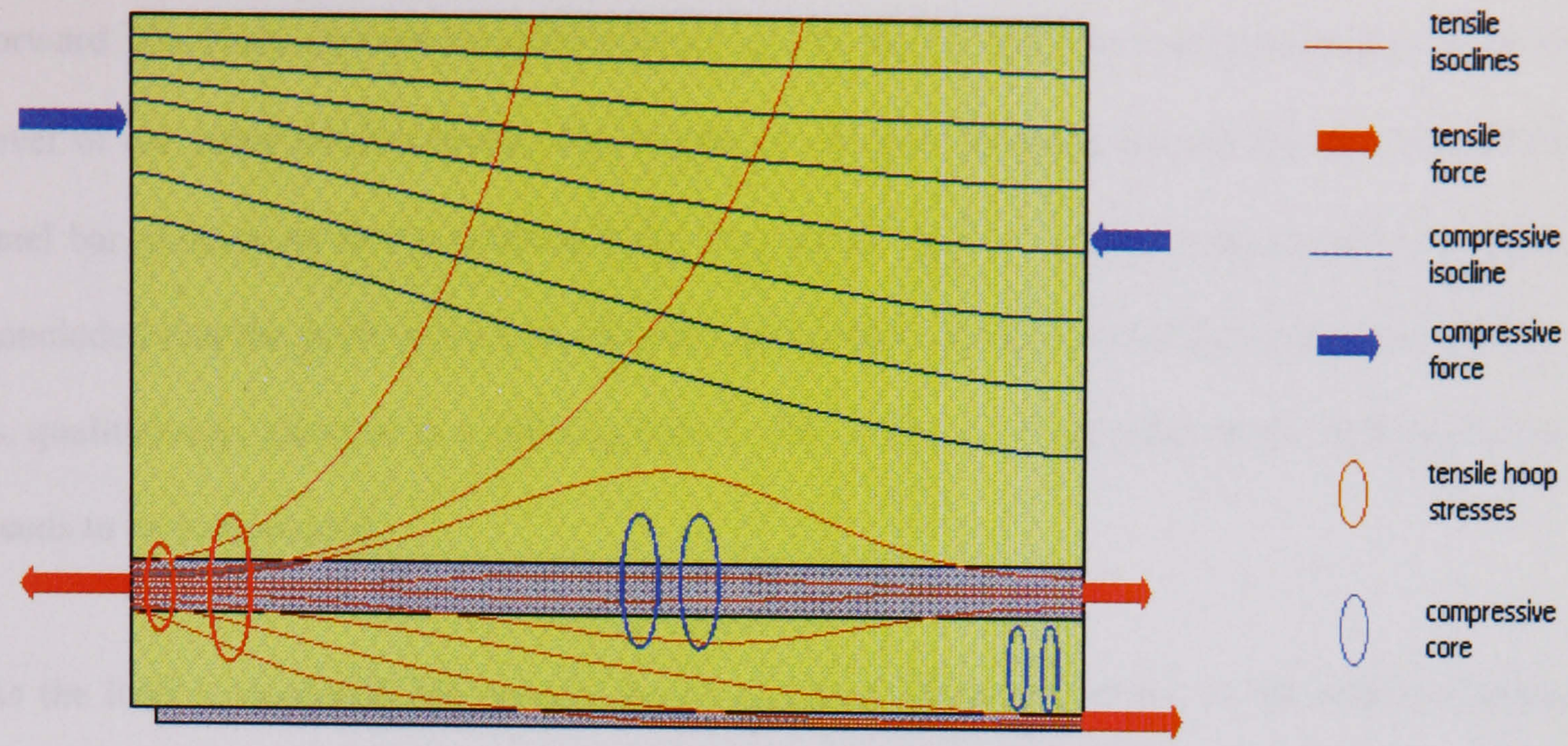

Fig. 5-13: Schematic drawing of the principal stress flow in a plated beam

At the section of the first flexural crack (unplated section), all the tensile stresses were assumed to be transmitted through the reinforcing bars. Beyond this section, part of the tensile forces were transferred to the surrounding (softened) concrete, as it would naturally happen, even in the case of the unplated beam. However, in the case of the plated beam, most of the tensile forces transferred to concrete must eventually end up in the steel plate. In the section of the second flexural crack, the redistribution of tensile forces was achieved according to the assumption of the plane cross-section remaining plane.

The σ_y stress concentration, Fig. 5-9, corresponds to Tepfers' splitting hoopstresses. In Tepfers' model, they take the form of tensile rings surrounding the reinforcing bars. In the 2D model adopted, such rings cannot be fully represented. Consequently, the splitting forces appear only in the σ_y distribution. It is important to bear in mind that, in practice, some tensile σ_z concentration must arise along with the σ_y concentration, although the 2D model is unable to simulate them. But, considering the consistency of the simulation with the experimental results, it will be assumed that the inability of the model to simulate the actual 3D behaviour does not affect significantly the magnitude and the distribution of the σ_y stresses.

Conclusions

Following these observations, a global explanation of the onset of the peeling crack can be put forward. The finite element simulation confirms that the critical stress concentration arises at the level of the inner reinforcement. The tensile σ_y stresses predicted around the first ribs of the steel bar correspond to the splitting hoop stresses of Tepfers' model. Consequently, it can be concluded that the peeling crack developing horizontally at the level of the inner reinforcement is, qualitatively, identical to a splitting failure. The influence of the plate on the splitting failure needs to be investigated.

As the load is increased, the transfer length becomes larger and larger, as the softened region progresses along the bar. The capacity of the bond mechanism to cope with the load increase is limited by the length available between the first flexural crack and the next flexural crack, formed further along the plate. If the softened bond mechanism is unable to take up any further load increase, because a flexural crack has arisen in its path, as occurred in the simulation, another mechanism has to overtake. At this point, the hoop stresses, induced by the conical internal cracks, exceed the concrete tensile strength. Consequently, a horizon crack develops and propagates at the reinforcement level up to the next flexural crack, resulting in a total loss of bond in the block of concrete between the two flexural cracks. Thus, the problem is shifted to the next concrete block, as if the plate had been curtailed at this new location. The same failure mechanism will once again take place, allowing for an increase in the load, only if the flexural cracks are located further apart than in the first case. Considering that, in tension tests, primary cracks (analogous to flexural cracks) arise with a random spacing comprised in the approximate range L_{max} and 2 L_{max}, as defined by (Eq. 3-8), it may be suggested that flexural cracks arising along the plated beam have the same type of spatial distribution. This would explain why:

- For identical specimens, the serviceability load exhibits experimentally a great scatter between half of the ultimate bending moment, $½M_u$, and M_u.
- when enough tests have been carried out on identical specimens, M_u is approximately twice as large as the minimum, M_s.

This does mean that, while the ultimate load would depend on L_{max}, the onset of the peeling crack would depend on the length of the first concrete block, which could vary between L_{max} and $2\ L_{max}$.

5.3. Application of the Fracture Mechanics Model

It appears from experimental observation that peeling is always caused by splitting of the concrete at the level of the inner reinforcement. As concluded in the previous section, this suggests that peeling is the same cracking mechanism as splitting in tension specimen and splitting in the flexural-shear failure of beams without stirrups. Consequently, the fracture mechanics model, which performed satisfactorily with these phenomena, can be applied to the peeling failure. The distinction made by Oehlers between peeling in pure bending and peeling in the flexural-shear mode is adopted in the following.

5.3.1. Peeling in pure bending mode

When peeling occurs in pure bending, the plate separates from the beam along with the concrete cover, thus releasing the inner reinforcement from its concrete encasement. This results in a dramatic decrease in the local flexural stiffness of the beam. If the energy balance of the system is considered, peeling occurs at a load for which exactly enough energy is released by the softening system to feed the fracture energy required by splitting.

Similarly to the splitting failure of tension specimens, the advance of peeling does not change the topology of the problem. Therefore, the transformation occurs at constant load in a critical state of equilibrium. This means that (Eq. 2-16) can be used to determine the critical peeling load. An approach very similar to the one used in section 3.3.2. is adopted.

Consider an uncracked plated beam in the vicinity of the plate end, Fig. 5-14, the flexural stiffness of the beam is discontinuous at the plate end, changing from unplated cross-section to plated cross-section. Both stiffnesses however, are very high as no cracking is present and the inner reinforcement acts compositely with the surrounding concrete.

The propagation of the splitting crack on a length δe results in the steel to be released for a length δe in the direction of the plate, resulting locally in a significant decrease in the flexural stiffness consisting only of the steel bar and the concrete compression area, Fig. 5-15. Therefore, a hinge is formed locally with rotation at constant load, with the incremental angle of rotation, $\delta\theta$, proportional to the crack extent, δe.

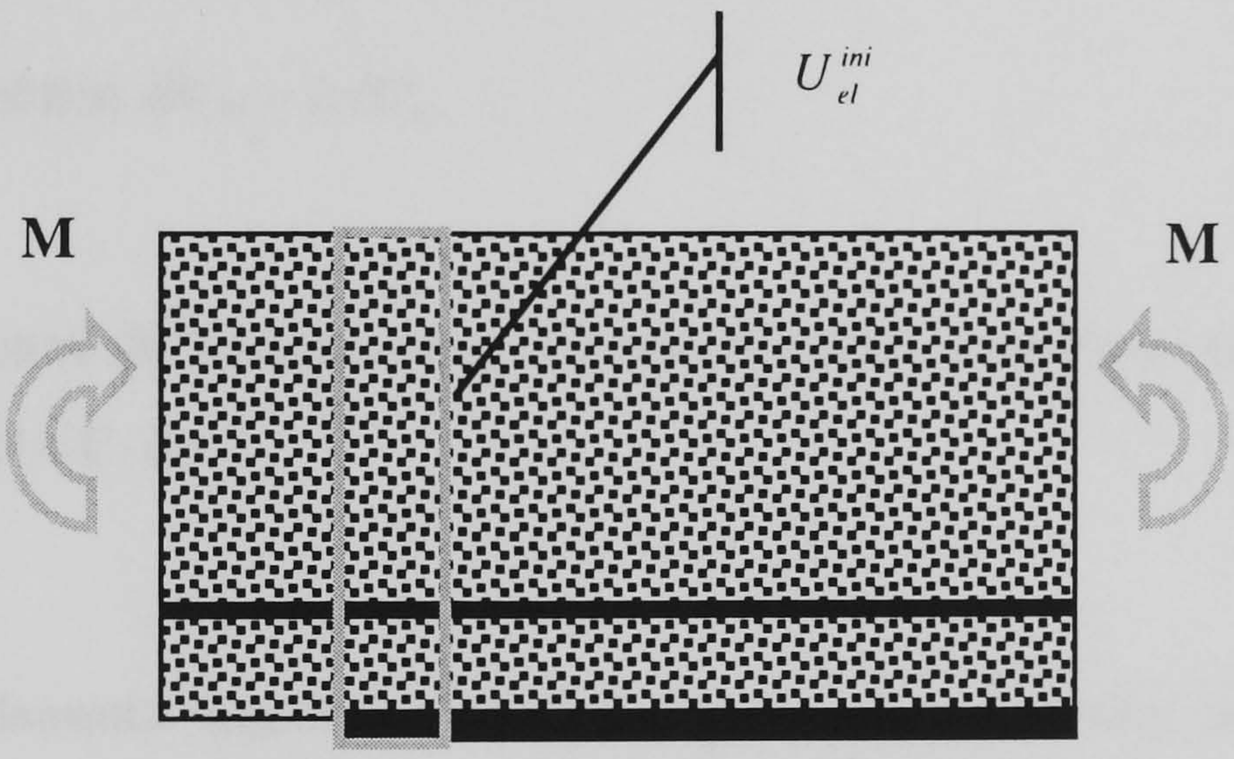

Fig. 5-14: Plated beam before peeling

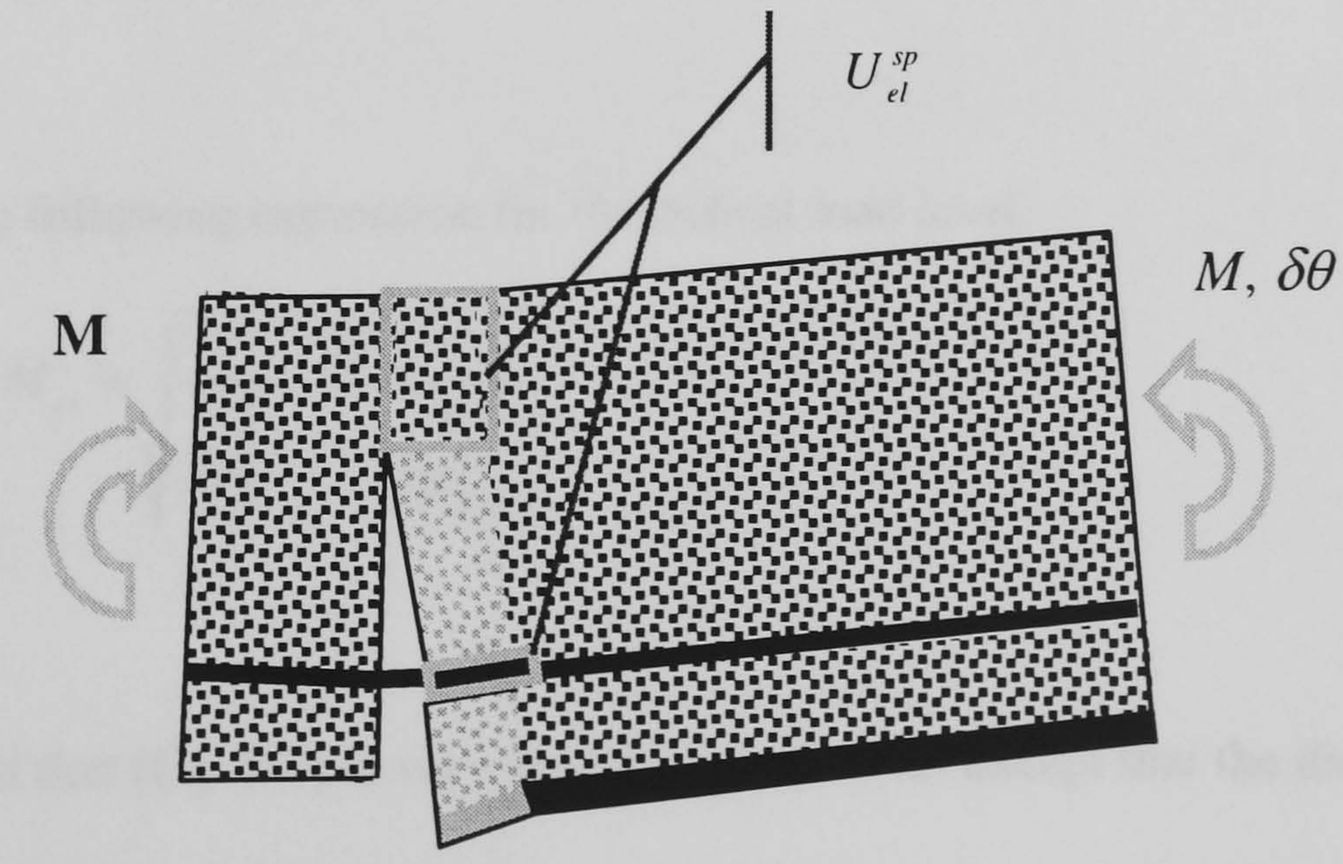

Fig. 5-15: Plated beam after splitting

During this transformation, the variation, of the strain energy is due to the decrease in the flexural stiffness:

$$\delta U_{el} = U_{el}^{sp} - U_{el}^{ini} \qquad \textit{(Eq. 5-3)}$$

$$= \frac{1}{2} M^2 \left(\frac{1}{(EI)_{sp}} - \frac{1}{(EI)_{ini}} \right) \cdot \delta e \qquad \textit{(Eq. 5-4)}$$

The work of external bending moment on the incremental angle of rotation results from the local softening of the structure:

$$\delta W_{ext} = M \cdot \delta\theta \qquad \textit{(Eq. 5-5)}$$

$$= M^2 \left(\frac{1}{(EI)_{sp}} - \frac{1}{(EI)_{ini}} \right) \cdot \delta e \qquad \textit{(Eq. 5-6)}$$

It can be verified that $\delta W_{ext} = 2\ \delta U_{el}$.

The consumption of the fracture energy is proportional to the splitting crack extent:

$$\delta G = \Gamma \cdot \delta e \qquad \textit{(Eq. 5-7)}$$

Using the fundamental equation of fracture mechanics at splitting propagation, the energy balance writes:

$$\delta W_{ext} - \delta U_{el} - \delta G = 0 \qquad \textit{(Eq. 5-8)}$$

which yields the following expression for the critical load level:

$$\therefore M_{cr} = \sqrt{\frac{2\Gamma}{\frac{1}{(EI)_{sp}} - \frac{1}{(EI)_{ini}}}} \qquad \textit{(Eq. 5-9)}$$

It can be noticed that (Eq. 5-9) is very similar to (Eq. 3-42) except that the direct stiffness (EA) is replaced by the flexural stiffness (EI).

5.3.2. Peeling in the flexural shear mode

In the flexural-shear mode, the peeling failure is very similar to the flexural-shear failure of reinforced concrete beams without stirrups. After a diagonal crack has formed in the cross-section of the plate end, splitting occurs, propagating towards the plate, thus releasing the inner reinforcement. The release of the steel bar allows the diagonal crack to further open and extend resulting in rotation, $\delta\theta$, about the tip of the diagonal crack, Fig. 5-16.

A splitting crack of extent δe results in an incremental rotation, $\delta\theta$, proportional to δe. Peeling occurs at a load such that just enough energy is released by the system during the transformation to feed the splitting crack extension. This mechanism is identical to the flexural-shear failure mode of beams without stirrups, except that the location of the critical diagonal crack is predefined by the plate end.

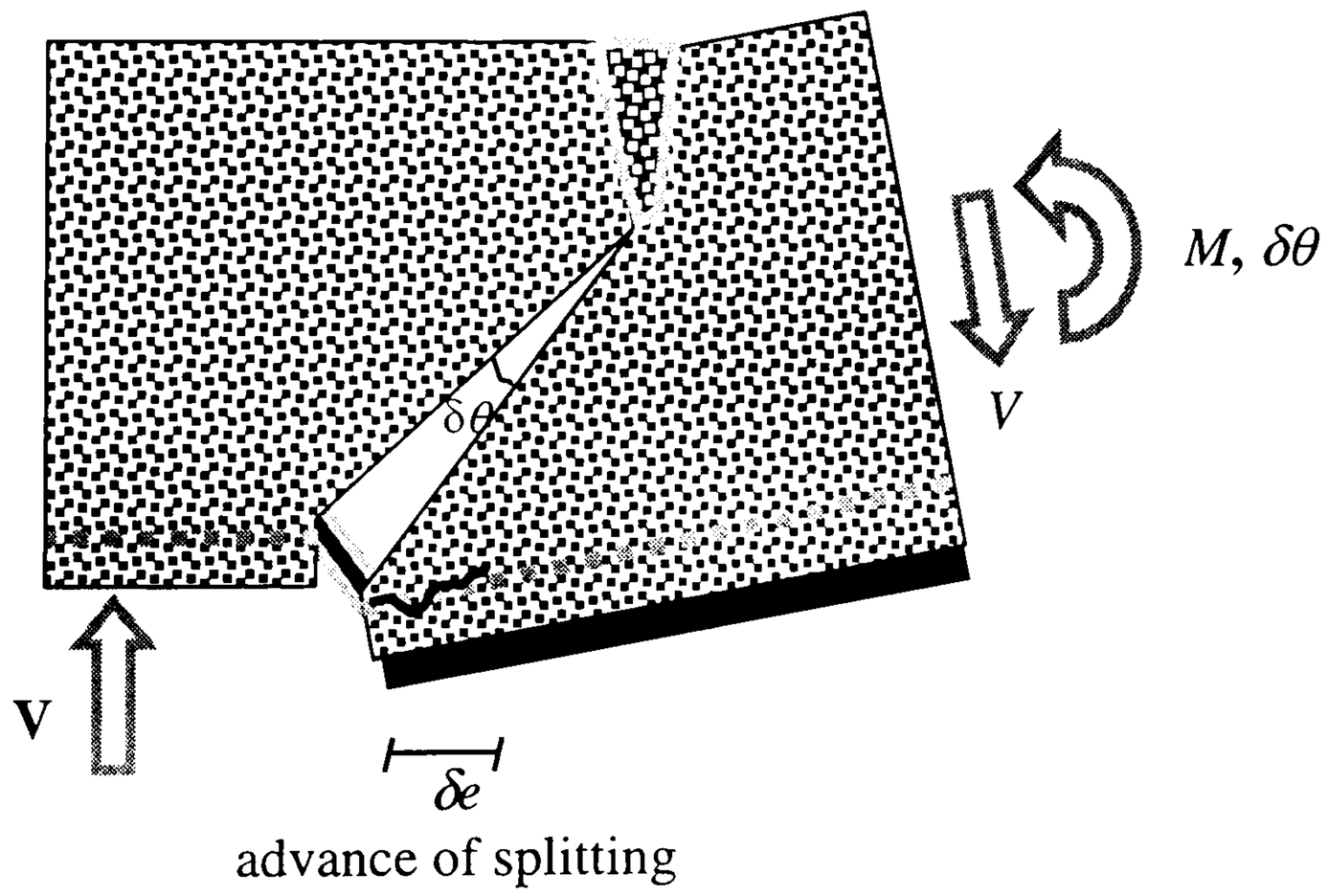

Fig. 5-16: Failure mechanism of the plated beam failing in flexural shear mode

If the same notation as in section 4.3.3. is adopted, and the distance between the support and the plate end is d_{pl}, then the critical shear force for a plated beam without stirrups can be deduced from (Eq. 4-35):

$$V_{cr} = \sqrt{\frac{9}{13} + 2\frac{\gamma}{\beta}} \cdot \frac{\beta \cdot H}{d_{pl} + \beta \cdot H} \cdot \sqrt{\Gamma A_s E_s} \qquad \textit{(Eq. 5-10)}$$

A similar approach can be adopted to determine the critical shear force of plated beams with stirrups. An additional vertical force representing the action of the stirrups, F_v, is added in the equilibrium equations, Fig. 5-17. The discrete distribution of stirrups is smeared over the length of the beam, thus considering an area of stirrups of A_v/s per unit length, where A_v is the area of one stirrup and s is the stirrup spacing. The stirrups are assumed to behave linear elastically. The opening of the diagonal crack is assumed to be linear, therefore the point of application of the stirrup forces is at two-third of the crack length from the crack tip. In the following the angle of the diagonal crack is assumed to be 45 deg.

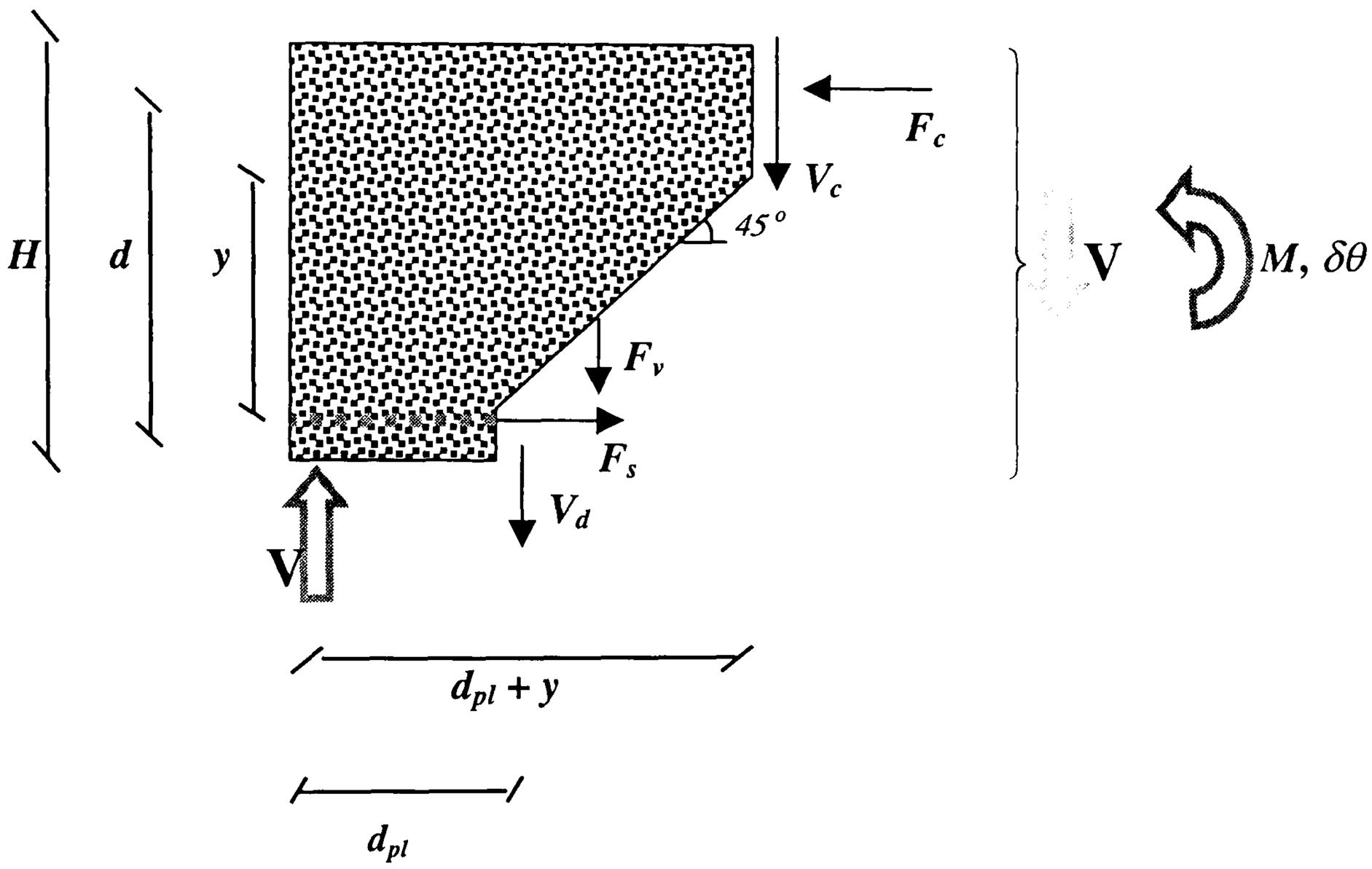

Fig. 5-17: Free body diagram and notation definition

The smeared axial stiffness of the stirrups is determined assuming that the unbonded length of the stirrups is known, equal to δ_v:

$$k_v = \frac{A_v E_s}{s \delta_v} \qquad \textit{(Eq. 5-11)}$$

Consequently, the forces acting on the free-body diagram can be formulated in function of θ:

$$\begin{cases} F_v = \int_0^y k_s \, 2t\theta \cdot dt = \dfrac{E_s A_v}{s \delta_s} y^2 \theta & \textit{(Eq. 5-12)} \\ F_s = \dfrac{E_s A_s}{\delta_s} \Delta u_s = \dfrac{E_s A_s}{\delta_s} y\theta & \textit{(Eq. 5-13)} \\ V_d = \dfrac{G_s \Sigma_s}{\delta_s} \Delta v_s = \dfrac{9}{26} \dfrac{E_s A_s}{\delta_s} y\theta & \textit{(Eq. 5-14)} \end{cases}$$

The equilibrium of the free-body diagram is satisfied in the horizontal direction, the vertical direction and about the tip of the diagonal crack:

$$\begin{cases} F_s = F_c & \textit{(Eq. 5-15)} \\ V_c + V_d + F_v = V & \textit{(Eq. 5-16)} \\ V \cdot \left(d_{pl} + y\right) = V_d \cdot y + F_s \cdot d + F_v \cdot \dfrac{2}{3} y & \textit{(Eq. 5-17)} \end{cases}$$

Substituting (Eq. 5-12) to (Eq. 5-14) in (Eq. 5-17) results in the equation:

$$V \cdot \left(d_{pl} + y\right) = \left(\frac{9}{26} + \frac{\gamma}{\beta} + \frac{2}{3} \frac{A_v}{A_s} \frac{\delta_s}{\delta_v} \frac{\beta h}{s} \right) \frac{E_s A_s}{\delta_s} \beta^2 H^2 \theta \qquad \textit{(Eq. 5-18)}$$

If the expression for θ is deduced from (Eq. 5-18) and differentiated about δ_s, the following equation is obtained:

$$\delta\theta = \delta \left(\frac{\delta_s}{A_s E_s} \frac{V\left(d_{pl} + y\right)}{\left(\frac{9}{26} + \frac{\gamma}{\beta} + \frac{2}{3} \frac{A_v}{A_s} \frac{\delta_s}{\delta_v} \frac{\beta h}{s} \right) \beta^2 H^2} \right) = \frac{V\left(d_{pl} + y\right)}{A_s E_s \left(\frac{9}{26} + \frac{\gamma}{\beta} \right) \beta^2 H^2} \left(1 + \frac{2}{3\left(\frac{9}{26} + \frac{\gamma}{\beta} \right)} \frac{A_v}{A_s} \frac{\delta_s}{\delta_v} \frac{\beta H}{s} \right)^{-2} \delta e$$

(Eq. 5-19)

The fundamental principal of fracture mechanics can now be applied to satisfy the energy balance of the transformation. Similarly to (Eq. 4-32) and (Eq. 4-33) of section 4.3.3:

$$\delta W_{ext} = 2 \delta G \qquad \textit{(Eq. 5-20)}$$

$$\left(d_{pl} + y\right) V_{crit} \cdot \delta \vartheta = 2 \Gamma \cdot \delta e \qquad \textit{(Eq. 5-21)}$$

Substituting (Eq. 5-19) in (Eq. 5-21) and assuming that $\dfrac{\delta_s}{\delta_v} = \dfrac{\Phi_s}{\Phi_v}$ initially, where Φ_s and Φ_v are the diameter of the main reinforcement and the diameter of the stirrups respectively, it is possible to determine an expression for the critical shear force for a plated beam with stirrups:

$$V_{cr}^2 = \left(1 + \frac{2}{3\left(\frac{9}{26} + \frac{\gamma}{\beta} \right)} \frac{A_v}{A_s} \frac{\Phi_s}{\Phi_v} \frac{\beta H}{s} \right)^2 \left(\frac{\beta H}{d_{pl} + \beta H} \right)^2 \left(\frac{9}{13} + 2 \frac{\gamma}{\beta} \right) A_s E_s \Gamma \qquad \textit{(Eq. 5-22)}$$

$$V_{cr} = \sqrt{\frac{9}{13} + 2\frac{\gamma}{\beta}} \left(1 + \frac{2}{3\left(\frac{9}{26} + \frac{\gamma}{\beta}\right)} \frac{A_v}{A_s} \frac{\Phi_s}{\Phi_v} \frac{\beta H}{s} \right) \left(\frac{\beta H}{d_{pl} + \beta H} \right) \sqrt{A_s E_s \Gamma} \qquad \textit{(Eq. 5-23)}$$

with V_{crit}, Γ, A_s and E_s in S.I. or alternatively V_{crit} in kN, Γ in kN.m/m, A_s in mm^2 and E_s in GPa.

It is possible to make a certain number of assumptions without losing much of the generality of the formula:

$d = \gamma.H = 0.9\ H$

$y = \beta.H = 0.8\ H$

(Eq. 5-23) then becomes:

$$V_{cr} = 1.372 \cdot \left(1 + 0.363 \frac{A_v}{A_s} \frac{\Phi_s}{\Phi_v} \frac{H}{s} \right) \frac{H}{d_{pl} + 0.8H} \sqrt{A_s E_s \Gamma} \qquad \textit{(Eq. 5-24)}$$

with all variables in S.I.

The further assumption of d_{agg} = 20 mm can be made and the CEB-FIP formula for the assessment of the fracture energy, (Eq. 2-40), can be used:

$$V_{cr} = 9.515 \cdot \left(1 + 0.363 \frac{A_v}{A_s} \frac{\Phi_s}{\Phi_v} \frac{H}{s} \right) \frac{H}{d_{pl} + 0.8H} f_c^{0.35} \sqrt{A_s E_s \left(b + \alpha \frac{A_{cc}}{r_s} \right)} \qquad \textit{(Eq. 5-25)}$$

with V_{crit} in kN, f_c in MPa, A_s in m^2, E_s in GPa and b in mm,

and where $(b + \alpha A_{cc}/r_s)$ is the assessment of the fractured area per unit length extension of the peeling crack.

Once more the difficulty resides in the assessment of Γ, which has been reduced here to the determination of the factor α. It is believed that α, as a measure of the level of damaged caused by conical cracking, is influence by several parameters. Considering the mechanics of the conical crack formation, as observed in the finite element simulation of section 3.3., it is believed that the two major parameters influencing α are the concrete cover and the tensile strain of the steel bar, inasmuch as the first parameter controls the distance to which the conical

crack can radiate from the bar, and the second parameter controls the crack mouth opening of the conical cracks. In the following the concrete cover will be ignored as it is usually large enough to allow full development of the conical crack, and the factor α will be made entirely dependent on the tensile strain of the steel bar, through a linear relation.

5.4. Benchmarking against Experimental Data

The validity of the formulae derived analytically must be tested against experimental data to confirm the assumed modes of failure. Many experimental programs on plated beams have been carried out over the last twenty years. Both steel plates and FRP plates have been tested, revealing that the modes of failure for the two types of plates are identical. Consequently, experimental data of plated beams failing in the peeling mode have been gathered, including both steel and FRP plates, plates ending either in the pure bending zone or in the shear span, beams with or without stirrups, and ribbed or plain reinforcing bars. Analytical and experimental results have been compared and statistical analyses carried out.

5.4.1. Peeling in pure bending

Considering the assumed modes of failure, peeling in pure bending appears a simpler failure mechanism than flexural-shear peeling. This mode of failure is therefore considered first and (Eq. 5-9) is compared with experimental data.

Oehlers (1990)[143] reported the results of a set of experiments where 32 plated beams had been tested in pure bending. All were plated with steel plates. The different parameters were varied within the following limits:

- depth of the beam, 150 mm < H < 240 mm
- breadth of the beam, 120 mm < b < 125 mm

- reinforcement cover, 10 mm < c < 50 mm
- reinforcement diameter, 12 mm < d_b < 20 mm
- plate thickness, 2 mm < t < 15 mm
- breadth of the plate, 25 mm < b_p < 125 mm
- concrete tensile strength, 2.7 MPa < f_t < 4.9 MPa
- concrete modulus of elasticity, 20 GPa < Ec < 32 GPa

All the beams failed in the peeling mode, displaying cracking patterns similar to those of Fig. 5–4. Two critical load levels were recorded. Firstly, the bending moment, M_s, at which the splitting crack became visible and started to propagate in a stable way, termed the serviceability load by Oehlers. Secondly, the bending moment M_u, at which the beam failed. M_u is generally approximately twice as large as M_s. As it was shown in the analytical approach that peeling in pure bending is a critically stable phenomenon, and as it was proposed in the phenomenological approach that the first cracking load was dependent on the spacing between the two first flexural cracks, it is considered that the load predicted by the analytical approach is the serviceability load, M_s.

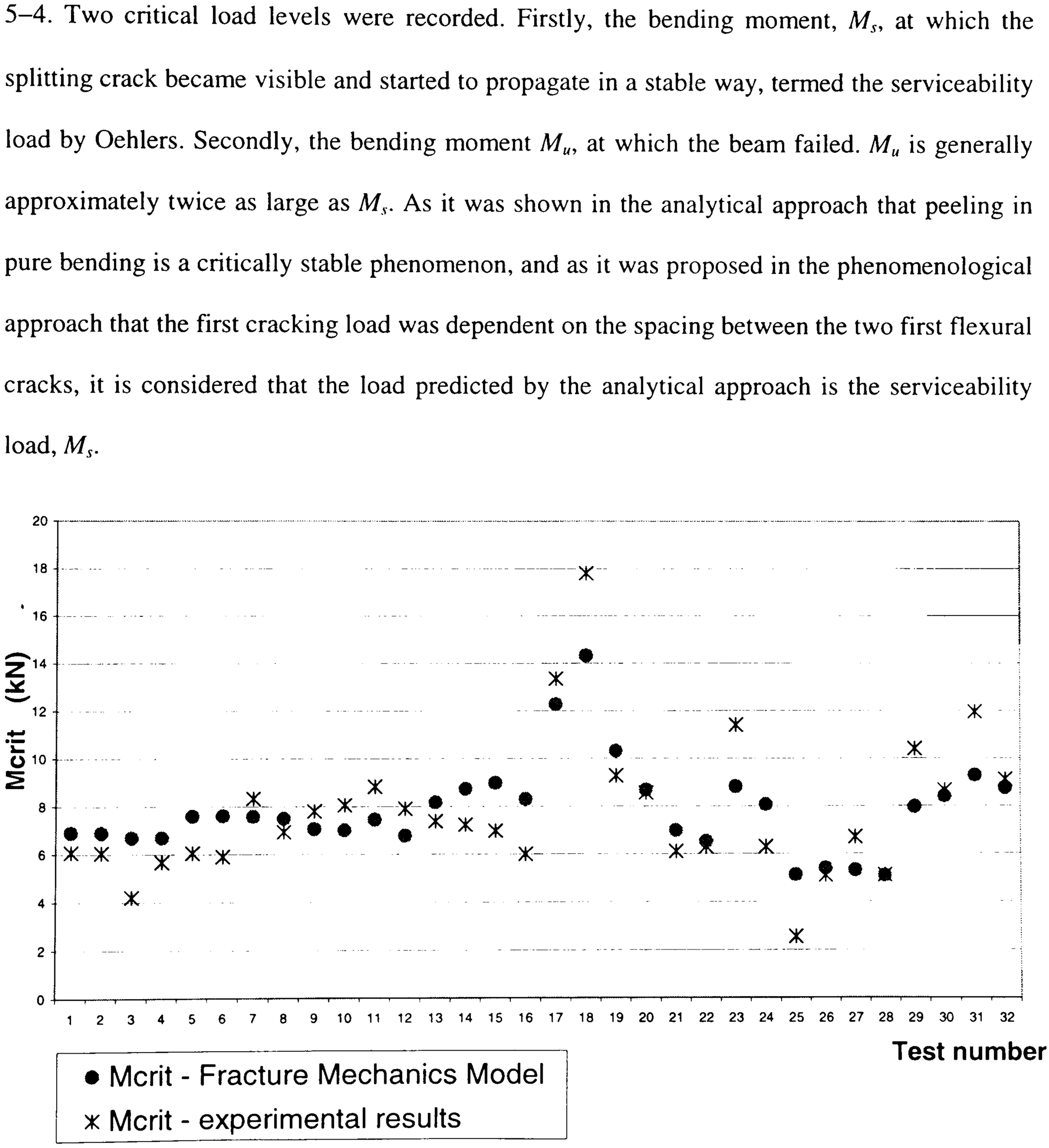

Fig. 5-18: Results scatter around prediction - experimental data from D. J. Oehlers (1991)

Consequently, the analytical prediction is compared with the serviceability load, Fig. 5-18. As the experimental observations indicate that the propagation of splitting is stable, the fracture energy required by the shifting of the conical crack has to be considered. Assessing this fracture energy is difficult. Therefore the assessed part of the fracture energy due to the conical cracks is factored with a tuning parameter, α. If α is taken equal to zero, the experimental results are higher than the predicted valued by an average of 65 %. Thus, α was chosen equal to 0.5 so that the average of the ratio of the experimental result over the predicted value approached 1. This choice may appear to lack objectivity. However, a low standard deviation of the discrepancy of the predicted values over the 32 results would still be significant enough to confirm the validity of the model. A more satisfying way however of assessing α is developed in the next section.

The predictions are expressed as a percentage of the experimental value for each beam and plotted in Fig. 5-19. All experimental values are within ±30% of the prediction except for tests number 3 and 25, i.e. Oehler's beams 3/1 and 13/17. The mean value is equal to 98%, that is very close to 100%. The accuracy of this result is essentially due to the tuning factor α. Most importantly, the standard deviation is relatively small at $\sigma_{exp/num}$ = 20 %, which is considered satisfactory.

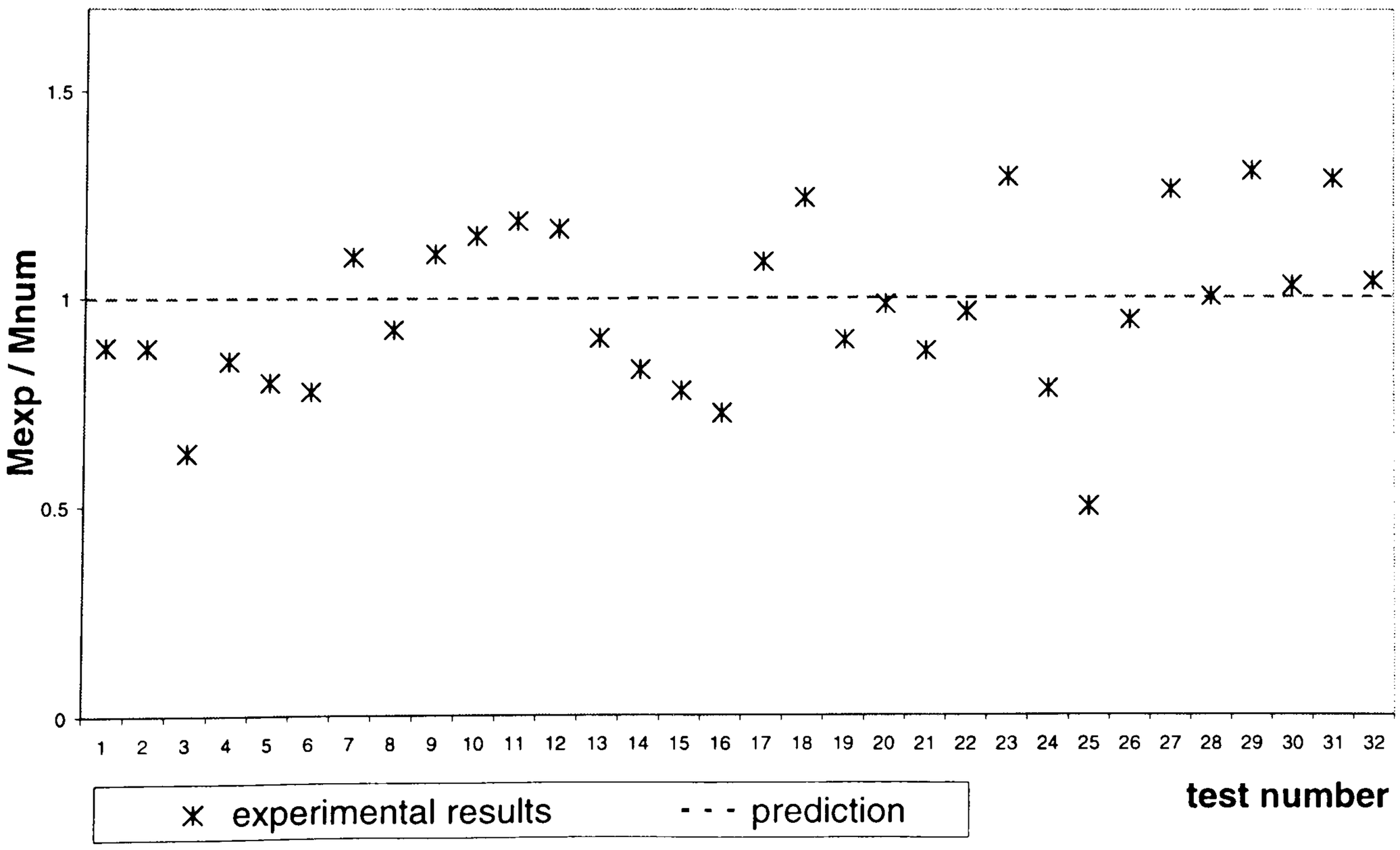

Fig. 5-19: Ultimate bending moment - experimental data from D. J. Oehlers (1990) [143]

Considering that any inaccuracy in the measurement of the geometric and material properties will produce some scatter and noting that the estimation of the fracture energy is made on the basis of many assumptions (validity of the empirical formula from the CEB-FIP, d_{agg}=20 mm, approximate assessment of the fracture area), such a standard deviation was to be expected.

An estimate of the inherent scatter of the peeling failure in pure bending can be obtained considering the experimental results of eight identical beams. Beams 5/1L to 5/4R and beams 6/1L to 6/4R have the same geometric properties and nearly identical material properties (less than 20% of variation). Using the distribution of Khi squared, their standard deviation is assessed to be comprised within 10% and 20% with a level of confidence of 90%. This proves that the standard deviation obtained for the distribution of the experimental results around the prediction is acceptable and can be mainly explained by the uncertainty inherent in the peeling failure and not by the inaccuracy of the analytical model.

In conclusion, the overall agreement between the experimental data and the predictions is remarkable. In comparison, Oehler's semi-empirical model, with its two tuning parameters, still displayed a standard deviation of 28% on the set of experimental data that it had been calibrated on.

5.4.2. Peeling in flexural-shear failure

Now that the fracture mechanics model and the assumed mode of failure have been validated for the peeling failure in pure bending, the more complex model for flexural-shear peeling can be benchmarked against experimental data. Many experimental programs have been carried out on plated beams with the plate ending in the shear span. Since the models for the flexural types of failures by plate rupture or concrete crushing are known to perform well, this study focuses on the failure in the peeling mode only. Thus, only the beams that were reported to fail by peeling

have been selected. Depending on the bending moment-to-shear ratio in the cross-section of the plate end, peeling is either due to flexural peeling, (Eq. 5-9) or flexural-shear peeling, (Eq. 5-23). Therefore, both shear capacities have been calculated for each beam and the lower value has been selected for the prediction.

The experimental data were extracted from the following papers:

- Oehlers (1992)[144], 23 beams (including 4 in flexural-shear and 19 in flexural peeling),
- Oehlers et al. (1998)[147], 7 beams (including 6 in flexural-shear and 1 in flexural peeling),
- Jones et al. (1982)[148], 3 beams (including 2 in flexural-shear and 1 in flexural peeling),
- Jones et al.(1988)[137], 3 beams (all in flexural-shear peeling),
- Swamy et al. (1995)[149], 5 beams (all in flexural-shear peeling),
- Swamy et al. (1987)[146], 13 beams (all in flexural-shear peeling),
- Ritchie et al. (1991)[145], 9 beams (including 2 in flexural-shear and 7 in flexural peeling),
- Quantrill et al. (1996)[150,151], 7 beams (all in flexural-shear peeling),
- Basunbul et al. (1990)[152], 3 beams (all in flexural peeling),
- Ziraba et al. (1994)[153], 10 beams (including 1 in flexural-shear and 9 in flexural peeling),
- Hussain et al.(1995)[154], 2 beams (all in flexural peeling),
- Spadea, Bencardino and Swamy (1998)[155], 1 beam in flexural-shear peeling,
- Arduini et al. (1997)[130], 2 beams (all in flexural peeling),

That is a total of 88 beams of which 44 failed in flexural-shear peeling and 44 failed in flexural peeling.

The main difficulty in the fracture mechanics models is the assessment of the fracture energy required per unit length of splitting crack extent. In the first models developed the problem was solved by introducing a tuning parameter α, calibrated on experimental data. This is not satisfying however as α can vary between 0 and 2, resulting in variations in the predicted failure load of up to 100%. Consequently, a more rational method is proposed for the assessment of the fracture energy. It has already been mentioned that α depends on the strain in the steel bar and

to some extent to the concrete cover. Assuming that the concrete cover is always large enough to allow full development of the conical cracks, a first approximation of α can be obtained by assuming a linear relationship with the steel strain ε_s. To verify this assumption, (Eq. 5-9) and (Eq. 5-23) are inverted to determine from the experimental results the value of α. For each beam, the steel strain at failure is then computed.

For the flexural type of peeling failure, ε_s is calculated using cross-sectional analysis at the plate end:

$$\varepsilon_s = \frac{V_{\exp} d_{pl}}{(EI)_{cr}} (H - c - y_{cr}) \qquad \textit{(Eq. 5-26)}$$

For the flexural-shear type of peeling, the force in the steel at the location of the diagonal crack is assessed using the free body diagram, Fig. 5-17:

$$\varepsilon_s = \frac{V_{\exp} (d_{pl} + \beta H)}{\gamma H \cdot E_s A_s} \qquad \textit{(Eq. 5-27)}$$

α is then plotted against the steel strain at failure, Fig. 5-20.

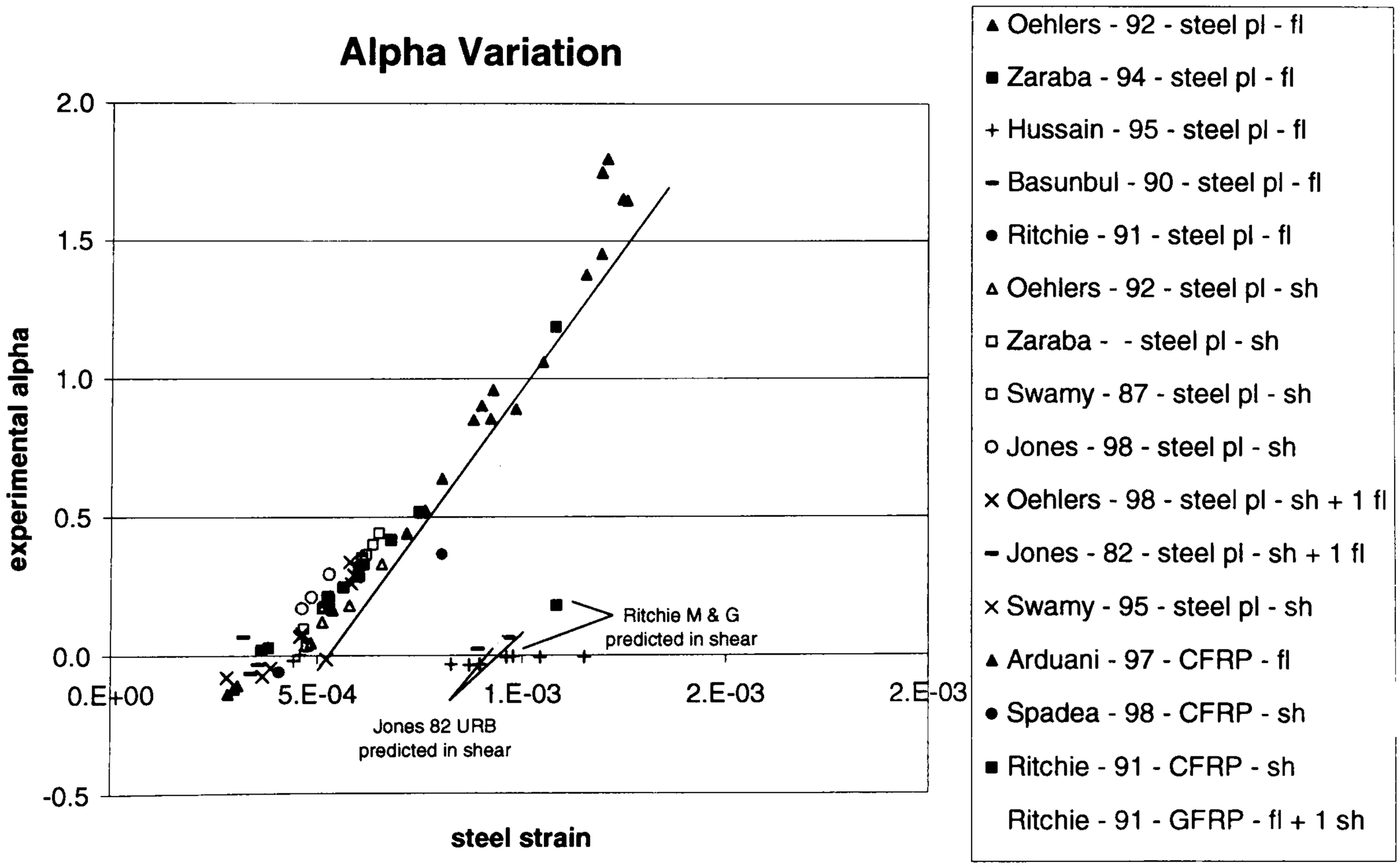

Fig. 5-20: Variation of alpha with the steel strain according to the experimental data

The results lie approximately on a straight line, except for the results from Quantrill et al. (1996)[150] and four other results, which lie on the axis of zero α. This is explained by the fact that Quantrill used plain bar, which do not induce conical cracking, and that the four other results, which all failed in the flexural-shear mode, must have failed dynamically, in an unstable manner. For the other results, a linear regression analysis can be used to assess the origin and the slope of the corresponding line. Such an analysis yields:

$$\alpha = 0 \qquad \text{for } \varepsilon_s < 5 \times 10^{-4} \qquad \textit{(Eq. 5-28)}$$

$$\alpha = -1.035 + 2.07 \times 10^3 \varepsilon_s \qquad \text{for } \varepsilon_s > 5 \times 10^{-4} \qquad \textit{(Eq. 5-29)}$$

(Eq. 5-28) and (Eq. 5-29) can be used as an evolution law for α, reflecting the opening of the conical cracks with the steel strain. An iterative procedure is then needed to assess the failure load and α at failure.

The expression for α obtained with the plates ending in the shear span is assumed to be a general law for splitting propagation. Its validity is checked against the experimental results of peeling in pure bending. The α are worked out by inverting (Eq. 5-9) and using the experimental results of Oehlers (1990)[143]. The corresponding steel strains are calculated using (Eq. 5-26). The results are plotted in Fig. 5-21.

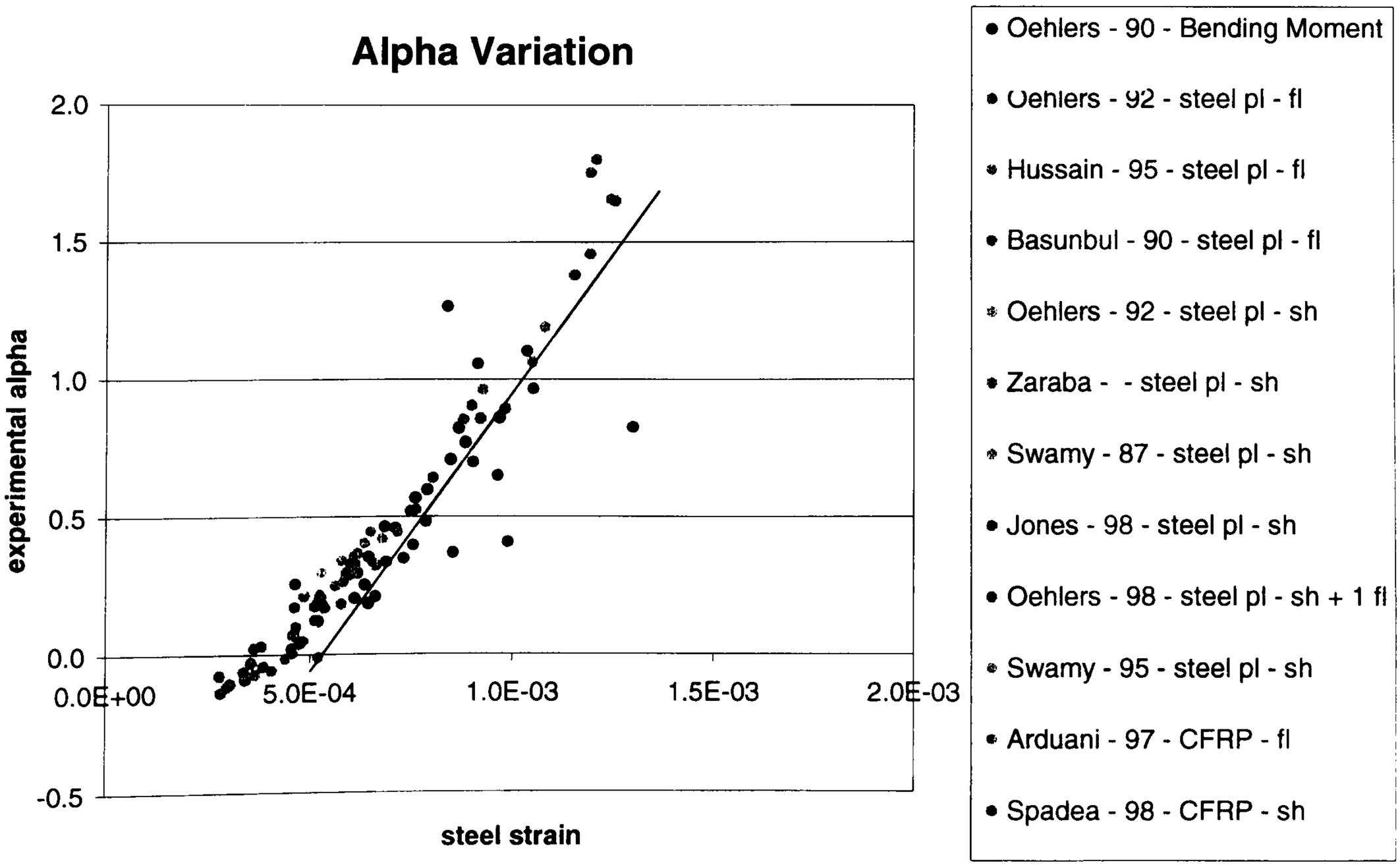

Fig. 5-21: Variation of alpha with the steel strain – comparison with bending mode

It can be seen that these results are in good agreement with the linear regression, although the scatter is larger than for the flexural-shear peeling. Consequently, it is assessed that (Eq. 5-28) and (Eq. 5-29) can be reliably used along with (Eq. 5-9) and (Eq. 5-23) to calculate the predicted failure load. However, if the iterative procedure diverges and predicts very large values of α, then α is limited to 1.6.

The full procedure to determine the predicted failure load is detailed in the following:

- Calculate the minimal flexural peeling capacity, V_{fl}^{0}, using (Eq. 5-9) and $\alpha = 0$.
- Calculate the corresponding ε_s.
- If ε_s is larger than 5×10^{-4}, use the iterative procedure with (Eq. 5-29) and (Eq. 5-9) to assess the new flexural peeling capacity, V_{fl}^{α}, limiting α to 1.6.
- Calculate the shear load at the onset of flexural cracking, V_{fl}^{cr}, using cross-sectional analysis at the plate end.
- Select the higher of V_{fl}^{α} and V_{fl}^{cr} as the flexural peeling load, V_{fl}.
- Calculate the minimal flexural-shear peeling capacity, V_{sh}^{0}, using (Eq. 5-23) and $\alpha = 0$.
- Calculate the corresponding ε_s.
- If ε_s is larger than 5×10^{-4}, use the iterative procedure with (Eq. 5-29) and (Eq. 5-23) to assess the new flexural-shear peeling capacity, V_{sh}^{α}, limiting α to 1.6.
- Select the lower of V_{fl} and V_{sh}^{α} as the peeling capacity, V_{cr}.

This procedure has been applied on the 88 experimental results and plotted in the following graphs, Fig. 5-22 to Fig. 5-29.

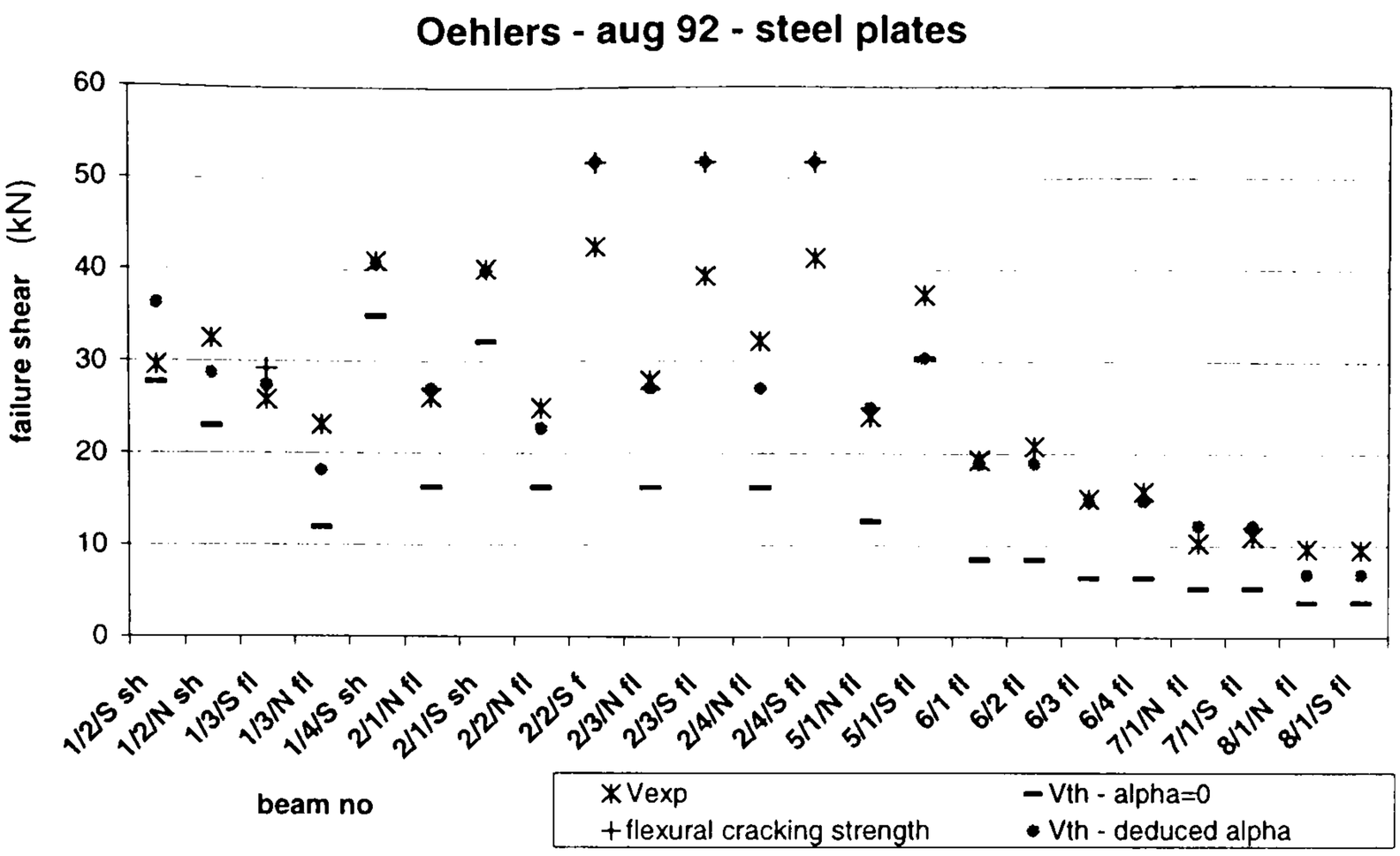

Fig. 5-22: Comparison of the predicted results with the experimental data – Oehlers (1992)

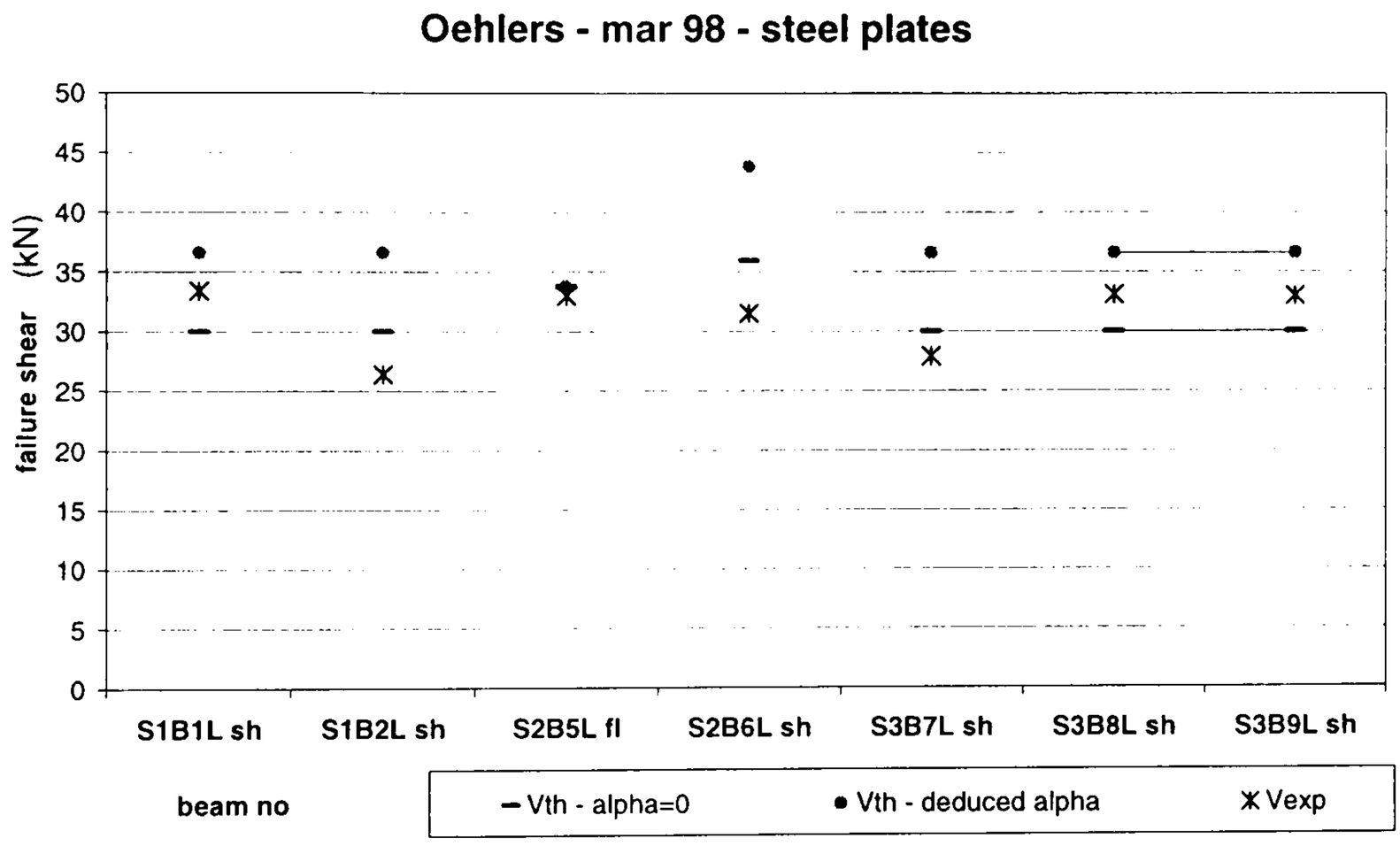

Fig. 5-23: Comparison of the predicted results with experimental data – Oehlers (1998)

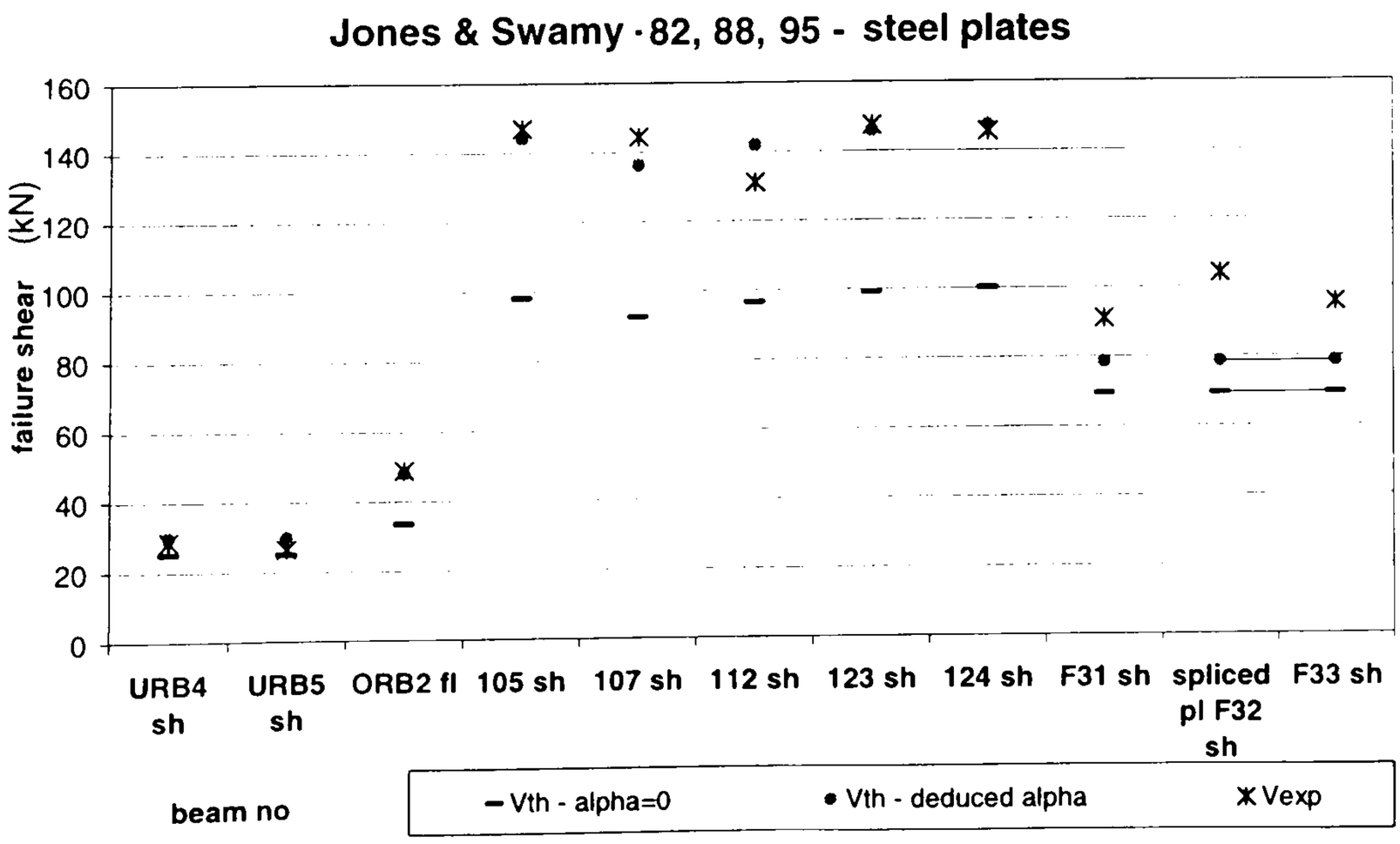

Fig. 5-24: Comparison of the predicted results with experimental data Jones et al. (1982, 1988, 1995)

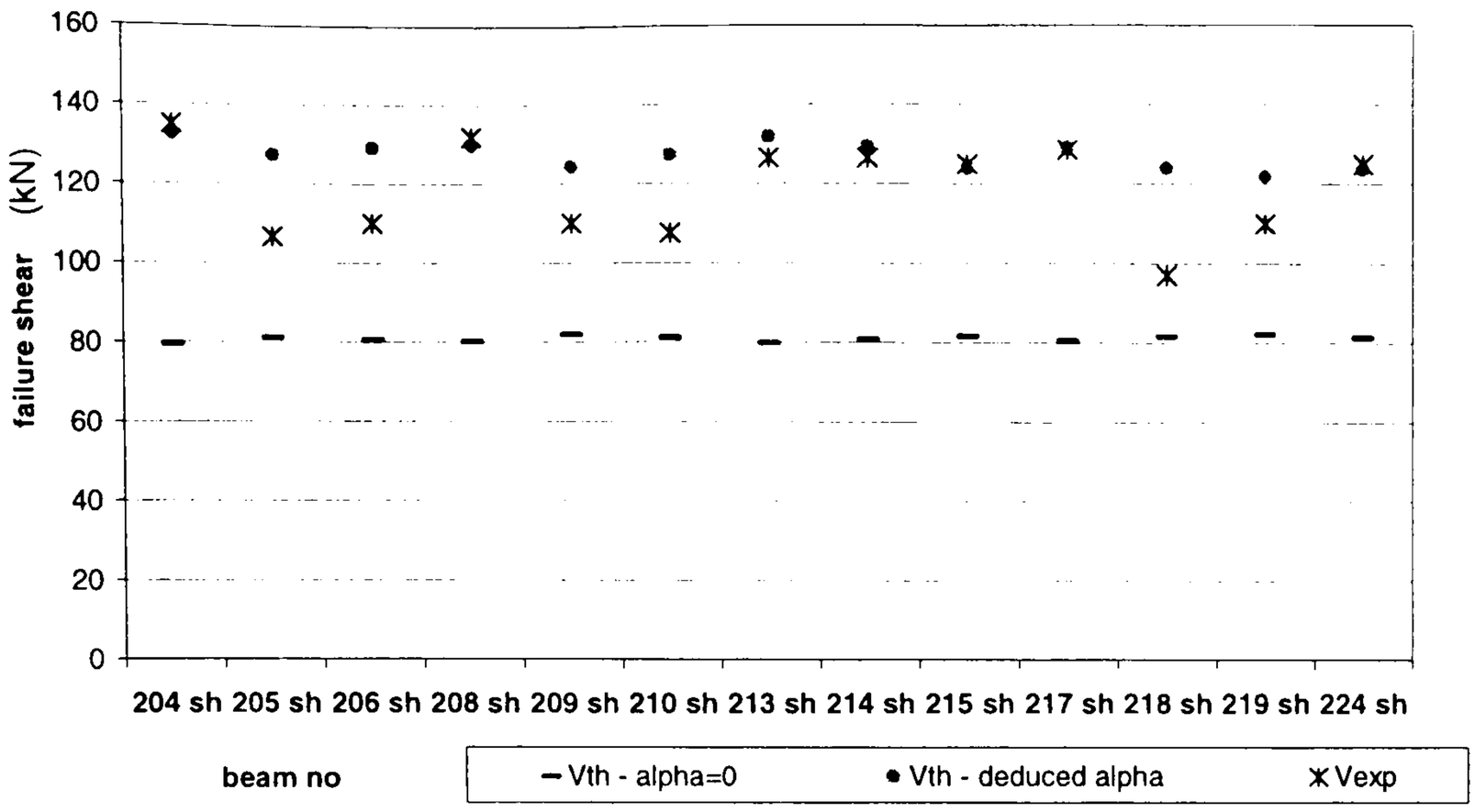

Fig. 5-25: Comparison of the predicted results with experimental data – Swamy (1987)

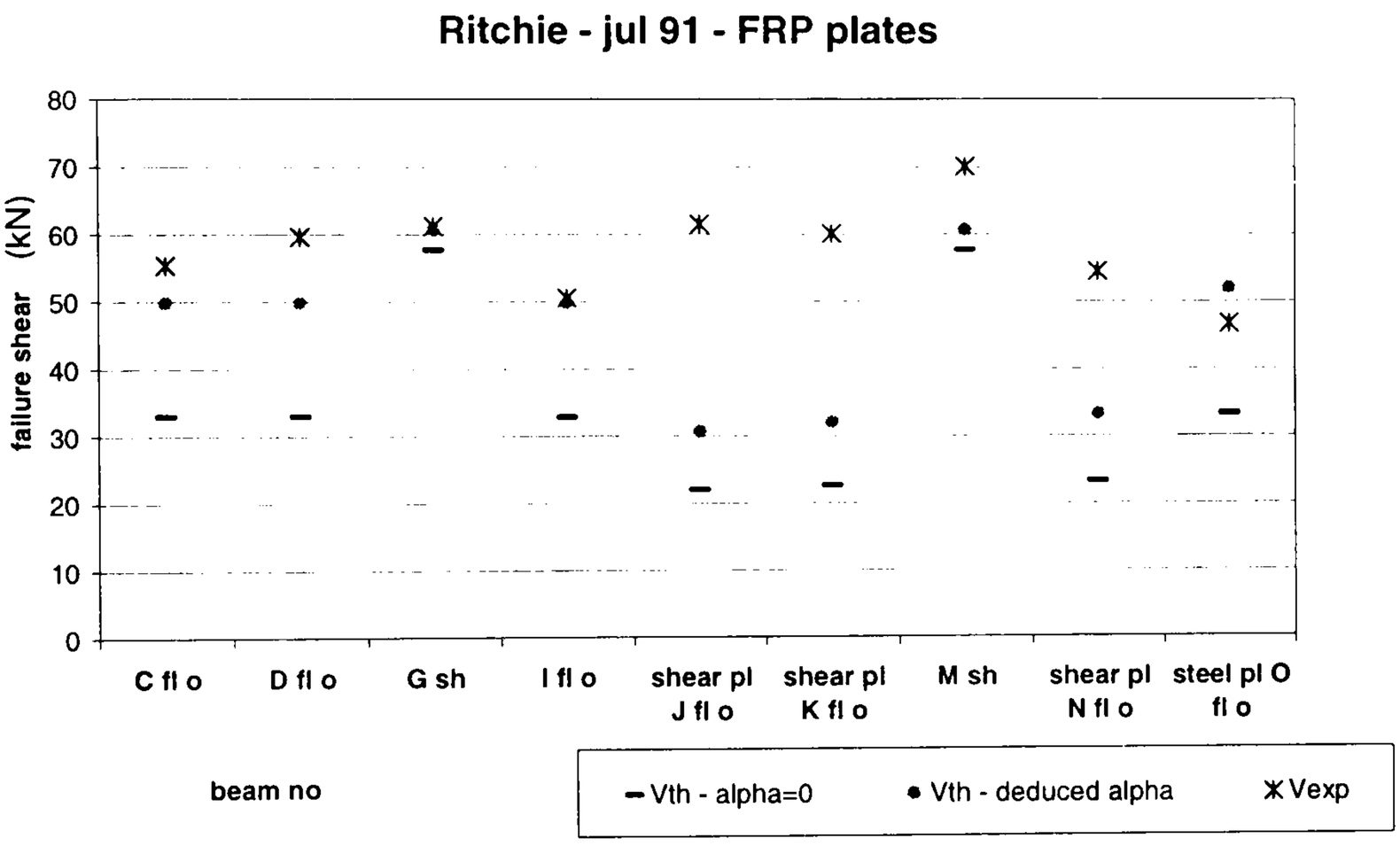

Fig. 5-26: Comparison of the predicted results with experimental data – Ritchie (1991)

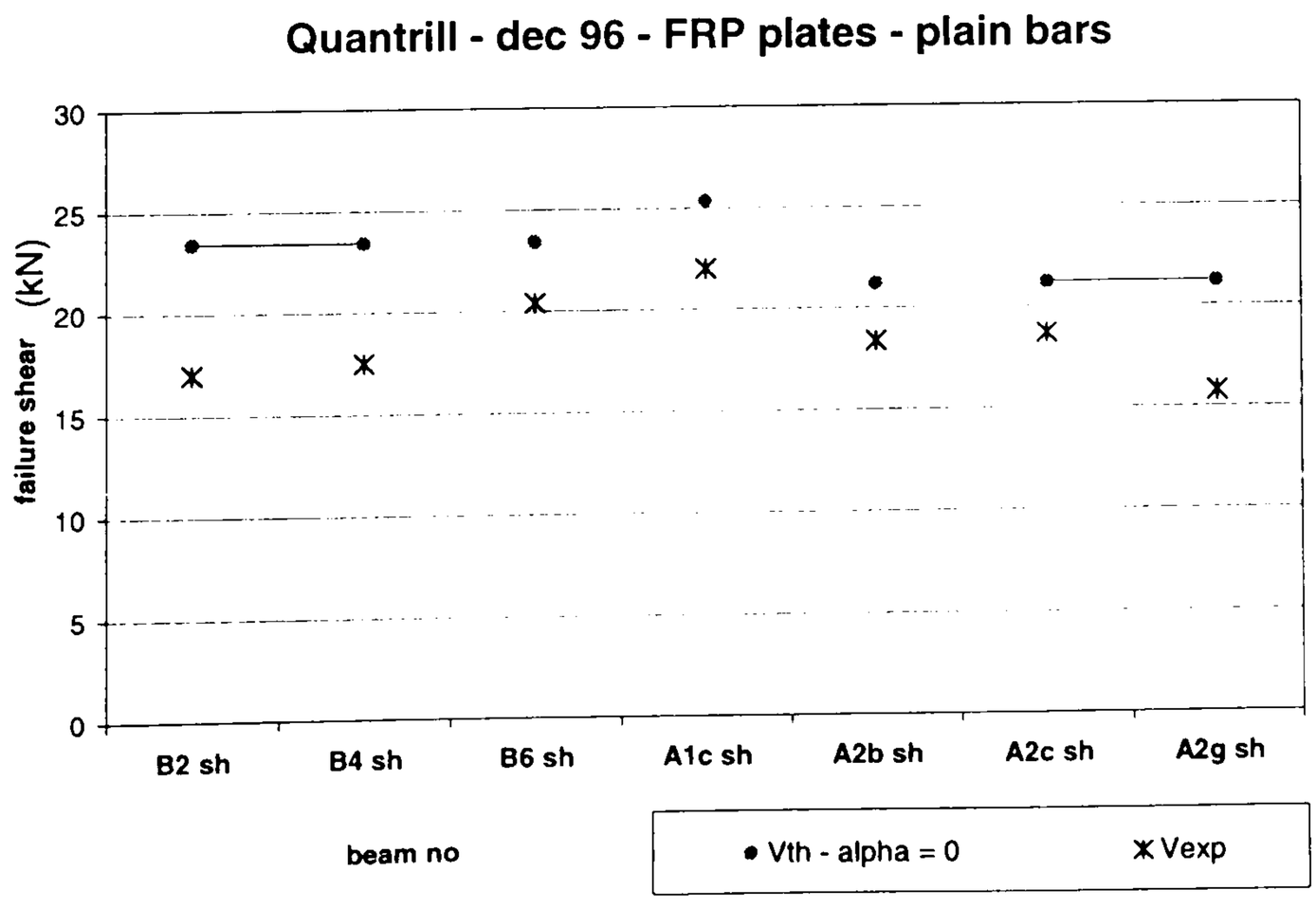

Fig. 5-27: Comparison of the predicted results with experimental data – Quatrill (1996)

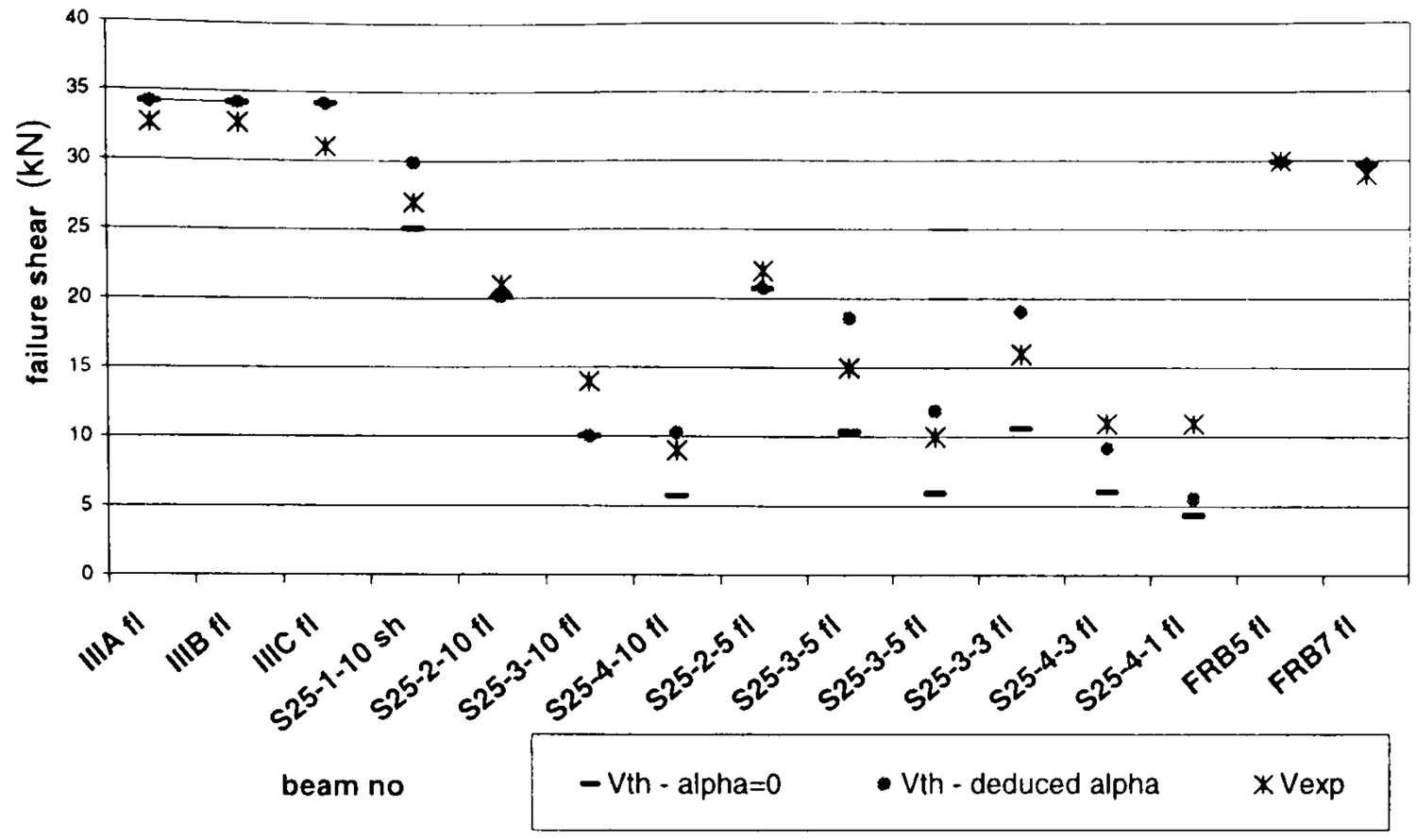

Fig. 5-28: Comparison of the predicted results with experimental data Basunbul, and Ziraba et al.(1990-1995)

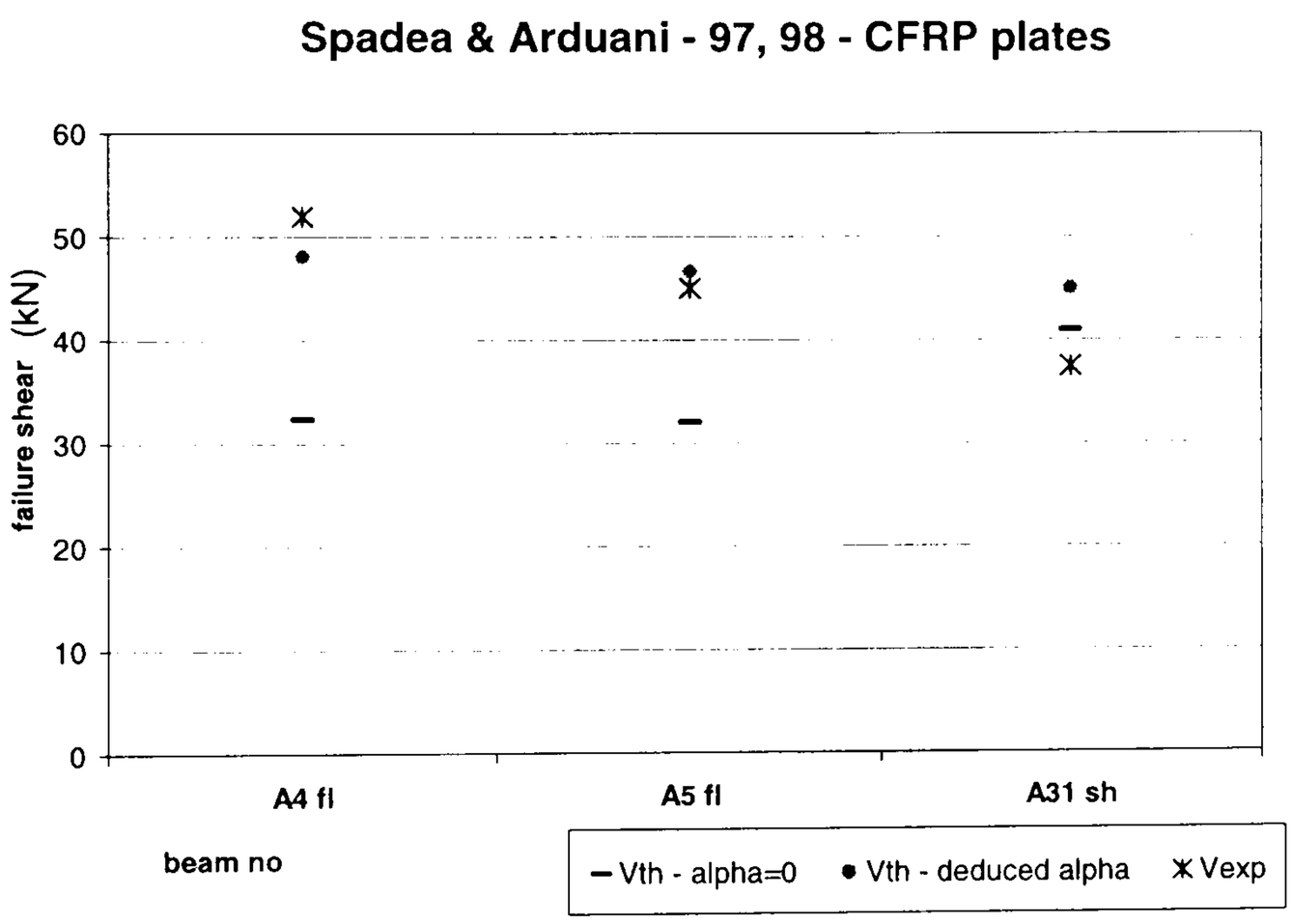

Fig. 5-29: Comparison of the predicted results with experimental data Spadea (1997) and Arduani (1998)

These graphs show that, in 90 % of the cases, the prediction is very close to the experimental results, within ±20 % of the experimental load. This is very satisfactory especially considering the difficulty, which occurs in assessing the fracture energy per unit length of splitting crack extension. For the results of Quantrill (1996), α was intentionally set to zero since no conical cracking can arise with plain reinforcing bars. The agreement between the experimental results and the predictions tends to confirm that the additional fracture energy corresponding to α is definitely linked with conical cracking. It is important to note that no significant difference can

be observed between steel plates and FRP plates. The prediction is equally accurate in both cases.

A better picture of the accuracy of the predictions can be gained by plotting the experimental data as a percentage of the prediction, Fig. 5-30. If a distinction is made between peeling in the flexural mode, V_{fl}, peeling at the onset of flexural cracking, V_{fl}^{cr}, and peeling in the flexural-shear mode, V_{sh}^{α}, it can be seen that the most accurate results are those failing in the flexural-shear peeling mode. The beams failing in the flexural mode are slightly less accurate, and the beams failing at the onset of flexural cracking display a greater scatter. This can be due to the fact that the onset of flexural cracking is not accurately predicted, or that shear cracking, playing an identical role as flexural cracking, appears earlier and triggers failure.

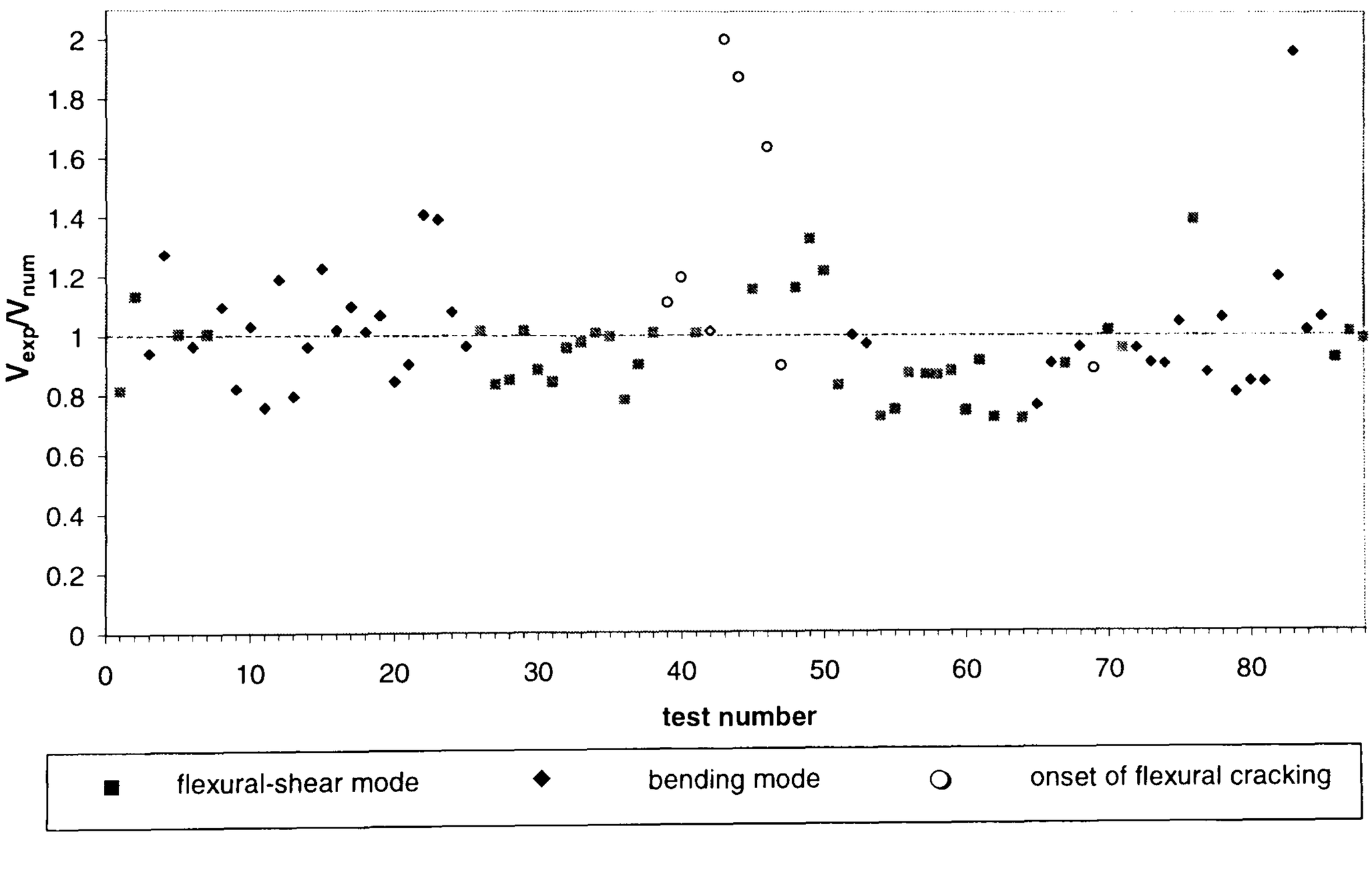

Fig. 5-30: Results scatter around prediction – all beams

The mean value of the 88 results, $\mu_{exp/num}$, is 102 %, which is very close to the expected 100%. The standard deviation, $\sigma_{exp/num}$, is 24 %. The relatively high value of the standard deviation is essentially due to the discrepancy of the predictions at the onset of flexural cracking.

If only the beams failing in the flexural-shear mode are considered, Fig. 5-31, far less scatter is observed. This may be due to the fact that generally the values of α in these cases are lower than the one in the flexural cases, as the steel is less strained close to the support. The uncertainty in the value of α is then likely to be less.

For these 44 results, the mean value, $\mu_{exp/num}$, is 94.5 %, which is very close as well to the expected 100%. The standard deviation, $\sigma_{exp/num}$, is 14.5 %, which is approximately half that calculated for the 88 beams. It should be stressed that this result is very satisfactory.

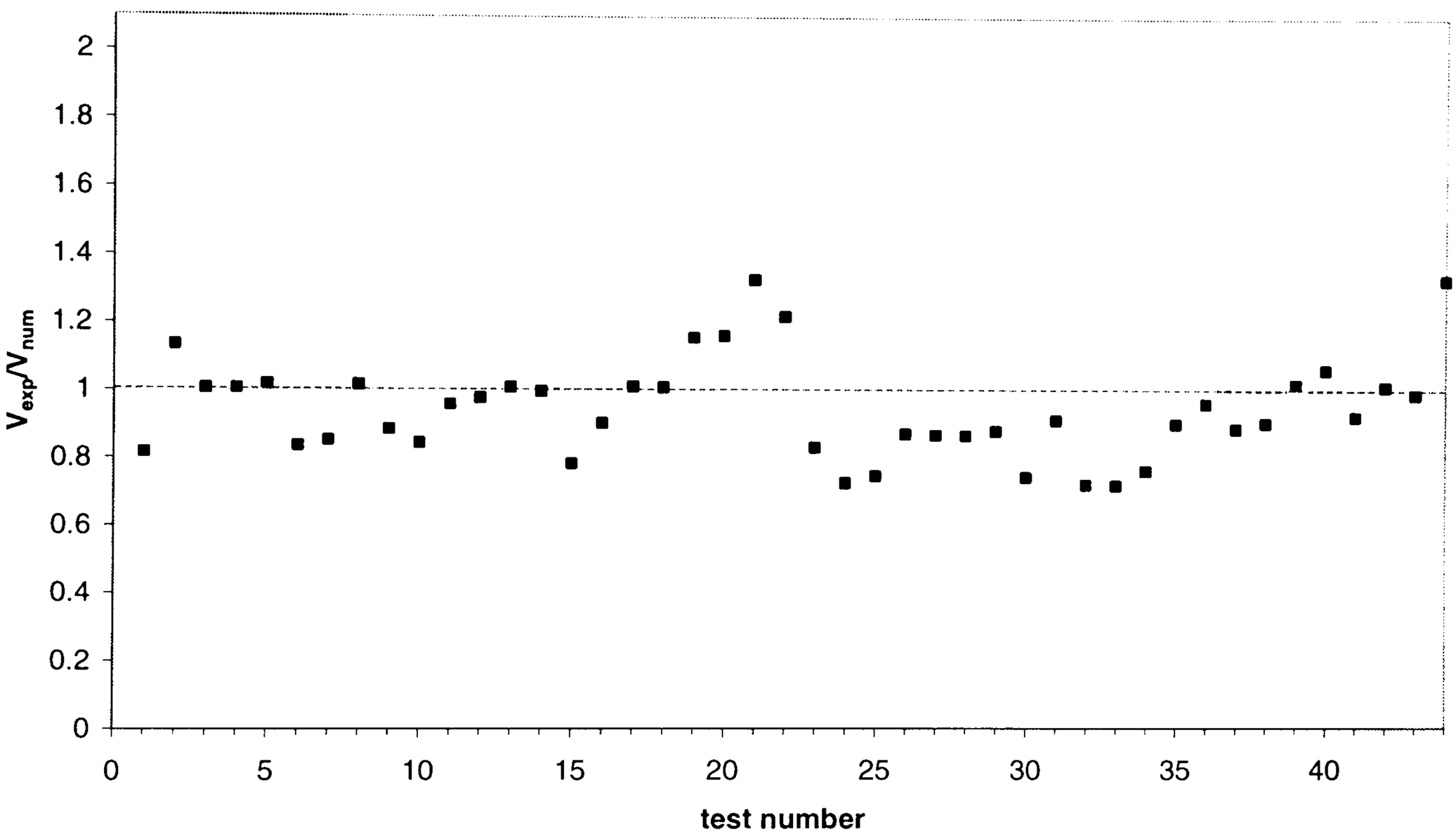

Fig. 5-31: Results scatter around prediction – beams failing in flexural-shear mode

To check that the standard deviation obtained is in the range of what should be expected considering the uncertainty inherent to this type of failure, the experimental scatter is estimated from 9 identical beams from Swamy and Jones (1987). Using the distribution of Khi squared, the experimental standard deviation is assessed to be comprised between 6% and 24 %with a level of confidence of 90%. As the standard deviation between the experimental results and the predictions lies in the centre of this range, it can be concluded that the observed scatter is essentially due to the uncertainty inherent in the flexural-shear peeling mode of failure and not to the inaccuracy of the predictive method.

In conclusion, the proposed procedure to assess the peeling load of plated beams appears to be reliable. If this approach was to be adopted for design, the following safe simplifications could be made:

- α could be taken, conservatively, as zero,
- the delaying of peeling up to the onset of flexural cracking should be ignored,
- obviously the appropriate safety factors should be adopted.

The prediction would then become the lower of the two values given by the factored (Eq. 5-9) and (Eq. 5-23) with α set to zero.

6. SUMMARY, DISCUSSION AND OUTLOOK

6.1. Summary

While it is desirable that reinforced concrete structures should be designed so that fracture phenomena do not play a decisive role, it is unavoidable for some designs to consider failures triggered by the fracture of concrete. It is especially the case when steel-to-concrete bond plays a crucial role in the load carrying mechanism of a structure.

Much research has been carried out in the last decade on the fracture mechanics of plain concrete without reaching any conclusive results directly applicable to reinforced concrete. This is because concrete acts compositely with its reinforcement and the fracture mechanics of the two materials cannot be considered separately.

A phenomenological approach to bond in reinforced concrete has shown that tensile softening can be achieved through conical cracking or transverse cracking, but that complete loss of bond is generally due to the propagation of a horizontal crack called the splitting crack. Empirical bond models described in the literature were shown to predict satisfactorily the softening behaviour of tension specimens and the onset of splitting, but it was concluded that no model was available to predict the onset of unstable splitting propagation, i.e. the ultimate bond. While Tepfers' models are able to predict the onset of splitting by considering the fracture mechanics of concrete alone, they are unable to predict the ultimate bond. Consequently, a new fracture mechanics approach has been developed based on the energy balance of the reinforcing bar and the surrounding concrete, Table 6-1.

Table 6-1: Summary of formulae proposed in the thesis

Application field	Formula	Assumptions
Bond failure by splitting in a reinforced concrete tie	$F_{cr} = \sqrt{\dfrac{2\Gamma}{\dfrac{1}{E_s A_s} - \dfrac{1}{E_s A_s + E_c A_c}}}$	–
	$F_{cr} = 3.724 \cdot f_c^{0.35} \sqrt{\dfrac{b}{\dfrac{1}{E_s A_s} - \dfrac{1}{E_s A_s + E_c A_c}}}$	dynamic splitting d_{agg} = 20 mm
	$F_{cr} = 3.724 \cdot f_c^{0.35} \sqrt{\dfrac{b + \alpha \dfrac{A_{cc}}{r_s}}{\dfrac{1}{E_s A_s} - \dfrac{1}{E_s A_s + E_c A_c}}}$	quasi-static splitting d_{agg} = 20 mm
Flexural-shear failure of a reinforced concrete beam without stirrups	$V_{cr} = \dfrac{\beta H}{a_c} \sqrt{\dfrac{9}{13} + 2\dfrac{\gamma}{\beta}} \sqrt{A_s E_s \Gamma}$	shear crack at 45 deg. $y = \beta H$ $d = \gamma H$
	$V_{cr} = 4.517 \cdot \dfrac{H}{a_c} \cdot f_c^{0.35} \cdot \sqrt{A_s E_s b}$ with $a_c = 3.3 a_s \left[\dfrac{\rho \left(\dfrac{d}{a_s} \right)^2}{\left(1 - \sqrt{\rho}\right)^2} \right]^{1/3}$	dynamic splitting d_{agg} = 20 mm $\beta = 0.8$ $\gamma = 0.9$
	$V_{cr} = 150 \cdot \dfrac{1.183}{\sqrt{d}} \cdot \left(\dfrac{3d}{a_s} \right)^{1/3} (100 \cdot \rho)^{1/6} \left(1 - \sqrt{\rho}\right)^{2/3} f_c^{0.35} \cdot bd$	
	$V_{cr} = 4.517 \cdot \dfrac{H}{a_c} \cdot f_c^{0.35} \cdot \sqrt{A_s E_s} \sqrt{b + \alpha \dfrac{A_{cc}}{r_s}}$	quasi-static splitting d_{agg} = 20 mm $\beta = 0.8$ $\gamma = 0.9$

Table 6-1: Summary of formulae proposed in the thesis - continued

Peeling failure of a externally plated beam in pure bending mode	$M_{cr} = \sqrt{\dfrac{2\Gamma}{\dfrac{1}{(EI)_{sp}} - \dfrac{1}{(EI)_{ini}}}}$	–
	$M_{cr} = 3.724 \cdot f_c^{0.35} \sqrt{\dfrac{b}{\dfrac{1}{(EI)_{sp}} - \dfrac{1}{(EI)_{ini}}}}$	dynamic splitting d_{agg} = 20 mm
	$M_{cr} = 3.724 \cdot f_c^{0.35} \sqrt{\dfrac{b + \alpha \dfrac{A_{cc}}{r_s}}{\dfrac{1}{(EI)_{sp}} - \dfrac{1}{(EI)_{ini}}}}$	quasi-static splitting d_{agg} = 20 mm
Peeling failure of an externally plated beam in flexural-shear mode **without stirrups**	$V_{cr} = \sqrt{\dfrac{9}{13} + 2\dfrac{\gamma}{\beta}} \cdot \dfrac{\beta \cdot H}{d_{pl} + \beta \cdot H} \cdot \sqrt{\Gamma A_s E_s}$	shear crack at 45 deg. $y = \beta H$ $d = \gamma H$
Peeling failure of an externally plated beam in flexural-shear mode **with stirrups**	$V_{cr} = \left(1 + \dfrac{2}{3\left(\dfrac{9}{26} + \dfrac{\gamma}{\beta}\right)} \dfrac{A_v}{A_s} \dfrac{\Phi_s}{\Phi_v} \dfrac{\beta H}{s}\right) \dfrac{\beta H}{d_{pl} + \beta H} \times \sqrt{\dfrac{9}{13} + 2\dfrac{\gamma}{\beta}} \sqrt{A_s E_s \Gamma}$	shear crack at 45 deg. $y = \beta H$ $d = \gamma H$ $\dfrac{\delta_s}{\delta_v} = \dfrac{\Phi_s}{\Phi_v}$
	$V_{cr} = 9.515 \cdot \left(1 + 0.363 \dfrac{A_v}{A_s} \dfrac{\Phi_s}{\Phi_v} \dfrac{H}{s}\right) \dfrac{H \cdot f_c^{0.35}}{d_{pl} + 0.8H} \times \sqrt{A_s E_s b}$	dynamic splitting d_{agg} = 20 mm $\beta = 0.8$ $\gamma = 0.9$
	$V_{cr} = 9.515 \cdot \left(1 + 0.363 \dfrac{A_v}{A_s} \dfrac{\Phi_s}{\Phi_v} \dfrac{H}{s}\right) \dfrac{H \cdot f_c^{0.35}}{d_{pl} + 0.8H} \times \sqrt{A_s E_s \left(b + \alpha \dfrac{A_{cc}}{r_s}\right)}$	quasi-static splitting d_{agg} = 20 mm $\beta = 0.8$ $\gamma = 0.9$

This fracture mechanics model has been validated against experimental data for tension specimens failing by splitting propagation. It was concluded that the model could therefore be applied generally to predict modes of failure in reinforced concrete structures where bond plays a critical role. A phenomenological study of the flexural-shear failure of beams without stirrups revealed that the failure is actually triggered by the release of the longitudinal reinforcement due to the unstable propagation of a splitting crack. Application of the fracture mechanics model, together with a mechanical model and an empirical rule proposed by Kim and White (1991) for the position of the critical flexural-shear crack, resulted in the formulation of an analytical expression for the ultimate shear force, Table 6-1. If a number of the usual assumptions are made, the simplified formula appeared to be very similar to the ultimate shear force predicted by the empirical formula given in the CEB-FIP Model Code (1990)[5]. The excellent agreement between the two predictions tended to confirm that the assumed mode of failure, i.e splitting, and the fracture mechanics approach are valid. The analytical formula proposed is estimated to be more satisfactory than the empirical formula as a better understanding of the failure mechanism is gained and ways of improving the design of such beams can be considered.

The failure modes of beams strengthened by plate gluing was then investigated. Three types of failure modes were identified:

- failure in the flexural mode with concrete crushing or plate rupture, which can be reliably predicted by cross-section analysis,
- bond failure at the interface between the plate and the concrete, which can be avoided by proper surface preparation and quality of workmanship during the gluing process,
- and peeling failures due to the propagation of a horizontal crack at the level of the inner reinforcement, resulting in the separation of the plate from the beam.

A phenomenological study showed that the peeling failures were similar in their nature to the splitting propagation. Consequently, it was concluded that the fracture mechanics model for splitting could be applied to this failure mechanism. Two models were developed. The first

model predict the peeling load of a plated beam subjected to pure bending. The second model, similar to the model for flexural-shear failure of unplated beams, predicts the peeling load of a plated beam with the plate ending in the shear span. The only parameter, which needs to be determined experimentally, included in these models was the proportion of fracture energy, α, required by conical cracking per unit length of the advance of the splitting crack. This proportion was assumed to be proportional to the steel strain and an empirical linear law was deduced from experimental results. Application of the models with the empirical law for α resulted in a very good agreement with over a hundred experimental results. It was concluded that the failure mechanisms assumed were correct and that the fracture mechanics model for splitting was applicable to these types of failure. Analytical formulae have been formulated and validated, Table 6-1. Some design guidelines for the peeling failure of plated beams have been formulated.

6.2. Discussion

The strength of the proposed models stems from the fact that very few assumptions have been made to develop them. This point is confirmed by the very good agreement between the analytical formula for flexural-shear failure of beams without stirrups and the corresponding empirical formula from the CEB-FIP model code. When assumptions have been made, it has been ensured that they were in agreement with the behaviour observed experimentally.

The only critical assumptions are the ones made for the assessment of the fracture energy per unit length of splitting crack advance. The choice of d_{agg} = 20 mm is in agreement with common practice, but if a special mix of concrete were to be used, a different value for d_{agg} should be chosen. The choice between dynamical and quasi-static failure is also difficult. While it depends mainly on the load control and the nature of the failure (stable, critically stable or unstable), the experimental results do not seem to be always consistent. Assuming dynamical failure is

always safe. It is however more realistic to assume quasi-static failure when the failure mode is stable and most of the time when the failure mode is critically stable. The more problematic choice is the assessment of the proportion of fracture energy due to the conical cracks, α. Choosing $\alpha = 0$ is always a safe choice, but the failure load can thus be dramatically underestimated by up to 75%. The linear relation determined experimentally between α and the steel strain may be used to obtain a more realistic assessment of α. However, considering the experimental scatter around this linear law, it is possible that the load is overestimated in some cases, especially if the iterative procedure used to compute it is unstable. It is therefore concluded that more experimental investigation is required on this subject. A better understanding of the mechanism of formation of the conical cracks could maybe even lead to the formulation of an analytical relation for α.

The range of validity of the models presented is larger than the empirical design rules, when such rules exist. That is to say that proposed formulae are valid for structures of exceptional size and as well as for exceptional concrete mixes, as long as the fracture mechanics properties of the material considered are known. On the contrary, the empirical formulae are only designed for the customary range of structures and materials. No guarantee is provided on the applicability of the empirical formulae to exceptional structures.

The use of the proposed formulae should however be limited to structures of a size large enough for the linear fracture mechanics theory to be valid. Although the splitting crack propagation has a limited fracture process zone compared to other types of cracking in reinforced concrete, the linear fracture mechanics model may overestimate the failure load of structures with sizes below the range of common practice. A way to improve the formulae would be to apply a size effect correction procedure as proposed by Bazant and Planas (1998)[7].

The range of application of the model for the flexural-shear failure of unplated beams is restricted to beams without stirrups. This is due to the fact that when stirrups are present they

tend to arrest the progression of the splitting crack. Although, in this case, the ultimate failure mechanism is very similar to flexural-shear triggered by splitting, the rotation is not allowed by the release of the reinforcement, but rather by the yielding of the steel. The plasticity model presented in section 4.3.2. is then applicable. For under-reinforced beams without stirrups it is possible that steel yielding is more critical than splitting. In such a case, the two models should be used and the lower load chosen as the failure load.

The formulae obtained for the plated beams are only valid if the flexural type of failure and the bond failure at the interface do not occur. A complete design method should include first a check on the flexural failure and then a check on the peeling failure. Interface bond failure should be avoided by ensuring that the surfaces are properly prepared and that the quality of workmanship is suitable during the gluing process. The accuracy of the prediction then depends mainly on the accuracy of the knowledge of the structure to be strengthened (topology and material properties), and the accuracy of the assessment of the fracture energy.

6.3. Outlook

The attractiveness of the plate bonding technique for improving structural performance together with its cost-effectiveness will increase its demand in the forthcoming years. And, although the technique has already existed for thirty years, new developments still take place. Therefore, a reliable design method is necessary to ensure effective and safe design. It is believed that the models proposed in this thesis could easily lead to design formulae useful for engineering practice.

To this aim, appropriate safety factors needs to be determined and introduced in the equations. Safe assumptions, like $\alpha = 0$, could equally be enforced. It is also recommended that the original form of the equations should be kept so that a transparent design method is provided to

the structural engineer who is generally not familiar with the additional failure mechanisms, i.e. peeling failures, introduced by plate bonding.

It is recommended that in future work an extensive experimental investigation of the fracture energy required by conical cracking is conducted, as this problem is not only linked to flexural-shear failure and peeling failure but is a general problem in reinforced concrete research. The empirical law proposed for the evolution of α with the steel strain should be further validated or improved. The issue of structural stability should also be studied further, as it was shown that dynamical or quasi-static failures lead to very different failure loads.

This study has proved that splitting is a critical problem in reinforced concrete. Its role has often been neglected in the past and few research studies have been devoted to splitting. It is believed that the failure mechanisms of other structures could also be explained by the proposed fracture mechanics model. Possible application of the model to the brittle failure of anchor pull-out and to the break-out failure of bore-holes should be considered.

References

[1] Chana P.S., "Investigation of the mechanism of shear failure of reinforced concrete beams ," *Magazine of Concrete Research*, Vol. 39, No. 141, pp. 196-204, 1987.

[2] So K.O. and Karihaloo B.L., "Shear capacity of longitudinally reinforced beams - A fracture mechanics approach ," *ACI Structural Journal*, Vol. 90, No. 6, pp. 591-600, 1993.

[3] ASCE-ACI Committee 426 on Shear, "The shear strength of reinforced concrete members ," *Journal of the Structural Division - ASCE*, Vol. 99, No. 6, pp. 1091-1187, 1973.

[4] ASCE-ACI Committee 445 on Shear and Torsion, "Recent approaches to shear design of structural concrete ," *Journal of Structural Engineering - ASCE*, Vol. 124, No. 12, pp. 1375-1417, 1998.

[5] Comité Euro-International du Béton, *CEB-FIP Model Code 1990*, Redwood Books, Wiltshire, England, 437 p., 1993.

[6] Hillerborg A., "Dimensionless presentation and sensitivity analysis in fracture mechanics," *Proceedings of the International Conference on Fracture Mechanics of Concrete - Fracture Toughness and Fracture Energy of Concrete*, Lausanne, Switzerland, 1985, ed. by Wittmann F.H., Elsevier, Amsterdam, The Netherlands, pp. 413-421, 1986.

[7] Bazant Z P and Planas J, *Fracture and Size Effect in Concrete and Other Quasi-Brittle Materials*, *New Directions in Civil Engineering*, CRC Press, London, 1998.

[8] Nawy E G, *Fundamentals of High Strength High Performance Concrete*, *Concrete Design & Construction Series*, Longman Group Ltd, Essex, England, 1996.

[9] ACI 440R-96, *State-of-the-Art Report on Fiber Reinforced Plastics (FRP) Reinforcement for Concrete Structures*, ACI Committee 440, 1996.

[10] Meier U., "Strengthening of structures using carbon fibre/epoxy composites ," *Construction and Building Materials*, Vol. 9, No. 6, pp. 341-351, 1995.

[11] Kotsovos M D and Pavlovic M N, *Structural Concrete : Finite Element Analysis for Limit-State Design*, Telford, 1995.

[12] Wittman F.H., "Structure of concrete with respect to crack formation," in *Fracture Mechanics of Concrete*, Elsevier, Amsterdam, The Netherlands, pp. 43-73, 1983.

[13] Van Mier J.G.M., "Fracture mechanics of concrete: will applications start to emerge?" *HERON (Edited by Delft University of Technology and TNO, the Netherlands)*, Vol. 40 , No. 2, pp. 147-162, 1995.

[14] Tandon S., Faber K.T. and Bazant Z.P., "Crack stability in the fracture of cementitious materials," *Materials Research Society Symposium Proceeding, Boston, USA*, 1994, Materials Research Society, Pittsburgh, USA, pp. 387-396, 1995.

[15] Schlangen E., "Experimental and Numerical Analysis of fracture Processes in concrete ," *HERON (Edited by Delft University of Technology and TNO, the Netherlands)*, Vol. 38, No. 2, 117 p., 1993.

[16] Hordijk D.A., "Tensile and Tensile Fatigue Behaviour of Concrete; Experiment, Modelling and Analyses ," *HERON (Edited by Delft University of Technology and TNO, the Netherlands)*, Vol. 37, No. 2, 79 p., 1992.

[17] Bazant Z.P. and Lin F.P., "Nonlocal smeared cracking model for concrete fracture ," *Journal of Structural Engineering - ASCE*, Vol. 114, No. 11, pp. 2493-2511, 1988.

[18] Otsuka. K., *Fracture Mechanics of Concrete Structures - FraMCosS1*, Colorado, USA, 1992, ed. by Bazant Z.P., Elsevier Applied Sciences, London, pp. 486-490, 1992.

[19] Noghabai K., *Effect of tension softening on the performance of concrete structures:*

experimental, analytical and computational studies, Doctoral Thesis 1998:21, Division of Structural Engineering, Luleä University of Technology, Luleä, Sweden, 147 p., 1998.

[20] Duda H., "Grain model for the determination of the stress-crack-width relation," in *Analysis of Concrete Structures by Fracture Mechanics*, ed. by Elfegren L. and Shah S.P., Chapman & Hall, LOndon, pp. 88-96, 1991.

[21] Van Mier J.G.M., "Mode I fracture of concrete: discontinuous crack growth and crack interface grain bridging ," *Cement and Concrete Research*, Vol. 21, 1-15, 1991.

[22] Reinhardt H.W., Cornelissen H.A.W. and Hordijk D.A., "Tensile tests and failure analysis of concrete ," *Journal of Structural Engineering - ASCE*, Vol. 112, No. 11, pp. 2462-2477, 1986.

[23] Reinhardt H.W., "Fracture mechanics of an elastic softening material like concrete ," *HERON (Edited by Delft University of Technology and TNO, the Netherlands)*, Vol. 29, No. 2, 1984.

[24] Van Mier J.G.M., "Fracture of concrete under complex stress ," *HERON (Edited by Delft University of Technology and TNO, the Netherlands)*, Vol. 31, No. 3, 1986.

[25] Hordijk D.A., *Local approach to fatigue of concrete*, PhD Thesis, Delft University of Technology, Delft, The Netherlands, 1991.

[26] Broberg K.B., "The foundation of fracture mechanics ," *Engineering Fracture Mechanics*, Vol. 16, No. 4, pp. 497-515, 1982.

[27] Inglis C.E., "Stresses in a plate due to the presence of cracks and sharp corners ," *Transactions of the Institute of Naval Architects*, Vol. 55, pp. 219-241, 1913.

[28] Griffith A.A., "The phenomena of rupture and flow in solids ," *Phil. Trans. Roy. Soc. of London*, No. 221A, pp. 163-198 (Sec. 12.1), 1921.

[29] Griffith A.A., "The theory of rupture," *Proceedings of the First International Conference of Applied Mechanics*, Delft, pp. 55-63, 1924.

[30] ACI Committee 446, "Part I: State of the art report, Fracture mechanics of concrete: concepts, models and determination of material properties," *Proceedings of the First International Conference on Fracture Mechanics of Concrete Structures (FRamCoS1)*, Breckenridge, Colorado, USA, 1992, ed. by Bazant Z.P., Elsevier, London, pp. 1-140, 1992.

[31] Bazant Z P and Cedolin L, *Stability of Structures : Elastic, Inelastic, Fracture and Damage Theory*, *The Oxford Engineering Science Series*, *Vol. 26*, ISBN: 0 19 505529 2, Oxford University Press, New York, 1991.

[32] Irwin G.R., "Analysis of stresses and strains near the end of a crack traversing a plate ," *Journal of Applied Mechanics - Transactions of ASME*, Vol. 24, pp. 361-364, 1957.

[33] Murakami Y 1987 *Stress Intensity Factors Handbook* (Oxford, U.K.: Pergamon Press).

[34] Irwin G.R., "Fracture," in *Handbuch Der Physik*, 6, ed. by Flügge, Springer-Verlag, Berlin, Germany, pp. 551-590, 1958.

[35] ASTM, *Annual Book of ASTM Standards* , 03.01, ASTM, Philadelphia, pp. 519-554, 1983.

[36] Bazant Z.P. and Pfeiffer P.A., "Determination of fracture energy properties from size effect and brittleness number ," *ACI Material Journal*, Vol. 84, No. 6, pp. 463-480, 1987.

[37] Kaplan M.F., "Crack prpoagation and the fracture of concrete ," *Proceedings, ACI Journal*, Vol. 58, No. 5, pp. 591-610, 1961.

[38] Swartz S.E., Hu K.K. and Jones G.L., "Compliance monitoring of crack growth in concrete ," *Journal of the Engineering Mechanics Division - ASCE*, Vol. 104, pp. 789-800, 1978.

[39] Jenq Y.S. and Shah S.P., "On the concrete fracture testing methods," in *Fracture*

Toughness and Fracture Energy, ed. by Mihashi H. and Takahashi H.W.F.H., Balkema, Rotterdam, pp. 443-463, 1988.

[40] Hillerborg A., Modéer M. and Petersson P.-E., "Analysis of crack formation and crack growth in concrete by means of fracture mechanics and finite elements ," *Cement and Concrete Research*, Vol. 6, No. 6, pp. 773-782, 1976.

[41] Planas J. and Elices M., "Non-linear fracture of cohesive materials ," *International Journal of Fracture*, Vol. 51, pp. 139-157, 1991.

[42] Ohtsu M. and Chahrour A.H., "Fracture analysis of concrete based on the discrete crack model by the boundary element method," in *Fracture of Brittle Disordered Materials: Concrete, Rock, Ceramics.*, ed. by Baker G. and Karihaloo B.L., E & FN Spon, London, pp. 335-347, 1995.

[43] Ingraffea A.R., Gerstle W.H., Gergely P. and Saouma V., "Fracture mechanics of bond in reinforced concrete ," *Journal of Structural Engineering - ASCE*, Vol. 110, No. 4, pp. 871-889, 1984.

[44] Bazant Z.P., "Size effect in blunt fracture: concret, rock, metal ," *Journal of the Engineering Mechanics Division - ASCE*, Vol. 110, pp. 518-535, 1984.

[45] Swartz S.E., Hu K.K. and Jones G.L., "Compliance monitoring of crack growth in concrete ," *Journal of the Engineering Mechanics Division - ASCE*, Vol. 104, pp. 789-800, 1978.

[46] Hillerborg A., "The theoretical basis of a method to determine the fracture energy G_F of concrete ," *Matériaux Et Construction / Materials and Structures, RILEM*, Vol. 18, No. 106, pp. 291-296, 1985.

[47] RILEM, "Determination of the fracture energy of mortar and concrete by means of three-point bend tests on notched beams. RILEM draft recommendation ," *Matériaux Et Structures / Materials and Structures, RILEM*, Vol. 18, No. 106, pp. 285-290, 1985.

[48] Guinea G.V., Plana J. and Elices M., "Measurement of the fracture energy usinf three point bend tests: part 1 to part 3 ," *Matériaux Et Structures / Materials and Structures (RILEM)*, Vol. 25, pp. 212-334, 1992.

[49] Bruhwiler E., *Fracture mechanics of dam concrete subjected to quasi-static and seismic loading conditions*, Thesis no. 739, Swis federal Institute of Technology (LMC), Lausanne, Switzerland, 1988.

[50] Hordijk D.A., *Deformation-Controlled Uniaxial Tensile Tests on Concrete: a Survey of the Litterature Up to 1981*, Delft, The Netherlands, 1989.

[51] Daerga P.A., *Some experimental fracture mechanics studies in mode I of concrete and wood*, Licenciate Thesis 1992:12L, Lulea Univesity of Technology, Division of Structural Engineering, Lulea, Sweden, 96 p., 1992.

[52] Petersson P.E., Report No. TVBM-1006, *Crack Growth and Development of Fractur Process Zone in Plain Concrete and Similar Materials*, Lund, Sweden, 1981.

[53] Wittmann F.H., Rokugo K., Bruhwiler E., Mihashi H. and Simonin P., "Fracture energy and strain softening of concrete as determined by means of compact tension specimens ," *Material and Structures* , Vol. 21, pp. 21-32, 1988.

[54] Van der Veen C., *Cryogenic bond stress-slip relationship*, PhD Thesis, Delft University of Technology, Delft, The Netherlands, 111 p., 1990.

[55] Rosati G. and Schumm C., "An identification procedure of fracture energy in concrete: mathematical modelling and experimental verification.," *Proceedings of the International RILEM/ESIS Conference on Fracture Process in Concrete, Rock and Ceramics*, Noordwijk, The Netherlands, 1991, ed. by Van Mier J.G.M., Rots J.G. and Bakker A., E & F.N. Spon, London, pp. 629-638, 1991.

[56] Destuynder P, *Modélisation Mécanique Des Milieux Continus, Collection Mathematiques*

Et Applications, Vol. 5, Societe de Mathematiques appliquees et industrielles, Editions Ellipses, Paris, 237 p., 1991.

[57] Lemaitre J and Chaboche J-L 1985 *Mecanique Des Materiaux Solides* (Paris: Dunod).

[58] de Borst R., Feenstra P.H., Pamin J. and Sluys L.J., "Some current issues in computational mechanics of conrete structures," *Proceedings of the International Conference on Computational Modelling of Concrete Structures: EURO-C 1994*, Innsbruck, Austria, 1994, ed. by Mang H., Bicanic N. and de Borst R., Pineridge Press Ltd, Swansea, UK, 1994.

[59] Bazant Z.P. and Oh B.H., "Crack band theory for fracture of concrete ," *Materials and Structures, RILEM*, Vol. 16, No. 93, pp. 155-177, 1983.

[60] Rots J.G., Nauta P., Kusters G.M.A. and Blaauwendraad J., "Smeared crack approach and fracture localization in concrete ," *HERON (Edited by Delft University of Technology and TNO, the Netherlands)*, Vol. 30, No. 1, 48 p., 1985.

[61] Rots J.G., *Computational modeling of concrete fracture*, doctoral thesis, Technische Universiteit Delft, Delft, The Netherlands, 132 p., 1988.

[62] Rots J.G. and Blaauwendraad J., "Crack models for concrete : Discrete or Smeard? Fixed, multidirectional or rotating?" *HERON (Edited by Delft University of Technology and TNO, the Netherlands)*, Vol. 34, No. 1, 59 p., 1989.

[63] Feenstra P.H. and de Borst R., "Aspect of robust computational modeling for plain and reinforced concrete ," *HERON (Edited by Delft University of Technology and TNO, the Netherlands)*, Vol. 38, No. 4, 76 p., 1993.

[64] Belytschko T., Fish J. and Englemann B.E., "A finite element with embedded localisation zones ," *Computer Methods in Applied Mechanics and Engineering*, Vol. 70, pp. 59-89, 1988.

[65] Simo J.C., Oliver J. and Armero F., "An analysis of strong discontinuities induced by strain-softening in rate-dependent inelastic solids ," *Computational Mechanics*, Vol. 12, pp. 227-296, 1993.

[66] Klisinski M., Runesson K. and Sture S., "Finite element with inner softening band ," *Journal of the Engineering Mechanics Division - ASCE*, Vol. 117, No. 3, pp. 575-587, 1991.

[67] Olofsson T., Klisinski M. and Nedar P., "Inner softening band: a newe approach to localisation in finite elements," *International Conference on Computational Modelling of Concrete Structures*, Innsbruck, Austria, 1994, ed. by Mang H., Bicanic N. and de Borst R., Pineridge Press Ltd, pp. 373-382, 1994.

[68] Klisinski M., Olofsoson T. and Tano R., "Mixed mode cracking of concrete modelled by inner softenng band," in *Proc. Computational Plasticity*, ed. by Owen D.R.J., Onate E. and Hinton E., Pineridge Press, Swansea, UK, pp. 1595-1606, 1995.

[69] Kroner E., "Elasticity theory of materials with long-range cohesive forces ," *International Journal of Solids and Structures*, Vol. 3, pp. 731-742, 1967.

[70] Bazant Z.P. and Pijaudier-Cabot G., "Nonlocal continuum damage, localization instability and convergence ," *Journal of Applied Mechanics (Transactions of the ASME)*, Vol. 55, pp. 287-293, 1988.

[71] Bazant Z.P. and Pijaudier-Cabot G., "Measurement of characteristic length of non-local continuum ," *Journal of the Engineering Mechanics Division - ASCE* , Vol. 115, No. 4, pp. 755-767, 1989.

[72] Doedel E.K.H.B. and Kernevez J.-P., "Numerical analysis and control of bifurcation in finite dimension ," *International Journal of Bifurcation and Chaos*, Vol. 1, No. 3, pp. 493-520, 1991.

[73] Crisfield M A, *Non-Linear Finite Element Analysis of Solids and Structures*, Vol. 2: advanced topics, ISBN: 0 471 95649 X, John Wiley & Sons Ltd, Chichester, UK, 494 p., 1997.

[74] Crisfield M.A. and Wills J., "Solution strategies and softening materials ," *Computer Methods in Applied Mechanics and Engineering*, Vol. 66, pp. 267-289, 1988.

[75] de Borst R., "Computation of post-bifurcation and post-failure behaviour of strain-softening solids ," *Computers and Structures*, Vol. 25, No. 2, pp. 211-224, 1987.

[76] Seydel R, *From Equilibrium to Chaos : Practical Bifurcation and Stability Analysis*, ISBN: 0 444 01250 8, Elsevier Science Publishing Co., New York, 1988.

[77] Crisfield M.A. and Shi J., "A semi-direct approach for the computation of singular points ," *Computers and Structures*, Vol. V. 51, No. No. 1, pp. 107-115, 1994.

[78] de Borst R., "Stability and uniqueness in numerical modelling of concrete structures," *Computational Mechanics of Concrete Structures, IABSE Colloquium*, Delft, The Netherlands, 1987, ed. by IABSE I.A.f.B.a.S.E., Delft University Press, pp. 161-175, 1987.

[79] Bazant Z.P., "Stable states and stable paths of propagation of damage zones and interactive fractures," *Cracking and Damage: Strain Localisation and Size Effect, Proceedings of the France-US Workshop*, Cachan, France, 1988, ed. by Mazars J. and Bazant Z.P., Elsevier, pp. 183-206, 1989.

[80] Hordijk D.A., Rots J.G. and Reinhardt H.W., "Finite element supported fracture testing of concrete," *Computational Mechanics of Concrete Structures, IABSE Colloquium*, Delft, The Netherlands, 1987, ed. by IABSE I.A.f.B.a.S.E., Delft University Press, pp. 189-195, 1987.

[81] Rots J.G. and de Borst R., "Analysis of concrete fracture in direct tension ," *International Journal of Solids and Structures*, Vol. 25, No. 12, pp. 1381-1394, 1989.

[82] Considère, "Influence des armatures métalliques sur les propriétés des mortiers et bétons (Influence of metal reinforcement on the properties of mortars and concrete) ," *Le Génie Civil*, Vol. 34, No. 15, pp. 229-233, 1899.

[83] Lutz L.A. and Gergely P., "Analysis of stresses in the concrete near a reinforcing bar due to bond transverse cracking ," *Journal of the Americal Concrete Institute*, Vol. 64-62, pp. 711-721, 1967.

[84] Bresler B. and Bertero V., "Behaviour of reinforced concrete under repeated load ," *Journal of the Structural Division - ASCE*, Vol. 94, No. ST6, pp. 1567-1590, 1968.

[85] Goto Y., "Cracks formed in concrete around deformed tension bars ," *Journal of the American Concrete Institute*, Vol. 68, pp. 244-251, 1971.

[86] Nilson A.H., "Internal measurement of bond-slip ," *Journal of the American Concrete Institute*, Vol. 69, pp. 439-441, 1972.

[87] Soretz S. and Hölzenbein H., "Influence of rib dimensions of reinforcing bars on bond and bendability." *Journal of the American Concrete Institute*, Vol. 76, No. 1, pp. 111-125, 1978.

[88] Mirza S.M. and Houde J., "Study of bond stress-slip relationships in reinforced concrete ," *Journal of the American Concrete Institute*, Vol. 76, pp. 18-46, 1979.

[89] Mitchell D. and Abrishami H.H., "Influence of splitting cracks on tension stiffening ," *ACI Structural Journal*, Vol. 93, No. 6, pp. 703-710, 1996.

[90] Tepfers R., "Cracking of concrete cover long anchored deformed reinforcing bars ," *Magazine of Concrete Research*, Vol. 31, No. 106, pp. 3-12, 1979.

[91] Darwin D. and Ebenezer K.G., "Effect of deformation height and spacing on bond strength of reinforcing bars ," *ACI Structural Journal*, Vol. 90, No. 6, pp. 646-657, 1993.

[92] Collins M P and Mitchell D, *Prestressed Concrete Structures*, Prentice Hall, Englewood Cliffs, New Jersey, USA, 766 p., 1991.

[93] Nilson A., *Finite element analysis of reinforced concrete*, PhD Thesis, University of California, Berkley, 1968.

[94] Popov E.P. (ed. By), "Thick-walled cylinders (chapter 16)," in *Mechanics of Materials* , , Macdonald and Co. Pub., London, pp. 415-421, 1952.

[95] International Organization for Standardization, "Steel for the Reinforcement of Concrete - Part 2: Ribbed Bars," ISO 6935-2:1991(E) , Switzerland, 1991.

[96] British Standards Institution, "Carbon Steel Bars for the Reinforcement of Concrete," BS 4449:1997 , London, 1997.

[97] American Society for Testing and Materials, "Deformed and Plain Billet-Steel Bars for Concrete Reinforcement," ASTM A 615/A 615M , Philadelphia, 1995.

[98] Bowie O.L. and Freese C.E., "Elastic analysis for a radial crack in a circular ring ," *Engineering Fracture Mechanics*, Vol. 4, pp. 315-321, 1972.

[99] Reinhardt H.W., "Splitting failure of a strain-softening material due to bond stresses," in *Applications of Fracture Mechanics to Reinforced Concrete (Edited by Alberto Carpenteri)*, Elsevier Applied Science, London and New York, pp. 333-346, 1992.

[100] Gerstle W., Ingraffea A.R. and Gergely P., "Tension stiffening : a fracture mechanics approach," in *Bond in Concrete* , Applied Sciences Publishers, London, pp. 98-106, 1983.

[101] Pijaudier-Cabot G., Mazars J. and Pulikowski J., "Steel-concrete bond analysis with non-local continuous damage ," *Journal of Structural Engineering - ASCE*, Vol. 117, pp. 862-882, 1991.

[102] Rots J.G., "Simulation of bond and anchorage : usefulness of softening fracture

mechanics," in *Applications of Fracture Mechanics to Reinforced Concrete (Edited by Alberto Carpenteri)*, Elsevier Applied Science, London and New York, pp. 285-306, 1992.

[103] Murray D.W. and Yao B., "Study of concrete cracking and bond using a distributed discrete crack finite element model ," *ACI Structural Journal*, Vol. 92, No. 1, pp. 93-104, 1994.

[104] El Naschie M S, *Stress, Stability and Chaos in Structural Engineering : An Energy Approach*, ISBN: 0 07 707248 0, McGraw-Hill Book Company, London, 1990.

[105] Leonhardt F. and Walther R., "Versuche an Plattenbalken mit hoher Schubbeanspruchung ," *Deutscher Ausschuss Fur Stahlbeton*, Vol. 152, 1962.

[106] Kani G.N.I., "The riddle of shear failure and its solution ," *ACI Journal*, Vol. 61, No. 4, pp. 441-465, 1964.

[107] Chana P.S., *Shear failure of reinforced concrete beams*, PhD Thesis, University of London, 256 p., 1986.

[108] Chana P.S., "Analytical and experimental studies of shear failures in reinforced concrete beams ," *Proceedings of the Institution of Civil Engineers*, Vol. 85, pp. 609-628, 1988.

[109] Zsutty T.C., "Beam shear strength prediction by analysis of existing data ," *ACI Journal*, Vol. 65, No. 11, pp. 943-951, 1968.

[110] Zsutty T.C., "Shear strength prediction for separate categories of simple beam tests ," *ACI Journal*, Vol. 68, No. 2, pp. 138-143, 1971.

[111] British Standards Institution, *Code of Practice for Design and Construction, 2nd Ed.*, ISBN: 0580262081, BSI, London, 1997.

[112] ACI Committee 318 1963 *Building Code Requirements for Reinforced Concrete* (Detroit: American Concrete Institute).

[113] ACI Committee 318 1989 *Building Code Requirements for Reinforced Concrete and Commentary (ACI 318-89)* (Detroit: American Concrete Institute).

[114] Okamura H. and Higai T., "Proposed design equation for shear strength of R.C. beams without web reinforcement ," *Proceedings of the Japanese Society of Civil Engineers*, Vol. 300, pp. 131-141, 1980.

[115] Niwa J., Yamada K., Yokozawa K. and Okamura M.p.s., "reevaluation of the equation for shear strength of R.C. beams without web reinforcement ," *Proceedings of the Japanese Society of Civil Engineers* , Vol. 5, No. 372, pp. 1986-1988, 1986.

[116] Nielson M P, Baestrup M W, Jensen B C and Bach F 1978 *Concrete Plasticity* (Lyngby: Danish Society for Structural Sciences and Engineering).

[117] Marti P., No. 104, *Zur Plastischen Berechnung Von Stahlbeton (On Plastic Analysis of Reinforced Concrete)*, Zurich, 1980.

[118] Al-Nahlawi K.A. and Wight J.K., "Beam analysis using concrete tensile strength in truss models ," *ACI Journal*, Vol. 89, No. 3, pp. 534-541, 1992.

[119] Reineck K.-H., "Ultimate shear force of structural members without transverse reinforcement derived from a mechanical model ," *ACI Structural Journal*, Vol. 88, No. 5, pp. 592-602, 1991.

[120] Collins M.P., Mitchell D., Adebar P. and Vecchio F.J., "A general shear design method ," *ACI Structural Journal*, Vol. 93, No. 1, pp. 36-45, 1996.

[121] Gustafsson P.J. and Hilerborg A., "Sensitivity in the shear strength of longitudinally reinforced beams to fracture energy of concrete ," *ACI Structural Journal*, Vol. 85, No. 3, pp. 286-294, 1988.

[122] Bazant Z.P. and Kim J.-K., "Size effect in shear failure of longitudinally reinforced

beams," *ACI Journal*, Vol. 81, pp. 456-468, 1984.

[123] Bazant Z.P. and Sun H.-H., "Size effect in the diagonal shear failure: influence of aggregate size and stirrups ," *ACI Material Journal*, Vol. 84, pp. 259-272, 1987.

[124] Jenq Y.S. and Shah S.P., "Shear resistance of reinforced concrete beams - afracture mechanics approach," in *Fracture Mechanics: Application to Concrete*, ed. by Li V. and Bazant Z.P., American Concrete Institute, Detroit, pp. 237-258, 1989.

[125] Buyukozturk O. and Hearing B., "Failure behaviour of precracked concrete beams retrofitted with FRP ," *Journal of Composites for Construction, ASCE*, Vol. 2, No. 3, pp. 138-144, 1998.

[126] Dereymaeker J., "Structural repair by epoxy bobded plates," *Proceedings of the Fifth International Conference on Structural Faults and Repair - 1993*, University of Edinburgh, 1993, ed. by Prof. M.C. Forde, Engineering Technics Press, pp. 225-231, 1993.

[127] L'Hermite R. and Bresson J., "Beton arme d'armatures collees," *RILEM International Symposium Synthetic Resins in Building Construction*, Paris, 1967, pp. 175-203, 1967.

[128] Rostasy F., Hankers C. and Ranish E., "Application of R/C and P/C-structures with bonded FRP plates," in *Advanced Composite Materials in Bridges and Structures*, Canadian Society for Civil Engineering, pp. 253-263, 1992.

[129] Jones R. and Swamy R.N., "Plate bonding - what can it do to your beams?" *Construction Repair*, Vol. 9, No. 3, pp. 43-47, 1995.

[130] Arduini M., Di Tommaso A. and Nanni A., "Brittle failure in FRP plate and sheet bonded beams ," *ACI Structural Journal*, Vol. 94, No. 4, pp. 363-370, 1997.

[131] Rostasy F.S., "Strengthening of R/C and P/C structures with bonded steel and FRP plates," *Proceedings of the Fifth International Conference on Structural Faults and Repair - 1993*,

University of Edinburgh, 1993, ed. by Prof. M.C. Forde, Engineering Technics Press, pp. 217-224, 1993.

[132] Nanni A., "Concrete repair with externally bonded FRP reinforcement ," *Concrete International*, Vol. 17, No. 6, pp. 22-26, 1995.

[133] Barboni M., Benedetti A. and Nanni A., "Carbon FRP strengthening of doubly curved precast PC shell ," *Journal of Composites for Construction, ASCE*, Vol. 1, No. 4, pp. 63-70, 1997.

[134] Arduini M. and Nanni A., "Parametric study of beams with externally bonded FRP reinforcement ," *ACI Structural Journal*, Vol. 94, No. 5, pp. 493-501, 1997.

[135] Kaiser H.P., *Bewehren von stalbeton mit kohlenstoffaserverstarker epoxidharzen*, dissertation no. 8418, ETH, Eidgenossische Technische Hochshule, Zurich, 1989.

[136] An W., Saadatmanesh H. and Ehsani M., "RC beams strengthened with FRP plates. II: Analysis and parametric study ," *Journal of Structural Engineering*, Vol. 117, No. 11, pp. 3434-3455, 1991.

[137] Jones R., Swamy R.N. and Charif A., "Plate separation and anchorage of reinforced concrete beams strengthened by epoxy-bonded steel plates ," *The Structural Engineer*, Vol. 66, No. 5, pp. 85-94, 1988.

[138] Roberts T.M., "Approximate analysis of shear and normal stress concentrations in the adhesive layer of plated RC beams ," *The Structural Engineer*, Vol. 67, No. 12, pp. 229-233, 1989.

[139] Roberts T.M. and Haji-Hazemi H., "Theoretical study of the behaviour of reinforced concrete beams strenghtened by externally bonded steel plates ," *Proceedings of the Institution of Civil Engineers*, Vol. 87, No. part 2, pp. 39-55, 1989.

[140] Sharif A., Al-Sulaimani G.J., Basunbul I.A., Baluch M.H. and Hussain M., "Strengthening of shear damage RC beams by external bonding of steel plates ," *Magazine of Concrete Research*, Vol. 47, No. 173, pp. 329-334, 1995.

[141] Mukhopadhyaya P., Swamy N. and Lynsdale C., "Optimizing structural response of beams strengthened with GFRP plates ," *Journal of Composites for Construction, ASCE*, Vol. 2, No. 2, pp. 87-95, 1998.

[142] Jansze W., Den Uijl J.A. and Walraven J.C., "Beams strengthened with bonded-on steel plates : numerical sumulation of beam shear and plate anchorage tests," *Finite Elemens in Engineering and Science*, Balkema, Rotterdam, 1997, pp. 273-284,

[143] Oehlers D.J. and Moran J.P., "Premature failure of externally plated reinforced concrete beams ," *Journal of Structural Engineering - ASCE*, Vol. 116, No. 4, pp. 978-995, 1990.

[144] Oehlers D.J., "Reinforced concrete beams with plates glued to their soffits ," *Journal of Structural Engineering - ASCE*, Vol. 118, No. 8, pp. 2023-2038, 1992.

[145] Ritchie P.A., Thomas D.A., Lu L.-W. and Connelly G.M., "External reinforcement of concrete beams using fiber reinforced plastics ," *ACI Structural Journal*, Vol. 88, No. 4, pp. 490-500, 1991.

[146] Swamy R.N., Jones R. and Bloxham J.W., "Structural behaviour of reinforced concrete beams by epoxy-bonded steel plates ," *The Structural Engineer*, Vol. 65, No. 2, pp. 59-68, 1987.

[147] Oehlers D.J., Mohamed Ali M.S. and Luo W., "Upgradng continuous reinforced concrete beams by gluing steel plates to their tension faces ," *Journal of Structural Engineering - ASCE*, Vol. 124, No. 3, pp. 224-232, 1998.

[148] Jones R., swamy R.N. and Ang T.H., "Under- and Over-reinforced concrete beams with glued steel plates ," *International Journal of Lightweight Concrete*, Vol. 4, No. 1, pp. 19-

32, 1982.

[149] Swamy R.N., Hobbs B. and Roberts M., "Structural behaviour of externally bonded steel plated RC beams after long-term exposure ," *The Structural Engineer*, Vol. 73, No. 16, pp. 255-261, 1995.

[150] Quantrill R.J., Hollaway L.C. and Thorne A.M., "Prediction of the maximum plate end stresses of FRP strengthened beams: part II ," *Magazine of Concrete Research*, Vol. 48, No. 177, pp. 343-351, 1996.

[151] Quantrill R.J., Hollaway L.C. and Thorne A.M., "Prediction of the maximum plate end stresses of FRP strengthened beams: part I ," *Magazine of Concrete Research*, Vol. 48, No. 117, pp. 343-351, 1996.

[152] Basunbul A.I., Gubati A.A., Al-Sulaimani G.J. and Baluch M.H., "Repair reinforced concrete beams ," *ACI Materials Journal*, Vol. 87, No. 4, pp. 348-354, 1990.

[153] Ziraba Y.N., Baluch M.H., Basanbul I.A., Sharif A.M., Azad A.K. and Al-Sulaimani G.J., "Guidelines towards the design of reinforced concrete beams with external plates ," *ACI Structural Journal*, Vol. 91, No. 6, pp. 639-646, 1994.

[154] Hussain M., Sharif A., Basunbul I.A., Baluch M.H. and Al-Sulaimani G.J., "Flexural behaviour of precracked reinforced concrete beams strengtened externally by steel plates ," *ACI Structural Journal*, Vol. 92, No. 1, pp. 14-22, 1995.

[155] Spadea G., Bencardino F. and Swamy R.N., "Structural behaviour of composite RC beams with externally bonded CFRP ," *Journal of Composites for Construction, ASCE*, Vol. 2, No. 3, pp. 132-137, 1998.

[156] Kim W. and White R.N., "Initiation of shear cracking in reinforced concrete beams with no web reinforcement ," *ACI Structural Journal*, Vol. 88, No. 3, pp. 301-308, 1991.